Justus Kuhlmann

Paving the way for applications of lattice QCD with stabilized Wilson fermions in charmed meson phenomenology

– 2025 –

Theoretische Physik

Paving the way for applications of lattice QCD with stabilized Wilson fermions in charmed meson phenomenology

Inaugural-Dissertation
zur Erlangung des Doktorgrades (Dr. rer. nat.)
der Naturwissenschaften im Fachbereich Physik
der Mathematisch-Naturwissenschaftlichen Fakultät
der Universität Münster

vorgelegt von
Justus Theodor Kuhlmann
aus Recklinghausen

– 2025 –

Dekan: Prof. Dr. Rudolf Bratschitsch

Erster Gutachter: Prof. Dr. Jochen Heitger

Zweiter Gutachter: Dr. Georg Bergner

Dritter Prüfer: Prof. Dr. Anton Andronic

Tag der mündlichen Prüfung: 21.10.2025

Tag der Promotion: 21.10.2025

Abstract

We investigate a young formulation of fermions on a spacetime lattice, which is called stabilized Wilson fermions and make advancements in the formulation with the motivation of investigating charm-physics. With this goal in mind, we determine several improvement coefficients and renormalization factors of quark-bilinears in a bottom-up approach. These technical constants have to be computed again, as stabilized Wilson fermions change the fermion action and therefore the cut-off effects.

Thus, we start by the determination of one of the most fundamental improvement quantities, the improvement coefficient of the axial-vector current, c_A, which can be computed with the wavefunction method. Aiming to improve and renormalize the axial-vector channel, we determine the renormalization factor Z_A next, for which the improvement coefficient is a prerequisite.

In the vector channel, the renormalization factor Z_V as well as the mass improvement coefficients to it, b_V and $\bar{b}_\mathrm{V}$, are determined as to fully renormalize this channel in the framework of stabilized Wilson fermions. Furthermore, the factors necessary for quark mass renormalization, $Z = (Z_m Z_\mathrm{P}/Z_\mathrm{A})$, $(b_\mathrm{A} - b_\mathrm{P})$ and b_m are investigated. The calculations necessary for the improvement and the renormalization are carried out in the Schrödinger functional, employing lattices with a box size of approximately 3 fm. Six different lattice spacings are investigated, with 20 ensembles interpolating between two lines of constant physics, one at the chiral limit and the other one at the $N_\mathrm{f} = 3$-symmetric point. The ensembles are designed to cater to the ensembles available from the OpenLat initiative.

We find that, as was the suspicion in early studies of stabilized Wilson fermions, the cut-off effects for stabilized Wilson fermions are generally smaller compared to traditional Wilson fermions.

A last step towards charm physics with the OpenLat ensembles is provided by the determination of the charm-quark mass parameter m_0^c. This is determined directly on the OpenLat lattices through spectroscopic quantities. Our determination includes first scaling tests, clearing the way for the investigation of charmed meson physics in the framework of stabilized Wilson fermions.

Zusammenfassung

In dieser Arbeit untersuchen wir eine junge Formulierung von Fermionen auf dem Gitter, die den Namen „stabilisierte Wilson Fermionen“ trägt und bereiten diese auf die Erforschung von Charm-Physik vor. Dafür werden Verbesserungskoeffizienten und Renormierungsfaktoren von Quark-Bilinearen in einem „Bottom-up“ Schema bestimmt. Diese technischen Konstanten müssen neu ermittelt werden, da stabilisierte Wilson Fermionen die Fermionwirkung auf dem Gitter und die damit einhergehenden Cut-Off Effekte verändern.

Daher bestimmen wir als Erstes eine der grundlegenden Verbesserungsgrößen, den Verbesserungskoeffizienten des Axial-Vektorkanals, c_{A}. Dieser kann mit der sogenannten Wellenfunktionsmethode bestimmt werden. Da wir diesen Kanal nicht nur verbessern, sondern auch renormieren wollen, berechnen wir als Nächstes die Renormierungskonstante des Axial-Vektorkanals, Z_{A}, für welche ein verbesserter Axialstrom die Voraussetzung ist.

Im Vektorkanal wird der Renormierungsfaktor Z_{V}, sowie dessen Massen-abhängigen Verbesserungskoeffizienten b_{V} und $\bar{b}_{\mathrm{V}}$ bestimmt. Mit der Bestimmung dieser drei Größen ist der Vektorkanal im Framework der stabilisierten Wilsonfermionen vollständig renormiert.

In einem weiteren Schritt werden die Faktoren $Z = (Z_m Z_{\mathrm{P}}/Z_{\mathrm{A}})$, $(b_{\mathrm{A}} - b_{\mathrm{P}})$ und b_m untersucht, welche zur Quarkmassenrenormierung nötig sind. Die zur Verbesserung und Renormierung nötigen Berechnungen werden im Schrödinger Funktional ausgeführt, auf Gittern von etwa 3 fm Gittergröße. Sechs verschiedene Gitterabstände werden untersucht, wobei die 20 verwendeten Ensembles zwischen zwei Linien konstanter Physik, eine am chiralen Limes und die andere am $N_{\mathrm{f}} = 3$-symmetrischen Punkt, interpolieren. Die Ensembles sind mit dem Ziel erstellt worden, kompatibel zu den OpenLat Ensembles zu sein.

Die Cut-off Effekte der stabilisierten Wilson-Clover Fermionen werden mit denen traditioneller Wilson Fermionen verglichen. Es stellt sich heraus, wie schon in früheren Arbeiten vermutet, dass die Cut-Off Effekte dieser neuen Formulierung generell kleiner sind als im traditionellen Fall.

Als letzten Schritt in Richtung der Untersuchung von Charm-Physik auf OpenLat Ensembles wird die Berechnung des Charm-Quark Massenparameters direkt auf den Gittern der OpenLat-Initiative mithilfe spektroskopischer Größen durchgeführt. Unsere Berechnungen in dieser Richtung beinhalten auch erste Skalierungstests des Massenparameters. Somit wird der Weg für eine Untersuchung von Mesonen mit Charm-Quarks auf Grundlage von stabilisierten Wilson Fermionen freigemacht.

Contents

1 Introduction **1**

I Groundwork **5**

2 QCD on the lattice **7**
- 2.1 A short primer on QCD . . . 7
- 2.2 On paths and lattices . . . 8
- 2.3 Simplifications . . . 12
- 2.4 Wilson fermions . . . 13
- 2.5 Symanzik improvement . . . 14
  - 2.5.1 Improvement of the gauge action . . . 14
  - 2.5.2 Improvement of the Wilson fermion action . . . 15
  - 2.5.3 Improvement of interpolators . . . 16
- 2.6 Renormalization . . . 17
- 2.7 The exponential Wilson clover action . . . 18
- 2.8 Boundary conditions . . . 19
  - 2.8.1 Periodic boundary conditions . . . 19
  - 2.8.2 Schrödinger functional boundary conditions . . . 20
- 2.9 Correlation functions . . . 21
  - 2.9.1 Two-point functions . . . 22
  - 2.9.2 Three-point functions . . . 24
  - 2.9.3 Four point functions . . . 25

3 Flavour symmetry and weak decays **27**
- 3.1 Flavour symmetry . . . 27
- 3.2 Flavour non-singlet Ward identities . . . 28
- 3.3 Weak decays . . . 30

4 Computational methods **35**
- 4.1 Markov-chain Monte Carlo . . . 36
- 4.2 The HMC and SMD algorithms . . . 36
  - 4.2.1 The Metropolis-Hastings algorithm . . . 37
  - 4.2.2 Hybrid Monte-Carlo . . . 37
  - 4.2.3 Stochastic Molecular Dynamics . . . 40
- 4.3 The Γ-method . . . 40
  - 4.3.1 The integrated auto-correlation time . . . 42
  - 4.3.2 Error estimation . . . 42
  - 4.3.3 Comparison to alternatives . . . 43
  - 4.3.4 Analysis setup . . . 44

II Improvement and Renormalization 45

5 Schrödinger functional ensembles 47
5.1 Preparatory analyses . . . 50
5.1.1 Evaluation of ϕ_4 . . . 51
5.1.2 Defining the lines of constant physics at each lattice spacing . . . 54

6 The axial-vector current 57
6.1 Improvement . . . 57
6.1.1 Improvement condition . . . 58
6.1.2 The wavefunction method . . . 59
6.1.3 Base analysis . . . 60
6.1.4 Ambiguities . . . 65
6.1.5 Choices, plateaus, and errors . . . 71
6.1.6 Interpolations . . . 73
6.1.7 Global fit . . . 77
6.1.8 Comparison to traditional Wilson clover fermions . . . 79
6.1.9 Conclusion . . . 81
6.2 Renormalization . . . 82
6.2.1 Setting up the renormalization condition . . . 82
6.2.2 Results and discussion . . . 85
6.2.3 Conclusion . . . 89

7 The vector current 91
7.1 Renormalization . . . 91
7.1.1 Setting up the renormalization condition . . . 92
7.1.2 Calculating the effective renormalization . . . 92
7.1.3 Interpolations from literature . . . 94
7.1.4 Linear and two-dimensional fits . . . 95
7.1.5 Interpolation in the coupling . . . 98
7.1.6 Comparison to traditional Wilson Clover fermions . . . 100
7.1.7 Conclusion . . . 100
7.2 Improvement . . . 101
7.2.1 Setup of the improvement condition . . . 103

8 Renormalization of the quark mass 105
8.1 The renormalized quark mass revisited . . . 105
8.2 Determination of the renormalization factors . . . 106
8.3 Analysis and encountered problems . . . 110
8.4 Possible solutions . . . 113
8.5 Conclusion . . . 114

III Meson decays and charmed physics 115

9 OpenLat ensembles 117

10 The charm-quark mass parameter 119
10.1 Determination through spectroscopy . . . 120
10.2 Scaling tests . . . 122
10.3 Conclusion . . . 125

11 Outlook **127**

12 Conclusion **131**

A The continuum approach of c_{A} **133**

B Discretization **135**
- B.1 Derivatives . . . 135
- B.2 Integration . . . 136

C Correlation functions in the Schrödinger functional **137**

Chapter 1

Introduction

The Standard Model of particle physics is the best model we have of particles and the forces governing their interactions at small scales. It describes, with stunning accuracy, the fundamental particles and forces and their interplay – except gravity. Early predictions included the existence of particles that have since been confirmed to exist, see e.g. [1] for a historical introduction. In recent years, the precision of the Standard Model has been tested to higher degrees than any other theory in physics, a prominent example is the anomalous magnetic moment of the muon [2, 3], which was determined to a precision of 127 ppb (parts per billion) by the E989 experiment at FermiLab [4–11].

Despite its success, the Standard Model fails to properly represent certain aspects of reality. Early on, for example, it was believed that neutrinos were massless. This idea had to be abandoned after neutrino oscillations were discovered, an effect that is only possible if neutrinos are massive particles. To this day, their exact mass is yet to be determined, however the upper limits on them are continuously improved, see e.g. [12].

There is also the issue of dark matter and dark energy, the effects of which cannot be explained by general relativity nor does the Standard Model provide suitable candidates for a particle based explanation. In short, we know that on large and small scales our understanding of physics is flawed. From a particle physics perspective, we try to understand these deviations from our model of gravity (i.e. general relativity) by the introduction of new particles to the Standard Model. This entails an extension of the Standard Model in such a way that these particles appear in the right amount, while not contradicting tested and established Standard Model predictions. The problem for physicists is to find those parts of the Standard Model, that are still not perfectly aligned with reality. In praxis, this search is carried out on the experimental as well as the theoretical side.

On the experimental side, tests of the Standard Model are carried out in two main ways: Direct and indirect detection. Direct detection in the high energy regime is done in accelerators, such as the LHC at CERN, whose speciality is the very high end of accessible energies. Other experiments, such as Belle-II [13, 14], BESIII [15–17] or KOTO-2 [18] extend the precision and intensity frontiers. Reference [19] gives a brief overview over the experimental prospects in this direction.

Indirect detection of dark matter through interaction with „normal“ matter, is carried out for example at the XENON experiment [20]. While plans for building new colliders are underway [21–24], we are yet several decades away from beginning to gather new data at the high energy frontier. Until then, precision tests of the Standard Model are an ideal way to solidify our understanding of the theory and point towards possible signs of new physics.

On the theoretical side, new models extending the Standard Model are built and tested against experimental results as to put exclusion limits on the proposed models. Tests of the Standard Model through high precision calculations are carried out to match experimental precision and identify tensions between the model and the data.

Prominent examples of the latter that are currently investigated are the anomalous magnetic moment of the muon $(g_\mu - 2)$ as well as the unitarity of the CKM-matrix, which both show the characteristics aimed for: The quantities in question are determinable to very high accuracy in both, theory and experiment. The CKM-matrix describes the flavour mixing of quarks, that is, the eigenstates of quarks interacting strongly and weakly are not the same. It is fully captured by three mixing angles (and a CP-violating phase), which play an important role in the weak decay of hadrons, where both, strong and weak interactions are relevant. The anomalous magnetic moment of the muon on the other hand, has, at first sight, nothing to do with hadrons. However, at higher loop orders of the interaction between the muon and the photon, hadronic polarizations of the vacuum are possible. In fact, this kind of polarization is one of the largest contributors to the overall uncertainties of the calculations [3]. Thus, both observables are directly connected to precision calculations in hadron physics.

From these examples, we can see that the search for new physics also relies on a deep understanding of hadrons. This however poses an immediate problem: Commonly, particle physics calculations rely on perturbative approximations of particle interactions. This implies the expansion in the coupling that is deemed to be small. However, the inside of a hadron cannot be examined in this way.

In this situation, we need to rely on non-perturbative techniques. The most successful approach to this problem is presented by the framework of lattice quantum chromodynamics (lattice QCD). The idea is to solve the QCD path integral by formulating QCD on a discretized spacetime lattice, allowing for the calculations of observables when the coupling is not small. The introduction of the lattice makes the path integral treatable through numerical methods. In particular, lattice calculations rely on specialized Monte-Carlo algorithms to estimate the path integral.

On the one hand, it is non-trivial to implement gauge and fermion fields on the lattice, due to various effects of discretization. On the other hand, we will also see that the formulation of the theory on the lattice leaves some freedoms of how the fields are discretized on the lattice.

A prominent choice of the formulation of fermions on the lattice is called *Wilson fermions*. While they have many advantages compared to other formulations, they suffer from cut-off effects in first order of the lattice spacing. For the precision needed from lattice predictions, the systematic errors introduced by this are not acceptable. It is therefore common to systematically add counter terms to this description of fermions. This procedure goes by the name *improvement*. The lattice formulation also introduces cut-offs at high (UV) and low (IR) energies. Thus, we also need to renormalize the quantities calculated from the lattice.

In this thesis, we want to concern ourselves with a variant of Wilson fermions, which goes by the name of *stabilized Wilson fermions*. As the name suggests, this variant introduces some changes to the common formulation of Wilson fermions in order to improve the stability of our simulations. It changes the implementation of the fermion action by exponentiating a part of it. The change guarantees, by construction, that the improved Dirac operator is positive definite, a measure that eases the instabilities introduced by low-lying eigenmodes. As changing the action impacts the cut-offs of the theory, the complete set of improvement and renormalization constants needs to be newly calculated. Our goal in this thesis is to enable the calculations of physical observables from charmed mesons in this new formulation of fermions, by determination of several prerequisites. The thesis is structured accordingly:

In the first part, we briefly review the most important concepts needed for our calculations. In chapter 2, we introduce QCD and its formulation on the lattice, focussing on the introduction of stabilized Wilson fermions. We also introduce the necessary tools for our calculations, such as Schrödinger functional boundary conditions, in which we will determine renormalization factors and improvement coefficients.

Chapter 3 will give a short introduction to the concept of flavour symmetry. Entangled with this is also the description of weak decays from the perspective of hadron physics. The part ends with a brief review of the computational methods that are employed for the evaluation of observables on the lattice in chapter 4.

The second part presents the calculation of various improvement and renormalization quantities needed in the framework of stabilized Wilson fermions. These are carried out on 20 Schrödinger functional ensembles at six lattice spacings, which are introduced in chapter 5. They are designed to cater to the large volume ensembles of the OpenLat initiative, which we will introduce later on. The ensembles interpolate between two lines of constant physics that are characterized by the chiral limit and the $N_\mathrm{f} = 3$-symmetric point and a volume of $\approx 3\,\mathrm{fm}$.

In a bottom-up approach, we start by the determination of the improvement coefficient of the axial-vector current, c_A, that is fundamental for the determination of many other quantities, as we will see. The calculation of this improvement coefficient by means of the wavefunction method is presented in section 6.1. While the method is standard by now and straightforward to implement in its basic form, the details of the calculations are quite intricate. In particular, hurdles in regard to the exact definition of the final values on each ensemble had to be overcome.

Furthermore, as the ensembles at hand interpolate between two lines of constant physics, we are able to define the improvement constant not only at the chiral limit, as usual, but also at the symmetric point. In order to leverage the full potential of the ensembles at hand, we interpolate in the coupling and a mass parameter at the same time. This interpolation also allows for the evaluation of the improvement coefficient directly at the correct mass, such that mass effects in the improvement can be included.

In section 6.2, we use the improvement coefficient in a second calculation crucial to our endeavour to prepare stabilized Wilson fermions for the calculations of physical observables. In this section, we dive into the calculation of the renormalization factor Z_A. We will see that, contrary to the improvement, the evaluation of this quantity is straightforward from a methodical perspective, however complications arise on the analytical side. This is complemented by the fact that the evaluation suffers from unexpected mass effects, as we will see.

The second quark-bilinear we want to investigate is the vector current, whose renormalization we discuss in section 7.1. As we will see, thanks to the renormalization condition having a simple expression in the Schrödinger functional, we are able to determine the overall renormalization constant Z_V as well as the mass improvements to the renormalization, b_V and $\bar{b}_\mathrm{V}$. All three factors can be estimated with quite good precision. The data produced also allows the determination of the three coefficients at the same time from a global fit.

The last chapter in this part, chapter 8, is dedicated to the determination of factors relevant for the renormalization of the quark mass: The factors $Z = (Z_m Z_\mathrm{P}/Z_\mathrm{A})$, $(b_\mathrm{A} - b_\mathrm{P})$ and b_m are needed to connect the bare quark mass, a parameter of the simulated theory with physical quark mass, a parameter of the Standard Model. The determination relies on an interpolation in the quark mass parameters, such that the renormalization factors can be evaluated at different points of the valence-quark mass. We will see, that the setup of these calculations is quite cumbersome, and some questions still remain in regard to the stability of the chosen method.

The calculations presented in part two are generally relevant for the advancement of the stabilized Wilson fermion framework. We find that, as already suspected in early studies of this variant of the Wilson fermion action, the cut-off effects observable from the improvement and renormalization factors calculated here are smaller than in the traditional Wilson-clover fermion framework.

In the last part, we provide a first determination of the mass parameter for the charm-quark. This is carried out on large volume ensembles form the OpenLat initiative, which are briefly introduced in chapter 9. At the moment, the quark-mass parameter is determined by spectroscopic quantities, in particular by employing the physical masses of the η_c- and D-meson as quantities to set the mass. Its determination by both masses is shown in chapter 10.

With the calculations we carry out, this thesis opens the door for estimations of relevant charm-physics parameters, such as semi-leptonic form factors. These form factors are crucial to estimate CKM-matrix elements. In particular, they provide another access to the quantities computed from lattice QCD that are relevant for the estimation of V_cd and V_cs. These second row elements of the CKM-matrix are needed for the investigation of whether the matrix is unitary. While the Standard Model predicts unitarity, deviations could point towards new physics in the interplay of strong and weak interactions. We give a comprehensive outlook towards the extensions of the presented calculations in chapter 11 before concluding in chapter 12.

Part I

Groundwork

Chapter 2

QCD on the lattice

Lattice quantum chromo-dynamics is the most well suited way to examine the properties of QCD in the low-energy regime. In this chapter, we will cover some relevant concepts and introduce the notation used throughout this thesis. Starting with the problems of calculating QCD quantities at low energies, we will briefly introduce the lattice approach as a possible formulation of QCD from first principles, with which these problems can be circumvented. Later on, we introduce the concrete theoretical framework this thesis is based on. Doing so will also further motivate the calculations carried out in part II, as we find well determined improvement and renormalization factors to be a necessity. In the end of the chapter, we will shortly review some practical notions.

For a more thorough treatment of the concepts discussed here, the reader may consult the well-known standard works on lattice QCD e.g., [25–27] that the overview given here is based on. Helpful are also earlier PhD theses of the group in Münster [28–31] whose concern were similar topics. A good impression of the main concepts can already be gained from [32].

2.1 A short primer on QCD

The strong force in the Standard Model is described by the theory of quantum chromo-dynamics. Quantum chromo-dynamics in its early stages was a proposal to explain the „jungle of particles“ that was discovered in the nineteen forties. It did so through the idea that mesons and baryons are – similar to the atom – constituent particles. Mesons consist of a quark — anti-quark pair ($q\bar{q}$), while baryons consist of three quarks (qqq) and the anti-baryon of three anti-quarks ($\bar{q}\bar{q}\bar{q}$) in the valence-sector. The differences in mass and electric charge between the bound quark states is explained through a difference in the type of quarks, the so-called flavour. There are 6 flavours of quarks (up, $d$own, $c$harm, $s$trange, $t$op and $b$ottom), arranged in 3 generations. Each generation consists of an isospin doublet, in which the up-type has a fractional charge of $2/3$e and the down-type has a fractional charge of $-1/3$e, in which e is the elemental charge with the electron having the charge -1e. The generations differ in mass, in that the first is lighter than the second and the second is much lighter than the third. An unexplained curiosity of the SM is the fact that in the second and third generation the positively charged quark is heavier than their negative counterparts. In the first generation, the up is lighter than the down, making the proton (not the neutron) the lightest baryon. Due to the discovery of the Ω^{--} baryon [33], an sss-state, quarks needed an additional property to account for the Pauli exclusion principle, as suggested by Greenberg [34]. This property became subsequently known as colour, which can be one of 3 (red, green, blue) and their inverse partners

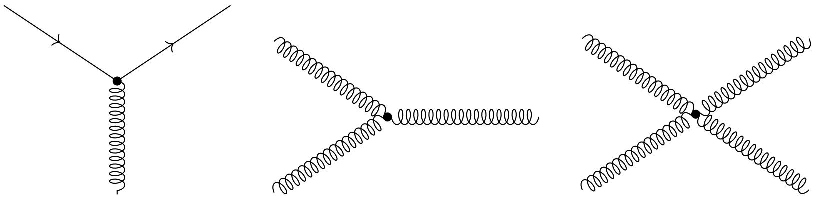

Figure 2.1: Sketches of the quark-gluon, three- and four-gluon-vertices arising from QCD Lagrangian.

(anti-red, anti-green, anti-blue). As this charge is not observed in experiments, it was proposed that nature only allows for *colourless* particles. Mesons would then have one colour and one anti-colour (e.g., red and anti-red), baryons all three colours. In principle, this would also allow for more exotic combinations, such as 4- and 5-quark bound states, that are also under investigation. The theory proposed for the proper description, coined quantum chromo-dynamics, is based on the non-Abelian gauge group, $SU(3)$. Its action $\mathcal{S}$ is given by

$$\mathcal{S} = \int \mathrm{d}^4x\mathcal{L} = \int \mathrm{d}^4x \left[\psi(\not{D}+m)\bar{\psi} - \frac{1}{4}\mathrm{tr}\left(F^2_{\mu\nu}\right)\right] \ . \tag{2.1}$$

The covariant derivative of the fermion fields

$$\not{D}\psi(x) = \left(\not{\partial} + ig\not{\mathcal{A}}^a(x)t_a\right)\,\psi(x) \tag{2.2}$$

generates a three point interaction vertex between the fermion and gauge field, shown in figure 2.1 on the left. The field-strength tensor $F_{\mu\nu}$ of the gauge field is given by

$$-igF^a_{\mu\nu} = ig(\partial\mu\mathcal{A}^a_\nu(x) - \partial_\nu\mathcal{A}^a_\mu(x)) - g^2 f^{abc}\left[\mathcal{A}_\mu(x), \mathcal{A}_\nu(x)\right] \ , \tag{2.3}$$

in which the commutator does not vanish, but instead makes the mediating particles (the gluons) interact with each other via 3 and 4 particle vertices, depicted in figure 2.1. The factors f^{abc} are the structure constants of the Lie algebra $\mathfrak{su}(3)$. Due to these gluon-self interactions, the running coupling becomes large at small energies

$$g_{\mathrm{eff}} = \left[\ln\left(q^2\Lambda^2_{\mathrm{QCD}}\right)\right]^{-\frac{1}{2}} \ , \tag{2.4}$$

in which Λ_{QCD} is the relevant scale, a parameter of the theory. This strong coupling in the low-energy regime is the reason for hadrons being strongly bound states. It is also the reason low-energy QCD cannot be treated through perturbation theory. Another first-principles approach for calculations is needed. In the past 50 years, the approach of choice was lattice QCD, which is introduced in the following.

2.2 On paths and lattices

Lattice field theory is formulated through the path integral formalism. Suppose we want to transition from a pure QCD state $\mathcal{O}$ to state $\mathcal{O}'$. The transition between them is fully governed by the QCD action introduced in equation (2.1). The path integral formalism tells us that the integral

$$\langle\mathcal{O}'\mathcal{O}\rangle = \frac{1}{Z}\int \mathcal{D}[\psi,\bar{\psi},\mathcal{A}]\ \mathcal{O}'\mathcal{O}\ e^{\mathrm{i}\mathcal{S}[\psi,\bar{\psi},\mathcal{A}]} \tag{2.5}$$

Table 2.1: Gamma structures with their respective quantum numbers and associated particles, as seen in [28, 40].

Γ-structure	quantum numbers	particles
$\mathbb{1}$	0^{++}	f_0, a_0, …
γ_0	0^{+-}	exotic
γ_5, $\gamma_5\gamma_0$	0^{-+}	π,η,K,D,D_s,η_c, …
γ_i, $\gamma_i\gamma_0$	1^{--}	ρ,ω, K^*, D^*, J/ψ, …
$\gamma_i\gamma_j$	1^{+-}	h_1, b_1, …
$\gamma_5\gamma_j$	1^{++}	a_1, f_1, …

in which ψ and $\bar{\psi}$ are the fermion fields and $\mathcal{A}$ the gauge field expresses this transition. The integration $\mathcal{D}[\psi, \bar{\psi}, \mathcal{A}]$ is understood as a symbolic way of writing the integration over the space of field configurations with each configuration being weighted by their respective probability $\left(e^{\mathrm{i}\mathcal{S}}\right)^2$. We will call this object a *correlator* as it, in fact, estimates the correlations between the states $\mathcal{O}$ and $\mathcal{O}'$.

The states $\mathcal{O}$ and $\mathcal{O}'$ are generic, however, for the cases discussed here, correlators are built of two or more 2-quark *interpolators* on a single time slice x_0. Specifically a two-quark interpolator can be written as

$$\mathcal{O}_\Gamma(x_0; \vec{x}, \vec{y}) = \bar{\psi}^a(x_0, \vec{x})\ f(\vec{x}, \vec{y}, \vec{p})\Gamma\ \psi^b(x_0, \vec{y}) \tag{2.6}$$

with Γ a matrix in Dirac- and colour-space and $f(\vec{x}, \vec{y}, \vec{p})$ a function in the 3 spatial dimensions of the theory and a, b the flavours of the participating quarks fields. The parameter $\vec{p}$ emphasized here is the 3-momentum of the bound state modelled by $\mathcal{O}$, that dictates the form of the operator in Fourier space. We note that the structures Γ, which are listed in table 2.1, prescribes the quantum numbers J^{PC} of $\mathcal{O}_\Gamma$ and that the operator generally has overlap with all states with the same quantum numbers. However, the spatial distribution $f(\vec{x}, \vec{y}, \vec{p})$ influences the overlap of the states produced by $\mathcal{O}$ with the eigenstates the Hamiltonian operator $\mathcal{H}$. There are many implications of this. We will see, that one may use this fact to excite different energy eigenstates with the same quantum numbers, an idea that is also employed in techniques like distillation [35], see e.g. [36–39] for recent examples. Similarly, the produced states may have more or less overlap with a state of specified momentum, as the spatial structure also has influence on the Fourier transform of the state. In the lattice approach, the correlation between two or more quark bilinears can be computed numerically. For the evaluation in this way, we need to discuss two issues with the path integral in equation (2.5). The appearance of the imaginary unit „i“ and the discretization of spacetime.

Wick rotation In continuous Minkowski space, the complex exponential in equation (2.5) leads to a highly oscillating term. However, a Wick rotation $t \to -\mathrm{i}\tau$ renders the term an exponential decay in imaginary time τ and the metric Euclidean. Investigating the normalization term $1/Z$, we assert $Z = \exp\{-\mathcal{S}\}$ to look similar to a partition function in statistical mechanics after the rotation.

Discretization Integrating over the space of all field configurations is not a simple task in continuous spacetime. As an approximation to Euclidean spacetime (i.e. $\mathbb{R}^4$ with euclidean metric), we introduce the idea of the lattice, a spacetime grid embedded in

Euclidean space. We define a finite set of points in $x_\mu \in \mathbb{L} \subset \mathbb{R}^4$, that are organized in the following way: The lattice spacing a between the points is equal in all directions μ, such that the smallest step possible is ae_μ, where e_μ is the unit vector in direction μ and every two directions μ and ν are orthogonal to each other. This introduces a UV cut-off, as everything over the energy associated with a cannot be accounted for on the lattice. Note that isotropic spacing is not necessary and there are lattice computations carried out with an-isotropic lattices in the time direction (see e.g. [41] for the tuning of three flavour QCD on these), which can have desirable properties for example for finite temperature [42–45], heavy quark [46–50] or glue-ball physics [51].

Furthermore, we organize the lattice points such that there are L points in each direction of space, and in time direction, there are T points. The physical dimensions of the lattice are therefore $Ta \times L^3a^3$, with $T \cdot L^3$ lattice sites. The spatial extent introduces an inherent IR cut-off. Similar to the UV cut-off, energies below the energy associated with the spatial lattice extent can also not be accounted for.

The discretization has two very direct consequences: Evidently, continuous translations and infinitesimal steps in spacetime are not allowed, such that integration and differentiation need to be replaced by finite differences, the replacements used in this thesis are listed in appendix B. Treatment of the path-integral in this way makes the space of field configurations less large. The dimension of the space of field configurations is still infinite, but to probe points in it is at least somewhat feasible. The space of all possible combinations of field values at each lattice point is called the *configuration space.*

This concludes the brief overview of how the introduction of a lattice can facilitate the calculation of the path integral. We will discuss the technical implementation of probing configuration space in chapter 4 and will first turn towards more theoretical matters. The discretization of spacetime introduces some delicate problems that need our attention. In particular, the QCD action needs to be discretized suitably. This is again done in two parts: First, the pure gauge action, then the fermion action is discretized.

The gauge action In a first step, we will ignore the fermions and discretize the part of the QCD action that only depends on the gauge fields

$$\mathcal{S}_\mathrm{G}[\mathcal{A}] = -\frac{1}{4}\int \mathrm{d}x^4\ \mathrm{tr}\left(F_{\mu\nu}^2\right)\ . \tag{2.7}$$

The covariant derivative of the fermion fields that connects it with the gauge fields will be treated later on as part of the fermion action.

In the continuum, the gauge field provides a connection

$$U(\gamma; x, y) = \mathcal{P}\left\{\exp\left\{-\mathrm{i}\int_0^1 \mathrm{d}t\ \left[\mathcal{A}^\mu(\gamma(t))\dot{\gamma}_\mu\right]\right\}\right\} \tag{2.8}$$

of two vector spaces living on two spacetime points x^μ and y^μ connected by a path γ with parametrization $t \in [0, 1] \to \gamma(t) \in \mathbb{R}^4$. Suppose we are only talking about the lattice we introduced in the last section and the paths between lattice sites are given by straight lines of length a. It is then natural to express the dependence of the action on the gauge field $\mathcal{A}$ through its dependence on the connection U_μ of neighbouring lattice points. If the lattice spacing is small, the following identity holds:

$$U_\mu(x) = \mathbb{1} - \mathrm{i}a\mathcal{A}(x) + \mathrm{O}(a^2)\ . \tag{2.9}$$

These objects are called *link variables* and are elements of $SU(3)$. They are however, unlike the field-strength tensor, not gauge invariant. To find the smallest possible gauge

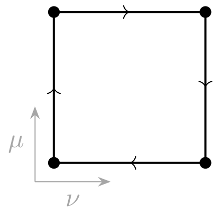

Figure 2.2: Sketch of a plaquette, a closed loop of four gauge links, as described by equation (2.10).

invariant combination on the lattice, we employ the analogous object to a Wilson loop on the lattice. The smallest possible object like this is a plaquette, an oriented path of 4 gauge links

$$P_{\mu\nu}(x) = U_\mu(x)U_\nu(x + ae_\mu)U_\mu^\dagger(x + ae_\nu)U_\nu^\dagger(x) \tag{2.10}$$

as shown in figure 2.2. It is easy to see that this object is invariant under gauge transformations. The gauge action can be expressed as

$$\mathcal{S}_\mathrm{G}[U] = \frac{2}{g_0^2}\sum_{x\in\mathbb{L}}\sum_{\mu<\nu}(\mathbb{1} - P_{\mu\nu}(x)) \ . \tag{2.11}$$

Note that this discretized version of the gauge action has discretization errors appearing in the second order of the lattice spacing. In the next section, we will push these deviations to $\mathrm{O}(a^3)$ in the lattice spacing, when discussing the improvement of the gauge action.

The fermion action The second part of the QCD action introduces the fermions (quarks) into the action. It is given by

$$\mathcal{S}_\mathrm{F}[\psi, \bar{\psi}, \mathcal{A}] = \int \mathrm{d}^4x \bar{\psi}(\not{D} + m)\psi \ . \tag{2.12}$$

The gluon-fermion interaction generated by the covariant derivative is treated in two separate ways, depending on whether the fermions are in the sea- or the valence-sector of the theory. We will see how the sea-sector will get incorporated into the gauge field configurations themselves. The effect the gauge field and the incorporated sea-sector on the valence-sector is evaluated in a separate step, which we will call *measurement* in the following. In the discretized case, contrary to the gauge field, the quark fields reside on the lattice sites x_μ. Replacing the derivative in the fermion action with symmetric finite differences yields the naive version of the fermion action

$$\mathcal{S}_\mathrm{F} = \int \mathrm{d}^4x \bar{\psi}(x)(\gamma_\mu\partial^\mu + m)\psi(x) \tag{2.13}$$

$$\Rightarrow \mathcal{S}_\mathrm{F} = \sum_{x\in\mathbb{L}}\sum_{a,b}\bar{\psi}^b(x)\gamma_\mu\frac{\psi^a(x + ae_\mu) - \psi^a(x - ae_\mu)}{2a} + \bar{\psi}^b(x)m^{ab}\psi^a(x) \tag{2.14}$$

This version of discretized fermions has a problem: The Fourier-transformed propagator

$$\tilde{D}(p) = m + \frac{\mathrm{i}}{a}\sum_{\mu=1}^{4}\gamma_\mu\sin(p_\mu a) \tag{2.15}$$

possesses unphysical poles (so-called doublers) due to the periodic behaviour of the sine-function. It shows that the most naive option for discretization is not a proper definition of fermions on the lattice. This problem is solved in different ways, and multiple fermion formulations are employed in current lattice calculations (see e.g. [25, ch. 10] for pedagogical introductions to these).

Before we introduce Wilson fermions, the discretization of choice for this work, we want to comment on some simplifications that we will be using.

2.3 Simplifications

As we are getting closer to practical calculations, we want to introduce a few simplifications that are specific to the concrete implementation of QCD in this thesis.

Pure QCD We have – so far – only looked at the formulation of pure QCD on the lattice, and we will keep it this way. The six quark flavours interact with the weak, the strong and the electromagnetic gauge bosons. In chapter 3 we will comment on how weak decays are recovered in the framework at hand.

The electric charges are neglected here, which is a common choice, as the expected deviations are below 1% (c.f. [52, ch. 3]). Note that these effects become relevant in recent years of lattice QCD calculations, and first steps towards including QED effects in directly lattice calculations are made, e.g., in [53–58]. Neglecting these charges restores isospin symmetry and renders the 6 quarks only different in terms of their masses.

Quark flavours As the masses of the different flavours are vastly different, it is customary to make another approximation:

The theory described in lattice QCD simulations is usually an effective theory with less than six flavours. This is due to the following reasons: The top and bottom quark are very heavy. Their exclusion from lattice simulations is on one hand of technical nature, as the lattice spacings needed for dynamical simulations with these flavours would be too fine for state-of-the-art lattice simulations. The top quark does not admit bound states in experiments as it decays very fast (see [59] for a review of top-quark physics) and is therefore not of interest for calculations in the low-energy regime with bound states. Note that partially quenched calculations including the bottom quark can be carried out on the lattice, by using the HQET framework, in which the theory is expanded in inverse quark masses, followed by an interpolation between multiple (heavy) valence-quarks and a static quark with infinite mass. Works in this direction are found for example in [60–62].

In [63] it was shown that charm effects in the sea can also be estimated to be below 1%. As current simulations are only just reaching this level of precision, it is also common to exclude dynamical charm-quarks. Works with dynamical charm-quarks are abundant in recent years, see [52] and references therein. In this work, we will reintroduce charm-quarks later on only in the valence-sector. Theories of this kind are known as partially quenched. Overall, we end up with three quarks in the sea $f \in \{\mathrm{u}, \mathrm{d}, \mathrm{s}\}$.

Quark masses The simplifications discussed are finalized by setting the masses of the sea-quarks to the same value,

$$m_{\mathrm{u}} = m_{\mathrm{d}} = m_{\mathrm{s}} = m_l \, , \tag{2.16}$$

we call the mass m_l the light-quark mass. The quark mass matrix is therefore given by

$$M_{\mathrm{q}} = m_l \, \mathbb{1}_{3\times 3} \, . \tag{2.17}$$

The specific value chosen is unimportant for now, it is however customary to simulate quarks at much larger masses than their physical masses. This renders the extrapolation towards the physical continuum harder to execute, but the gain in computational time outweighs this drawback. We will call mesons in our theory with unphysical masses by the names of their physical counterparts (e.g., a pseudo-scalar $l\bar{l}$-state is a pion, etc.). The pion mass is a good measure of how far we are from the physical point. In the large volume ensembles we will employ pion masses of $m_\pi \approx 400$ MeV, while the mass of the physical charged pion is only $m_{\pi^\pm} = 139.57039 \pm 0.00017$ MeV [64]. On a last note, we will call the point at which $\mathrm{Tr}\left\{M_\mathrm{q}\right\} = \mathrm{Tr}\left\{M_\mathrm{q}^\mathrm{phys}\right\} = m_\mathrm{u}+m_\mathrm{d}+m_\mathrm{s}$ the $N_\mathrm{f} = 3$-symmetric point.

2.4 Wilson fermions

The naive fermion discretization that we introduced in equation (2.14) had fermion doublers that appeared due to the sine-function in the Fourier transformed propagator. Early on, Wilson found a way to circumvent this pitfall of the naive formulation [65]. He introduced the *Wilson term* that augments the naive action in the following way:

$$\mathcal{S}_\mathrm{F} \to \mathcal{S}_\mathrm{W} = \mathcal{S}_\mathrm{F} + \frac{a}{2}\bar{\psi}(x)\hat{\partial}_\mu^2 U_\mu(x)\psi(y) = \bar{\psi}(x) D_W \psi(y) \ . \tag{2.18}$$

The Fourier transformed Dirac operator of this action receives an additional term

$$\tilde{D}(p) \to \tilde{D}_\mathrm{W}(p) = m + \frac{\mathrm{i}}{a}\sum_{\mu=1}^{4} \gamma_\mu \sin(p_\mu a) + \frac{1}{a}\sum_{\mu=1}^{4}(1-\cos(p_\mu a)) \ , \tag{2.19}$$

which can be seen as an additional mass term only affecting the doublers. In the continuum limit $a \to 0$, the doublers become infinitely heavy and can be integrated out. This trick proves very valuable, however the price to pay is that chiral symmetry is broken explicitly by this term, even when the quark mass is set to zero. As to regain a proper notion of the quark mass, we introduce the subtracted quark mass

$$m_\mathrm{q} = m_0 - m_\mathrm{crit} \ , \tag{2.20}$$

which is zero when the chiral limit is reached. The critical point is parametrized by m_crit, which is a measure of how badly the symmetry is broken. Note that m_crit can only be extracted from an observable that is proportional to the quark mass and tuning it to 0 (prime candidates that we will introduce later are the effective mass in the axial-vector channel or the PCAC mass). At this point, let us also introduce the hopping parameter

$$\kappa = \frac{1}{2am_0 + 8} \tag{2.21}$$

which commonly parametrizes the mass of quarks on the lattice. Note that the hopping parameter depends on m_0, which does not vanish at zero quark mass as per equation (2.20). The subtracted quark mass in terms of this parameter is then given as

$$m_\mathrm{q} = \frac{1}{2a}\left(\frac{1}{\kappa} - \frac{1}{\kappa_\mathrm{crit}}\right) \ . \tag{2.22}$$

Furthermore, deviations in the first order of the lattice spacing appear, making the continuum extrapolation prone to systematic errors. To make continuum extrapolations within second order of the lattice spacing, like the naive gauge action, we need to introduce counter terms that lift discretization effects in the first order. This can be achieved systematically with the Symanzik improvement program.

2.5 Symanzik improvement

When we introduced the gauge action, we had seen that its ambiguities are of order $\mathrm{O}(a^2)$. In the case of the fermions, the ambiguities introduced through discretization were even of $\mathrm{O}(a)$. This is – in principle – not a problem, however the systematic errors picked up through these ambiguities may spoil the calculation of sensitive quantities. We are therefore interested in setting up an improved approach from the lattice to the continuum. The systematic way to reduce lattice effects was formulated by Symanzik [66]. It relies on the idea that continuum QCD can be viewed as a fundamental theory to the lattice theory. This effective description is valid up to the cut-off introduced by the lattice spacing. In this regard, it is natural to expand the action in terms of the lattice spacing a, such that the action is represented by the power series

$$\mathcal{S} = \mathcal{S}_0 + c_1 a\ \mathcal{S}_1 + c_2 a^2\ \mathcal{S}_2 + c_3 a^3\ \mathcal{S}_3 + \dots \tag{2.23}$$

in which $\mathcal{S}_i$ are terms of dimension $4+i$. They contribute at the i-th order of the lattice spacing with the c_i being the appropriate coefficients. Similarly, an operator $\mathcal{O}$ is also only an effective description of its continuum counterpart, such that they can be written as

$$\mathcal{O} = \mathcal{O}_0 + c_1 a\ \mathcal{O}_1 + c_2 a^2\ \mathcal{O}_2 + c_3 a^3\ \mathcal{O}_3 + \dots\ . \tag{2.24}$$

The coefficients can be obtained in multiple ways, either through perturbative calculations, renormalization group transformations (for an introduction see e.g., [25, ch. 9.2]) or non-perturbative calculations, as carried out later on. In the following, we will briefly discuss the terms added to the action as well as to two currents in particular, the non-singlet axial-vector and vector current.

2.5.1 Improvement of the gauge action

Improving the gauge action is standard in current calculations. In particular, the gauge action is usually augmented by including larger plaquette-like objects. In the practical calculations carried out later, a form of the tree-level Symanzik improved gauge action, introduced in [67–69],

$$\mathcal{S}_\mathrm{G} = \sum_{x \in \mathbb{L}} \frac{2}{g_0^2} \left(\frac{5}{3} (\mathbb{1} - P_{\mu\nu}(x)) - \frac{1}{12} (\mathbb{1} - R_{\mu\nu}(x)) \right) \tag{2.25}$$

is employed. This is also known as the Lüscher-Weisz action. It improves the accuracy of the gauge action to third order in the lattice spacing by including a term proportional to closed loops of 6 link variables. These have rectangular shape and are denoted by $R_{\mu\nu}(x)$ (possible shapes are shown in figure 2.3). The choice presented here relies only on rectangular contributions in figure 2.3a) with no „bent“ contributions. A popular alternative for the choice of the prefactors was introduced in [70] by Iwasaki on grounds of renormalization group analyses.

In principle, it is possible to use even larger gauge-link loops to improve the gauge field action to higher orders. So-called perfect or fixed point actions take this idea to the extreme. They are also based on renormalization group transformations and have been studied already in the nineties, for example in [71–73]. In recent years, there have been efforts [74, 75] to rely on machine learning techniques to extract the coefficients for these highly improved actions.

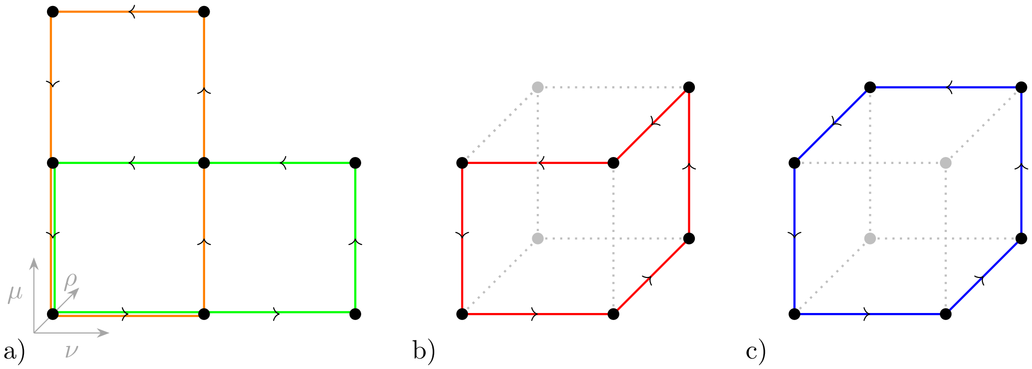

Figure 2.3: Sketch of the possible expansions of the plaquette in the Symanzik improved gauge action.

2.5.2 Improvement of the Wilson fermion action

While the introduction of discretization effects of O(a) by the Wilson term – in principle – does not pose a problem, the systematic errors of the approach towards the continuum would make predictions from Wilson fermions weaker. Similar to the gauge action, we are interested to add counter terms to the fermionic part of the Wilson Dirac operator from equation (2.18).

Writing down all dimension-5 terms that transform like the action

$$\mathcal{S}_1^{(1)} = \bar{\psi}(x)\sigma_{\mu\nu}F_{\mu\nu}(x)\psi(x) \ , \tag{2.26a}$$

$$\mathcal{S}_2^{(1)} = \bar{\psi}(x)\left(D_\mu D_\mu + \overleftarrow{D}_\mu \overleftarrow{D}_\mu\right)\psi(x) \ , \tag{2.26b}$$

$$\mathcal{S}_3^{(1)} = m \ \mathrm{Tr}\left\{F_{\mu\nu}(x)^2\right\} \ , \tag{2.26c}$$

$$\mathcal{S}_4^{(1)} = m \ \bar{\psi}(x)\left(\gamma_\mu D_\mu - \gamma_\mu \overleftarrow{D}_\mu\right)\psi(x) \ , \tag{2.26d}$$

$$\mathcal{S}_5^{(1)} = m^2 \ \bar{\psi}(x)\psi(x) \ , \tag{2.26e}$$

we find that (2.26b) and (2.26d) can be related to (2.26a) through the field equation. Equations (2.26c) and (2.26e) can be absorbed into the renormalization, as we will discuss later. The only term that survives, (2.26a), is added to the Wilson action

$$\mathcal{S}_\mathrm{W}^\mathrm{I} = \mathcal{S}_\mathrm{W} + c_\mathrm{sw} a^5 \sum_{x\in\mathbb{L}} \sum_{\mu<\nu} \bar{\psi}(x)\frac{1}{2}\sigma_{\mu\nu}F_{\mu\nu}(x)\psi(x) \tag{2.27}$$

in which the field-strength tensor is of discretized form and $\sigma_{\mu\nu} = [\gamma_\mu, \gamma_\nu]$. This is the Sheikholeslami-Wohlert term [76], also known as the clover term, due to its form that is, in two dimensions, reminiscent of a clover leaf (see figure 2.4). The improved Wilson action is therefore also known as *Wilson-clover* action. It is obvious, but nevertheless noteworthy that this action recovers the correct continuum action, as the improvement term is linear in the lattice spacing a. What is left is the determination of the prefactor of the clover term, c_sw. While in case of the gauge action it was sufficient to consider perturbatively calculated tree-level values, in case of the fermion action it is necessary to determine it non-perturbatively. In [77, 78] early discussions in the quenched approach have been carried out, and later on [79–84] followed up with various determinations in two- and three-flavour setups.

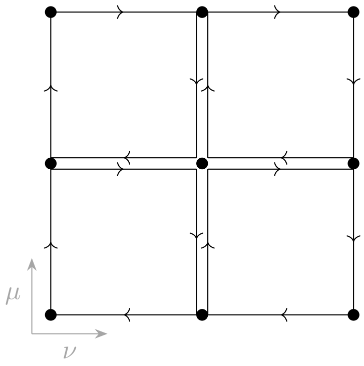

Figure 2.4: Sketch of the clover term in two dimensions. Equation (2.27) describes the four dimensional generalization.

Before carrying on with the improvement of interpolators, we comment that the clover-term is not positive definite. This is important, as this hampers simulations of lattice QCD with Wilson-clover fermions.

2.5.3 Improvement of interpolators

We have seen that, after absorbing the rest into renormalization or using relations between the possible terms, the Wilson action can be improved by adding only one counter-term. The effective descriptions of the interpolators $\mathcal{O}_\Gamma$ on the lattice are treated similarly. Seeing them as effective descriptions of the continuum interpolators, we also add terms with higher dimension. As with the prefactor c_{sw}, the suitable prefactor needs to be determined non-perturbatively.

In this work, we concentrate on the improvement and renormalization of the axial-vector current and the vector current. For a more general discussion, the reader may be referred to [85]. The improvement terms needed for the two currents can be constructed analogously to the improvement of the action just discussed:

The non-singlet axial-vector current For the axial-vector current, there are three dimension-4 terms that are allowed

$$\left(\mathrm{A}_1^{(1)}\right)_\mu^a(x) = \bar{\psi}(x)\;\gamma_5(D_\mu - \overleftarrow{D}_\mu)\frac{\lambda^a}{2}\;\psi(x) \tag{2.28a}$$

$$\left(\mathrm{A}_2^{(1)}\right)_\mu^a(x) = \partial_\mu\left(\bar{\psi}(x)\;\gamma_5\frac{\lambda^a}{2}\;\psi(x)\right) \qquad = \partial_\mu \mathrm{P}^a(x) \tag{2.28b}$$

$$\left(\mathrm{A}_3^{(1)}\right)_\mu^a(x) = m\;\bar{\psi}(x)\;\gamma_\mu\gamma_5\frac{\lambda^a}{2}\;\psi(x) \qquad = m\mathrm{A}_\mu^a(x) \tag{2.28c}$$

out of which (2.28a) can again be related to the other two by the Dirac equation. The Gell-Mann matrices λ^a appearing here act on the flavour indices of the fields ψ. As in case of the action, (2.28c) can be absorbed into the renormalization coefficient, such that the axial vector current A_μ^a is also improved by only a single term, (2.28b), as shown in [77,86] (cf. [25, ch. 9.1.3]). The $O(a)$-improved axial vector current therefore takes the form

$$\left(\mathrm{A}_\mathrm{I}\right)_\mu^a(x) = \mathrm{A}_\mu^a(x) + ac_\mathrm{A}\partial_\mu \mathrm{P}^a(x)\;, \tag{2.29}$$

where the improvement factor c_{A} is to be determined non-perturbatively. Determining this factor is one of the main goals of this thesis and will be worked out explicitly in section 6.1.

The non-singlet vector current The vector current receives improvement similarly. As discussed in [85], the terms

$$\left(\mathrm{V}_1^{(1)}\right)_\mu^a(x) = \mathrm{i}\; m\; \bar{\psi}\gamma_\mu \frac{\lambda^a}{2}\psi \qquad = m\mathrm{V}_\mu^a \tag{2.30a}$$

$$\left(\mathrm{V}_2^{(2)}\right)_\mu^a(x) = \mathrm{i}\; \bar{\psi}(D_\mu - \overleftarrow{D}_\mu)\frac{\lambda^a}{2}\psi \tag{2.30b}$$

$$\left(\mathrm{V}_3^{(3)}\right)_\mu^a(x) = \mathrm{i}\; \bar{\psi}\sigma_{\mu\nu}(D_\nu + \overleftarrow{D}_\nu)\frac{\lambda^a}{2}\psi \qquad = \partial_\nu \mathrm{T}_{\mu\nu}^a \tag{2.30c}$$

transform in the right way to be added to the vector current (see also [28, ch. 1.4]). This time, (2.30b) is eliminated by the field equations, while (2.30a) is of the same form as the vector current itself and is absorbed into the renormalization coefficient. The improved vector current is therefore of the form

$$(\mathrm{V}_{\mathrm{I}})_\mu^a(x) = \mathrm{V}_\mu^a(x) + ac_{\mathrm{V}}\partial_\nu \mathrm{T}_{\nu\mu}^a(x)\;. \tag{2.31}$$

The determination of c_{V} is also to be carried out non-perturbatively. We will see in section 7.2 that the setup for this determination needs direct input from the other determinations carried out here. We only discuss it shortly to see how it is affected by our results. First steps towards improvement of the exponential Wilson Clover framework worked on here have been made in [87].

2.6 Renormalization

As usual in quantum field theory, we have introduced a cut-off, in our case through the lattice spacing a (and a second one through the lattice extent). Calculated physical quantities therefore need to be renormalized. This can be done in various schemes, of which the Wilsonian renormalization group approach is the most common one on the lattice. We omit the general introduction to renormalization and advise the reader to consult the well known literature, such as [88, ch. 23] and the look into the Wilsonian and continuum way of renormalization given in [28]. Here, we oriented ourselves on the discussion in [29].

When improving the action, two terms were absorbed into the renormalization of the gauge coupling (cf. equation (2.26c)) and the quark mass (cf. equation (2.26e)). Both of which add a quark mass dependent term to the renormalized action. In fact, by chiral perturbation theory arguments, one finds that the subtracted quark mass m_{q} is only renormalized multiplicatively, such that it can be written as

$$m_{\mathrm{R}} = Z_m m_{\mathrm{q}}\;. \tag{2.32}$$

The renormalization factor Z_m is dependent on the scale μ that is fixed e.g., by the hadronic scheme. However, we will see later that this dependence drops out in the calculations carried out here. As extensively discussed in [85], away from the chiral limit, a plethora of new renormalization constants appear. For the quark mass, the renormalization factor is augmented by the mass dependent term from improvement and terms that come from higher orders in perturbation theory, multiplying the quark mass matrix. The complete expression is of the form

$$m_\mathrm{R} = Z_m \left\{ \left[m_\mathrm{q} + (r_m - 1)\frac{\mathrm{Tr}\left\{M_\mathrm{q}\right\}}{N_\mathrm{f}} \right] + aB_i \right\} + \mathrm{O}(a^2) \tag{2.33}$$

$$\begin{aligned} B_i = {} & b_m m_\mathrm{q}^2 + \bar{b}_m m_\mathrm{q} \mathrm{Tr}\left\{M_\mathrm{q}\right\} + (r_\mathrm{m} d_\mathrm{m} - b_m)\frac{\mathrm{Tr}\left\{M_\mathrm{q}^2\right\}}{N_\mathrm{f}} \\ & + (r_m \bar{d}_m - \bar{b}_m)\frac{\mathrm{Tr}\left\{M_\mathrm{q}\right\}^2}{N_\mathrm{f}} \ . \end{aligned} \tag{2.33a}$$

See [89] for a concise discussion of the different terms multiplying $\mathrm{Tr}\left\{M_\mathrm{q}\right\}$ and how they relate to the appearing loops. We can see that the renormalization is quite convoluted, when massive sea-quarks are present. In chapter 8, we will look into this calculation with chiral sea-quarks, employing the relation of the quark mass to the PCAC mass. The bare coupling itself is also renormalized [77] and receives an additional term through improvement,

$$\tilde{g}_0^2 = \left(1 + b_g a \mathrm{Tr}\left\{M_\mathrm{q}\right\}\right) g_0^2 \ , \tag{2.34}$$

which is then used to renormalize the coupling

$$g_\mathrm{R}^2 = Z_g(\tilde{g}_0^2, a\mu)\tilde{g}_0^2 \ . \tag{2.35}$$

We will not dive into the determination of these renormalization constants, however the determination of b_g for Wilson clover fermions is carried out in [90]. The meaning of b_g is somewhat interesting. As the coupling is (non-trivially) connected to the lattice spacing, we infer from this term that quantum effects of the simulated quarks change the lattice spacing. We will discuss this shortly in chapter 5.1.1, as we would have to slightly shift all values calculated based on this influence. In this work, this is avoided by defining the lattice spacing at a certain quark mass (i.e., at the $N_\mathrm{f} = 3$-symmetric point).

Apart from the action, the currents of interest are also to be renormalized. Similar to the action, we employ a massless renormalization scheme [85, 91], meaning the renormalized and improved currents are expressed as

$$\mathcal{O}_\mathrm{RI} = Z_\mathcal{O}\left(1 + b_\mathcal{O} a m_\mathrm{q} + \bar{b}_\mathcal{O} a \mathrm{Tr}\left\{M_\mathrm{q}\right\}\right)\left(\mathcal{O} + a c_\mathcal{O} \mathcal{Q}\right) \ . \tag{2.36}$$

As before, the overall renormalization constant $Z_\mathcal{O}$ is augmented by mass dependent terms, that come from the improvement, as we just discussed, meaning that renormalization and improvement are not clearly distinguishable. We will call these terms *improvement terms to the renormalization* for the rest of this work. In the last section, we have seen that mass dependent terms $b_\mathcal{O}$ are expected. However, working with non-chiral sea-quarks allows for terms dependent on the trace of sea-quark masses $\mathrm{Tr}\left\{M_\mathrm{q}\right\}$ to appear at two-loop order in perturbation theory. Reference [85] distinguishes between them, while some earlier works only introduce one improvement factor. We will see that the introduction of both factors is important when working with valence-quarks of masses other than the degenerate sea-quark mass.

In the presented studies, we will determine all three coefficients for the vector current, Z_V, b_V and $\bar{b}_\mathrm{V}$, as well as the renormalization Z_A for the axial-vector current.

2.7 The exponential Wilson clover action

When introducing the discretized actions for the gauge and fermion fields, we have seen that there are freedoms in the choice of the discretization. The alterations that we have introduced thus far in order to arrive at improved Wilson fermions always targeted specific problems with the preceding action.

As the clover term is not guaranteed to be positive definite, the inversion of the Dirac operator needed in the gauge field simulation and the calculation of observables may be hampered. Hence, we have an action that is has good properties in terms of its convergence towards the continuum, however it is evidently worse in terms of how well it can be simulated. This is especially a problem when simulating on very large lattices, such as the lattices needed for the master-field approach [92]. To accomplish the needed stability of the simulation algorithm, an alternative definition of the clover term in equation (2.27) was introduced in [93]. The specific form chosen relies on a short-cut to inverting the Dirac operator that we will introduce later on, when we look at the computational aspects of lattice QCD in more detail. For now, we state that there is a way to only calculate parts of the Dirac operator and infer the rest of it through the symmetries of the lattice. This is called even-odd preconditioning and is a standard technique for lattice computations. For now, it is only important that this preconditioning technique will split the Wilson Dirac operator into a form

$$D_{\mathrm{W}} = \begin{pmatrix} D_{\mathrm{ee}} & D_{\mathrm{eo}} \\ D_{\mathrm{oe}} & D_{\mathrm{oo}} \end{pmatrix} \tag{2.37}$$

In which o designates the odd sites of a given lattice and e the even sites. The proposed fermion action replaces the diagonal entries of the even-odd preconditioned Dirac operator, such that they are given by an exponentiated version of themselves:

$$D_{\mathrm{ee}} + D_{\mathrm{oo}} = (4+m_0) + ac_{\mathrm{sw}}\frac{\mathrm{i}}{4}\sigma_{\mu\nu}\hat{F}_{\mu\nu} \rightarrow (4+m_0)\exp\left\{\frac{ac_{\mathrm{sw}}}{4+m_0}\frac{\mathrm{i}}{4}\sigma_{\mu\nu}\hat{F}_{\mu\nu}\right\}\ , \tag{2.38}$$

which, when expanded in powers of the lattice spacing a returns the clover term if truncated after the first order. However, the great advantage of this form of the Wilson clover action is that, by construction, this term *is* positive definite, thereby stabilizing the simulation. Stabilized Wilson clover fermions, as introduced by the OpenLat initiative in [93], employ this action. They also introduce further stabilizing measures such as the use of a specific Monte Carlo algorithm (SMD), which we will also discuss later on.

2.8 Boundary conditions

At this point it is worth to discuss another aspect of lattice gauge theories. The lattice always being of finite size leads to a decision on how to treat the boundaries. In lattice QCD in particular, three types of boundary conditions, *fixed*, *periodic* and *open*, and possible combinations of them are usual.

We will have a look into two particular choices: The Schrödinger functional, which is periodic in space and fixed in time and periodic boundary conditions in all spacetime dimensions, which both play a role in the context of this thesis.

2.8.1 Periodic boundary conditions

A simple representation of infinite spacetime with a finite number of points is to impose periodicity in all directions. Employing periodic boundary conditions in all directions saves translational symmetry in its most complete form on the lattice. This is employed in many fields of physics, for example also in condensed matter physics, as the highly symmetrical construction of these boundaries makes calculations easier. Due to the saved translational symmetries, they also come closer to the physical world in this regard. For

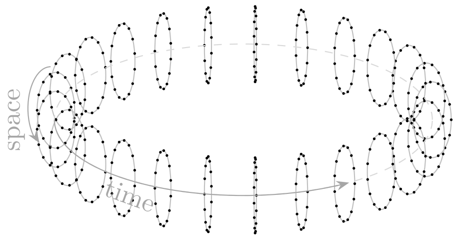

Figure 2.5: Sketch of a lattice with periodic boundary conditions. The point-to-point connections in time are omitted here for readability.

lattice QCD, these boundary conditions have one particular computational advantage. They allow us to also exploit temporal translations in order to reduce correlations between two calculations on successive Monte-Carlo steps or extend the statistics of the calculations inexpensively. The drawback of these boundary conditions is, that in correlation functions, which we will discuss in section 2.9, quarks are allowed to wrap around the lattice and come back. In modern calculations, however, these around-the-world effects can be neglected due to the rather large temporal lattice extents. This will also be the case later on in part III, where the lattices employed have temporal extents of 6 to 12 fm.

2.8.2 Schrödinger functional boundary conditions

The Schrödinger functional is the quantum field theoretical equivalent to the Schrödinger picture in quantum mechanics, meaning that we see the reaction as a time-evolution of the fields. In particular, the state of the fields is fixed at both time boundaries.

It is essential to the calculations that are carried out in the projects presented. These boundary conditions have been introduced in [94] and were extended to gauge fields and full QCD in [95,96]. In particular, it is of interest for the improvement and renormalization studies, as we are able to work very close to and at the chiral limit. This property comes from a spectral gap appearing in the Dirac operator of Schrödinger functional boundary conditions [97], which is bounded from below for positive quark masses. The obvious practical upside is that, when employing a massless renormalization scheme, the mass dependence is factored out explicitly. If we are able to work in the chiral limit, the massive parts drop out, giving direct access to the renormalization factors. Additionally, as we will see later on, the determination of these factors and of some improvement constants can be done through chiral Ward identities which have to be evaluated in the chiral limit.

In any case, the boundaries are composed as follows: In time direction, we have fixed Dirichlet boundary conditions, while in spatial direction, they are periodic for the gauge fields and anti-periodic for the fermion fields. A typical sketch of these boundary conditions is shown in figure 2.6. On the time-like boundaries, the fields have to be identified with functional derivatives of the action towards parity projected fields

$$\rho = P_+\psi(x)|_{x_0=0}\,,\; \rho' = P_-\psi(x)|_{x_0=T}\;, \tag{2.39a}$$

$$\bar\rho = \bar\psi(x)P_-|_{x_0=0}\,,\; \bar\rho' = \bar\psi(x)P_+|_{x_0=T}\;, \tag{2.39b}$$

in which P_+ and P_- are the positive and negative parity projectors, respectively. The

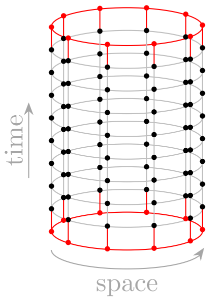

Figure 2.6: Sketch of a lattice with Schrödinger functional boundary conditions. The red points and lines are fixed fields in this approach.

boundary fields are then defined as

$$\zeta(\vec{x}) \mathrel{\hat{=}} -\frac{\partial \mathcal{S}}{\partial \bar{\rho}(\vec{x})} = \tilde{c}_t P_- U_0(0,\vec{x})\psi(a,\vec{x}) \;, \tag{2.40a}$$

$$\bar{\zeta}(\vec{x}) \mathrel{\hat{=}} +\frac{\partial \mathcal{S}}{\partial \rho(\vec{x})} = \tilde{c}_t \bar{\psi}(a,\vec{x}) P_+ U_0^\dagger(0,\vec{x}) \;, \tag{2.40b}$$

$$\zeta'(\vec{x}) \mathrel{\hat{=}} -\frac{\partial \mathcal{S}}{\partial \bar{\rho}'(\vec{x})} = \tilde{c}_t P_+ U_0^\dagger(T-a,\vec{x})\psi(T-a,\vec{x}) \;, \tag{2.40c}$$

$$\bar{\zeta}'(\vec{x}) \mathrel{\hat{=}} +\frac{\partial \mathcal{S}}{\partial \rho'(\vec{x})} = \tilde{c}_t \bar{\psi}(T-a,\vec{x}) P_- U_0(T-a,\vec{x}) \;. \tag{2.40d}$$

The fields receive an extra boundary improvement $\tilde{c}_t$, see [77, 95] for a discussion. For a more thorough discussion of Schrödinger functional boundary conditions and the boundary fields, the reader may be referred to [28, ch. 1.5] and [31, ch. 3.8] that this short review is based on. From the projectors in the fields, it follows that the possible Γ-matrices on the boundaries of the Schrödinger functional are restricted, as the constructed mesons are $\bar{\zeta}\zeta$ states and therefore bracket the Dirac structures as $P_+\Gamma P_-$ on the lower and $P_-\Gamma' P_+$ on the upper boundary. The allowed Dirac matrices are γ_5, $\gamma_0\gamma_5$, γ_i, $\gamma_0\gamma_i$. The parity projectors also mix the structures γ_5 and $\gamma_0\gamma_5$ and also γ_i and $\gamma_0\gamma_i$ with each other, such that calculations with only γ_5 and γ_i suffice. In the next section, we will discuss the possible contractions of the fields, that are called correlation functions.

2.9 Correlation functions

Now we have built the theoretical foundation of what we are trying to achieve. On the practical side, the evaluation of all quantities we are interested in are handled through correlators, or correlation functions. We will use these words interchangeably.

In our case, the correlation functions are built from two or more interpolators. In particular, we will need functions with two, three, and four points of interpolator insertion in the quark lines for the definitions we are investigating. The concrete evaluation of them is dependent on the quark flavours. However, in most cases, the flavours are chosen in such a way, that only the connected diagrams are left after Wick contraction.

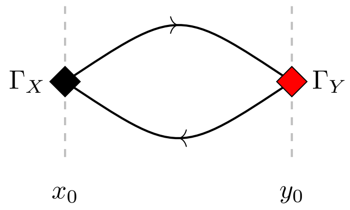

Figure 2.7: Sketch of a generic 2-point correlation function, inspired by [28, fig. 1.2]. In the following, we refer to the black diamond as the source term and the red diamond as the sink term.

2.9.1 Two-point functions

The simplest correlation functions we can build are 2-point functions:

$$\begin{aligned} C_{XY} &= \sum_{\vec{v},\vec{w},\vec{x},\vec{y}} \langle \mathcal{O}_Y(t_2,\vec{w},\vec{y})^{ab} \;\; \mathcal{O}'_X(t_1,\vec{v},\vec{x})^{ba} \rangle \\ &= \sum_{\vec{v},\vec{w},\vec{x},\vec{y}} \langle \bar{\psi}^a(t_2,\vec{w})\Gamma_Y\psi^b(t_2,\vec{y}) \;\; \bar{\psi}^b(t_1,\vec{v})\Gamma_X\psi^a(t_1,\vec{x})\rangle \end{aligned} \tag{2.41}$$

Note the superscripts of the quark fields, which are the flavours chosen in such a way that the disconnected (point-to-point) diagrams drop out, see e.g., [28, eq. (1.33)] for the derivation. In equation (2.41), Γ_X and Γ_Y can be matrices in Dirac space, compare the Γ-structures in table 2.1. These can however also be extended to include derivatives. Carrying out the Wick contractions, only quark-connected terms survive, whose diagrams are depicted in figure 2.7. We call the interpolator at t_1 the *source*, and the interpolator at t_2 the *sink*. We can introduce functions $f : \mathbb{R}^3 \times \mathbb{R}^3 \to \mathbb{R}$, as in equation (2.6) in spatial directions at the time slices t_1 and t_2, such that the quarks and anti-quarks are not created at the same point in space or are smeared out. In physical applications, this can dramatically improve the overlap between the created state and e.g., the meson state targeted. This will also come in handy in section 6.1.2, where exactly this property is exploited.

Note that the positioning of the source and the sink are generally not predetermined. In the boundary conditions introduced, the following is, however, natural: In periodic boundary conditions, we have full discretized temporal symmetry, such that the correlator is (anti-)symmetric in time, where the symmetry properties are fully determined by the Dirac structure of the interpolators. We choose the time slice t_1 of the source to be the origin. In the Schrödinger functional, temporal symmetry is broken by the fixed boundaries. The natural choices for the source time slice are therefore $t_1 = 0$ or $t_1 = T$, as can be seen in figure 2.8.

We can write the QCD transition amplitude from equation (2.5) by employing the time evolution operator $\mathcal{T}$ in Euclidean time. As already discussed, the states produced by the interpolators $\mathcal{O}$ have overlap with all energy states $|n\rangle$ with the same quantum numbers. The 2-point correlation function is then equal to

$$\begin{aligned} C_{XX} &= \langle \mathcal{O}^\dagger(t_2)\mathcal{O}(t_1)\rangle \\ &= \langle \mathcal{O}^\dagger \mathcal{T}(t_2-t_1)\mathcal{O}\rangle \\ &= \sum_n^\infty \left(\sqrt{c_n}\right)^2 \langle n|e^{-Ht}|n\rangle \\ &= \sum_{n=0}^\infty c_n e^{-E_n(t_2-t_1)} \end{aligned} \tag{2.42}$$

in which we sum over all states n with the same quantum numbers given as the source and sink operators. The prefactors c_n then parametrize the overlap of the states created by the source and sink operators with the energy states. In the exponent, E_n labels the energy of state n. In the absence of momentum, the energy coincides with the mass m_n of the given state via the energy-momentum-relation. For 2-point functions, a brief investigation of the effective mass

$$m_{\text{eff}} = -\partial_0 \ln\left(C_{XX}\right) \tag{2.43}$$

proves useful, an expression that singles out the energies of the states targeted by the correlator. We will make the following approximations:

$$\begin{aligned} \ln(C_{XX}) &= \ln\left(\sum_{n=0}^\infty c_n e^{-m_n x_0}\right) \\ &= \ln\left(c_0 e^{-m_0 x_0}(1+\sum_{n=1}^\infty \frac{c_n}{c_0} e^{-(m_n-m_0)x_0})\right) \\ &= \ln\left(c_0 e^{-m_0 x_0}\right) + \left(1+\sum_{n=1}^\infty \frac{c_n}{c_0} e^{-(m_n-m_0)x_0}\right) \\ &= \ln\left(c_0 e^{-m_0 x_0}\right) + \sum_{k=1}^\infty \frac{(-1)^{(k-1)}}{k}\left(\sum_{n=1}^\infty \frac{c_n}{c_0} e^{-(m_n-m_0)x_0}\right)^k \\ &= \ln\left(c_0 e^{-m_0 x_0}\right) + \sum_{n=1}^\infty \frac{c_n}{c_0} e^{-\Delta_n x_0} + \mathrm{O}(e^{-2\Delta_1 x_0}) \end{aligned} \tag{2.44}$$

$$-\partial_0 \ln(C_{XX}) = m_0 + \frac{c_1\Delta_1}{c_0} e^{-\Delta_1 x_0} + \mathrm{O}(e^{-\Delta_2 x_0}) + \mathrm{O}(e^{-2\Delta_1 x_0})\ . \tag{2.45}$$

This approximation is useful for the examination of contaminations from the first excited state. It is easy to see that after higher states have decayed, $m_{\text{eff}}(x_0) = m_0$, i.e. the ground state mass of the meson represented by the correlator. This ansatz will be exploited when we a plateau for the ground state mass, inspired by [98], as the plateau is the only surviving term after some time $x_0^{\min}$ in this approximation.

In the Schrödinger functional, as introduced in section 2.8.2, it is custom to use $t_1 = 0$ or $t_1 = T$. In these cases, the replacements $\psi(0,\vec{x}) \to \zeta(\vec{x})$ ($\bar{\psi}(0,\vec{x}) \to \bar{\zeta}(\vec{x})$) and $\psi(T,\vec{x}) \to \zeta'(\vec{x})$ ($\bar{\psi}(T,\vec{x}) \to \bar{\zeta}'(\vec{x})$) need to be carried out as to adhere to the boundary conditions.

As only γ_5 and γ_μ are allowed as boundary source structures, it is custom to shorten their names: Correlation functions with a pseudo-scalar source (γ_5)

$$\mathcal{O} = \bar{\zeta}_2\gamma_5\zeta_1 \quad \mathcal{O}' = \bar{\zeta}_1'\gamma_5\zeta_2' \tag{2.46}$$

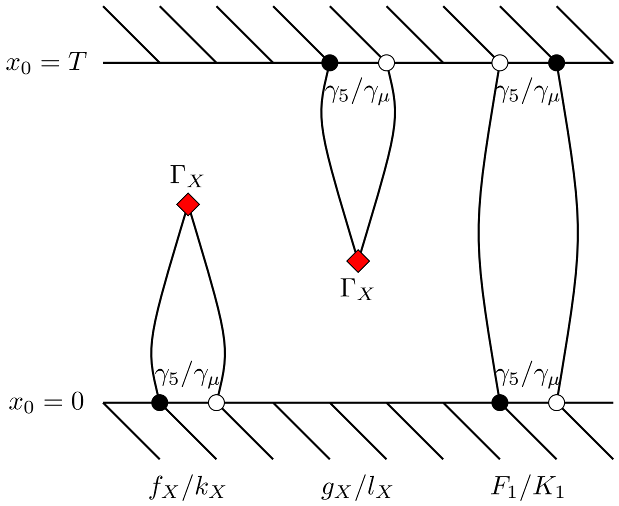

Figure 2.8: Two-point functions in the Schrödinger functional. The open (closed) circles represent quark (anti-quark) boundary fields. The red diamonds on the other hand are current insertions.

are referred to as f_X, if $x_0 = 0$ and g_X if $x_0 = T$. Similarly, if a vector source

$$\mathcal{Q} = \bar{\zeta}_1 \gamma_i \zeta_2 \quad \mathcal{Q}' = \bar{\zeta}'_1 \gamma_i \zeta'_2 \tag{2.47}$$

is employed, the correlators are referred to as k_X and l_X respectively. These are depicted in figure 2.8.

A special case that also needs to be introduced for later convenience are the correlators

$$F_1 = \langle \mathcal{O}\mathcal{O}' \rangle = \langle \bar{\zeta}_2 \gamma_5 \zeta_1 \; \bar{\zeta}'_1 \gamma_5 \zeta'_2 \rangle \tag{2.48}$$

and

$$K_1 = \langle \mathcal{Q}\mathcal{Q}' \rangle = \langle \bar{\zeta}_2 \gamma_\mu \zeta_1 \; \bar{\zeta}'_1 \gamma_\mu \zeta'_2 \rangle \tag{2.49}$$

that are the boundary-to-boundary correlators in the Schrödinger functional, compare figure 2.8 on the right.

2.9.2 Three-point functions

As the name suggests, three point functions receive three gamma insertions. The general correlator has the form

$$C_{XYZ} = \sum_{\vec{x},\vec{y},\vec{z}} \langle \bar{\psi}_1(z) \Gamma_Z \psi_3(z) \; \bar{\psi}_3(y) \Gamma_Y \psi_2(y) \; \bar{\psi}_2(x) \Gamma_X \psi_1(x) \rangle \; . \tag{2.50}$$

Interacting meson can be modelled with this type of correlator. This will become quite important in tests for physics, that we will see in part III. We will also see that terms proportional to these correlation functions appear when trying to renormalize the vector channel later in chapter 7, when we talk about Ward identities.

As in equation (2.41), the flavours are chosen in such a way that only quark-connected diagrams are allowed. We will call the operators at x and z the source and sink operators, the one at y a current insertion. Note that the time slices have no natural order. To fix

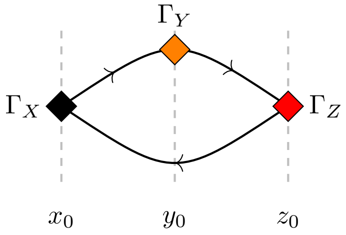

Figure 2.9: Sketch of a generic 3-point function. In the following, we call the black diamond the source, and the red diamond the sink of the correlator, while the orange diamond will be called an insertion.

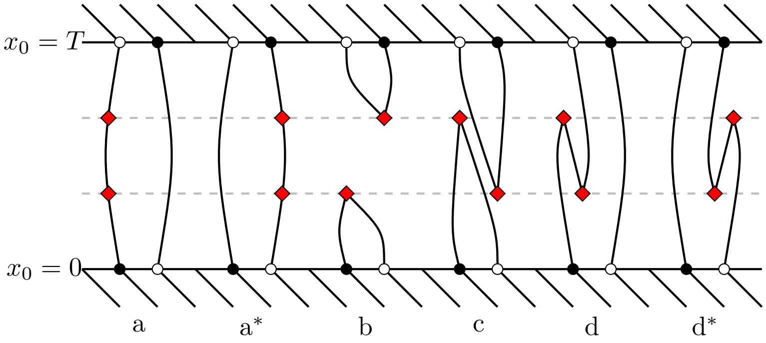

Figure 2.10: Possible contributions to 4-point functions, inspired by [31, fig. 6.1]. The terms a and a^* and d and d^* are related to each other by hermitian conjugation. Terms b and c are possible disconnected contributions to the diagrams, that only occur with the correct flavour combinations. As in figure 2.8, the open (closed) circles represent quark (anti-quark) boundary fields while the red diamonds are current insertions.

$x_0 = 0$ is again a natural choice. In practical computations, the time-distance $z_0 - x_0 = \Delta T$ is fixed, as calculations of all y_0-z_0-combinations are too time intensive. In this case, calculation-wise they are very similar to 2-point functions. Most properties of 2-point functions also apply to three point functions. Again, momenta can be introduced at each interaction point, as long as kinematics and energy-conservation are implemented correctly.

In the Schrödinger functional, one or two operators can be placed on the boundaries, which will be used for the renormalization of the vector current.

2.9.3 Four point functions

As we will see in chapter 6, the Ward identity needed for our endeavour to renormalize the axial-vector current depend on 4-point correlation functions. The Wick contractions for these are more complicated and allow for disconnected diagrams that do not include free quark loops, as e.g., shown in figure 2.10. This renders the evaluation of these functions rather unwieldy. We postpone the discussion of the particular contractions contributing to them to section 6.2, as the relative factors of the contributions depend on the flavour choices made.

Chapter 3

Flavour symmetry and weak decays

In the last chapter, we have built a well suited picture of QCD on a spacetime lattice. We have seen that employing the lattice, the path integral formulation of QCD has the potential to make predictions about the low-energy regime of the theory. Through the study of this formulation, we can properly predict the behaviour of quarks at low energies.

We have also introduced structures in Dirac-space that can be used to describe particles with specific quantum numbers (cf. table 2.1). In this chapter, we want to discuss the vector and axial-vector current further, focusing on their connection to weak decays and the formulation of Ward identities.

3.1 Flavour symmetry

Considering the QCD Lagrangian we introduced in equation (2.1) with three quarks of equal mass, we find that it obeys several symmetries. The spacetime and gauge symmetries are not to be discussed here, for these the reader is referred to [31, ch. 2.3]. Instead, we want to discuss the flavour symmetry along the lines of [99, ch. 8.2] with some details filled in from [31].

The flavour symmetry expresses rotations of the flavours of the quark field ψ into each other. Generally, it has the symmetry group $U(N_\mathrm{f})$. The right- and left-handed components of the fields, which can be separated by the projectors

$$P_\mathrm{R} = \frac{1+\gamma_5}{2} \ , \quad P_\mathrm{L} = \frac{1-\gamma_5}{2} \tag{3.1}$$

can be rotated independently by the angles $\vartheta_\mathrm{R} \in U(N_\mathrm{f})$ and $\vartheta_\mathrm{L} \in U(N_\mathrm{f})$ respectively. The overall symmetry group can therefore be expressed as $U(N_\mathrm{f})_\mathrm{R} \times U(N_\mathrm{f})_\mathrm{L}$, which we will discuss for the case of $N_\mathrm{f} = 3$. The symmetry is broken by the mass terms in the QCD Lagrangian, however, for physical quark masses, remnants of the symmetry are still to be found, as the physical mass of the quarks is small compared to Λ_QCD. The symmetry group $U(3)_\mathrm{R} \times U(3)_\mathrm{L}$ can be decomposed into four subgroups $SU(3)_\mathrm{L} \times SU(3)_\mathrm{R} \times U(1)_\mathrm{L} \times U(1)_\mathrm{R}$. For our discussion, we first look at the rotations in the $U(1)_\mathrm{L} \times U(1)_\mathrm{R}$ subgroup, which is the singlet case. From the projectors in equation (3.1), we can gather that the rotations can be re-parametrized with two vectors multiplied by the angles ϑ_V and ϑ_A as

$$\left(\vartheta_\mathrm{V} \frac{\mathbb{1}}{2}\right) \ , \quad \left(\vartheta_\mathrm{A} \frac{\gamma_5}{2}\right) \tag{3.2}$$

in which the new angles are given in terms of the original rotation angles ϑ_{L} and ϑ_{R} by

$$\vartheta_{\mathrm{V}} = (\vartheta_{\mathrm{L}} + \vartheta_{\mathrm{R}}) \;, \quad \vartheta_{\mathrm{A}} = (\vartheta_{\mathrm{L}} - \vartheta_{\mathrm{R}}) \tag{3.3}$$

such that the symmetry becomes that of $U(1)_{\mathrm{A}} \times U(1)_{\mathrm{V}}$, the singlet axial-vector and vector group. By Noether's theorem [100], we know that both symmetries have a Noether current attached to them, which are

$$\mathrm{V}_\mu = \bar{\psi}\gamma_\mu\psi \;, \tag{3.4a}$$

$$\mathrm{A}_\mu = \bar{\psi}\gamma_5\gamma_\mu\psi \;. \tag{3.4b}$$

We want to concern ourselves with the $SU(3)_{\mathrm{L}} \times SU(3)_{\mathrm{R}}$ components of the overall symmetry. These can be re-parametrized analogous to their $U(1)$ counterparts. The difference is that ϑ is part of $SU(3)$, such that it can be described as a vector ϑ^a multiplying the generators T^a of the group. For $SU(3)$, the parametrization $T^a = \lambda^a/2$, in which λ^a are the Gell-Mann matrices is customary. The respective rotations in flavour space are

$$\psi(x) \to \psi'(x) = e^{-\mathrm{i}\alpha(x)\frac{\lambda^c}{2}}\;\psi(x) \tag{3.5a}$$

$$\bar{\psi}(x) \to \bar{\psi}'(x) = \bar{\psi}(x)\;e^{+\mathrm{i}\alpha(x)\frac{\lambda^c}{2}} \tag{3.5b}$$

for the vector current and

$$\psi(x) \to \psi'(x) = e^{-\mathrm{i}\alpha(x)\gamma_5\frac{\lambda^c}{2}}\;\psi(x) \tag{3.6a}$$

$$\bar{\psi}(x) \to \bar{\psi}'(x) = \bar{\psi}(x)\;e^{+\mathrm{i}\alpha(x)\gamma_5\frac{\lambda^c}{2}} \tag{3.6b}$$

for the axial-vector current. The respective (non-singlet) vector and axial-vector Noether currents are given by

$$\mathrm{V}^a_\mu = \bar{\psi}\gamma_\mu T^a\psi \;, \tag{3.7a}$$

$$\mathrm{A}^a_\mu = \bar{\psi}\gamma_5\gamma_\mu T^a\psi \;. \tag{3.7b}$$

Note that the vector currents are conserved also for the case of massive, degenerate quarks, while the axial-current is only conserved for the massless case. This will become of interest in the next section, where we derive the partially-conserved axial-current (PCAC) relation. Also note that

$$\bar{\psi}\gamma_\mu P_{\mathrm{L}} T^a\psi = \frac{\mathrm{V}^a_\mu - \mathrm{A}^a_\mu}{2} \tag{3.8}$$

as is seen easily by the form of the projectors.

We will discuss the implications of these symmetries in the rest of this chapter. First, we will derive Ward Identities from them, as the improvement and renormalization conditions that we will set up in part II are based on those. In the last section, we then have a look at the implications of the vector and axial-vector current for Standard Model processes, in particular for weak leptonic and semi-leptonic decays.

3.2 Flavour non-singlet Ward identities

The determinations we will present in part II rely on Ward Identities. While the concrete evaluation may be postponed to later chapters, it is nevertheless useful to discuss the ground layers of these techniques.

If $\alpha(x)$ is small for all x, the rotations in the vector and axial channels presented in equations (3.5) and (3.6) are given by

$$\psi(x) \to \psi(x) - \mathrm{i}\alpha(x)\frac{\lambda^c}{2}\psi(x) \tag{3.9a}$$

$$\bar{\psi}(x) \to \bar{\psi}(x) + \mathrm{i}\bar{\psi}(x)\alpha(x)\frac{\lambda^c}{2} \tag{3.9b}$$

and

$$\psi(x) \to \psi(x) - \mathrm{i}\alpha(x)\gamma_5\frac{\lambda^c}{2}\psi(x) \tag{3.10a}$$

$$\bar{\psi}(x) \to \bar{\psi}(x) + \mathrm{i}\bar{\psi}(x)\alpha(x)\gamma_5\frac{\lambda^c}{2} \tag{3.10b}$$

respectively. These local rotations are not changing the expectation value of an operator $\mathcal{O}$, such that the following relations hold:

$$\delta_{\mathrm{V/A}}(x)\langle\mathcal{O}\rangle = 0 \tag{3.11a}$$

$$\langle\delta_{\mathrm{V/A}}(x)\mathcal{O}\rangle - \langle\mathcal{O}\delta_{\mathrm{V/A}}(x)\mathcal{S}\rangle = 0 \tag{3.11b}$$

$$\langle\delta_{\mathrm{V/A}}(x)\mathcal{O}\rangle = \langle\mathcal{O}\delta_{\mathrm{V/A}}(x)\mathcal{S}\rangle \ , \tag{3.11c}$$

in which δ is the variation operator. We set the support of the variation to an arbitrary part of the finite box that is the lattice: $\sup(\delta\alpha(x)) = R \subset \mathbb{L}$. The variation of the expectation value relies evidently on the variation of the action $\delta\mathcal{S}$. The action is transformed under vector-like variations as

$$\begin{aligned}\delta^a_{\mathrm{V}}\mathcal{S} &= \mathrm{i}\int_R \mathrm{d}^4x\partial_\mu \mathrm{V}^a_\mu(x)\alpha(x) \\ &= \mathrm{i}\alpha(x)\int_{\partial R}\mathrm{d}^3x\ \mathrm{V}^c_\mu(x)\ ,\end{aligned} \tag{3.12}$$

while, under chiral transformations, we receive

$$\delta^a_{\mathrm{A}}\mathcal{S} = -\mathrm{i}\int_R \mathrm{d}^4x\ \left(2m\ \alpha(x)\ \mathrm{P}^a(x) - \alpha(x)\ \partial^\mu \mathrm{A}^a_\mu(x)\right) \tag{3.13a}$$

$$= -\mathrm{i}2m\ \alpha(x)\int_R \mathrm{d}^4x\ \mathrm{P}^a(x) + \mathrm{i}\alpha(x)\int_{\partial R}\mathrm{d}^3x\ \mathrm{A}^a_\mu(x)\ . \tag{3.13b}$$

Now we consider the rest of the equation (3.11c). Indeed, we need to consider multiple variants, which differ in

- the type of variation that is carried out (V or A)
- the support R, in which the variation $\delta^a_{\mathrm{V/A}}$ does not vanish
- the operator (or operator combination) $\mathcal{O}$.

We will call operators $\mathcal{O}(x)$ with $x \in R$ internal operators $\mathcal{O}_{\mathrm{int}}$ and operators with $x \notin R$ external operators $\mathcal{O}_{\mathrm{ext}}$. Note that external operators are not affected by the variation.

As a first, simple but powerful example, we consider the case of an external operator $\mathcal{O}_{\mathrm{ext}}$ chosen as the pseudo-scalar density $\mathrm{P}^a(y)$. As external operators are not affected by the variation, the left-hand side of (3.11c) vanishes, and we receive

$$\langle\mathrm{P}^a(y)\delta^a_{\mathrm{A}}\mathcal{S}\rangle = 0\ . \tag{3.14}$$

Using equation (3.13a), we realize that the relation can be solved for all x separately, meaning that the following holds:

$$2m \left\langle \mathrm{P}^a(x)\mathrm{P}^a(y)\right\rangle = \left\langle \mathrm{A}^a_\mu(x)\mathrm{P}^a(y)\right\rangle \ . \tag{3.15}$$

This relation defines the current quark mass m, as a parameter of the symmetry breaking of the axial symmetry. It will serve us as the start into the improvement program in chapter 6.

As more complicated relations arise from the axial and vector transformations, we will see that the evaluation of the mass defined here is important to many other calculations that involve Ward identities. In these, when internal operators are involved, we need to set the region of variation explicitly. We will evaluate these identities in the Schrödinger functional, such that the spatial directions are periodic. It is therefore customary to set

$$\alpha(x) = \varepsilon\ \chi(x) \text{ with } \varepsilon \ll 1 \tag{3.16}$$

and $\chi : \mathbb{L} \to \{0,1\}$ a function with compact support R on the lattice. The support is chosen to be of the form

$$R = S^1 \times S^1 \times S^1 \times [t_1, t_2] \subset \mathbb{L} \tag{3.17}$$

such that the integration runs over all of space and part of time. Due to periodicity, the surface terms in space direction vanish, allowing us to simplify the second term in equation (3.13b) even further:

$$\int \mathrm{d}^3x\ \mathrm{A}^a_\mu(x) = \left[\mathrm{A}^a_0(x)\right]^{x_0=t_2}_{x_0=t_1} \tag{3.18}$$

where we have set $\mu = 0$ in the integrated part, as the spatial components of the axial-vector current have to cancel due to periodicity in the spatial dimensions.

3.3 Weak decays

The goal of the work presented is to prepare the stabilized Wilson fermion framework to derive first results for leptonic and semi-leptonic decays in charm-physics. While we have seen that the strong interaction is well described on the lattice, we now turn towards the implementation of weak decays from the perspective of a hadron. These decays are mediated by the vector bosons $W^\pm$ and Z^0 and can be brought in contact with the weak currents by the interaction Lagrangian

$$\mathcal{L} = g(W^+_\mu J^{+,\mu} + W^-_\mu J^{-,\mu}) + \bar{g} Z^0_\mu J^{0,\mu} \ . \tag{3.19}$$

The weak currents $J^{Q,\mu}$ consist of leptonic parts $J^{Q,\mu}_{\mathrm{l}}$ and hadronic parts $J^{Q,\mu}_{\mathrm{h}}$. Note that the eigenstates coupling to the weak interaction are not the same as the ones in contact with other interactions. In particular, they are related through the PMNS-matrix for the leptons (neutrinos) [101, 102] and through the CKM-matrix [103] in the case of the quarks, which we will investigate in a second.

In the following, we briefly discuss the structure of weak decays in the Standard Model, for which the reader may also be referred to [88, 99, 104] for pedagogical introductions to this topic. Here, we only introduce the necessary concepts to make contact with lattice QCD.

We will start by briefly introducing the expression of weak decays through currents before discussing the CKM-matrix. In the end, we want to shortly discuss two specific decays, which are prominent examples for the decays described by this framework.

Weak decays in the current algebra To arrive at the decays we are interested in, we concern ourselves with the charged currents $J^{\pm}$ coupling to the $W^{\pm}$-bosons, which we want to discuss along the lines of [99, ch. 8.2, 8.3]. We neglect the leptonic part of the currents and only view the charged, hadronic current

$$J_{\mathrm{h}}^{-\mu} = \frac{1}{\sqrt{2}} \left[\bar{\mathrm{d}}'_{\mathrm{L}} \gamma^{\mu} \mathrm{u}_{\mathrm{L}} + \bar{\mathrm{s}}'_{\mathrm{L}} \gamma^{\mu} \mathrm{c}_{\mathrm{L}} + \bar{\mathrm{b}}'_{\mathrm{L}} \gamma^{\mu} \mathrm{t}_{\mathrm{L}} \right] \tag{3.20}$$

where ψ_{L} are only the left-handed components of the fields and the colours are summed over.

The projector P_{L} from equation (3.1) can be inserted for each quark field, such that the expression in terms of the full Dirac spinors is

$$\begin{aligned} J_{\mathrm{h}}^{-\mu} =& \frac{1}{\sqrt{2}} \left[\bar{\mathrm{d}}' \left(\frac{1+\gamma_5}{2} \right) \gamma^{\mu} \left(\frac{1-\gamma_5}{2} \right) \mathrm{u} + \bar{\mathrm{s}}' \left(\frac{1+\gamma_5}{2} \right) \gamma^{\mu} \left(\frac{1-\gamma_5}{2} \right) \mathrm{c} \right. \\ & \left. + \bar{\mathrm{b}}' \left(\frac{1+\gamma_5}{2} \right) \gamma^{\mu} \left(\frac{1-\gamma_5}{2} \right) \mathrm{t} \right] \\ =& \frac{1}{\sqrt{2}} \left[\bar{\mathrm{d}}' \gamma^{\mu} \left(\frac{1-\gamma_5}{2} \right) \mathrm{u} + \bar{\mathrm{s}}' \gamma^{\mu} \left(\frac{1-\gamma_5}{2} \right) \mathrm{c} + \bar{\mathrm{b}}' \gamma^{\mu} \left(\frac{1-\gamma_5}{2} \right) \mathrm{t} \right] \end{aligned} \tag{3.21}$$

where we have used $\bar{\psi}_{\mathrm{L}} = \bar{\psi} P_{\mathrm{R}}$ and $P_{\mathrm{L}}^2 = P_{\mathrm{L}}$. The primed quark flavours appearing here are the weak flavour eigenstates, that are related to the common quark flavours through the CKM-matrix that is discussed in the next paragraph. Remembering equation (3.8), we realize that each term is related to the vector and axial-vector current.

The CKM-matrix In the weak Lagrangian, not only the left-handedness of the particles at hand play a role, but also primed quark fields $\mathrm{d}', \mathrm{s}', \mathrm{b}'$ of the down-type fields were introduced. As already mentioned, they are related to the quark flavours taking part in the strong interactions by the *C*abibbo-*K*obayashi-*M*askawa matrix [103] through the relation

$$\begin{pmatrix} \mathrm{d}' \\ \mathrm{s}' \\ \mathrm{b}' \end{pmatrix} = \underbrace{\begin{pmatrix} V_{\mathrm{ud}} & V_{\mathrm{us}} & V_{\mathrm{ub}} \\ V_{\mathrm{cd}} & V_{\mathrm{cs}} & V_{\mathrm{cb}} \\ V_{\mathrm{td}} & V_{\mathrm{ts}} & V_{\mathrm{tb}} \end{pmatrix}}_{M_{\mathrm{CKM}}} \begin{pmatrix} \mathrm{d} \\ \mathrm{s} \\ \mathrm{b} \end{pmatrix} . \tag{3.22}$$

The two-generation case of this matrix is realized by the Cabibbo angle [105], which is found to be $\theta_c = 13.04°$. The squared absolute of each matrix entry $|V_{xy}|^2$ is the probability of flavour change from quark flavour x to quark flavour y. Therefore, the relation

$$|V_{xd}|^2 + |V_{xs}|^2 + |V_{xb}|^2 = 1 \tag{3.23}$$

must hold for each row and the matrix must be unitary in case of no BSM physics going on in the weak decays mediated by $W^{\pm}$-bosons. The most recent review of the unitarity of the CKM-matrix is found in [64], where we find the first row to add up to 0.9984 ± 0.0007, the second to 1.001 ± 0.012. Note that the uncertainties of the second row are about 20 times larger than those of the first.

We want to finish this chapter by discussing two prominent decays: $\pi(p) \to l^+ \nu_l$ and $D \to \pi + l \nu_l$, to show how we can contribute to the estimation of the matrix elements.

Leptonic π^+ decays The leptonic pion decay is a prominent example of a weak decay investigated in lattice QCD. As we have seen in the last paragraph, from the point of view of flavour physics, the weak decays can be modelled by the currents we introduced in the

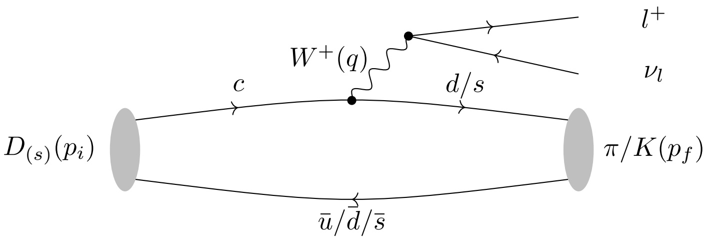

Figure 3.1: Sketch of the semi-leptonic $D_{(s)}$-meson decay. The charged current W^+ changes the flavour from charm $Q_\mathrm{e} = 2/3\mathrm{e}$ to a lighter flavour of charge $Q_\mathrm{e} = -1/3\mathrm{e}$. The energy difference between the heavy D-meson and the lighter π/K is absorbed in a change of the momenta.

first section of this chapter. The decay we are concerned with is $\pi(p) \to l^+\nu_l$, which we want to discuss along the lines of [99, ch. 8.3].

The pion is a pseudo-scalar particle with spin zero. We can parametrize the decay as

$$\langle 0|\bar{\mathrm{d}}\,[\gamma_\mu(1-\gamma_5)]\,\mathrm{u}|\pi(p)\rangle = -f_\pi p_\mu \;, \tag{3.24}$$

where we call f_π the pion decay constant. The momentum p_μ is the only four-vector allowed and f_π has to be Lorentz invariant. The decay is characterized by the weak current appearing on the left-hand side. Note that the right-hand side transforms like a Lorentz-vector (as opposed to an axial-vector). The left-hand side, as we have seen in the last section, is composed of the vector and the axial-vector current. As the result of the right-hand side must evidently also transform as a vector, we deduct that the part proportional to the vector current needs to vanish:

$$\langle 0|\bar{\mathrm{d}}\gamma_\mu \mathrm{u}|\pi(\mathrm{p})\rangle = \langle 0|\mathrm{V}_\mu|\pi(\mathrm{p})\rangle = 0 \;. \tag{3.25}$$

And only the axial-vector current contributes, as combined with the pseudo-scalar particle, it indeed transforms like a vector

$$\langle 0|\bar{\mathrm{d}}\gamma_\mu\gamma_5 \mathrm{u}|\pi(\mathrm{p})\rangle = \langle 0|\mathrm{A}_\mu|\pi(\mathrm{p})\rangle = \mathrm{f}_\pi \mathrm{p}_\mu \;. \tag{3.26}$$

In order to derive the pion decay constant f_π it is therefore sufficient to only consider the axial-vector part of the decay.

Semi-leptonic D-meson decays This decay is another prominent example for lattice calculations. We follow the discussion in [99, ch. 8.3] and [106, ch. 1.1.5] to see the significance of the currents we introduced for the semi-leptonic D-meson decay. The decay $D \to \pi + l\nu_l$ is depicted in figure 3.1. The amplitude of the decay is parametrized by

$$\mathrm{i}\mathcal{M} = \frac{-\mathrm{i}g^2}{8}\; V_\mathrm{cd}\; H_\mu \left(\frac{-g^{\mu\nu} + \frac{q^\mu q^\nu}{m_W^2}}{q^2 - m_W^2} \right) L_\nu \tag{3.27a}$$

$$= -\mathrm{i}\frac{G_F}{\sqrt{2}}\; V_\mathrm{cd}\; H_\mu L^\mu \;. \tag{3.27b}$$

In which H_μ is the hadronic and L_ν the leptonic part of the diagram. As this parametrization depends explicitly on the CKM-matrix element V_cd, we can probe it if we know all other quantities in the relation. The matrix element $\mathcal{M}$ can be related to the scattering matrix S through the LSZ-formula as usual and can therefore be estimated from experiment. The leptonic part appearing on the right-hand side can be calculated in perturbation theory.

The hadronic part H_μ needs to be treated non-perturbatively. On the quark level, the charm-quark decays weakly to a light quark via a charged current $\bar{\mathrm{l}}\,[\gamma_\mu(1-\gamma_5)]\,\mathrm{c}$. A convenient parametrization for our purposes was first introduced by [107]. It is given by

$$\begin{aligned} H_\mu &= \langle\pi(p_f)|\bar{l}\,[\gamma_\mu(1-\gamma_5)]\,\mathrm{c}|D(p_i)\rangle && \text{(3.28a)} \\ &= f_+(q^2)\left[(p_i+p_f)_\mu - \left(\frac{m_D^2-m_\pi^2}{q^2}\right)q_\mu\right] + f_0(q^2)\left(\frac{m_D^2-m_\pi^2}{q^2}\right)q_\mu\ , && \text{(3.28b)} \end{aligned}$$

where q is the momentum going towards the boson, while p_π and p_D are the momenta of the respective mesons. The factors f_0 and f_+ are called the scalar and vector form factor respectively. They fulfil the kinematic relation $f_+(q^2=0)=f_0$. Note that this parametrization is not unique and there are cases, where different parametrizations are more convenient.

The Dirac-structure of the decay is similar to the pion decay. The D and the π are both pseudo-scalar particles. The full contribution H_μ is again a Lorentz-vector. The decay is evidently again characterized by the combination $\mathrm{V}_\mu - \mathrm{A}_\mu$. However, as two pseudo-scalar states are present on the left-hand side. Including the axial-vector current, the result would transform as an axial-vector, as $\gamma_5\gamma_\mu\gamma_5\gamma_5 = -\gamma_\mu\gamma_5$. Hence, this contribution must vanish. Instead, the vector contribution transforms like a Lorentz-vector, as $\gamma_5\gamma_\mu\gamma_5 = -\gamma_\mu$. We receive:

$$\begin{aligned} \langle\pi|\bar{\mathrm{d}}\gamma_\mu\mathrm{c}|D\rangle &= \langle\pi|\mathrm{V}_\mu|D\rangle = H_\mu && \text{(3.29a)} \\ \langle\pi|\bar{\mathrm{d}}\gamma_\mu\gamma_5\mathrm{c}|D\rangle &= \langle\pi|\mathrm{A}_\mu|D\rangle = 0\ . && \text{(3.29b)} \end{aligned}$$

The matrix elements V_{cd} and V_{cs}, parametrizing the decay from a charm-quark to a down or strange quark can therefore be inspected from the point of view of hadron physics by the vector current.

Chapter 4

Computational methods

In chapter 2 we have worked towards the solution of the QCD path integral through numerical methods. The solution provided in the end of that chapter was to integrate over the configuration space of the fields appearing in the path integral. We have briefly discussed that this is equivalent to the integration over an infinite dimensional space. Numerical integration methods are abundant, however, most only perform well in low-dimensional spaces, making them not a suitable choice.

There is however an integration method with which high-dimensional integrals can be solved efficiently: Monte-Carlo integration. In short words, this method approximates the desired integral by probing its value at different points in the space that is integrated over. In our case, this is the configuration space of the fields, such that the expectation value of an operator $\mathcal{O}$ is calculated as

$$\langle \mathcal{O} \rangle = \frac{1}{N} \sum_{n=1}^{N} \mathcal{O}(U_n) \tag{4.1}$$

in which U_n denotes a specific field configuration.

We have also briefly alluded to the fact that the integration measure used in the path integral depends on the probability of each field configuration. Therefore, we would like to probe the configuration space according to these weights rather than completely randomly. Thus, we introduce importance sampling with the weight proportional to the probability $\left(e^{-\mathcal{S}[U_n]}\right)^2$ of the field configuration into our treatment of the integral. As probing randomly, even with importance sampling, is not feasible by itself, we need to relate the field configurations to each other. This is implemented in practice by a *Markov-chain*, a series of configurations in *Monte-Carlo time*. While the introduction of a Markov-chain makes the evaluation of the integral feasible, it has the downside that the probes this procedure yields are correlated with each other, an issue we cannot leave unaddressed.

In this chapter, while we will not get into the intricate details that make modern lattice calculations the powerful tool they are. However, we want to give an overview over the general principle of the calculations that are part of the basis our investigations are founded on. In the first part of the chapter we will therefore give a brief introduction to Markov-chain Monte-Carlo algorithms. Focus is laid on the introduction of the hybrid Monte-Carlo and stochastic Molecular dynamics algorithm that are at play in the generation of the gauge fields we use. The second part will be concerned with the treatment of the correlations inherent to these algorithms.

4.1 Markov-chain Monte Carlo

As we have just discussed Monte-Carlo integration is only feasible in lattice calculations if the probed points are generated through a so-called Markov-chain. The reader may be referred to [25, ch. 4] for a pedagogical introduction to this matter. For the moment, it is enough to list the main aspects that characterize a Markov-chain:

Suppose you have a sequence of configurations $U_1, U_2, \ldots$ each of which is fully characterized by the set of gauge links $\{U_n^\mu(x)\}$. We will equate the progression of the index n with the progression of Monte-Carlo time. The sequence is called a Markov-chain if it has the following properties:

- The Markov property
$$P(U_n = U'|U_{n-1} = U) = T(U'|U) \; , \tag{4.2}$$
which means that the transition $T(U'|U)$ only depends on the probability of U' following on U and is not dependent on the index n.
- The transitions $T(U'|U)$ are characterized by
$$0 \leq T(U'|U) \leq 1 \, , \; \sum_{U'} T(U'|U) = 1 \quad \forall \, U, U' \; . \tag{4.3}$$
- The transitions $T(U'|U)$ and the probabilities of the configurations $P(U)$ furthermore respect the detailed balance condition
$$T(U'|U)P(U) = T(U|U')P(U') \; , \tag{4.4}$$
which describes the symmetry of the path between U and U'.
- The sequence of variables is ergodic, meaning that for each pair U, U' there is a finite number k of applications of the transition function T such that $T^k(U'|U) > 0$. This includes that the sequence is aperiodic.

Note that, as mentioned in [108], the detailed balance condition is not always obeyed in practice, meaning that the probability of paths can be slightly asymmetric. Before we see how we can estimate the margins of error for an observable estimated by Monte-Carlo techniques, we want to give a brief overview over the algorithms employed to generate Markov-chains in lattice calculations.

4.2 The HMC and SMD algorithms

While this thesis is not concerned with the generation of gauge field ensembles, it is still worthwhile to have a general understanding how the data basis we work with is generated. Here, this is presented in three steps: we will first introduce the basic steps of the Metropolis-Hasting algorithm that is used to evolve pure gauge fields. As dynamical fermions are incorporated in modern lattice field simulations, the next step is then to introduce fermions to the picture by the introduction of the hybrid Monte-Carlo algorithm. At last, we will briefly discuss a slight change in the hybrid Monte-Carlo algorithm, dubbed Stochastic Molecular Dynamics (SMD) algorithm that is used for the simulations of the OpenLat initiative. For more complete discussions of the topics discussed, the reader may be referred to [27, ch. 2 & 3.4], [93, ch. 3] and [25, ch. 8].

4.2.1 The Metropolis-Hastings algorithm

The Metropolis-Hastings algorithm [109] is the basis of the algorithms used for the generation of gauge fields configurations. It evolves the gauge field configuration U_n at a point n in the Markov-chain to the next piece of the chain U_{n+1}. The generation of which should follow the properties of a Markov-chain. This can be implemented in three successive steps:

1. Choose a site x and a direction μ to change. Propose a new link variable $U'_\mu(x) \in SU(3)$ that replaces $U_\mu(x) \in SU(3)$.
    - It is customary to set $U'_\mu(x) = \chi U_\mu(x)$ and choose χ to be Gaussian distributed around $\mathbb{1}$ to respect the weighting of the ensembles.
2. Compute the change of the action $\Delta\mathcal{S} = \mathcal{S}[U] - \mathcal{S}[U']$ between the old and new gauge field.
    - In the case that the links are only connected by nearest neighbour interactions, such as the gauge links, the change of the action is indeed local, such that change can be expressed only in terms of $U(x)$ and $U'(x)$.
3. Compute a random number $r \in [0,1)$ and accept the change $U_\mu(x) \to U'_\mu(x)$ in case that $r \leq \min\{\exp(-\Delta S),\, 1\}$. If this is not the case, reject the change ($U_{n+1} = U_n$).

Note that with this algorithm, we indeed draw random configurations U_n from the space of possible field configurations. Tuning the change of the links proposed in the first step evidently lets us find a way to have a good acceptance rate in the last step. A detail that is not to be neglected in this procedure is the choice of a high-quality random number generator for r. A popular choice used in calculations is the `RANLUX` generator [110]. While the described algorithm is suitable for Yang-Mills theories, lattice simulations in their current stage also have dynamical fermionic degrees of freedom.

4.2.2 Hybrid Monte-Carlo

As a next step, we introduce dynamical fermionic degrees of freedom to the generation of configurations. In principle, we would need to implement the anti-commutation relations of fermions into our calculations. However, instead of doing so, we first rewrite the fermions as Grassmann variables. As we can integrate over the fermionic degrees of freedom separately, our goal is actually to integrate an exponential over a set of Grassmann variables. Therefore, we can make use of the Matthews-Salam formula

$$\int d\bar{\eta}_n d\eta_n \dots d\bar{\eta}_1 d\eta_1 \exp\left(\sum_{i,j=1}^{n} \bar{\eta}_i M_{ij} \eta_j\right) = \det(M) \tag{4.5}$$

to circumvent the evaluation of anti-commuting variables all together. Comparison with the fermion action in equation (2.18), shows that the matrix M is evidently the matrix representation of the Dirac operator D.

While this is already a step in the right direction, we now have to compute the determinant of a matrix with $\dim[D] = T \times L^3 \times 3 \times 4$. This is also known as the fermion determinant, for which the dimension comes about from each lattice point in the volume $T \times L^3$ having 3 colour and 4 spin degrees of freedom. In modern calculations $\dim[D]$ can exceed $\mathrm{O}(10^9)$. In very small calculations, the determinant could be computed by LU-decomposition of the matrix, however this is not practical for matrices this large.

We will not go into all the details how this conundrum is solved, however, we want to point out two techniques that are standard in modern calculations, even-odd preconditioning and the introduction of pseudo-fermions.

Even-odd preconditioning Before solving the problem introduced by the large dimension of the fermions determinant, we try to simplify the problem as much as possible. A standard technique in case of the fermion determinant is even-odd (or red-black) preconditioning, which is introduced here along the lines of [27, sec. 3.2.2.4]. It relates the lattice sites to each other in the following way: Suppose you divide the lattice into *e*ven and *o*dd lattice sites, depending on the sum of the spacetime index of each lattice site. ($x = (1, 1, 1, 1)$ → even, $x = (1, 1, 1, 2)$ → odd, etc.) The Dirac operator D can then be expressed as a 2×2 matrix

$$D_{\mathrm{W}} = \begin{pmatrix} D_{\mathrm{ee}} & D_{\mathrm{eo}} \\ D_{\mathrm{oe}} & D_{\mathrm{oo}} \end{pmatrix} \tag{4.6}$$

as we have already used in equation (2.37). The diagonal parts D_{ee} and D_{oo} are block-diagonal for the Dirac operator of improved Wilson fermions. And the Schur-decomposition is given by

$$D = \begin{pmatrix} \mathbb{1}_{\mathrm{ee}} & D_{\mathrm{eo}} D_{\mathrm{oo}}^{-1} \\ 0 & \mathbb{1}_{\mathrm{oo}} \end{pmatrix} \begin{pmatrix} D_{\mathrm{ee}} - D_{\mathrm{eo}} D_{\mathrm{oo}}^{-1} D_{\mathrm{oe}} & 0 \\ 0 & D_{\mathrm{oo}} \end{pmatrix} \begin{pmatrix} \mathbb{1}_{\mathrm{ee}} & 0 \\ D_{\mathrm{oo}}^{-1} D_{\mathrm{oe}} & \mathbb{1}_{\mathrm{oo}} \end{pmatrix} , \tag{4.7}$$

in which $\hat{D} = D_{\mathrm{ee}} - D_{\mathrm{eo}} D_{\mathrm{oo}}^{-1} D_{\mathrm{oe}}$ is called the preconditioned operator. The Dirac equation

$$D\psi = \eta , \tag{4.8}$$

with the even and odd parts of the fermion field $\psi = (\psi_{\mathrm{e}}, \psi_{\mathrm{o}})^{\top}$ can be solved by first solving

$$\hat{D}\psi_{\mathrm{e}} = \eta_{\mathrm{e}} - D_{\mathrm{eo}} D_{\mathrm{oo}}^{-1} \eta_{\mathrm{o}} , \tag{4.9}$$

to find the even part of the fermion fields, followed by a second step

$$\psi_{\mathrm{o}} = D_{\mathrm{oo}}^{-1} (\eta_{\mathrm{o}} - D_{\mathrm{oe}}^{-1} \psi_{\mathrm{e}}) \tag{4.10}$$

to solve for the odd parts of the field. Note that the preconditioned operator $\hat{D}$ is only defined on the even lattice sites. We can recover the determinant of the full Dirac operator by

$$\det[D] = \det[D_{\mathrm{oo}}] \det[\hat{D}] . \tag{4.11}$$

As the D_{oo} is block-diagonal, we can solve for the determinant much more easily, as the calculation decomposes. The determinant of the preconditioned operator $\hat{D}$, is carried out differently, using pseudo-fermions.

Pseudo-fermions After preconditioning, we still need to compute the determinant $\det[\hat{D}]$, which is non-trivial. It is customary to not compute the determinant directly, as the matrix is still high dimensional, but instead approximate it stochastically.

In the case of $N_{\mathrm{f}} = 2$ Wilson fermions and with a few assumptions (see [27, eqs. (3.32)-(3.39)]), one can show (see e.g. [27, p. 76]) that, in this case, $\det(D) = \det(DD^{\dagger})$ as the Wilson Dirac operator is „γ_5-hermitian“, meaning that $D^{\dagger} = \gamma_5 D \gamma_5$. Therefore, we can formulate the determinant as an integral

$$\det[DD^{\dagger}]^{-1} = \int \mathcal{D}[\phi]\; e^{-\mathcal{S}_{\mathrm{pf}}[U,\phi]} \tag{4.12}$$

in which ϕ is a complex-valued field that is known as the *pseudo-fermion* field, which is not Grassmann valued. As the fermions are dynamical, the pseudo-fermions are as well. They have the action

$$\mathcal{S}_{\mathrm{pf}}[U,\phi] = \phi(DD^{*})^{-1}\phi \; . \tag{4.13}$$

Thus, we have avoided the implementation of Grassmann variables that we needed to integrate over originally. Instead, we can evaluate the fermion determinant for $N_{\mathrm{f}} = 2$ by approximating its integral representation that depends on the complex valued field ϕ. This approximation can be carried out through Monte-Carlo methods due to the form of equation (4.12), which again allows for probing with a Markov-chain and importance sampling. The algorithm to do exactly this is the hybrid Monte-Carlo algorithm we are about to introduce.

Hybrid Monte-Carlo Coming back to the original goal of this section, we can collect from the previous paragraphs that the calculation of the fermion determinant can be carried out in two steps: We precondition the Dirac operator D and solve the determinant of the block-diagonal matrix. The preconditioned operator $\hat{D}$ is then solved with pseudo-fermions by approximating its integral representation through Monte-Carlo methods. The combinations of this and the evolution of the gauge fields together is implemented in the hybrid Monte-Carlo algorithm [111]. For this short review, we follow [27, ch. 3.4.1]. We write down the Hamiltonian of the gauge and pseudo-fermion fields

$$\mathcal{H} = \frac{\pi\pi^{*}}{2} + \mathcal{S}_{\mathrm{G}}[U] + \mathcal{S}_{\mathrm{pf}}[U,\phi] \; . \tag{4.14}$$

Based on this, we evolve the equations of motion inside an algorithm that is similar to the Metropolis-Hastings algorithm in its bare structure, but also evolves the fermionic degrees of freedom (see also [112]):

1. The new pseudo-fermion momenta π' are generated with a probability density $P(\pi')$ proportional to $\exp\{-(\pi'\pi'^{*})/2\}$. A new set of pseudo-fermion fields is also generated with their probability proportional to $\exp\{-S_{\mathrm{pf}}[U]\}$. This is commonly done by setting $\phi' = D^{\dagger}\rho$, where ρ is a normally distributed field.

2. The molecular dynamics equations

$$\dot{\pi} = -\partial_{x,\mu}(\mathcal{S}_{\mathrm{G}}[U] + \mathcal{S}_{\mathrm{pf}}[U,\phi]) \; , \; \dot{U}_{\mu} = P_{\mu}(x)U_{\mu}(x) \; , \tag{4.15}$$

   are integrated over some time interval $[\tau_0, \tau_1]$ in molecular dynamics time τ. The (dotted) derivatives are to be taken with respect to τ. The pseudo-fermion field ϕ is kept fixed in this step.

3. The evolution of the fields changes the value of the Hamiltonian, prompting an accept-reject step as in the Metropolis-Hastings algorithm. We calculate the difference $\Delta\mathcal{H} = \mathcal{H}(\phi_{\tau_1}, U_{\tau_1}) - \mathcal{H}(\phi_{\tau_0}, U_{\tau_0})$ and compare it to a random variable r, allowing the change if $r \leq \min\{\exp(-\Delta\mathcal{H}), 1\}$. If the step is rejected, as before, the configuration U is kept the same $U' = U$.

This algorithm is commonly used in lattice QCD calculations. However, part of the stabilization is the change of this algorithm in a particular way, which we will discuss as the last part of this section.

4.2.3 Stochastic Molecular Dynamics

The Stochastic Molecular Dynamics (SMD) algorithm introduces a slight change to the hybrid Monte-Carlo algorithm we have just discussed, which we will briefly review here along the lines of [93]. In the first step, we drew the fields π' and ϕ' according to a Gaussian distribution. This is still the case with the SMD algorithm, however, the newly proposed fields are constructed as follows [93, eqs. (3.2, 3.3)]:

$$\pi \to c_1\pi + c_2\pi', \tag{4.16a}$$

$$\phi \to c_1\phi + c_2 D^\dagger \rho, \tag{4.16b}$$

where c_1 and c_2 are given by

$$c_1 = e^{-\gamma\varepsilon}\ ,\ c_2 = \sqrt{1-c_1^2}\ , \tag{4.17}$$

in which $\varepsilon = \tau_1 - \tau_0$ is the molecular dynamics integration time. Evidently, when $c_1 \to 0$ and $c_2 \to 1$ (i.e. when γ is large), we recover the usual hybrid Monte-Carlo algorithm. On the other hand, for $\varepsilon \to 0$ with fixed γ, this algorithm solves the stochastic molecular-dynamics equations.

The stability of this algorithm for lattice QCD has, for example been tested in [93, ch. 6.5], where it has been seen that for fine lattices this algorithm is stable.

4.3 The Γ-method

We have laid out a computational framework with which we are able to probe configuration space efficiently. However, as pointed out in the beginning of the chapter, there is still an unsolved problem: The configurations this procedure yields are correlated, which calls into question the usual way of error estimation, which assumes uncorrelated data. Enlarging the margins of error is not easily done, as we also do not want to overestimate the error of the quantities calculated. Modern Monte-Carlo methods in other realms than lattice QCD may produce enough samples to bin or leave out extracted points of the Monte-Carlo chain. This has the benefit that the samples accumulated can be viewed as uncorrelated. Binning is also used in lattice QCD, however due to the high costs of generating field configurations, we want to formulate a more reliable way of treating the data, that can also accommodate phenomena like *critical slowing down* [113]. Furthermore, while binning is a fairly straightforward approach it can become problematic in situations, in which the longest correlation modes are not visible in primary observables. Even though we may introduce algorithmic changes, such as the use of the overrelaxation algorithm (see e.g. [27, ch. 2.2.3]) these issues make more sophisticated treatment of auto-correlations quite important in modern calculations, especially on fine lattices.

In the following, we introduce a framework of estimating and treating the correlations that is used in our calculations efficiently. It is called the Γ-method, which was originally introduced in [114] and introduced to lattice QCD in [108], which this section is based on.

The goal we try to accomplish here is to find a way of neither over- nor underestimating the margins of error of correlated data. To receive an entry point to the Γ-method, we first need to introduce the basics of error estimation and error propagation together with the necessary notation.

Suppose we have a set of values $\{a_\alpha^n\}$, which could be evaluations of some operator $\mathcal{O}_\alpha$ on a gauge-field configuration U^n. We define, as usual, the mean as

$$\bar{a}_\alpha = \frac{1}{N}\sum_{n=1}^{N} a_\alpha^n \tag{4.18}$$

and state that in the limit of infinite samples N this approaches the *real* value A_α of the operator $\mathcal{O}_\alpha$

$$\lim_{N\to\infty} \bar{a}_\alpha = A_\alpha \,, \tag{4.19}$$

as by the central limit theorem. Furthermore, we define the square of the statistical variance as

$$\sigma^2_{\bar{\alpha}} = \frac{\langle \bar{a}^2_\alpha \rangle - \langle \bar{a}_\alpha \rangle^2}{N} \,. \tag{4.20}$$

It is customary to also define the fluctuations of our measurement around the real value

$$\delta^n_\alpha = a^n_\alpha - A_\alpha \tag{4.21}$$

The expectation value of the fluctuations should then vanish,

$$\langle \delta^n_\alpha \rangle = 0 \,. \tag{4.22}$$

It should be noted that this, together with equation (4.19) is natural and essential to all measurements, as if any of these conditions is not given, the measurements are flawed as they do not approximate the actual value.

In terms of the fluctuations we now define the object

$$\Gamma_{\alpha\beta}(t) = \langle \delta^n_\alpha \delta^{n+t}_\beta \rangle \tag{4.23}$$

that measures the correlations between two measurements at Monte-Carlo times n and $n+t$. Intuitively, this can be understood as a generalization of equation (4.18), where the generalization takes place in two different dimensions. If we fix $t = 0$, the function above becomes the symmetric covariance matrix. The Γ-function makes it feasible to measure covariances also at separated Monte-Carlo times. From the symmetry in the covariances as well as the symmetry in paths (cf. fourth bullet point on page 36) in Monte-Carlo simulations, it is intuitive that

$$\Gamma_{\alpha\beta}(-t) = \Gamma_{\beta\alpha}(t) \tag{4.24}$$

should hold.

We furthermore define the normalized auto-correlation function as

$$\rho(t) = \frac{\Gamma_{\alpha\beta}(t)}{\Gamma_{\alpha\beta}(0)} \propto \exp\left(-\frac{t}{\tau_{\text{exp}}}\right) \,, \tag{4.25}$$

where the proportionality to an exponential decay is expected, as discussed for example in [113]. The sum over the autocorrelation function is denoted as

$$C_{\alpha\beta} = \sum_{t=-\infty}^{\infty} \Gamma_{\alpha\beta}(t) \,. \tag{4.26}$$

So far we have only looked at primary observables. However, relevant observables are usually derived from of these. We therefore also need to expand our definitions to the case of derived observables. The estimator for an arbitrary function $f(x)$ depending on some primary observable is

$$\bar{F} = f(\bar{a}_\alpha) \,. \tag{4.27}$$

We state that this can be expanded as a Taylor-series if the fluctuations defined by equation (4.21) are small

$$\bar{F} = F + \sum_\alpha \partial_\alpha f(A_\alpha) \bar{\delta}_\alpha + \frac{1}{2} \sum_{\alpha\beta} \partial_\alpha \partial_\beta f(A_\alpha)\ \bar{\delta}_\alpha \bar{\delta}_\beta + ... \tag{4.28}$$

for the case discussed here, we truncate the series after the linear order. For derived observables, we can then define the variance as

$$\sigma_F^2 = \langle (\bar{F} - F)^2 \rangle \approxeq \frac{1}{N} C_F \tag{4.29}$$

where

$$C_F = \sum_{\alpha\beta} \partial_\alpha f \; \partial_\beta f \; C_{\alpha\beta}(t) \tag{4.30}$$

similar to $C_{\alpha\beta}$ before. With these definitions, primary and derived observables are on equal footing.

4.3.1 The integrated auto-correlation time

After the necessary definitions, we can proceed to rewrite equation (4.29) by expanding the fraction with

$$v_F = \sum_{\alpha\beta} \partial_\alpha f \; \partial_\beta f \; \Gamma_{\alpha\beta}(0) \tag{4.31}$$

and receive

$$\sigma_F^2 = \frac{2\tau_{\text{int},F}}{N} v_F \tag{4.32}$$

with

$$\tau_{\text{int},F} = \frac{1}{2v_F} \sum_{t=-\infty}^{\infty} \sum_{\alpha\beta} \partial_\alpha f \; \partial_\beta f \; \Gamma_{\alpha\beta}(t) \; . \tag{4.33}$$

It should be noted that the integrated auto-correlation time τ_{int} encodes the correlations between the measurements directly.

In the case of $\tau_{\text{int}} = 1/2$, equation (4.32) equals equation (4.29), the uncorrelated situation. From this fixed point, we can look at situations, in which $\tau_{\text{int}} > 1/2$. In this case, as $\sigma_F \propto \tau_{\text{int}}$, it is clear that correlations enlarge the error. As explained in [108], one can understand the fraction $2\tau_{\text{int},F}/N$ as the inverse effective number of measurements. In binning techniques, this would be dictated by the bin size, while here this is directly dependent on the correlations exhibited by the observable of interest. Finally, as Monte-Carlo algorithms aim to exhibit the smallest auto-correlation possible, this is also a good parameter for how well this goal is achieved with the algorithm in use.

4.3.2 Error estimation

As all we have is the measurements that we took from the data, we simply cannot define everything in the way we first planned to. This already starts with the notion of the *real* value of our operator that we used in equation (4.21), as the real value is only a construct that can be achieved with infinitely many samples of the operator. Therefore, we reformulate everything in terms of estimators. The fluctuations are then estimated as

$$\bar{\delta}_\alpha^n = a_\alpha^n - \bar{a}_\alpha \, . \tag{4.34}$$

In the same way, we find the estimator of the auto-correlation function to be

$$\bar{\Gamma}_{\alpha\beta}(t) = \frac{1}{N-t} \sum_{n=1}^{N-t} (a_\alpha^n - \bar{a}_\alpha)(a_\beta^{n+t} - \bar{a}_\beta) \, . \tag{4.35}$$

For derived data, this is generalized as

$$\bar{\Gamma}_F(t) = \sum_{\alpha\beta} \partial_\alpha f(\bar{a})\ \partial_\beta f(\bar{a})\ \bar{\Gamma}_{\alpha\beta}(t)\,. \tag{4.36}$$

This is also what we need for an estimation of v_F and $\tau_{\mathrm{int},F}$. As in [108], we use, for practical reasons:

$$\bar{v}_F = \bar{\Gamma}_F(0) \tag{4.37}$$

Contrary to the reference, we choose the following approach to estimate $\bar{\tau}_{\mathrm{int}}$: As $\rho(t) \propto \exp(-t/\tau)$, we can model

$$2\tau_{\mathrm{int},F}(W) = \sum_{n=-\infty}^{\infty} \exp(-S|t|/\bar{\tau}(W)) \tag{4.38}$$

from which we get

$$\tau_{\mathrm{int},F}(W) = \frac{1}{2} + \sum_{t=1}^{W} \frac{\Gamma_{\alpha\beta}(t)}{\Gamma_{\alpha\beta}(0)}\,. \tag{4.39}$$

We truncate the summation after several Monte-Carlo steps W, which we will call the summation window. Due to this truncation, we introduce a bias $\propto -\exp(-W/\tau)$. Now we need to decide on a method to find the optimal window W. Often, this is done by monitoring the error itself as well as the error of the error. In our case, we do not consider the error of the error, but instead the normalized auto-correlation function ρ and estimate its error as

$$(\delta\rho(t))^2 \approx \frac{1}{N} \sum_{m=1}^{W} \left(\rho(m+t) + \rho(m-t) - 2\rho(m)\rho(t)\right)\,. \tag{4.40}$$

Now, as we do not want to underestimate contributions made by the correlations, we take the summation window W to be the first value, in which $\rho = 0$ within errors. Furthermore, we then state that

$$\sigma_F = \sqrt{2\tau_{\mathrm{int},F} \frac{\mathrm{var}(\delta_F^n)}{N}} \tag{4.41}$$

which is already enough for the analysis done here.

4.3.3 Comparison to alternatives

Commonly used alternatives to the Γ-method are binning and Jackknifing. The Γ-method has a few advantages over these. In particular, this method estimates the correlations on the final quantity calculated, while in binning, the bin sizes are, as already alluded to, determined at an early stage of the analysis and cannot be changed after the fact. Correlations may therefore be overlooked, if they are only visible in certain rare or derived observables and are not obvious in the observables examined to set the bin size. The Γ-method would capture these, but the method adds a lot of complexity to the analysis. It also cannot capture asymmetric error bars, as we truncate the expansion of the errors of derived observables in equation (4.28). Other methods are able to do so. However, the Γ-method has the advantage that the metadata and the originally measured data from the configurations can be easily conserved at all times. This facilitates to use the FAIR guiding principles [115], as the data can easily be traced back to its origin.

4.3.4 Analysis setup

The analyses that were carried out for this thesis are written in python. The error estimation is done with the Γ-method described in this section. The concrete implementation is the one provided by version `2.14.0` of the `pyerrors` package that the author contributed to develop. The package is described in our publication [116].

The core concept of the `pyerrors` package is the introduction of a new class, `Obs`, which represents an observable calculated on a range of gauge field configurations. The class provides function overloading of most `numpy` functions [117]. This allows for the calculation of observables in a straightforward python workflow. The error can be estimated for both, primary and secondary observables with one call of the function `gamma_method()`, in which the Γ-method is implemented as we have described it in this section. The error estimation of secondary observables relies on automatic differentiation, which is implemented in [118]. The plots presented in the following are made with `matplotlib` [119]. Care has been taken to make the outcomes of this thesis as reproducible as possible by employing Datalad [120] and Snakemake [121].

Part II

Improvement and Renormalization

Chapter 5

Schrödinger functional ensembles

The renormalization and improvement of stabilized Wilson fermions is one of the main objectives of this thesis. In the following, we will describe the procedures to estimate various renormalization factors and improvement coefficients with focus on the axial-vector and vector current. As these currents are important for the description of leptonic and semi-leptonic decays, their renormalization and improvement is of direct importance for the correct estimation of physical quantities from the lattice.

In the renormalization scheme that we introduced, the renormalization factorizes into mass independent ($Z_{\mathcal{O}}$) and mass dependent terms ($ab_{\mathcal{O}}m_{\mathrm{q}}$, $a\bar{b}_{\mathcal{O}}\mathrm{Tr}\left\{M_{\mathrm{q}}\right\}$).

As introduced in section 3.1, the identities used here to determine the renormalization factors and improvement constants are chiral Ward identities. One has easier access to these constants if the valence- and sea-quarks are massless, and it is crucial to work at or close to the chiral limit. One therefore needs to be able to simulate as close to the chiral limit as possible. The Schrödinger functional that we have introduced in section 2.8.2 enables us to simulate at the chiral limit, where $m_{\mathrm{q}} = 0$ due to its inherent spectral gap. Traditionally, also the improvement constants have been calculated in the chiral limit. However, for c_{A}, this is a choice and the improvement condition can be evaluated with massive quarks as well.

For these calculations, we employ a set of ensembles with Schrödinger functional boundary conditions, designed for the determination of these quantities for stabilized Wilson fermions. They use the improved exponential Wilson fermion action from equation (2.38) with c_{sw} as determined in [93] and the Lüscher-Weisz action from equation (2.25) for the gauge fields. The ensembles were generated and graciously provided by Patrick Fritzsch and were already used our earlier presentations of the following projects [122–124] as well as in [87, 125]. The placement of the ensembles in the mass-coupling parameter-space is presented in figure 5.1. Their key attributes are also listed in table 5.1.

Other important features are the approximation of two lines of constant physics, defined by the parameter ϕ_4, (cf. equation (5.5)) and the volume of the ensembles of $\approx 3\,\mathrm{fm}$. Due to this comparatively large volume, boundary improvement as discussed in section 2.8.2 is neglected and set to the tree level values of $c_t = \tilde{c}_t = 1$. The lines of constant physics we aim for are at the chiral limit ($\phi_4 = 0$) and the $N_{\mathrm{f}} = 3$-symmetric point, which is defined by the OpenLat guidelines as $\phi_4 = 1.115$, the same value as the CLS consortium employs in their calculations.

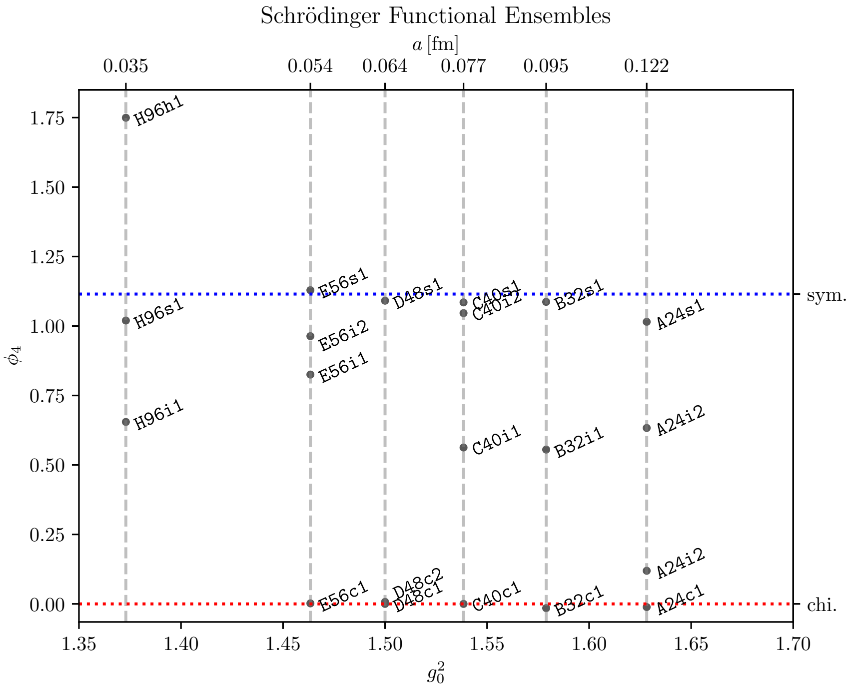

Figure 5.1: Positioning of the ensembles with Schrödinger functional boundary conditions in the mass-coupling plane. The red and blue lines show the position of the chiral and symmetric point, respectively.

Table 5.1: The ensembles with Schrödinger functional boundary conditions employed in this thesis. The ensembles have 6 different values of the inverse coupling β that can be related to the lattice spacing a. The hopping parameter κ (compare equation (2.21)) is the measure by which the mass of the quarks are given in the simulations. The lattice geometry is fully determined by the boundary conditions and the number of lattice sites T in time and L in space direction. ϕ_4, as introduced in this chapter is a dimensionless measure for the mass, that does not depend on the lattice spacing. The column #MDU shows the number of molecular dynamic units covered by all replica of the ensemble combined and is a measure of how „long“ the Monte-Carlo chain is in Monte Carlo time.

Name	β	T	L	κ	a [fm]	ϕ_4	# MDU
`A24s1`	3.685	24	24	0.139440000	0.1223(15)	1.015(64)	13292
`A24i2`	3.685	24	24	0.139550000	0.1223(15)	0.633(11)	17232
`A24i2`	3.685	24	24	0.139660174	0.1223(15)	0.1192(89)	16116
`A24c1`	3.685	24	24	0.139698000	0.1223(15)	-0.011(12)	7488
`B32s1`	3.800	32	32	0.138963000	0.0946(11)	1.0868(85)	12472
`B32i1`	3.800	32	32	0.139100000	0.0946(11)	0.5553(44)	17904
`B32c1`	3.800	32	32	0.139250000	0.0946(11)	-0.0152(51)	13648
`C40s1`	3.900	40	40	0.138603000	0.07737(94)	1.0850(87)	3136
`C40i2`	3.900	40	40	0.138614800	0.07737(94)	1.0464(65)	4276
`C40i1`	3.900	40	40	0.138729484	0.07737(94)	0.5626(61)	7868
`C40c1`	3.900	40	40	0.138856200	0.07737(94)	-0.000020(62)	5964
`D48s1`	4.000	48	48	0.138272000	0.06411(78)	1.0911(70)	10120
`D48c2`	4.000	48	48	0.138488000	0.06411(78)	0.0071(15)	4970
`D48c1`	4.000	48	48	0.138494200	0.06411(78)	0.0000012(57)	9020
`E56s1`	4.100	56	56	0.137945000	0.05404(66)	1.1290(76)	7340
`E56i2`	4.100	56	56	0.137975000	0.05404(66)	0.9635(66)	3872
`E56i1`	4.100	56	56	0.138000000	0.05404(66)	0.8252(88)	3320
`E56c1`	4.100	56	56	0.138141000	0.05404(66)	0.00189(61)	4228
`H96h1`	4.370	96	96	0.137050000	0.03453(43)	1.749(21)	400
`H96s1`	4.370	96	96	0.137130000	0.03453(43)	1.020(16)	524
`H96i1`	4.370	96	96	0.137175000	0.03453(43)	0.655(12)	656

Table 5.2: The ensembles with Schrödinger functional boundary conditions employed in this thesis. The description of the columns can be inferred from the table above, the differing column is the effective mass in the axial-vector channel $m_{\text{eff}}(f_{\text{A}})$. The value of β is not exact, hence the asterisk. The real value is $\beta = 6/0.7$, which we have rounded in the table.

Name	β	T	L	κ	$m_{\text{eff}}(f_{\text{A}})$	# MDU
`M3216c1`	8.57*	32	16	0.13049252054	0.000126(42)	4680
`M4824c1`	8.57*	48	24	0.13049252054	0.000062(24)	3292
`M32c1`	8.57*	32	32	0.13049252054	0.000014(17)	3876

From these features, the identifiers of the ensembles as listed in the figure and table are, on the example of ensemble `A24c1`, abstracted as follows:

`A`: The first letter encodes the inverse coupling β, starting at the lowest with `A` at $\beta = 3.685$ to `E` at $\beta = 4.10$. We leave two placeholders (`F` and `G`) for prospective additions to the ensembles presented and denote $\beta = 4.37$ with `H`.

`24`: The numbers in the second place signify the lattice extension in the four space time dimensions $T/a = L/a$. As the lattices introduced here all have equal time and space extension, only one number for the identifier is used. In other cases, one may use the time and space extension concatenated, like `2416` for $T/a = 24$ and $L/a = 16$.

`c`: The lower case letter identifies the position of the lattices with respect to the lines of constant physics. Lattices close to the chiral limit are denoted with a `c`, the ones close to the symmetric point with an `s` and the ones in between with an `i` for intermediate. The identifier `h` denotes heavy lattices with $\phi_4 > 1.115$.

`1`: The last number is a serial number for the cases in which two ensembles are not distinguishable by the other identifiers, e.g. when we have two ensembles between the lines of constant physics, as in the case of `E56i1` and `E56i2`. The serial numbers start with `1`.

Separate from these ensembles, also three ensembles at $\beta = (6/0.7) \approx 8.57$ were produced, which are listed in table 5.2. They do not lie on either of the lines of constant physics, as their volume is much smaller, however an estimate for their lattice spacing is not given. We can see from their effective mass that they lie close to the chiral limit. We will employ these ensembles in order to check whether our extrapolations in g_0^2 hold approximately at smaller couplings.

With the ensembles at hand, we are able to set up interpolations for the improvement and renormalization to the exact points of interest as to smooth out inaccuracies in the tuning of the ensembles. In particular, we aim for the improvement of the axial-vector current at the symmetric point as an alternative definition of improvement, defining a „massive“ improvement scheme. The improvement of the currents is defined through this directly at the mass point of further calculations, the $N_\mathrm{f} = 3$-symmetric point in our case.

As the ensembles are created with `openQCD` [126], which implements exponential Wilson fermions in version `2.0` and higher, some basic calculations are already carried out during generation, employing the appropriate programs from the `openQCD` library. In particular, the (reweighting) measurements for the rational HMC algorithm and the flowed observables, that we will introduce in a minute are already carried out. Further calculations, in particular of the correlation functions needed for the analyses for improvement and renormalization have been calculated with `SFCF` [127]. On a technical note: We will deal with a lot of interpolations and extrapolations from the ensembles to the lines of constant physics described. The ensembles at hand only allow for interpolation in the strict sense in a few scenarios (namely, when the smallest quark mass is slightly negative). Thus, we will use the words interchangeably in the interest of readability, and keep in mind that – strictly speaking – there are only a few cases in which this is actually an interpolation.

5.1 Preparatory analyses

Before carrying out the calculations we aim for, we need to do a few preparatory analyses, which are necessary for the self-sufficiency of the discussed analyses. They amount essentially to the evaluation of the dimensionless mass parameter ϕ_4 for the ensembles at hand. The parameter is built from the effective pion mass and the scale parameter t_0. The mass parameters m_0^{crit} and m_0^{sym}, which are needed to implement the two lines of constant physics for each lattice spacing are evaluated by interpolation.

The scale parameter t_0 makes its first appearance here, and we will only introduce it briefly. In short terms, as the inverse coupling β is used as the simulation parameter, the lattice spacing is not known a priori. We need to determine it and, as was the case with the renormalized coupling in equation (2.35), it depends on the quark masses as well. Over the years, many strategies to set the scale have been introduced, like the scale setting through hadron masses [25, ch. 6.4] or the Sommer scale r_0 [25, ch. 3]. Reference [128] gives an overview over some strategies in use. A popular method today is to use the parameter t_0. It is derived through the flow-equation [129]

$$\frac{\mathrm{d}B_\mu}{\mathrm{d}t} = D_\nu G_{\nu\mu}\,,\ B_\mu\big|_{t=0} = \mathcal{A}_\mu \tag{5.1}$$

$$G_{\mu\nu} = \partial_\mu B_\nu - \partial_\nu B_\mu + [B_\mu, B_\nu] \tag{5.1a}$$

$$D_\mu X = \partial_\mu X + [B_\mu, X]\,, \tag{5.1b}$$

a differential equation in the *flow time*, t, which has dimension 2. As is evident, at $t = 0$, the flowed field B coincides with the lattice gauge-field. The scale can be determined via the energy density E of the flowed field. The advantage of this method is that at finite flow time, the fields renormalize in a simple way [129–131]. In fact, the energy density does not have to be renormalized. This property, together with the fact that this the clover energy is a local quantity that is comparatively inexpensive to calculate makes for a good scale setting parameter, as it can be determined to relative high accuracy. The parameter t_0 is then implicitly defined through

$$t_0^2\langle E\rangle = 0.3\,. \tag{5.2}$$

The 0.3 on the left-hand side is an empirical choice, as the scales received are comparable to earlier determination with the parameter r_0, and they are such that QCD is non-perturbative regime at these scales. Note that this is a purely theoretical quantity with no physical meaning. In [132, eq. (5.5)], the physical counterpart t_0^{phys} to this scale parameter was calculated for the traditional Wilson Clover action with the same gauge action as our ensembles are based on. The numerical value we cite for the rest of this thesis is

$$\sqrt{8t_0^{\mathrm{phys}}} = 0.415(5)\,\mathrm{fm}\,, \tag{5.3}$$

as by the OpenLat guidelines. Note that this scale is defined at the $N_\mathrm{f} = 3$-flavour symmetric point and that there is a newer scale setting available on the CLS ensembles [133, eq. (7.1)]. The newer scale parameter is not used in the context of this thesis, but is compatible with the one cited here.

5.1.1 Evaluation of ϕ_4

The dimensionless parameter ϕ_4 is often used to compare the mass of quarks across lattice spacings. It is defined by

$$\phi_4 = \frac{3}{2} 8 t_0 m_{\mathrm{eff}}^2\,, \tag{5.4}$$

in which the effective mass is that of the pion on the lattice. Through the Gell-Mann–Oakes–Renner relation [134], ϕ_4 is linearly proportional to the quark masses. To be fully able to leverage the linearity, in the Schrödinger functional, we redefine ϕ_4 as

$$\phi_4 = \frac{3}{2} 8 t_0 m_{\mathrm{eff}} |m_{\mathrm{eff}}|\,, \tag{5.5}$$

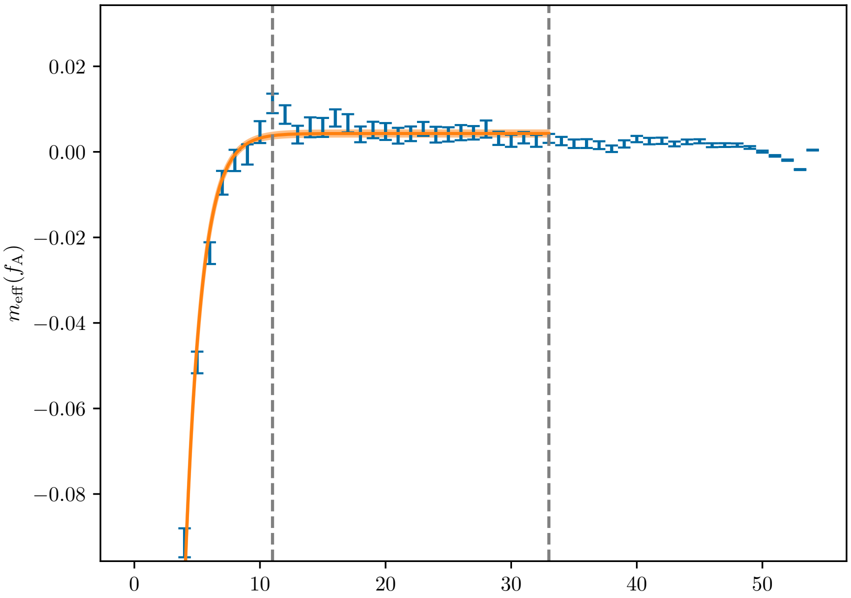

Figure 5.2: Example of the fit (orange) to the effective mass (data points in blue) in the axial-vector channel used to fix ϕ_4 on ensemble `E56c1`.

which equals taking the sign of the quark masses into account, such that negative quark masses also fall in line.

The determination of the effective mass on the Schrödinger functional ensembles we introduced amounts to fixing a plateau range in the effective masses in the axial-vector channel, while keeping the contaminations from higher states in mind.

Compared to analyses such as the one carried out in [135], we vastly simplify our strategy as we will not estimate the glue-ball mass that dominates the boundary effects on the upper ($[1/2T, T]$) part of the lattice. Instead, we fit the first half of the lattice with equation (2.45) as our ansatz, evaluating the first excited state contributions. The final time slice of the fit is successively moved through the second half of the lattice, while we evaluate the χ^2/d.o.f. for each fit. The time-slice with the minimal χ^2/d.o.f. defines the final time slice of the fit. For the beginning of the plateau, we demand

$$\frac{c_1\Delta_1}{c_0}e^{-\Delta_1 x_0} < \sigma_{\text{stat}}(x_0)/4 \tag{5.6}$$

in which σ_{stat} is the statistical uncertainty of the effective mass. An example of the fit to the effective mass and to the correlator are shown in figure 5.2.

Through this procedure, we receive a reliable plateau range in the effective mass, and are able to extract the means of the masses from the plateau, which are listed in table 5.3.

At the same time, t_0 is evaluated on the Schrödinger functional ensembles as to calculate ϕ_4 and fix the lattice spacing. The expectation value of the flowed clover energy-density $\langle E(t)\rangle$ is averaged over a range $x_0 \in [1/3, 2/3]T$ at different values of the flow time. The averaging range is chosen quite conservatively, as can be seen in figure 5.3. On the finest ensembles (`H96`), we take a few more time slices into account and define $x \in [29, 67]$. The fit to find the point in question is shown in figure 5.4. With the values of m_{eff} and t_0, we can evaluate the parameter ϕ_4 on each ensemble. The values are listed

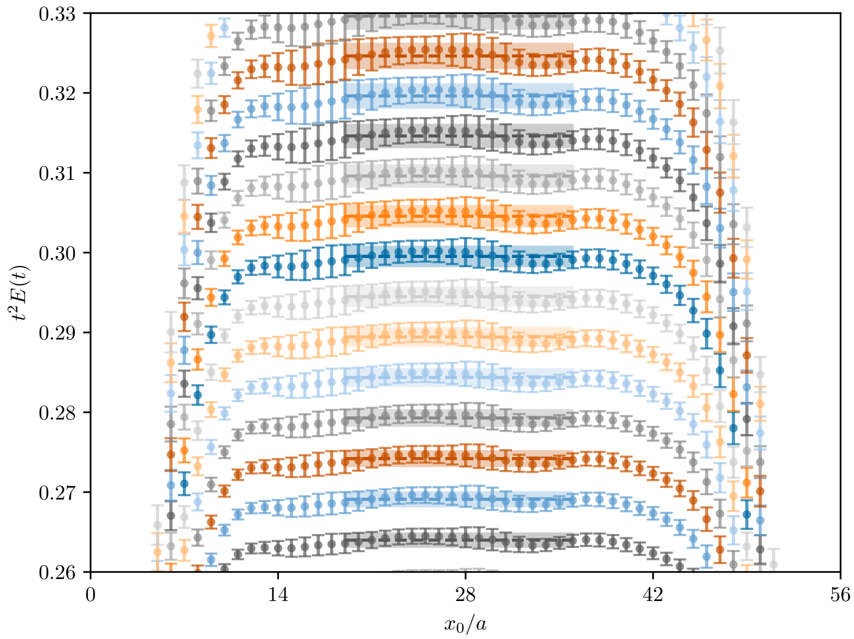

Figure 5.3: Plateaus in the Yang-Mills clover action energy on ensemble `E56c1` at different flow times t. The flow-times are marked by the different colors, whose description we omit here.

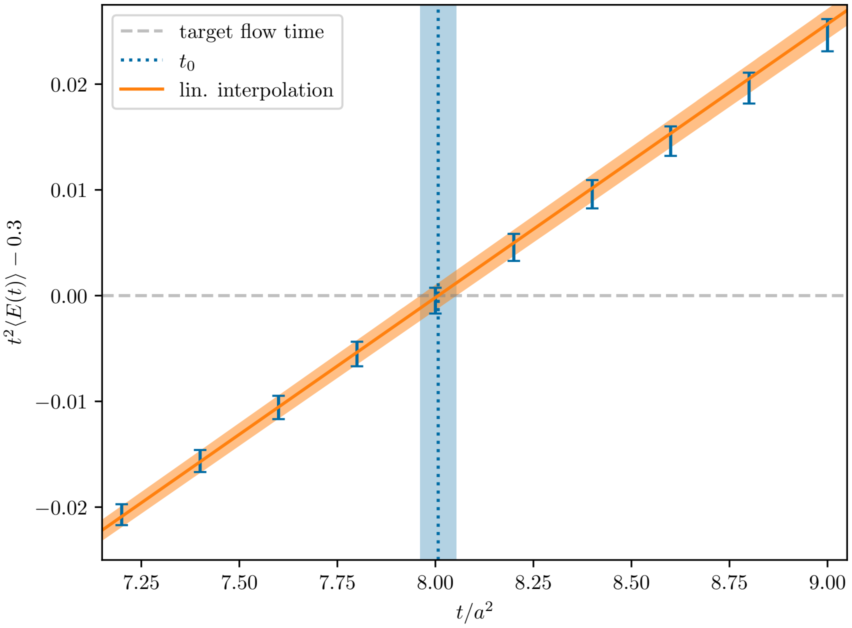

Figure 5.4: Linear fit of $t^2\langle E(t)\rangle$ at a range around the point of interest, at which t_0 is defined. This example is also taken from ensemble `E56c1`.

Table 5.3: Table of the final evaluations of the effective masses in the axial-vector channel $m_{\mathrm{eff}}(f_{\mathrm{A}})$ and the scale parameter t_0 the Schrödinger functional ensembles that are needed for the evaluation of ϕ_4 by equation (5.5).

Name	$m_{\mathrm{eff}}(f_{\mathrm{A}})$	t_0	ϕ_4
A24s1	0.2458(18)	1.400(88)	1.015(64)
A24i2	0.1826(17)	1.5815(57)	0.633(11)
A24i2	0.0763(30)	1.7080(40)	0.1192(89)
A24c1	-0.023(12)	1.7561(66)	-0.011(12)
B32s1	0.19312(82)	2.4284(47)	1.0868(85)
B32i1	0.13364(61)	2.5907(51)	0.5553(44)
B32c1	-0.0213(36)	2.7808(59)	-0.0152(51)
C40s1	0.15822(71)	3.6118(100)	1.0850(87)
C40i2	0.15489(62)	3.635(17)	1.0464(65)
C40i1	0.11075(56)	3.8226(86)	0.5626(61)
C40c1	-0.00065(100)	4.016(13)	-0.000020(62)
D48s1	0.13151(39)	5.258(13)	1.0911(70)
D48c2	0.0101(10)	5.722(29)	0.0071(15)
D48c1	0.00013(32)	5.747(14)	0.0000012(57)
E56s1	0.11270(45)	7.407(30)	1.1290(76)
E56i2	0.10423(37)	7.391(33)	0.9635(66)
E56i1	0.09509(55)	7.605(39)	0.8252(88)
E56c1	0.00444(73)	8.020(49)	0.00189(61)
H96h1	0.09110(60)	17.57(13)	1.749(21)
H96s1	0.06866(49)	18.02(17)	1.020(16)
H96i1	0.05417(44)	18.59(22)	0.655(12)

together in table 5.3.

As the scale t_0^{phys} is defined at the symmetric point, we need to extrapolate the extracted values of t_0 to $\phi_4 = 1.115$ to fix the lattice spacing. This is shown for $\beta = 3.900$ in figure 5.5. The lattice spacings that we find through this procedure have been listed in table 5.1.

5.1.2 Defining the lines of constant physics at each lattice spacing

With the values of ϕ_4 at hand, it is convenient to define the chiral and symmetric LCP in terms of the mass m_0 by linearly interpolating in ϕ_4 at different lattice spacings, which is shown exemplary in figure 5.6. In table 5.4 the bare quark masses m_0 are listed for each value of β.

This concludes the introduction of the Schrödinger functional ensembles. With the values that we were able to define here, the improvement and renormalization that we set out to determine is discussed in the following.

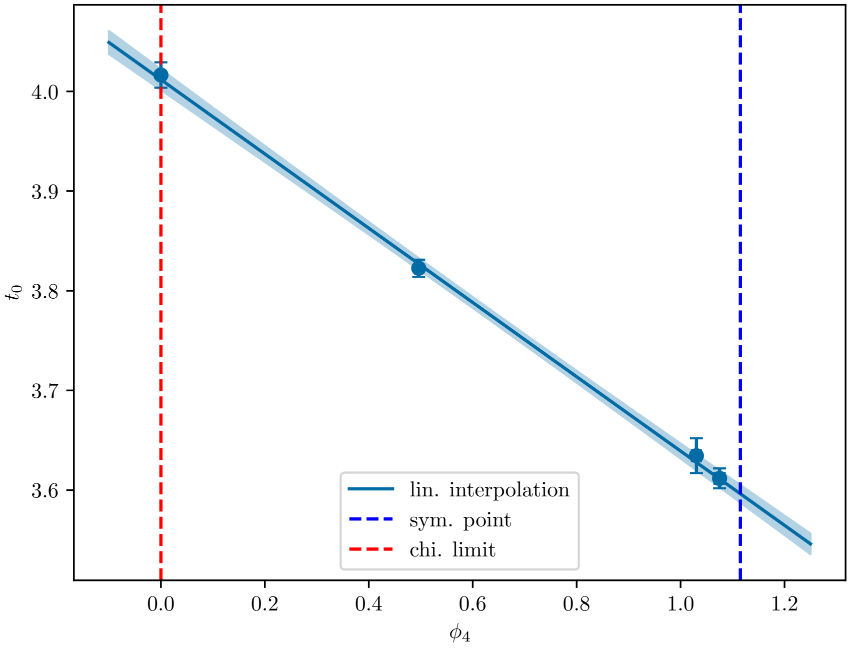

Figure 5.5: Interpolation of t_0 to the symmetric point ($\phi_4 = 1.115$) at $\beta = 3.900$.

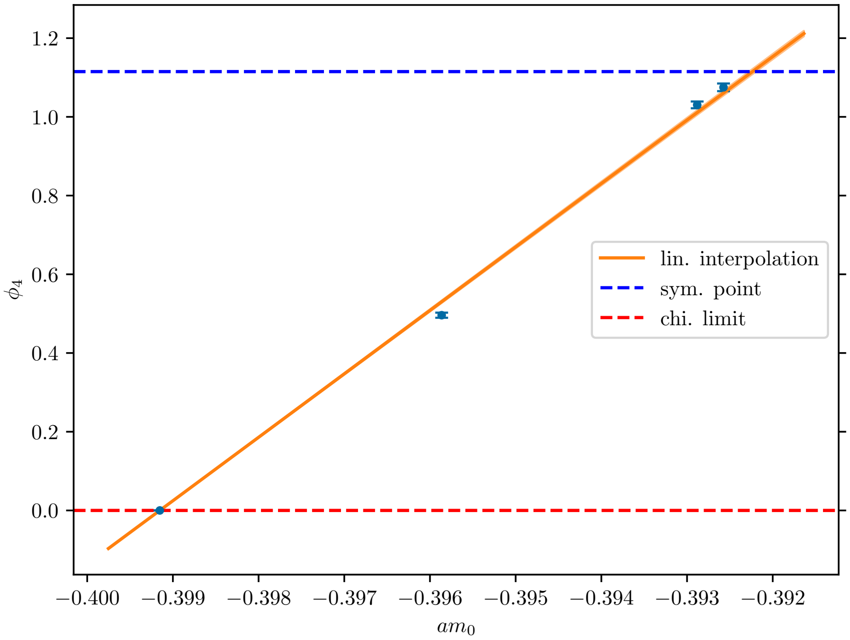

Figure 5.6: An exemplary interpolation in the mass parameter to find the mass parameters of interest for the two lines of constant physics.

Table 5.4: The bare quark masses m_0 at the couplings investigated for the chiral m_0^{chi} and symmetric m_0^{sym} lines of constant physics.

β	3.685	3.800	3.900
am_0^{chi}	-0.420694(30)	-0.409231(20)	-0.39915243(43)
am_0^{sym}	-0.41361(12)	-0.401380(42)	-0.392236(38)

β	4.000	4.100	4.370
m_0^{chi}	-0.38973957(48)	-0.3805141(21)	-0.356805(52)
m_0^{sym}	-0.383525(45)	-0.375377(25)	-0.353567(23)

Chapter 6

The axial-vector current

One of the ground layers of improving and renormalizing a fermion formulation on the lattice is the improvement of the axial-vector current. As the renormalization and improvement strategies detailed in the following chapters are derived from equation (3.11c), and the axial variation of the action includes the introduction of the PCAC mass, identities from this variation rely on the axial current. Therefore, after improving the action itself, the next step is usually the improvement of the non-singlet axial-vector current. It is one of the major focus points of the projects presented and is discussed in section 6.1.

The improved current also allows us to non-perturbatively renormalize it, which is presented in section 6.2. For the case of the axial-vector current, we are however only able to estimate the mass-independent part of the renormalization, Z_{A}.

Parts of the project presented have already been discussed in my master thesis [122] and our proceedings [123]. In this chapter, we expand on these references.

6.1 Improvement

The improvement of the axial-vector current relies on the PCAC relation. We revisit equation (3.15), as to expand on some details we have not discussed earlier. For this chapter, we use the PCAC relation with the external operator O defined by equation (2.46) as a pseudo-scalar boundary operator

$$O = \bar{\zeta}(\vec{x}, \theta)\ \gamma_5 \omega(\vec{x}, \vec{y})\ \zeta(\vec{y}, \theta)\ , \tag{6.1}$$

in which ζ are the Schrödinger functional boundary fields at $t = 0$. They may carry a phase θ, as described in [77, sec. 4.2]. The counterpart of the source operator on the other side of the lattice is accordingly defined by

$$O' = \bar{\zeta}'(\vec{x}, \theta)\ \gamma_5 \omega(\vec{x}, \vec{y})\ \zeta'(\vec{y}, \theta) \tag{6.2}$$

where ζ' are the fermion boundary fields at $t = T$. The function $\omega(\vec{x}, \vec{y}) : (\mathbb{R}^3, \mathbb{R}^3) \mapsto \mathbb{R}$ is a smooth, arbitrary function on the space-like directions of the lattice.

With this replacement, we find a specific case of the PCAC relation:

$$2m \left\langle \mathrm{P}(x) \mathcal{O}_{\mathrm{ext}}(\omega) \right\rangle = \left\langle \partial_\mu \mathrm{A}_\mu(x) \mathcal{O}_{\mathrm{ext}}(\omega) \right\rangle\ . \tag{6.3}$$

Renormalization cancels in this setup. We therefore postpone the introduction of the renormalized currents and discuss it later, in chapter 8. Transitioning to the lattice formulation and integrating over the spatial extent of the lattice, the quark-current mass is defined in terms of Schrödinger functional correlation functions as

$$am = \frac{a\hat{\partial} f_{\mathrm{A}}(x)}{2f_{\mathrm{P}}(x)} + \mathrm{O}(a^n)\ , \tag{6.4}$$

(see app. C for quick reference) in which the order n is given by the order to which our theory is improved. The lattice derivative $\hat{\partial}$ is given by the symmetric derivative as detailed in equation (B.3), if not stated otherwise. With this alone, we are able to improve the axial-vector current.

6.1.1 Improvement condition

An improvement condition for the axial-vector current was already formulated in quenched QCD [78]. The approach relies on the fact that the external source operator $\mathcal{O}_{\mathrm{ext}}$ is arbitrary. The PCAC mass in the continuum is invariant under changes in the boundaries, such that any difference Δm in the current quark mass has to be induced by lattice artefacts. This provides the leverage needed to improve the axial-vector current up to $\mathrm{O}(a^2)$.

As the pseudo-scalar density P^a does not receive improvement in first order that is absorbed into renormalization factors, it is for our intents and purposes already improved, meaning that the $\mathrm{O}(a)$-improved PCAC mass is given by

$$am^{\mathrm{I}} = \frac{a\hat{\partial} f_{\mathrm{A}}^{\mathrm{I}}(x)}{2f_{\mathrm{P}}(x)} + \mathrm{O}(a^2) = \frac{a\hat{\partial} f_{\mathrm{A}}(x) + c_{\mathrm{A}} a^2 \hat{\partial}^2 f_{\mathrm{P}}(x)}{2f_{\mathrm{P}}(x)} + \mathrm{O}(a^2) \tag{6.5}$$

in terms of Schrödinger functional correlation functions. If two improved PCAC masses $(m^{\mathrm{I}})^{(0)}$ and $(m^{\mathrm{I}})^{(1)}$ are not the same due to a change in the boundary fields, we are able to extract c_{A} from this difference in the following way:

$$\begin{aligned}
(m^{\mathrm{I}})^{(0)} &= (m^{\mathrm{I}})^{(1)} && (6.6)\\
\frac{\hat{\partial}(f_{\mathrm{A}}^{\mathrm{I}})^{(0)}(x)}{2f_{\mathrm{P}}^{(0)}(x)} &= \frac{\hat{\partial}(f_{\mathrm{A}}^{\mathrm{I}})^{(1)}(x)}{2f_{\mathrm{P}}^{(1)}(x)} + \mathrm{O}(a^2)\\
\frac{\hat{\partial} f_{\mathrm{A}}^{(0)}(x) + c_{\mathrm{A}} a \hat{\partial}^2 f_{\mathrm{P}}^{(0)}(x)}{2f_{\mathrm{P}}^{(0)}(x)} &= \frac{\hat{\partial} f_{\mathrm{A}}^{(1)}(x) + c_{\mathrm{A}} a \hat{\partial}^2 f_{\mathrm{P}}^{(1)}(x)}{2f_{\mathrm{P}}^{(1)}(x)} + \mathrm{O}(a^2)\\
r^{(0)}(x) + ac_{\mathrm{A}} s^{(0)}(x) &= r^{(1)}(x) + ac_{\mathrm{A}} s^{(1)}(x) + \mathrm{O}(a^2)\\
c_{\mathrm{A}} a \left(s^{(0)}(x) - s^{(1)}(x)\right) &= \left(r^{(1)}(x) - r^{(0)}(x)\right) + \mathrm{O}(a^2)\\
c_{\mathrm{A}} &= -\frac{\left(r^{(1)}(x) - r^{(0)}(x)\right)}{a\left(s^{(1)}(x) - s^{(0)}(x)\right)} + \mathrm{O}(a)\\
c_{\mathrm{A}} &= -\frac{\Delta r}{a\Delta s} + \mathrm{O}(a)\ . && (6.7)
\end{aligned}$$

The helper functions

$$r = \frac{\hat{\partial} f_{\mathrm{A}}(x)}{2f_{\mathrm{P}}(x)} \text{ and } s = \frac{\hat{\partial}^2 f_{\mathrm{P}}(x)}{2f_{\mathrm{P}}(x)} \tag{6.8}$$

denote the unimproved mass and the improvement part, respectively. The differences Δr and $a\Delta s$ are of interest to look at, as they are directly related to the signal of c_{A}.

6.1.2 The wavefunction method

There are multiple ways in which the boundary fields of the lattice can be varied. For example, in quenched lattice QCD, the boundary phase θ was varied [78] (cf. equations (6.1) and (6.2)). This however entailed the generation of new gauge field ensembles for each angle θ to examine. In the $N_\mathrm{f} = 2$-flavour case, this was abandoned in favour of the wavefunction method [136], as this does not require new (expensive) simulations for the variation of the boundary conditions. Since then, this has been the standard method for estimating c_A and has also been employed in [137, 138] to estimate the improvement of the axial-vector current for the theory with $N_\mathrm{f} = 3$ traditional Wilson-clover fermions. The method is presented here in short terms along the lines of [31, ch. 4.4].

Instead of varying the boundary quark fields themselves, the function ω in the boundary operator O is varied and the phase θ is kept constant (we hold $\theta = 0$ in the case presented). The independence of the PCAC mass discussed above holds in this scenario as well. Therefore, altering this function enables a determination of the improvement parameter c_A without expensive new gauge field generation.

The idea in the wave function method is to optimize the functions ω employed in regard to signal clarity and stability of the produced states. As a cornerstone, we assume that it is possible to find a set of functions $\{\omega_0, \omega_1\}$ that approximate the spatial form of the two lowest energy eigenstates of the pion. It is furthermore assumed, that this form can be approximated well by a linear combination of the hydrogen wavefunctions (hence the name of the method). The following functions have been chosen traditionally as a basis:

$$\omega_{\mathrm{b}1}(r) = e^{-r/a_0} \tag{6.9a}$$

$$\omega_{\mathrm{b}2}(r) = r\ e^{-r/a_0} \tag{6.9b}$$

$$\omega_{\mathrm{b}3}(r) = e^{-r/(2a_0)}\ . \tag{6.9c}$$

In our analysis, we have complemented this basis by two more functions

$$\omega_{\mathrm{b}4}(r) = \mathrm{cons.} \tag{6.10a}$$

$$\omega_{\mathrm{b}5}(r) = r^2\ e^{-r/a_0}\ , \tag{6.10b}$$

in which the function $\omega_{\mathrm{b}4}$ would resemble an infinitely smeared out state, while $\omega_{\mathrm{b}5}$ resembles a higher excited state of the hydrogen wavefunction.

The parameter a_0 is arbitrary and parametrizes the spatial extent of the bound state. In earlier calculations, this was set as $a_0 = L/6 \approx 0.16\,\mathrm{fm}$. We use the physical extent as a guideline and take $a_0 = L/18$, as the lattices in this analysis are larger ($L \approx 3\,\mathrm{fm}$). In section 6.1.3, an example analysis is shown.

To achieve the best overlap with the ground state and the first excited state, a linear combination of the wavefunctions is employed. As the prefactors of the linear combination are not known a priori, we need a way to estimate these reliably.

The boundary-to-boundary correlation function

$$(F_1)_{ij} = \langle O'(\omega_{\mathrm{b}j}) O(\omega_{\mathrm{b}i}) \rangle \tag{6.11}$$

is employed for this goal (cf. equation (C.5)). In which, at both ends of the lattice, the base wavefunctions $\omega_{\mathrm{b}i}$ are placed in the boundary operator.

The correlator is calculated with all possible combinations of the base wavefunctions, defining a matrix $(F_1)_{ij}$. The boundary-bulk correlation functions

$$(f_X(t))_i = \langle X(t) O(0, \omega_{\mathrm{b}i}) \rangle \tag{6.12}$$

can be seen as vectors in this regard. The matrix $(F_1)_{ij}$ is hermitian due to time-symmetry. It is therefore diagonalizable and the eigenvectors of the matrix are orthogonal to each other. We denote the eigenvalues of the matrix as λ_n in descending order of magnitude, $\lambda_{n+1} < \lambda_n$ and order their respective eigenvectors as η_n accordingly. To see how this helps the analysis, we remember the energy expansion,

$$F_1(\omega_i, \omega_j) = \sum_{n=0}^{\infty} v_i^{(n)} e^{-m_\pi^{(n)} t} v_j^{(n)} + \mathrm{O}(e^{-m_\mathrm{G} t}) \tag{6.13}$$

in which $v_i^{(n)}$ $(v_j^{(n)})$ are the overlaps of the spatial state produced by ω_i (ω_j) and the n-th energy state with mass $m_\pi^{(n)}$ (cf. [135,139]). The mass m_G denotes the mass of the lowest scalar state in this context. As the masses $m_\pi^{(n)}$ are ordered such that $m_\pi^{(n+1)} > m_\pi^{(n)}$, the term with $n = 0$ dominates, when t is large. This term is the ground state of the pseudo-scalar channel $(\pi^{(0)})$, with the overlap vectors $v_i^{(0)}$ $(v_j^{(0)})$. The ground state is then equal to the state produced by the eigenvector η_0, as can be seen by the following argument:

When multiplying the energy expansion with η_0, one receives

$$F_1(\omega_{\mathrm{b}i}, \omega_{\mathrm{b}j}) \eta_j^{(0)} = v_i^{(0)} e^{-m_\pi^{(0)} t} \left(v_j^{(0)} \eta_j^{(0)} \right) + \mathrm{O}\left(e^{-m_\pi^{(n)} t} \right) + \mathrm{O}\left(e^{-m_\mathrm{G} t} \right) \ , \tag{6.14}$$

where the left-hand side can be written as $\lambda_0 \eta_0$, such that

$$\lambda^{(0)} \eta_j^{(0)} = v_i^{(0)} e^{-m_{\pi(0)} t} \left(v_j^{(0)} \eta_j^{(0)} \right) + \mathrm{O}\left(e^{-m_{\pi(n)} t} \right) + \mathrm{O}\left(e^{-m_\mathrm{G} t} \right) \tag{6.15}$$

$$\eta_i^{(0)} = \alpha v_i^{(0)} + \mathrm{O}\left(e^{-m_{\pi(n)} t} \right) + \mathrm{O}\left(e^{-m_\mathrm{G} t} \right) \tag{6.16}$$

with a complex phase α, that can be absorbed by defining $\eta^{(0)}$ and $v^{(0)}$ with suitable complex phases. The vector η_0 is therefore an approximation of the ground state.

Due to the hermiticity of the matrix, the eigenvectors η_0 and η_1 are orthogonal to each other. The ground state is therefore suppressed:

$$0 = \eta_0 \eta_1 \approx v_0 \eta_1 + \mathrm{O}(e^{-(m_{\pi(1)} - m_{\pi(0)}) T}) + \mathrm{O}(e^{-(m_\mathrm{G} - m_{\pi(0)}) T}) \ . \tag{6.17}$$

In conclusion, we receive the ground state and first excited state

$$\omega_{\pi(0)} = \sum_i \omega_{\mathrm{b}i} (\eta_0)_i \ , \quad \omega_{\pi(1)} = \sum_i \omega_{\mathrm{b}i} (\eta_1)_i \tag{6.18}$$

of the pseudo-scalar channel in this way. By scalar multiplication, the correlators f_A and f_P are projected onto these states as well:

$$(f_X(t))_{\pi(0)} = \sum_i (f_X(t))_i (\eta_0)_i \ , \quad (f_X(t))_{\pi(1)} = \sum_i (f_X(t))_i (\eta_1)_i \tag{6.19}$$

and the determination of c_A through the difference in the current quark mass as suggested in 6.1.1 can be evaluated with these states.

6.1.3 Base analysis

In practice, the analysis is carried out as follows: The correlation functions $f_\mathrm{A}(\omega_{\mathrm{b}i}; x_0)$, $f_\mathrm{P}(\omega_{\mathrm{b}i}; x_0)$, $g_\mathrm{A}(\omega_{\mathrm{b}i}; x_0)$, $g_\mathrm{P}(\omega_{\mathrm{b}i}; x_0)$ are calculated for all basis wavefunctions, as well as $F_1(\omega_{\mathrm{b}i}, \omega_{\mathrm{b}j})$ for all wavefunction combinations. As in reference [31], multiple sources on the boundaries are used in order to improve the statistical yield. In the analysis presented, 64 sources are employed, with equidistant spacing along the lattice, such that there is a source at every

$$\vec{x}_{\mathrm{src}} = \begin{pmatrix} x_1 \\ x_2 \\ x_3 \end{pmatrix} \quad \text{with } x_1, x_2, x_3 \in \left\{0,\ \frac{1}{4}L,\ \frac{1}{2}L,\ \frac{3}{4}L\right\} . \tag{6.20}$$

As the box size in this project is about three times larger in each direction than in previous determinations, e.g. [138], this choice is not expected to increase correlations significantly. The only exception being the constant wavefunction ω_{b4}, which has larger correlations at small x_0 compared to the other wavefunctions. The source terms and time-reverse partners f_{A} (f_{P}) and g_{A} (g_{P}) are averaged over with their respective time symmetries in mind.

As an example, let us look at the ensemble `C40c1`, which is chosen due to the following properties: It lies in the middle of the lattice spacings of interest, while being close to the chiral limit. Its setup is therefore one that is more comparable to the traditional one. The matrix $(F_1)_{ij}$ in wavefunction space is determined to be

$$(F_1)_{ij} = \begin{pmatrix} 824(10) & 1060(13) & 1202(15) & 927(14) & 1164(15) \\ 1060(13) & 1364(18) & 1547(20) & 1192(19) & 1497(20) \\ 1202(15) & 1547(20) & 1753(24) & 1351(22) & 1698(23) \\ 927(14) & 1192(19) & 1351(22) & 1038(21) & 1308(21) \\ 1164(15) & 1497(20) & 1698(23) & 1308(21) & 1644(22) \end{pmatrix} , \tag{6.21}$$

where the matrix is already symmetrized $\bar{M} = (M + M^T)/2$ as to cancel out numerical inaccuracies and the imaginary part.

As mentioned, we are free to choose any subspace of the wavefunction space to find the best overlap with the two desired states. It is easy to see (cf. [122, app. B]) that the case of a 2-dimensional subspace makes the determination of the second eigenvector trivial. In order to not over constrain the system, it was decided to only use subspaces with dimension $d > 2$. Two cases are considered in this example: The traditional case of $d = 3$ with basis wavefunctions $\omega_{\mathrm{b1,b2,b3}}$ (the upper left 3×3 matrix of F_1) and the case of an extended basis with $\omega_{\mathrm{b1,b2,b3,b5}}$, which has been seen to improve the signal of c_{A} in some cases. We will call these the *standard* and the *preferred* projection respectively.

For both cases, the sub-matrices of $(F_1)_{ij}$ are diagonalized and one finds the following eigenvectors and eigenvalues

$$\lambda_0 = 3941(51) \qquad \lambda_1 = -0.15(14) \qquad \lambda_2 = 0.0016(11)$$

$$\eta_0 = \begin{pmatrix} 0.45717(62) \\ 0.648(34) \\ 0.610(36) \end{pmatrix} \qquad \eta_1 = \begin{pmatrix} 0.58829(22) \\ 0.294(42) \\ -0.753(16) \end{pmatrix} \qquad \eta_2 = \begin{pmatrix} 0.66702(62) \\ -0.703(14) \\ 0.247(39) \end{pmatrix}$$

$$\lambda_0 = 5585(73) \qquad \lambda_1 = -0.17(16) \qquad \lambda_2 = 0.0043(32) \qquad \lambda_3 = 0.000019(52)$$

$$\eta_0 = \begin{pmatrix} 0.38404(62) \\ 0.691(32) \\ 0.379(55) \\ 0.481(25) \end{pmatrix} \quad \eta_1 = \begin{pmatrix} 0.49419(30) \\ 0.389(25) \\ -0.295(71) \\ -0.719(22) \end{pmatrix} \quad \eta_2 = \begin{pmatrix} 0.56032(38) \\ -0.538(54) \\ 0.610(44) \\ -0.156(44) \end{pmatrix} \quad \eta_3 = \begin{pmatrix} 0.54252(32) \\ -0.288(58) \\ -0.630(49) \\ 0.476(43) \end{pmatrix}$$

for the standard and preferred projection respectively.

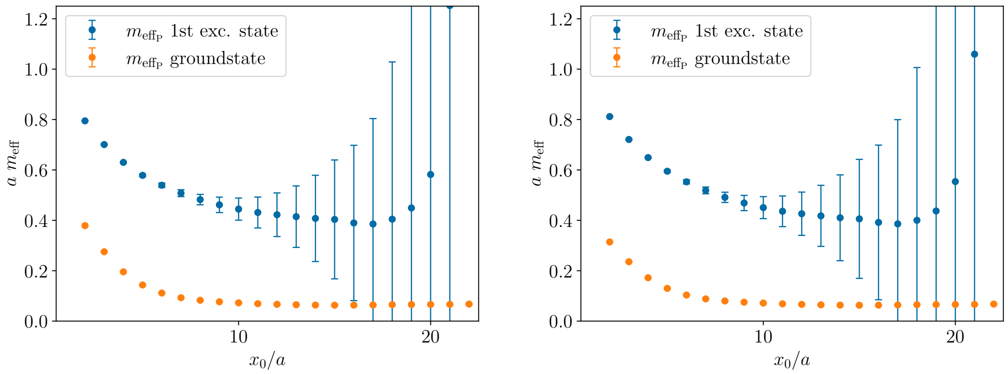

Figure 6.1: The effective mass in the pseudo-scalar channel on `C40c1`. We can visually see no difference between the two projections show. Here, the standard projection is shown on the left and the preferred projection is shown on the right.

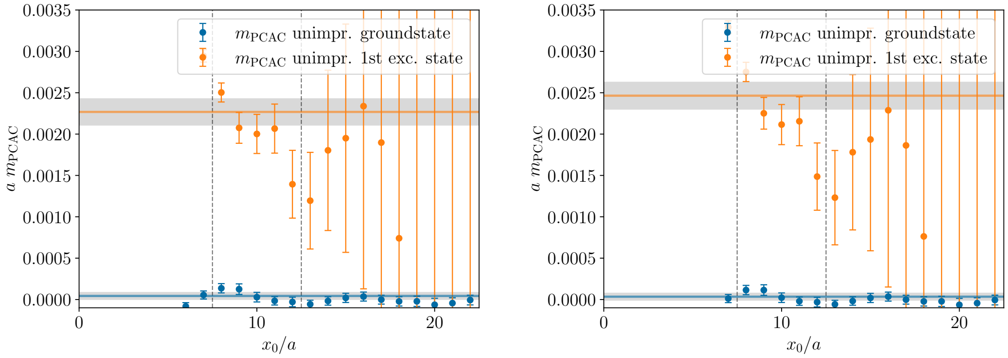

Figure 6.2: The unimproved PCAC current quark masses of the ground and first excited state on `C40c1`. As in the figure above, the standard projection is shown on the left and the preferred projection is shown on the right.

Note that, of the eigenvectors determined, the margins of error are not taken into account in the following. Since they are in principle not unique, but instead are just a convenient choice to build the pion states from the chosen base states. One may equally well carry out the calculations with fixed base wavefunction prefactors.

The projection of the correlation functions can be examined in the effective masses of the pseudo-scalar correlators, shown in figure 6.1, as F_1 projects onto the eigenstates of the pseudo-scalar channel.

As the improvement condition does not rely on the mass splitting in this channel directly, but the mass splitting in the PCAC masses, this is also inspected in figure 6.2. If the axial-vector current was improved, the splitting would vanish and the masses would be the same, as demanded by the improvement condition. The derivatives opted for in this example have discretization artefacts of $\mathrm{O}(a^2)$ (cf. equation (B.3)).

Summed up, we see that the projection in the standard and the preferred subspace are both promising, judging by the pseudo-scalar meson masses and the PCAC masses. However, it is also obvious that we need to define a place at which we extract c_{A}. The functions Δr and Δs are shown in figure 6.3. Due to the definition in the improvement condition, the signal of c_{A} depends on Δs in particular, which has clear signal that

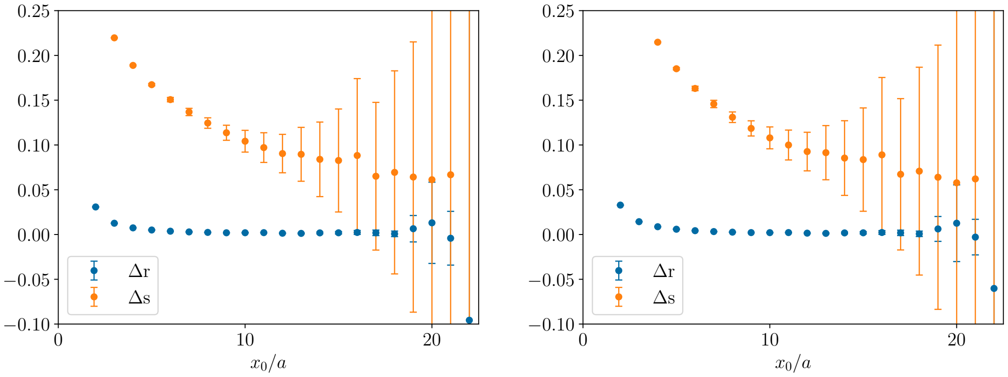

Figure 6.3: The difference functions Δr and Δs on ensemble `C40c1`, against the time x_0 on the lattice. Again, we cannot visually differentiate between the two projections. As in the figure above, the standard projection is shown on the left and the preferred projection is shown on the right.

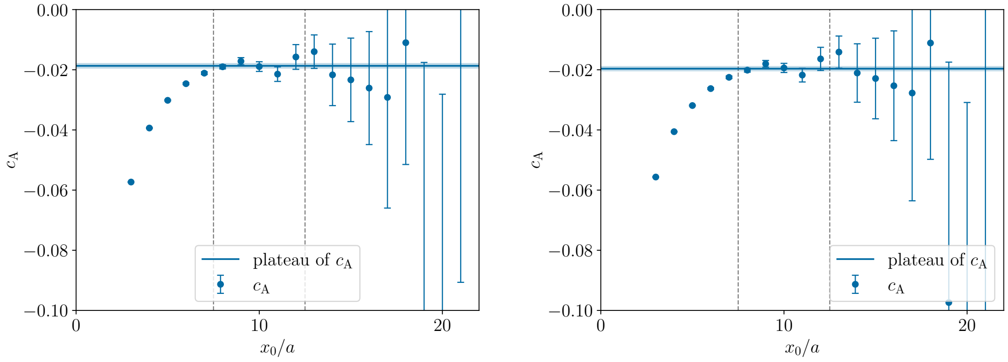

Figure 6.4: The improvement coefficient c_A shown with its time-dependency on `C40c1`. Again, we cannot visually differentiate between the two projections. As in the other figures, the standard projection is shown on the left and the preferred projection is shown on the right.

is sufficient in both projections investigated. The result of the basic analysis is the improvement coefficient c_A shown in figure 6.4, which is still time dependent.

We now make the choice for the definition of c_A as to where on the lattice we extract the value. In earlier calculations, $x_0 = T/2$ was chosen, as the boundary effects are evidently lowest in the middle of the lattice. However, as the signal on the larger lattices presented here vanishes before the middle of the lattice this is not an option in our case. Instead, we opt for an average over the range of time-slices $x_0 \in [0.2,\ 0.3]T$, which is presented in figure 6.4. While – in principle – all choices are valid, this range is has two properties that are desirable:

1. The range is far enough from the boundary such that boundary effects are negligible.
2. There is no signal-to-noise issue for c_A. The value within the plateau range is clear.

For these properties, the plateau around $x_0 = T/4$ is a compromise. With the definition of $x_0 \in [0.2,\ 0.3]T$, both demands are met on lattices with $0.055\,\text{fm} \leq a \leq 0.094\,\text{fm}$.

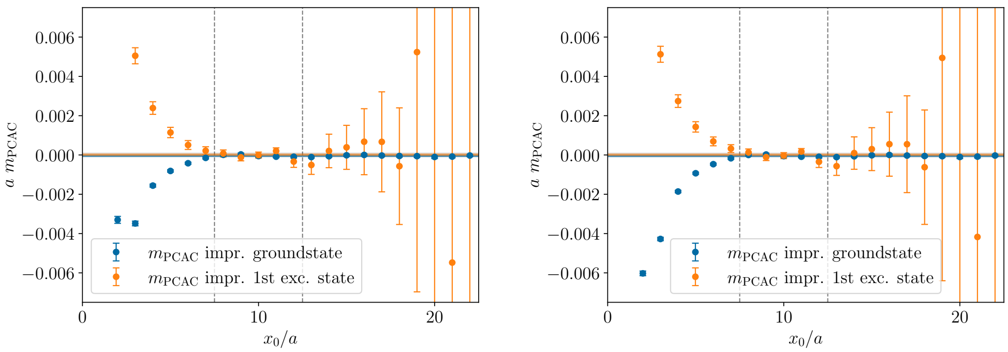

Figure 6.5: The improved PCAC current quark masses of the ground and first excited state on `C40c1`. Again, we cannot visually differentiate between the two projections. As in the other figures, the standard projection is shown on the left and the preferred projection is shown on the right.

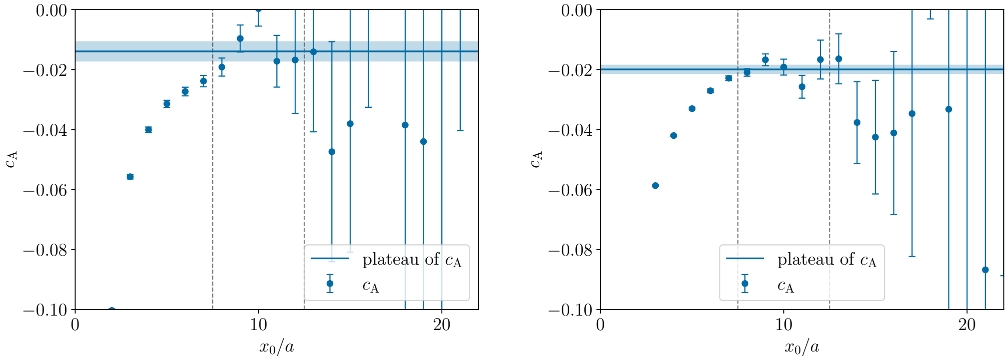

Figure 6.6: The time-dependent improvement coefficient c_{A} in the preferred projection, once with one single source (left) and with eight sources (right) on ensemble `C40c1`.

The final values extracted from this example are $c_{\mathrm{A}} = -0.01869(74)$ and $c_{\mathrm{A}} = -0.01963(69)$ for the standard and the preferred projection respectively. Re-evaluation of the PCAC masses with improved currents shows that the improvement condition is fulfilled, as shown in figure 6.5.

In figure 6.6 the results for c_{A} are shown with one and eight source terms on the boundary. Between them and the right plot in figure 6.4 a large reduction in statistical errors is seen, confirming that the introduction of more source terms is an option for error reduction on lattices of this size.

For the finest and coarsest lattice spacings, that is, $a \approx 0.035\,\mathrm{fm}$ and $a \approx 0.122\,\mathrm{fm}$, exceptions in regard to the plateau range were made. On the coarsest set of lattices, only one point is chosen to contribute, namely $x_0 = 7 \approx 0.292T$. In figure 6.7 the reason is clearly demonstrated: The boundary effects on these lattices are reaching far into the bulk, such that the compromise found earlier does not apply here.

On the fine end, the plateau range was altered to $x_0 \in [0.125,\ 0.250]T$. Figure 6.8 demonstrates the reason for this. In this case, while the „conventional“ choice of the plateau region would be possible, it is clear that this choice is not the most advantageous. With the plateau range presented here, lower margins of error are achieved and the quality of the result improves. On the other ensembles, the standard plateau range chosen is well-

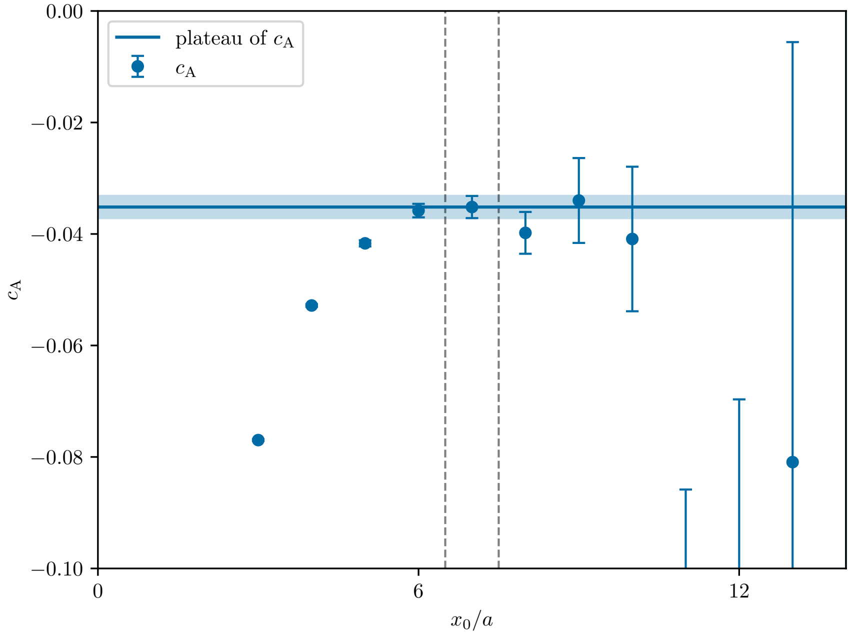

Figure 6.7: The improvement coefficient c_A, in dependence of the time on the lattice, in the preferred projection on ensemble `A24c1` with $a \approx 0.122\,\mathrm{fm}$. The vertical lines show the proposed plateau range.

supported, as can be seen in figure 6.9. This closes our discussion of the base analysis of c_A. The final results on the ensembles considered are listed in table 6.1. The rest of this section is structured out as follows:

First, some ambiguities of the strategy laid out in this example are examined more closely. Due to these, a systematic error is formulated that is estimated on grounds of the ambiguities found. Afterwards, the analysis of c_A is extended by interpolations to the exact lines of constant physics that we are interested in. For these extrapolations, two approaches are shown: A two-step approach, in which the value for c_A at a single squared coupling g_0^2 is determined first by extrapolating to the mass points of interest (cf. table 5.4 in the last chapter). An alternative to this is a single global fit, expressing c_A as a function of (g_0^2, ϕ_4). After those, a conclusion for this project is drawn, and we move on to the renormalization of the axial-vector current.

6.1.4 Ambiguities

So far, we have been investigating the same setup for two different choices of the wavefunction basis. Broadening the scope, the analysis discussed has to be investigated towards several ambiguities in the definition of the improvement factor.

We expect them to be not discernible in the $\mathrm{O}(a)$ improved theory. That is, the ambiguities in the improvement coefficient itself are at most of $\mathrm{O}(a)$, such that they play a role only at $\mathrm{O}(a^2)$ overall. In the next paragraphs, these are discussed shortly, as we investigate different types of ambiguities relevant for the analysis discussed above.

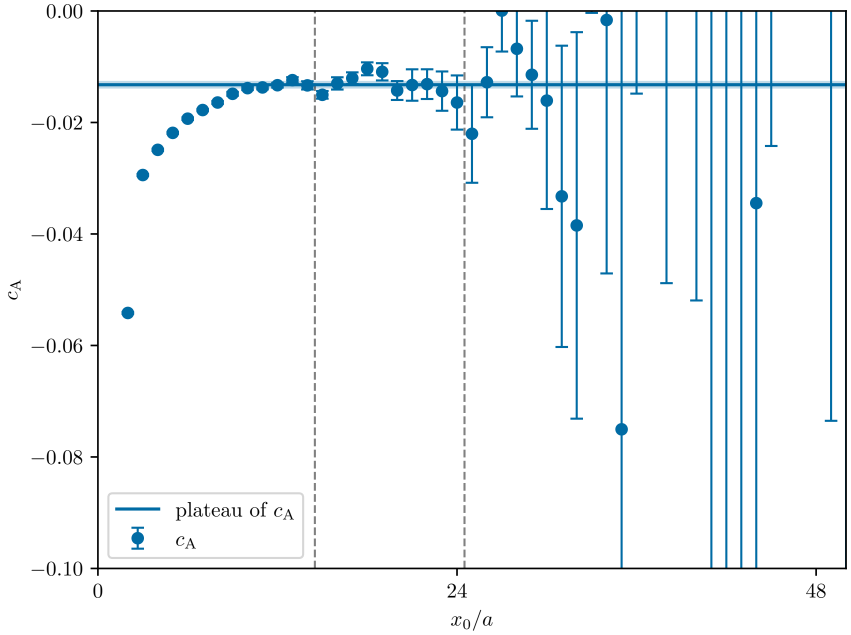

Figure 6.8: The improvement coefficient c_A in the preferred projection on ensemble `H96i1` with $a \approx 0.035$ fm, shown with its time-dependence and the proposed plateau range.

Wavefunctions When setting up the wavefunction method, we have argued that the choice of the wavefunction basis is arbitrary, as long as the margins of error on the PCAC masses are small enough to extract c_A. As we calculate of the F_1-matrix on each ensemble, we have made the determination of the concrete wavefunction part of the analysis. The choice of the basis wavefunctions is however still arbitrary and enters the analysis at a fundamental level.

With the example above as our guideline, we can compare the two bases shown on each ensemble and look at the differences

$$\Delta^{\mathrm{WF}} c_A = c_A^{\mathrm{std}} - c_A^{\mathrm{pref}} \tag{6.22}$$

in the final values. In figure 6.10, these differences are shown with a linear and a quadratic fit in the lattice spacing. As can be seen, when the fit is less constrained by the functions form, 0 is within statistical errors. In figure 6.11 one can see that this is not the only occasion: If one carries out the same ambiguity analysis for other wavefunction bases, one sees that the resulting interpolations are similar. In this particular example, the basis $\omega_{1,2,5}$ is compared to the two at hand.

Reuse of wavefunction coefficients So far, the base analysis and the differences inspected played out on a single ensemble, before being compared to other ensembles. The arbitrariness of the wavefunctions used can also be inspected differently:

In earlier determinations, e.g., [138], the linear combinations that are the eigenvectors η_0 and η_1 were determined on one ensemble and the result was reused for the rest of the analysis. In contrast, in the analysis presented here, the wavefunction combination was determined on every ensemble inspected.

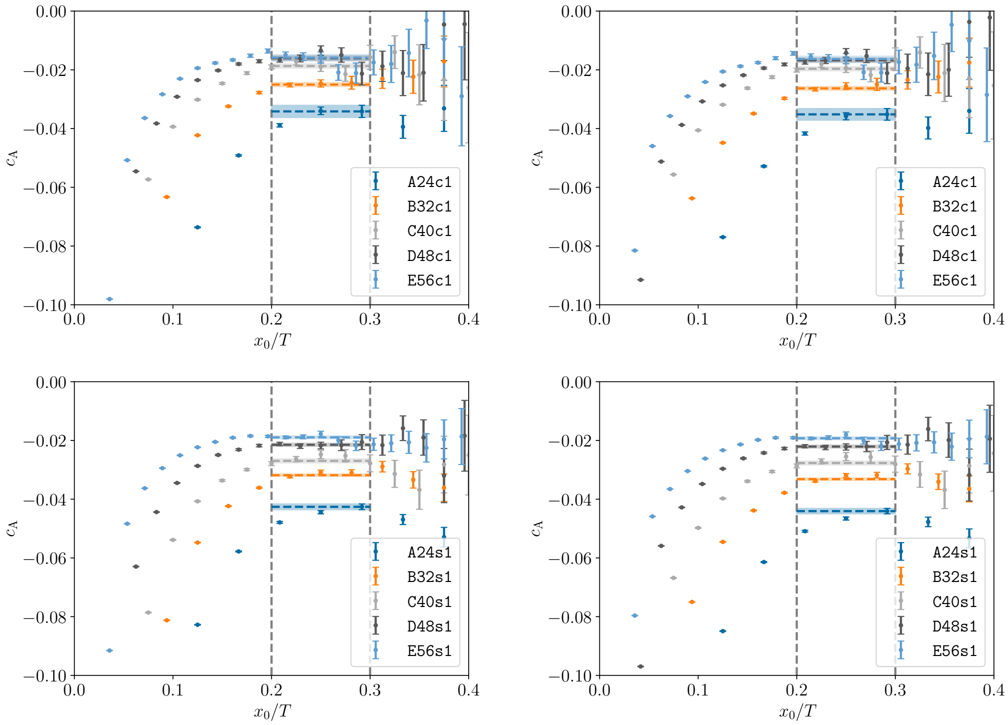

Figure 6.9: Plateaus for the ensembles close to the chiral limit (upper plots) and close to the symmetric point (lower plots) each once with the standard (left) and the preferred (right) wavefunction basis. Note that the coarsest (in this plot lowest) plateaus are only taking the right-most point in the plateau-range into consideration.

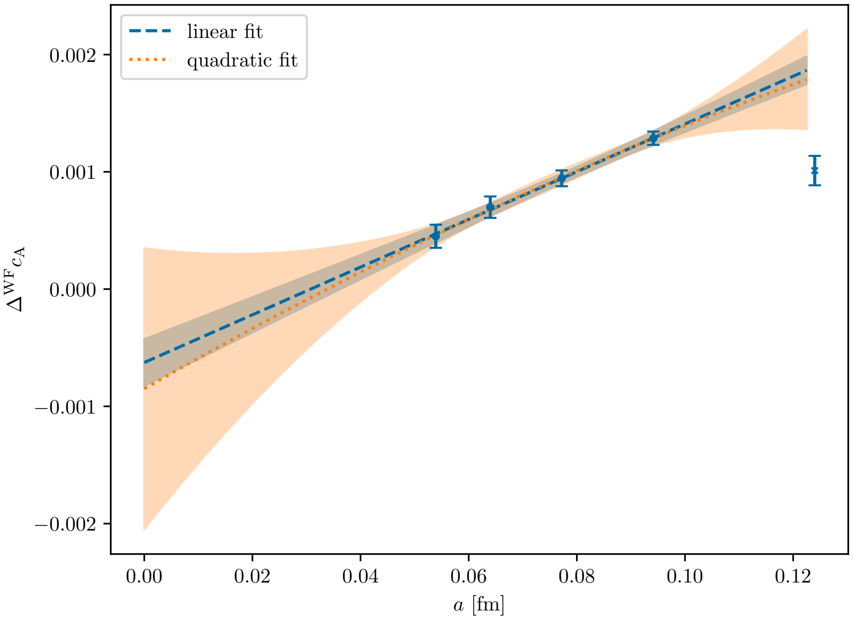

Figure 6.10: Linear and quadratic fits of the differences in c_{A} with respect to the wave-function selection at the lattice spacings of $\beta \in [3.800, 4.100]$. The coarsest lattice spacing has been left out, as the scaling at these lattices is not fully trusted. At the chiral limit, no ensemble with smaller lattice spacing is present.

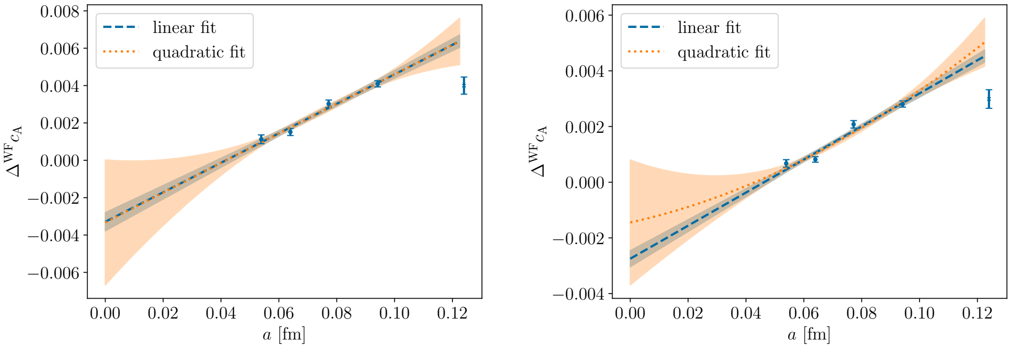

Figure 6.11: Linear and quadratic fits of the differences in c_{A} with respect to the wave-function selection at the lattice spacings of $\beta \in [3.800, 4.100]$, similar to figure 6.10, comparing the additional basis made out of $\omega_{1,2,5}$ with the standard projection on the left and with the preferred projection on the right.

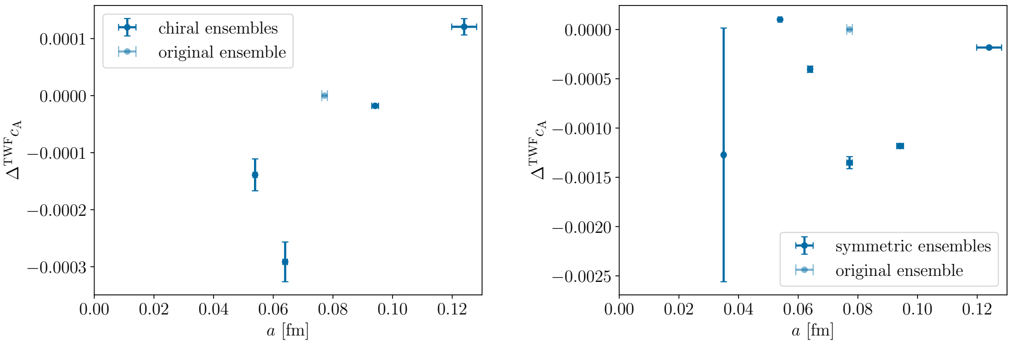

Figure 6.12: Differences of calculating the eigenvectors on each ensemble separately compared to reusing the eigenvectors from the chiral ensemble `C40c1` on the ensembles of the two LCPs, the chiral on the left and the symmetric on the right.

Reusing the eigenvectors is cheaper than calculating them anew on each ensemble, as the eigenvector can be handed over to the measurement program. Then, the eigenvectors determined in section 6.1.3 for the preferred combination of wavefunctions can be used on all ensembles. Comparing the fixed eigenvectors and the ones determined on each ensemble close to the chiral limit, we observe differences of $< 3\%$, as presented in figure 6.12 on the left. On the right, the same is shown with the ensembles at the symmetric point, showing larger deviations of $\approx 5\%$.

In both cases, there is no pattern discernible in the ambiguities.

Derivatives In the improvement condition, derivatives of two correlators are to be taken. Finite differences allow us to carry them out with discretized data points (cf. Appendix B). To inspect the ambiguities in these, the base analysis described is carried out with two different discretizations of finite differences, namely the central-differences method (B.3) and once with the second-order improved central-differences method (B.4). Subtracting the two formulations

$$\Delta c_{\mathrm{A}}^{\partial} = c_{\mathrm{A}}^{\partial_{\mathrm{i}}} - c_{\mathrm{A}}^{\partial_{\mathrm{s}}} \tag{6.23}$$

we can assert the differences, shown in figure 6.13 for one sole lattice. Evaluating plateaus on a range of ensembles close to the chiral limit, one may evaluate how the differences behave towards the continuum limit. The normal and higher order derivative are expected to show a difference of $\mathrm{O}(a^2)$. In figure 6.14 differences of exactly this order are indeed visible in c_{A}.

Masses As a part of the aim of this analysis is to define c_{A} away from the chiral limit, the reader may not be surprised that the quark mass also plays a role in the determination of the improvement coefficient. We will deal with this circumstance by introducing the quark mass as a new degree of freedom in the analysis and interpolate c_{A} with respect to it in sections 6.1.6 and 6.1.7. Therefore, we only note at this point that we expect those ambiguities to only be of order $\mathrm{O}(am_0)$.

Summary The ambiguities inspected are indeed either negligible or are at least of $\mathrm{O}(a)$. Ambiguities coming from the quark masses of the lattices are dealt with by interpolation to the lines of constant physics set up in section 5.1.1. Other than those, we conclude that the ambiguities to the first-order improved formulation of the current behave as expected.

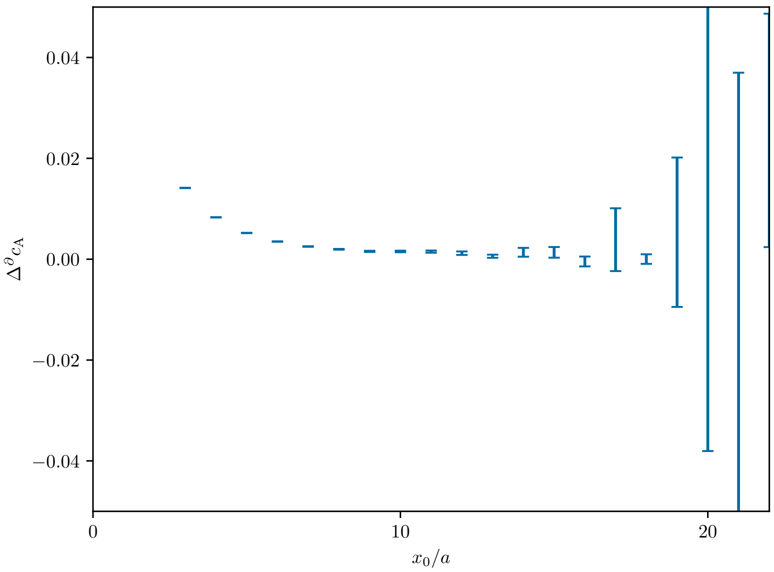

Figure 6.13: The difference of c_{A} extracted on ensemble `C40c1` once with the symmetric (equation (B.3)) and once with improved (equation (B.4)) derivative in direction of x_0.

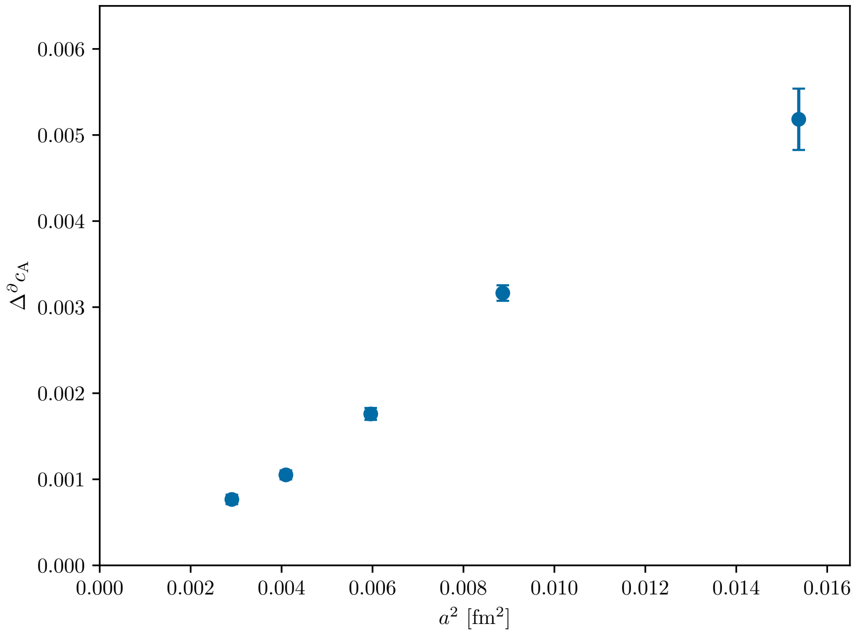

Figure 6.14: Extrapolation of the differences of c_{A} extracted with the symmetric (equation (B.3)) and once with improved (equation (B.4)) derivative on the ensembles close to the chiral limit.

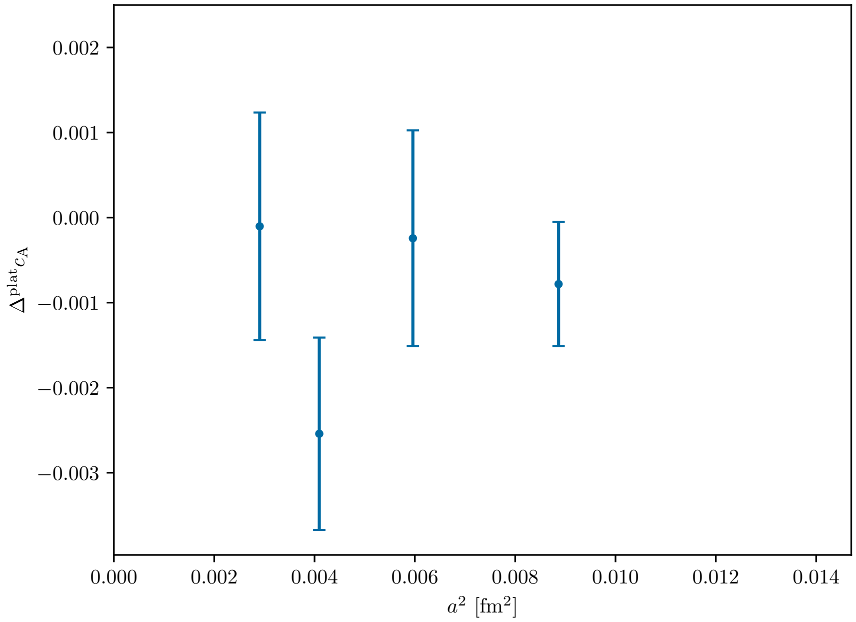

Figure 6.15: The differences of the chosen plateau and the evaluation of c_{A} at $x_0 = T/4$. The differences are existent but marginal and enclose 0 over all chiral ensembles.

The systematic error we introduce does not rely on the introspection given here, but is based on a more relevant ambiguity that we want to review now: the choice of the plateau region.

6.1.5 Choices, plateaus, and errors

The base analysis of the improvement factor c_{A} described earlier differs compared to the ones carried out in earlier works in particular in the choice of employing plateau means in the definition. In contrast to the other ambiguities examined, this is a choice that is not inherent from the discretization or similar. The advantages of this change are evident: Plateaus retain more information of the calculations and can vastly improve the final outcome of the calculations when the range of the plateau is chosen correctly. However, averaging over multiple time slices introduces two minor inconveniences that we should account for:

The main concern is the quality of the plateau identified. While choosing a plateau can improve the quality of the final result, identifying a good range to average over can be quite difficult. An alternative choice for the improvement coefficient would for example be to set $x_0 = T/4$ and extract c_{A} on just a single time slice. Figure 6.15 compares the plateau range discussed in the example with this choice for the ensembles close to the chiral LCP. A comparison to different choices on the ensemble shown in the example can be found in figure 6.16.

While retaining the information of the plateau value is desirable, we have introduced a choice influencing the statistical error in such a way, that the resulting margins of error may not represent the uncertainties of the value properly.

To circumvent both of these problems, a systematic error is added. In this analysis, the idea is to give penalties for values that are incompatible with the fitted plateau and

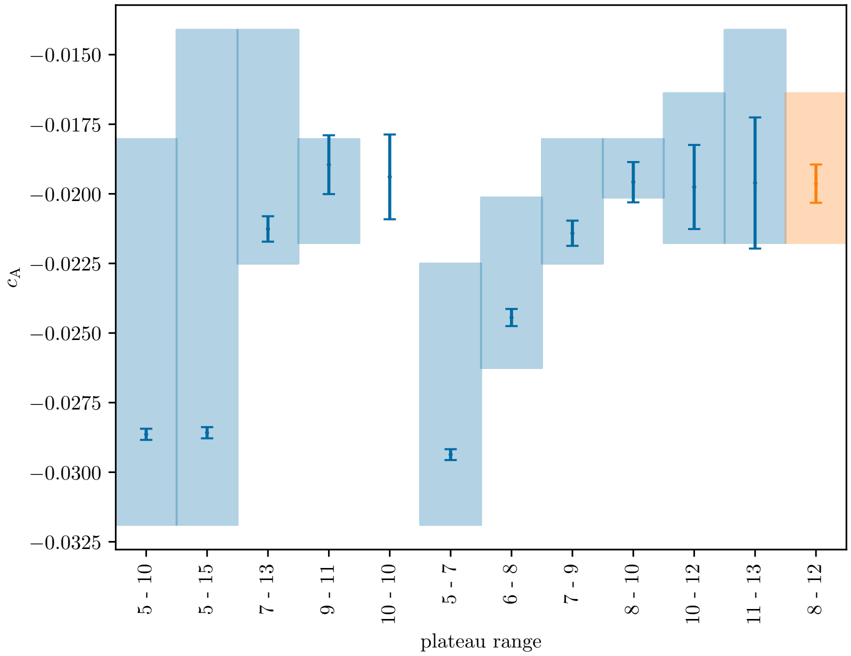

Figure 6.16: Plateau values for different choices of the plateau range on ensemble `C40c1`. The mean value and errors are those of the plateau evaluated, while the blue box shows the spread of the mean values in the plateau range. The orange data point shows the plateau range chosen.

enlarge the margins of error accordingly. This is implemented as follows:

The plateau $\bar{y}$ over the points $y(x_0)$ with the respective statistical margins of error $\sigma_{\text{stat}}(\bar{y})$ and $\sigma_{\text{stat}}(y(x_0))$ is evaluated. For points $y(x_0)$, whose margins of error $\sigma_{\text{stat}}(y(x_0))$ have no overlap with the margins of error of the mean $\sigma_{\text{stat}}(\bar{y})$, the difference between the upper (lower) and lower (upper) end of the margin is summed up and added to the statistical margins of error:

$$\sigma_{\text{tot}}(\bar{y}) = \sigma_{\text{stat}}(\bar{y}) + \sigma_{\text{sys}}(\bar{y}) \tag{6.24}$$

This formulation gives minor penalties in the cases, where the data points do not settle into a plateau at the proposed range. The result is a more conservative estimation margins of error for c_{A} on ensembles where the plateau is not of good quality. At the same time, this implementation does also not give penalties so large that the margins of error of the plateau are larger than the ones extracted from a single point.

One exception has to be made: At the coarsest lattice spacing, the plateau range chosen consists of only one point. Per definition, the formulation of the error given above does not account for this. In this case, we instead compare the points $x_0 \in \{6, 7, 8\}$ and employ

$$\sigma_{\text{sys}} = \frac{\max(y(x_0)) - \min(y(x_0))}{3} \tag{6.25}$$

as the systematic error.

The values received with and without these penalties are listed in table 6.1, from which it is apparent that the preferred projection has marginally smaller statistical errors on most of the ensembles. In the next sections, we will exclusively work with the values for c_{A} presented here in the preferred projection and with systematic errors added (the right-most column of the table). With the values extracted, two paths towards interpolating the improvement constant in the region that we are interested in are discussed. Both times, we aim to extrapolate to the exact lines of constant physics to make an interpolation in the coupling at those.

6.1.6 Interpolations

With the data extracted from each ensemble, an interpolation in terms of the squared coupling (g_0^2) is already possible in principle. However, as can be seen in the introduction of the Schrödinger functional ensembles (cf. figure 5.1, table 5.1), the ensembles at hand are not perfectly aligned with the lines of constant physics we aim for ($\phi_4 = 0$ and $\phi_4 = 1.115$). In order to circumvent residual mass effects, it is customary to interpolate the values for c_{A} to the exact values in the mass parameter defining the lines of constant physics from section 5.1. One is then able to perform interpolations in the squared coupling at these LCPs. For our discussion, the simplest form of the mass ambiguities is chosen: We expect ambiguities of $\mathrm{O}(am)$. In fact, one can see that this expectation is well-supported by the data in figure 6.17.

Carrying out the interpolation at every lattice spacing at hand, we receive the values for c_{A} that are listed in table 6.2. The fits have a $\chi^2/\text{d.o.f.} < 3$, apart from the fit at $\beta = 3.800$ that is of worse quality with $\chi^2/\text{d.o.f.} \approx 5.9$. However, great dependence on the margins of error of the data is observed, with $\chi^2/\text{d.o.f.} < 1$ for the cases in which the ensembles have small statistics, while the combined statistics of the ensembles with $\beta = 3.800$ is large compared to all other lattice spacings. The slopes of the linear fits employed are listed in table 6.3. The mass ambiguities we postulated in the last section can therefore be confirmed. In figure 6.18, the difference between the two masses is shown in two ways: The blue points show the difference between the ensembles closest to the chiral limit (ensembles with a `c`) and closest to the symmetric point (ensembles with an `s`),

Table 6.1: The values of c_{A} extracted with the choice of the plateau discussed in section 6.1.3. The start and end of the plateau listed together with the values for c_{A} with their statistical error only and their inflated margins of error after taking the quality of the plateau into consideration.

Ensemble	x_0^{start}	x_0^{end}	$c_{\mathrm{A}}^{\mathrm{std}}(\sigma_{\mathrm{stat}})$	$c_{\mathrm{A}}^{\mathrm{pref}}(\sigma_{\mathrm{stat}})$	$c_{\mathrm{A}}^{\mathrm{std}}(\sigma_{\mathrm{tot}})$	$c_{\mathrm{A}}^{\mathrm{pref}}(\sigma_{\mathrm{tot}})$
A24s1	7	7	-0.04260(98)	-0.04407(93)	-0.0426(24)	-0.0441(22)
A24i2	7	7	-0.0377(14)	-0.0370(15)	-0.0377(26)	-0.0370(29)
A24i2	7	7	-0.0338(13)	-0.0354(12)	-0.0338(26)	-0.0354(29)
A24c1	7	7	-0.0342(21)	-0.0352(20)	-0.0342(39)	-0.0352(35)
B32s1	7	9	-0.03182(43)	-0.03317(41)	-0.03182(43)	-0.03317(60)
B32i1	7	9	-0.02747(38)	-0.02851(36)	-0.02747(38)	-0.02851(36)
B32c1	7	9	-0.02502(68)	-0.02631(64)	-0.02502(68)	-0.02631(64)
C40s1	8	12	-0.02696(69)	-0.02768(66)	-0.02696(77)	-0.02768(82)
C40i2	8	12	-0.02459(62)	-0.02561(61)	-0.02459(62)	-0.02561(78)
C40i1	8	12	-0.02244(43)	-0.02338(41)	-0.02244(56)	-0.02338(67)
C40c1	8	12	-0.01869(74)	-0.01963(69)	-0.01869(74)	-0.01963(69)
D48s1	10	14	-0.02148(54)	-0.02209(51)	-0.02148(54)	-0.02209(51)
D48c2	10	14	-0.0166(10)	-0.01731(97)	-0.0166(10)	-0.01731(97)
D48c1	10	14	-0.01607(83)	-0.01677(76)	-0.0161(10)	-0.0168(11)
E56s1	12	16	-0.01895(48)	-0.01926(47)	-0.0190(12)	-0.0193(10)
E56i2	12	16	-0.01760(58)	-0.01790(56)	-0.01760(99)	-0.01790(99)
E56i1	12	16	-0.01589(70)	-0.01622(67)	-0.01589(70)	-0.01622(67)
E56c1	12	16	-0.0159(10)	-0.01631(94)	-0.0159(24)	-0.0163(21)
H96h1	12	24	-0.01499(34)	-0.01524(33)	-0.01499(57)	-0.01524(42)
H96s1	12	24	-0.01349(29)	-0.01377(29)	-0.0135(16)	-0.0138(13)
H96i1	12	24	-0.01260(39)	-0.01310(37)	-0.0126(14)	-0.0131(12)

Table 6.2: Table of the c_{A} values extrapolated to the mass points of interest with the preferred wavefunction basis.

β	chi. LCP	sym. LCP
3.685	-0.0341(23)	-0.0442(23)
3.800	-0.02556(53)	-0.03287(56)
3.900	-0.01967(64)	-0.02721(59)
4.000	-0.01698(72)	-0.02245(55)
4.100	-0.0143(18)	-0.01813(69)
4.370	-0.0120(22)	-0.01420(87)

Table 6.3: Slopes of the linear fits employed to the extrapolation of c_{A} with the preferred choice of wavefunctions to the mass points of interest, as presented in table 6.2.

β	3.685	3.800	3.900	4.000	4.100	4.370
$\partial c_{\mathrm{A}}/\partial am_0$	$-1.43(51)$	$-0.93(12)$	$-1.09(14)$	$-0.88(15)$	$-0.75(43)$	$-0.69(78)$

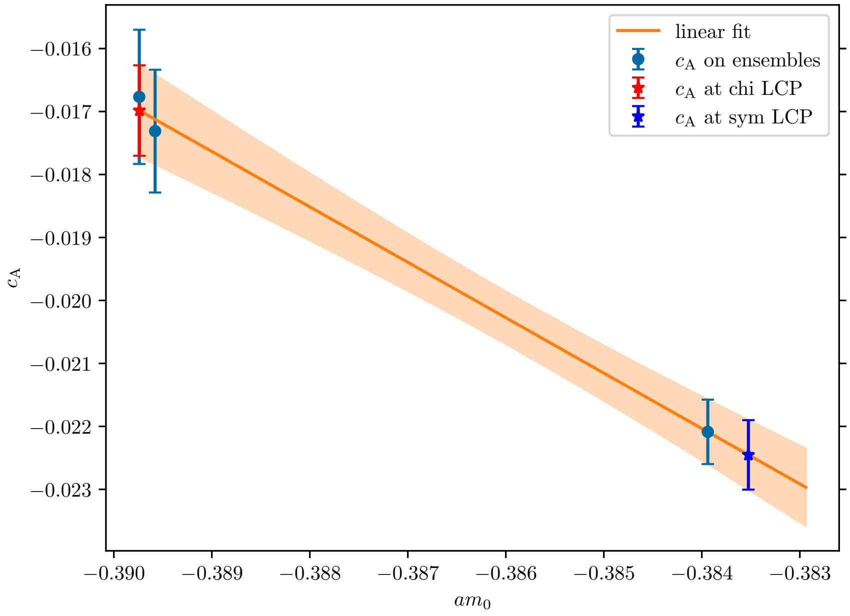

Figure 6.17: Example for the interpolation of c_A in the mass parameter am_0 to the points of interest at $\phi_4 = 0$ and $\phi_4 = 1.115$, marked by the red and blue starred point, respectively. The data shows the interpolation at $\beta = 4.000$.

while the orange points show the data extrapolated to the exact masses of interest. One can see, that the differences are similar in the two cases, and approach zero faster than $\mathrm{O}(a)$. The behaviour is rectified when interpolating, showing that the effect aimed for is achieved. After the mass interpolations, the fits in g_0^2 are carried out with a conventional Padé fit of the form

$$c_\mathrm{A}(g_0^2) = -0.006033\ g_0^2\ \frac{1 - a\ g_0^2}{1 - b\ g_0^2} \tag{6.26}$$

for both lines of constant physics. The overall prefactor comes from the 1-loop perturbative value for c_A [140, tab. 1]. We can adapt it here, as the 1-loop value for the exponential clover action coincides with it [93, app. C]. The fits have a $\chi^2/\text{d.o.f.} = 1.3176$ and $\chi^2/\text{d.o.f.} = 2.9153$ for the chiral and symmetric LCP respectively. The parameters of the fit in the chiral limit are

$$a = 0.5126(95)\,,\ b = 0.5870(36) \quad \mathrm{cov}_{a,b} = \begin{pmatrix} 8.968227 \cdot 10^{-5} & 2.456908 \cdot 10^{-5} \\ 2.456908 \cdot 10^{-5} & 1.319251 \cdot 10^{-5} \end{pmatrix}\ , \tag{6.27}$$

while the parameters at the symmetric point are

$$a = 0.4554(91)\,,\ b = 0.5813(28) \quad \mathrm{cov}_{a,b} = \begin{pmatrix} 8.327217 \cdot 10^{-5} & 2.590252 \cdot 10^{-5} \\ 2.590252 \cdot 10^{-5} & 8.057199 \cdot 10^{-6} \end{pmatrix}\ . \tag{6.28}$$

The fits are shown in figure 6.19. The same fit was carried out excluding the coarsest lattice spacing ($\beta = 3.685$), as to see how they behave excluding the lattice spacing the least trusted. Their parameters are

$$a = 0.541(13)\,,\ b = 0.5991(52) \tag{6.29}$$

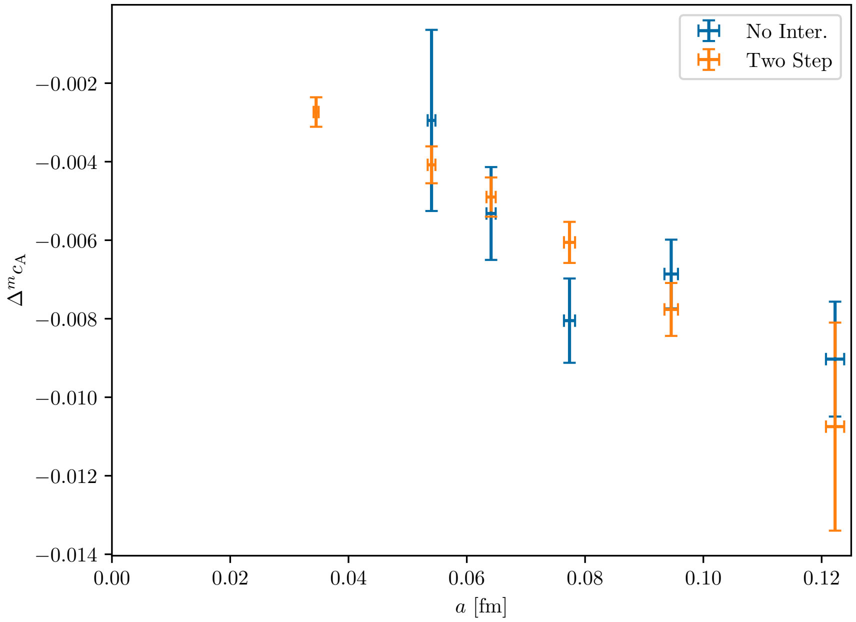

Figure 6.18: Difference in the improvement factor c_A with regard to the mass, once directly determined from the ensembles at hand (blue), and once from the data points extrapolated to the lines of constant physics (orange).

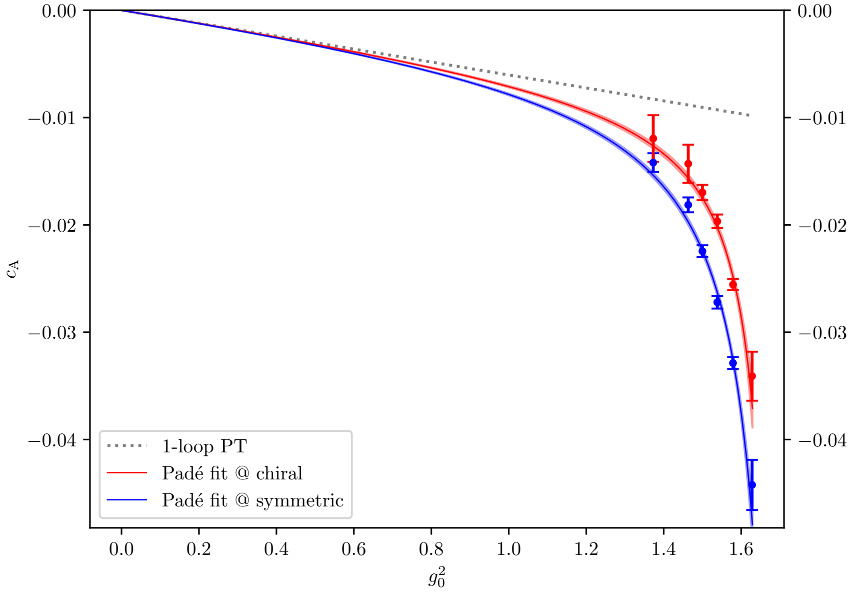

Figure 6.19: Interpolations at the chiral and symmetric line of constant physics of the improvement coefficient c_A, using the values extracted at the respective lines of constant physics. As in the plots above, the red data points and interpolation are at the chiral point, while the blue counterparts show the data at the symmetric point.

and

$$a = 0.473(11)\,,\ b = 0.5874(37)\ , \tag{6.30}$$

respectively. It was found, that the fits excluding these values have a slightly smaller reduced χ^2 (χ^2/d.o.f. = 0.0757 and χ^2/d.o.f. = 2.4888, respectively) however the chiral case is over-fitted in this case. In appendix A, we evaluate c_A on the `M` ensembles. As volume dependence is clearly visible, we omit the values in the fits above.

6.1.7 Global fit

An alternative approach to the two-step method we presented in the last section is to model the dependence of c_A on g_0^2 and the mass, represented by ϕ_4, at once and find a global fit ansatz. With this, the fit procedure is able to take advantage of all data points at the same time, possibly reducing margins of error. This ansatz was originally introduced to fill out parts of the parameter-space where fewer data points were available, for example when there were only two ensembles available at a specific lattice spacing. As we are interested in the interpolations at the LCPs at $\phi_4 = 0$ and $\phi_4 = 1.115$, after fitting with all data available, the fit function is evaluated at fixed ϕ_4 to compare with the fits discussed before. As a fit ansatz, we choose

$$c_\mathrm{A}(g_0^2, \phi_4) = -0.006033\ (1 + b_0\phi_4)\ g_0^2\ \frac{1 - a_1\ (1 + b_1\phi_4)\ g_0^2}{1 - a_2 g_0^2}\ , \tag{6.31}$$

where – evidently – we have replaced the fit constants in equation (6.26) with linear dependencies on the mass parameter, inspired by the linear fits from the two-step fit in the last section. Note that the given fit function also implements mass dependencies of $\mathrm{O}(\phi_4^2)$, which were evaluated to be $\propto (10^{-5}\phi_4^2 g_0^4)$ and compatible with zero. It was furthermore observed that a potential additional mass dependence of a_2 was compatible with zero and was avoided to not spoil the reduced χ^2. The final global fit employing the function above has the parameters

$$b_0 = -0.062(50)\,,\ a_1 = 0.5013(59)\,,\ b_1 = -0.097(24)\,,\ a_2 = 0.5828(22) \tag{6.32}$$

with χ^2/d.o.f. = 1.9996 and a covariance matrix of

$$\mathrm{cov}_{b_0,a_1,b_1,a_2} = \begin{pmatrix} 2.458964\cdot10^{-3} & 1.553000\cdot10^{-5} & 8.129246\cdot10^{-4} & 2.588227\cdot10^{-5} \\ 1.553000\cdot10^{-5} & 3.500638\cdot10^{-5} & 2.724344\cdot10^{-5} & 1.051471\cdot10^{-5} \\ 8.129246\cdot10^{-4} & 2.724344\cdot10^{-5} & 5.522720\cdot10^{-4} & 1.944825\cdot10^{-5} \\ 2.588227\cdot10^{-5} & 1.051471\cdot10^{-5} & 1.944825\cdot10^{-5} & 4.780059\cdot10^{-6} \end{pmatrix}\ . \tag{6.33}$$

The fixed ϕ_4 values that are comparable to the fits extracted with the two-step method are shown in figure 6.20.

Carrying out the same fit without constraining the 1-loop perturbative value employing the function

$$c_\mathrm{A}(g_0^2, \phi_4) = a_0\ (1 + b_0\phi_4)\ g_0^2\ \frac{1 - a_1\ (1 + b_1\phi_4)\ g_0^2}{1 - a_2 g_0^2}\ , \tag{6.34}$$

one finds the parameters

$$a_0 = -0.000016(16)\,,\ b_0 = 0.129(11)\,,\ a_1 = -78(76)\,,\ b_1 = 0.130(11)\,,\ a_2 = 0.5537(35)\ . \tag{6.35}$$

While this benefits the fit (χ^2/d.o.f. = 1.0191), the continuum approach is overshot (see figure 6.21), which is why we ruled this fit out.

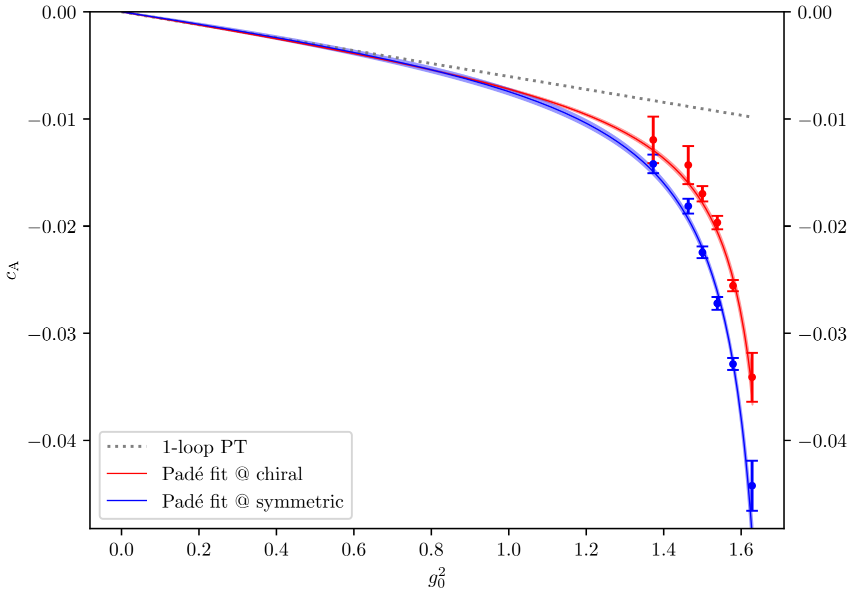

Figure 6.20: Global fit at $\phi_4 = 0$ (red) and $\phi_4 = 1.115$ (blue) shown together with the extrapolated data from the two-step fit. Note that the fits, even if extracted at the correct mass points do not follow from the data shown, but instead are only comparable to it.

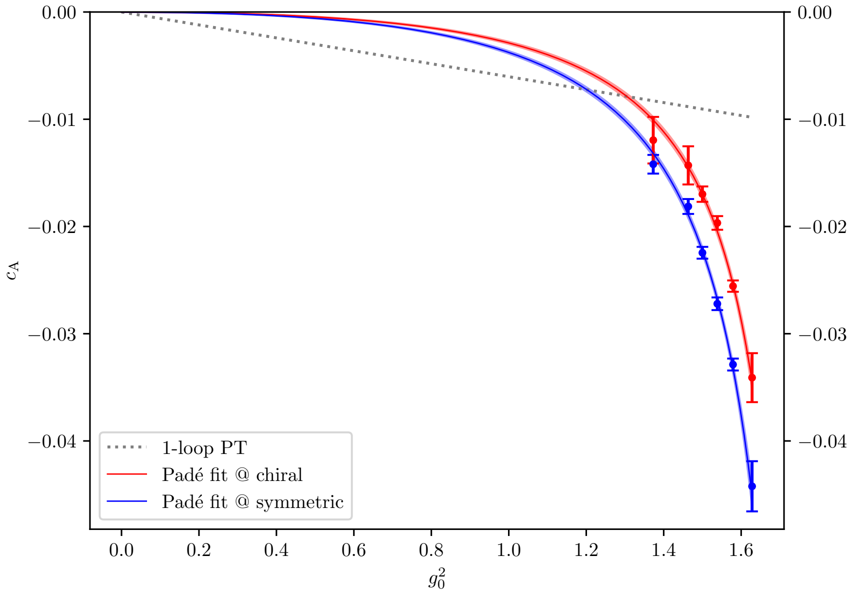

Figure 6.21: Global fit at $\phi_4 = 0$ and $\phi_4 = 1.115$ shown together with the extrapolated data from the two-step fit. Without restriction of the 1-loop perturbative value. As in earlier plots, the red data points and interpolation are at the chiral point, while the blue counterparts show the data at the symmetric point.

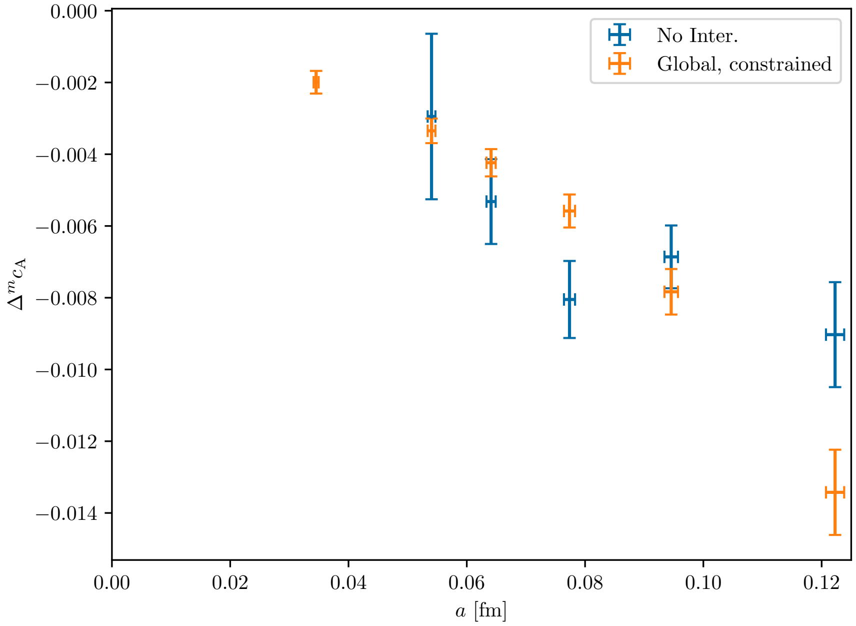

Figure 6.22: Difference in the improvement factor c_A with regard to the mass, once directly determined from the ensembles at hand (blue), and once from the globally fitted data points at the lines of constant physics (orange).

Similar to the two-step case, the differences of c_A at the symmetric and the chiral point are evaluated in and compared to the non-interpolated differences in figure 6.22. For this fit procedure, it is also evident that the differences are smoothed in the continuum approach and approaches zero faster than $\mathrm{O}(a)$. In table 6.4, the two methods (two-step and global constrained) are compared at the inverse couplings of interest. The global constrained fit is advantageous in terms of the error-budget. The two fits are compatible and represent the data equally well. This can be inferred from figure 6.23, in which the residues of the two methods are compared to the data interpolated to the lines of constant physics in the first step of the two-step fit.

Overall, the global fit uses fewer parameters and does not produce outliers such as the ones seen in the first step of the two-step fit, while maintaining smaller error budgets in the final fit parameters.

In the following, we therefore employ the constrained global interpolation function for our purposes.

6.1.8 Comparison to traditional Wilson clover fermions

When improving the action, it turns out that the coefficient of the clover term for the exponential action is smaller at comparable lattice spacings, compared with the traditional formulation of Wilson Clover fermions (cf. [93, fig. 2]). This fact motivates the investigation of the possibility of similar statements for the improvement coefficients of quark bilinears. For the axial-vector current, we compare the findings of [138] with the findings from this chapter in figure 6.24. These are compared in terms of the lattice spacing, as the dependence of the spacing on the coupling is non-trivial. While we know the spacings

Table 6.4: Values for c_{A} received from the different fit methods examined at the inverse couplings of the original data.

	chiral, $\phi_4 = 0$		symmetric, $\phi_4 = 1.115$	
β	2 step	Global, constr.	2 step	Global, constr.
3.685	-0.0367(17)	-0.03531(99)	-0.0475(16)	-0.0487(13)
3.800	-0.02481(41)	-0.02488(40)	-0.03258(41)	-0.03271(39)
3.900	-0.02024(35)	-0.02053(31)	-0.02629(30)	-0.02611(29)
4.000	-0.01750(34)	-0.01784(26)	-0.02240(29)	-0.02208(28)
4.100	-0.01564(32)	-0.01598(23)	-0.01972(28)	-0.01933(28)
4.370	-0.01264(25)	-0.01292(17)	-0.01538(23)	-0.01491(29)

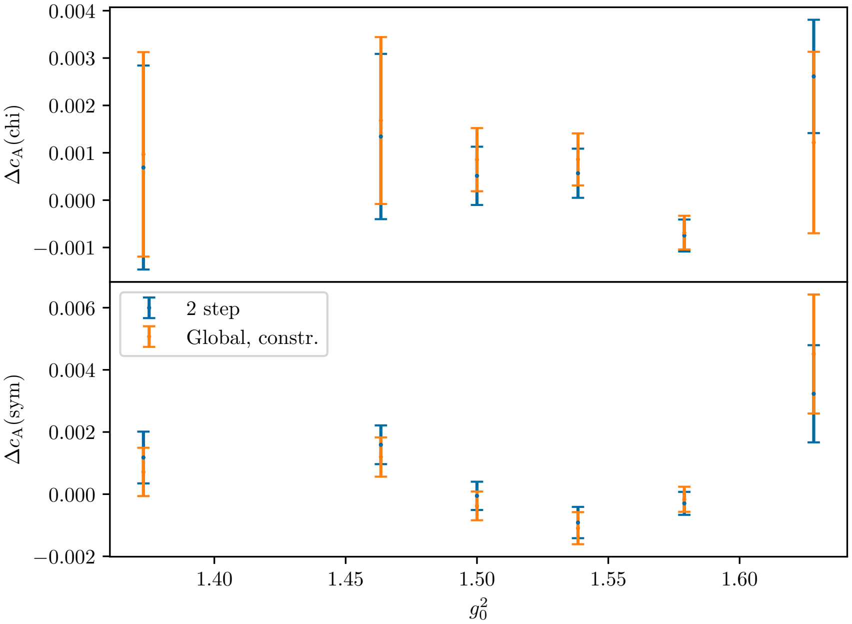

Figure 6.23: Residues of the interpolated data after the first step of the two-step procedure and the two-step fit (blue) as well as the global fit (orange).

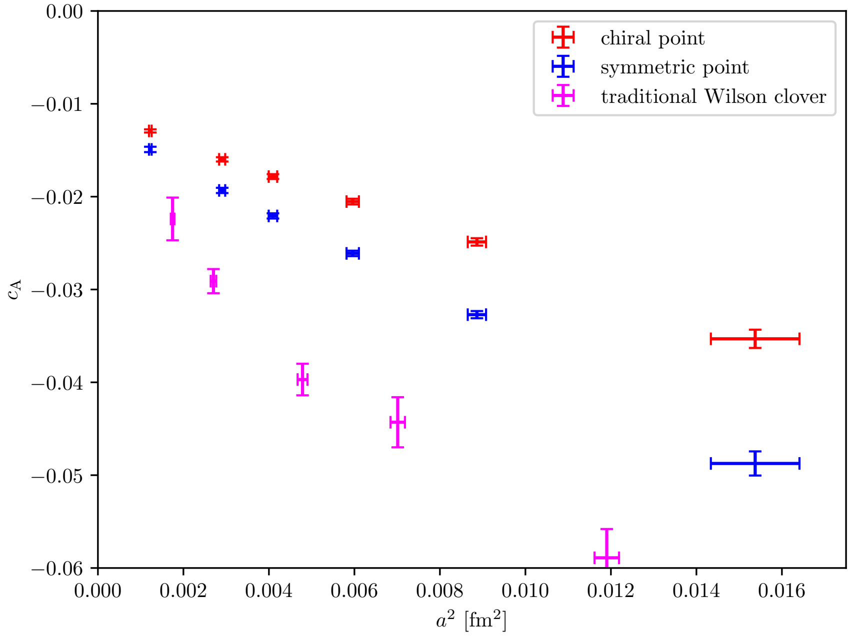

Figure 6.24: Comparison of the improvement coefficient for the axial-vector current in the traditional Wilson clover case (magenta) with the two points (red for chiral and blue for symmetric) of the exponential Wilson fermion action considered here. The data for the exponential cases is taken from the constrained global fit.

of the ensembles presented here from the last chapter, the interpolation equation for the lattice spacing in terms of the gauge coupling in the traditional Wilson clover action was empirically determined as [133, eq. (3.38)]

$$\frac{t_0^*}{a^2} = f_{\mathrm{eff}}(g^2) + 0.285 - 1.566 f_{\mathrm{eff}}^{-1/2}(g^2) \tag{6.36}$$

$$f_{\mathrm{eff}}(g^2) = \exp\{17.54596 g^{-2} - 7.507 + 0.790123 \ln(g^2) - 0.9334 g^2\} \,, \tag{6.36a}$$

$$\sqrt{8t_0^*} = 0.99974(4)\sqrt{8t_0^{\mathrm{phys}}} \,. \tag{6.36b}$$

The corrections introduced by the improvement are – as is evident by the plot – smaller than in the traditional case. The improvement of the exponential clover is also approximately of $\mathrm{O}(a^2)$, while the dependence of the Symanzik improvement factor follows $\mathrm{O}(a)$.

6.1.9 Conclusion

We have discussed the base method of the calculation and have expanded the wavefunction basis to four dimensions. We needed to overcome the problem that the signal of c_A in the determination shown is lost before the middle of the lattice. Our solution was the introduction of an average at earlier times ($x_0 \in [0.2, 0.3]\,T$), to which we made two exceptions for the coarsest and finest lattices.

We have investigated the ambiguities that are present in the determination discussed and assessed that they have the expected scaling or are only small and randomly distributed. The two most prevalent ambiguities – the choice of the plateau and the mass dependence of the parameter – were solved in two different ways: The systematic error is based on the plateau range, while we incorporated the mass parameter ϕ_4 as a part of the interpolation.

Finally, two different approaches to the fits in the squared coupling were shown. While the two-step fit yields reasonable results, a constrained global fit yields lesser errors and can be easily evaluated at the parameter points needed. From a fitting perspective it is therefore better suited to represent the data. Hence, the next projects presented are carried out with the constrained global fit discussed here.

6.2 Renormalization

The massless renormalization pattern we introduced in equation (2.36) calls for three factors to be determined for each current: the multiplicative renormalization, and the two factors of mass improvement to it. While the currents are – in principle – not fully renormalized when either of the factors is missing, the determination of the mass improvement factors to the renormalization of the axial current, b_{A} and $\bar{b}_{\mathrm{A}}$, remains challenging.

In reference [141] the determinations of b_{A} and $\bar{b}_{\mathrm{A}}$ were carried out with coordinate space methods. While the results in the reference are close to the respective perturbative expectations, the mean values show deviations.

Note also, that an alternative form of the renormalization condition can be found in the chirally rotated Schrödinger functional (χSF) [142, 143], which was quite successful for traditional Wilson clover fermions [144]. A similar determination was carried out for exponential Wilson fermions [125], which left some questions as $\mathrm{O}(a)$ contributions were seen that are expected to cancel in this framework.

The Ward Identity determination used here will be carried out along the lines of [31]. As was the case with c_{A}, earlier stages of this project were presented in the references [122, 123]. It takes mass effects into account and is therefore not suited to determine the coefficients b_{A} and $\bar{b}_{\mathrm{A}}$.

6.2.1 Setting up the renormalization condition

The renormalization of the axial-vector current relies on a slightly more complicated Ward Identity. It was developed in [139] in the 2-flavour theory (see also [145]) and subsequently employed in [146] for $N_{\mathrm{f}} = 3$ fermion flavours. Previously, in reference [91], another renormalization condition was used for the quenched case. In the following, we want to convey the idea of the calculation, but will skip a lot of details, which are discussed further in [31, 122], along the lines of which this chapter is structured.

From the general identities in section 3.2, we take the following turn: Consider

$$\delta_{\mathrm{A}}^{a}\langle \mathrm{A}_{\nu}^{b}(y)\mathcal{O}_{\mathrm{ext}}\rangle \tag{6.37}$$

where the axial current is an internal operator, affected by the variation ($y \in R$). Thus, considering equation (3.11c) we receive:

$$\langle \delta_{\mathrm{A}}^{a}\mathrm{A}_{\nu}^{b}(y)\ \mathcal{O}_{\mathrm{ext}}\rangle = \langle \mathrm{A}_{\nu}^{b}(y)\delta_{\mathrm{A}}^{a}\mathcal{S}\ \mathcal{O}_{\mathrm{ext}}\rangle\ . \tag{6.38}$$

We already know how to treat the variation of the action on the right-hand side from the considerations in section 3.2, but still need to calculate the axial variation of the axial current. Plugging transformation (3.10a) into the axial-vector current (3.4b), we find

$$\delta_{\mathrm{A}}^{a}\mathrm{A}_{\nu}^{b}(x) = \alpha(x)f_{c}^{ab}\mathrm{V}_{\nu}^{c}(x) \tag{6.39}$$

after some algebra. Employing $\{\gamma_\nu, \gamma_5\} = 0$ and $\gamma_5^2 = 1$ and exploiting the commutation of the Gell-Mann matrices, we find

$$-\alpha(x) f_c^{ab} \langle \mathrm{V}_\nu^c(x)\ \mathcal{O}_{\mathrm{ext}} \rangle = \\ \mathrm{i} \int \mathrm{d}^4x \mathrm{d}^4y\ \alpha(x) \left[2m \langle \mathrm{P}^a(x) \mathrm{A}_\nu^b(y)\ \mathcal{O}_{\mathrm{ext}} \rangle - \partial_x^\mu \langle \mathrm{A}_\mu^a(x) \mathrm{A}_\nu^b(y)\ \mathcal{O}_{\mathrm{ext}} \rangle \right] \tag{6.40}$$

To simplify the left-hand side, locality of the variation is employed and the region of variation is chosen as in equation (3.17) to restrict the integral to a part of the lattice and use Gauss's law as in equation (3.18) to receive

$$\mathrm{i}\alpha(x) f_c^{ab} \langle \mathrm{V}_\nu^c(x)\ \mathcal{O}_{\mathrm{ext}} \rangle = \\ = \int \mathrm{d}^3x \mathrm{d}^3y\ 2m \int_{t_1}^{t_2} \mathrm{d}x_0 \langle \mathrm{P}^a(x) \mathrm{A}_\nu^b(y)\ \mathcal{O}_{\mathrm{ext}} \rangle - \left[\langle \mathrm{A}_0^a(x) \mathrm{A}_\nu^b(y)\ \mathcal{O}_{\mathrm{ext}} \rangle \right]_{x_0=t_1}^{x_0=t_2} \tag{6.41}$$

To simplify the equation further, we apply the fundamental theorem of calculus to make two shifts in the integration variables in the last term, which amount to

1. $t_1 \to y_0$

$$\langle \mathrm{A}_0^a(t_1, \vec{x}) \mathrm{A}_\nu^b(y)\ \mathcal{O}_{\mathrm{ext}} \rangle = \langle \mathrm{A}_0^a(y_0, \vec{x}) \mathrm{A}_\nu^b(y)\ \mathcal{O}_{\mathrm{ext}} \rangle - 2m \int_{t_1}^{y_0} \mathrm{d}x_0 \langle \mathrm{P}^a(x) \mathrm{A}_0^b(y)\ \mathcal{O}_{\mathrm{ext}} \rangle \tag{6.42a}$$

2. $y_0 \to t_2$

$$\langle \mathrm{A}_0^a(y_0, \vec{x}) \mathrm{A}_\nu^b(y)\ \mathcal{O}_{\mathrm{ext}} \rangle = \langle \mathrm{A}_0^a(y) \mathrm{A}_\nu^b(t_2, \vec{x})\ \mathcal{O}_{\mathrm{ext}} \rangle - 2m \int_{y_0}^{t_2} \mathrm{d}x_0 \langle \mathrm{A}_0^a(y) \mathrm{P}^b(x)\ \mathcal{O}_{\mathrm{ext}} \rangle \tag{6.42b}$$

where the integrated PCAC relation (cf. equation (3.15)) in y can be used due to the vanishing boundary terms in space (cf. [139, eq. 2.6]). We have also exchanged the spatial vectors in the second shift. This rises questions concerning the contact terms that would be at play between the two shifts. As argued in [31], this is of no concern, as one could equally well do the first shift to some $y_0 - \varepsilon$, proceed with the second shift and complete the first shift afterwards. Including the shifts, we receive

$$\mathrm{i} \int \mathrm{d}^3y\ f_c^{ba} \langle \mathrm{V}_0^c(y) \mathcal{O}_{\mathrm{ext}} \rangle = \\ = \int \mathrm{d}^3y \mathrm{d}^3x\ \ - \langle \mathrm{A}_0^a(t_2, \vec{x}) \mathrm{A}_0^b(y) \mathcal{O}_{\mathrm{ext}} \rangle + \langle \mathrm{A}_0^a(y) \mathrm{A}_0^b(t_2, \vec{x}) \mathcal{O}_{\mathrm{ext}} \rangle \\ + \int \mathrm{d}^3y \mathrm{d}^3x\ 2m \int_{y_0}^{t_2} \mathrm{d}x_0 \langle \mathrm{P}^a(x) \mathrm{A}_0^b(y) \mathcal{O}_{\mathrm{ext}} \rangle - \langle A_0^a(y) P^b(x) \mathcal{O}_{\mathrm{ext}} \rangle\ , \tag{6.43}$$

where we still have $y \in R$. Setting $x_0 = t_2$ and using the convenient notation $v^a u^b - v^b u^a = 2v^{[a} u^{b]}$, we can write

$$\mathrm{i} \int \mathrm{d}^3y\ f_c^{ab} \langle \mathrm{V}_0^c(y) \mathcal{O}_{\mathrm{ext}} \rangle = -\,4m \int \mathrm{d}^3y \mathrm{d}^3x \int_{y_0}^{x_0} \mathrm{d}z_0 \langle \mathrm{P}^{[a}(z) \mathrm{A}_0^{b]}(y) \mathcal{O}_{\mathrm{ext}} \\ + 2 \int \mathrm{d}^3y \mathrm{d}^3x\ \langle \mathrm{A}_0^{[a}(x) \mathrm{A}_0^{b]}(y) \mathcal{O}_{\mathrm{ext}} \rangle\ . \tag{6.44}$$

The external operator is set to

$$\mathcal{O}_{\mathrm{ext}} = O^e (O')^f \tag{6.45}$$

as introduced in section 2.9.1. The boundary renormalization factors necessary, as discussed in [139], are present on both sides of the equation and therefore cancel. To simplify the left-hand side, we will employ equation (7.5) which we will derive later on, as it is the equation that is needed for the renormalization of the vector current. With it, we arrive at

$$\begin{aligned} -f_c^{ab} f_g^{ce} \left\langle \mathcal{O}^g (O')^f \right\rangle =& -4m \int \mathrm{d}^3 y \mathrm{d}^3 z \int_{y_0}^{x_0} dz_0 \left\langle \mathrm{P}^{[a}(z) \mathrm{A}_0^{b]}(y) O^e (O')^f \right\rangle \\ &+ 2 \int \mathrm{d}^3 y \mathrm{d}^3 x \left\langle \mathrm{A}_0^{[a}(x) \mathrm{A}_0^{b]}(y) O^e (O')^f \right\rangle \,. \end{aligned} \tag{6.46}$$

The respective lattice expression to the continuum expression above is rather straightforward:

$$\begin{aligned} -f_c^{ab} f_g^{ce} \left\langle O^g (O')^f \right\rangle = -4 m_{\mathrm{RI}} a^7 \sum_{\vec{y}\vec{z}} \sum_{z_0 = y_0}^{x_0} w(z) \left\langle (\mathrm{P}_{\mathrm{RI}})^{[a}(z) (\mathrm{A}_{\mathrm{RI}})_0^{b]}(y) O^e (O')^f \right\rangle \\ +2a^6 \sum_{\vec{x}\vec{y}} \left\langle (\mathrm{A}_{\mathrm{RI}})_0^{[a}(x) (\mathrm{A}_{\mathrm{RI}})_0^{b]}(y) O^e (O')^f \right\rangle \,. \end{aligned} \tag{6.47}$$

This relation is valid for renormalized, improved currents. Note that the term $m\partial_\mu \mathrm{P}^a$ renormalizes like A_μ^a due to the PCAC relation.

The trapezoidal rule as detailed in equation (B.10) is employed for the temporal sums. Later on, the spatial integral is carried out implicitly in the correlation functions we introduced in section 2.9. We still have open flavour indices, which will make a difference only in the allowed contributions and prefactors, such that we can postpone their discussion. For now, we carry on with this high level picture and repackage it in the form of correlation functions. We carry out the contraction of the quark lines implicitly and replace the flavour indices with a new superscript j, which signifies a flavour combination (a, b). While all spatial coordinates are summed over, the temporal coordinates only receive sums over parts of the lattice. We fix $x_0 = T/3$ and $y_0 = 2T/3$ as to maximize the temporal spacing between the two insertions and the boundaries. Defining the correlation functions accordingly, we write the renormalization condition on a high level as

$$-F_1^j = -2m_{\mathrm{I}} (\tilde{F}_{\mathrm{PA}_0}^j)_{\mathrm{RI}} + (F_{\mathrm{A}_0\mathrm{A}_0}^j)_{\mathrm{RI}} \tag{6.48}$$

$$F_{QR}(x_0, y_0) = - N^j a^6 \sum_{\vec{x}\vec{y}} \langle Q^1(x) R^2(y) O_{\mathrm{ext}}^{21} \rangle \,, \tag{6.48a}$$

$$\begin{aligned} (F_{\mathrm{A}_0\mathrm{A}_0}^j)_{\mathrm{I}}(x_0, y_0) =& F_{\mathrm{A}_0\mathrm{A}_0}^j(x_0, y_0) \\ &+ a c_{\mathrm{A}} (\hat{\partial}_{x_0} F_{\mathrm{PA}}^j(x_0, y_0) + \hat{\partial}_{y_0} F_{\mathrm{AP}}^j(x_0, y_0)) \\ &+ a^2 c_{\mathrm{A}}^2 \hat{\partial}_{x_0} \hat{\partial}_{y_0} F_{\mathrm{PP}}^j(x_0, y_0) \,, \end{aligned} \tag{6.48b}$$

$$(\tilde{F}_{\mathrm{PA}_0}^j)_{\mathrm{I}}(x_0, y_0) = \tilde{F}_{\mathrm{PA}_0}^j(x_0, y_0) + c_{\mathrm{A}} \hat{\partial}_{y_0} \tilde{F}_{\mathrm{PP}}^j(x_0, y_0) \,, \tag{6.48c}$$

$$\tilde{F}_{QR}^j(x_0, y_0) = a \sum_{z_0 = x_0}^{y_0} w(z) F_{QR}^j(z_0, y_0) \,, \tag{6.48d}$$

where the weight $w(z)$ is that of the trapezoidal sum and N^j the normalization needed for each flavour choice. The lattice derivatives are again written as $\hat{\partial}_\mu$ (see appendices C and B). Neglecting the mass improvement terms of the renormalization, on the left-hand side of the equation an overall factor of Z_{A}^2 can be factored out, and we receive

$$-F_1^j = Z_{\mathrm{A}}^2 (-4m_{\mathrm{I}} (\tilde{F}_{\mathrm{PA}_0}^j)_{\mathrm{I}} + 2(F_{\mathrm{A}_0\mathrm{A}_0}^j)_{\mathrm{I}}) \tag{6.49}$$

Rearranging this expression, we find that the renormalization factor can be written as

$$Z_{\mathrm{A}} = \sqrt{\frac{F_1^j}{(4m_{\mathrm{I}}(\tilde{F}^j_{\mathrm{PA_0}})_{\mathrm{I}} - 2(F^j_{\mathrm{A_0A_0}})_{\mathrm{I}})}}\,. \tag{6.50}$$

The open flavour indices determine, which contractions are allowed. As in reference [31], we inspect two flavour choices:

$$j = 1: \quad a = 1,\ b = 2,\ e = 2,\ f = 1 \quad \to f_c^{12} f_g^{c2} = -\delta_{1g} \quad \to\ N^j = 2 \tag{6.51a}$$

$$j = 2: \quad a = 1,\ b = 2,\ e = 5,\ f = 4 \quad \to f_c^{12} f_g^{c5} = -\frac{1}{2}\delta_{4g} \quad \to\ N^j = 4 \tag{6.51b}$$

Such that in both cases, F_1 receives an additional minus sign and the normalization N^j in the 4-point functions changes due to the structure constants. The 4-point functions also receive different contributions depending on the flavour choices.

The first choice allows for the disconnected diagrams b) and c) shown in figure 2.10, while the second choice does not. Thus, we call the first choice *full* definition, the second choice *connected* definition, accordingly. The difference between the choices are $O(a^2)$-ambiguities, as discussed in [136].

The renormalization condition is in principle also valid for massive quarks and Z_{A} is received in the limit $m \to 0$, such that only $\mathrm{O}(am)$ ambiguities are expected. As was the case for c_{A}, we can therefore use all available Schrödinger functional ensembles for the determination.

6.2.2 Results and discussion

We evaluate the renormalization condition on each ensemble with all four definitions and list them in table 6.5. For the moment, we employ the definition of the global fit of c_{A} with $\phi_4 = 0$ fixed, as this is the case seen in literature. In the following, we use superscripts to distinguish between the full (f) and connected (c) definitions. The addition *msl* stands for the massless definition, for which we set $m_{\mathrm{I}} = 0$ in equation (6.50). In the massive case, we define the plateau range of the current quark mass as $x_0 \in [1/3, 2/3]\,T$, which is a good estimator on the large volume lattices at hand. It is chosen here to resemble the summation window chosen for the temporal sums in equation (6.47).

We take the limit of all values to $m \to 0$. In the literature [136, 146], this limit was accomplished by linear extra- or interpolation. In figure 6.25 we show, that this cannot be achieved here. The mass dependencies are not what we expect. While the massive, connected definition $Z_{\mathrm{A}}^{\mathrm{c}}$ shows the expected behaviour, with negligible mass dependence, the other definitions show clear differences to the traditional three-flavour case of reference [146]:

Note that the interpolation in the literature is often against the (PCAC) current quark mass am that also enters the renormalization condition. This is not the case here. We instead plot the mass dependence against the bare subtracted quark mass am_{q}, as we have extracted the bare quark mass of the chiral point from the effective meson mass in the axial channel, as described in section 5.1.2. (cf. table 5.4). This way of fitting is more in line with the fits we did for c_{A} and is therefore preferred in this context.

The slope of the mass dependence of the connected definition that neglects the mass term, $Z_{\mathrm{A}}^{\mathrm{c,msl}}$, is positive, not negative as in earlier studies [138, 139].

Furthermore, the full definitions receive large corrections from the disconnected diagrams. These clearly have strong higher order cut-off effects, that were parametrized in figure 6.25 with a polynomial of second degree. While the fits with second degree polynomials fit the data well, an investigation towards better fit strategies for the effects seen is

Table 6.5: Table of the evaluated renormalization condition on the ensembles at hand, up to $\beta = 4.100$. The four definitions are all given by equation (6.50), the differences between the values are as follows: The *full* definition $Z_{\mathrm{A}}^{\mathrm{f}}$ uses all diagrams shown in figure 2.10, while the *connected* definition $Z_{\mathrm{A}}^{\mathrm{c}}$ only allows the connected diagrams (a, a^* and d, d^*). If the value shows the addition *msl*, m_{I} in equation (6.50) was set to zero, neglecting the mass terms.

Ensemble	$Z_{\mathrm{A}}^{\mathrm{f}}$	$Z_{\mathrm{A}}^{\mathrm{f,msl}}$	$Z_{\mathrm{A}}^{\mathrm{c}}$	$Z_{\mathrm{A}}^{\mathrm{c,msl}}$
`A24s1`	0.2507(39)	0.1239(11)	0.7662(17)	1.3863(74)
`A24i2`	0.3893(63)	0.1963(24)	0.7584(26)	1.1419(77)
`A24i2`	0.648(16)	0.451(12)	0.7552(67)	0.8579(98)
`A24c1`	0.725(28)	0.818(58)	0.737(15)	0.711(22)
`B32s1`	0.2171(25)	0.09327(60)	0.77731(87)	1.3713(43)
`B32i1`	0.4023(46)	0.1732(11)	0.77332(96)	1.1059(33)
`B32c1`	0.768(15)	1.146(84)	0.7777(47)	0.7410(61)
`C40s1`	0.2342(45)	0.0940(10)	0.7862(11)	1.5251(97)
`C40i2`	0.2455(30)	0.09763(83)	0.78832(98)	1.5002(88)
`C40i1`	0.4276(68)	0.1749(15)	0.7850(10)	1.1837(45)
`C40c1`	0.767(12)	0.799(31)	0.7804(57)	0.7753(74)
`D48s1`	0.2664(26)	0.10008(57)	0.79532(64)	1.4750(56)
`D48c2`	0.778(10)	0.664(17)	0.7910(19)	0.8127(36)
`D48c1`	0.8119(87)	0.836(25)	0.7902(29)	0.7868(44)
`E56s1`	0.2704(21)	0.09326(57)	0.80381(38)	1.4480(62)
`E56i2`	0.3155(30)	0.10649(72)	0.80402(53)	1.3848(67)
`E56i1`	0.3696(50)	0.1286(13)	0.80323(73)	1.2958(82)
`E56c1`	0.7901(63)	0.730(16)	0.8032(17)	0.8124(30)
`M32i1`	0.92703(11)	0.92686(19)	0.927267(20)	0.927304(39)

Table 6.6: Table of the evaluated renormalization condition at each inverse coupling, up to $\beta = 4.100$ at $am_{\mathrm{q}} = 0$. The notation is the same as in the table above.

β	$Z_{\mathrm{A}}^{\mathrm{f}}$	$Z_{\mathrm{A}}^{\mathrm{f,msl}}$	$Z_{\mathrm{A}}^{\mathrm{c}}$	$Z_{\mathrm{A}}^{\mathrm{c,msl}}$
3.685	0.712(24)	0.759(42)	0.7493(47)	0.7791(80)
3.800	0.758(15)	1.120(77)	0.7707(20)	0.7735(40)
3.900	0.767(12)	0.799(31)	0.7825(22)	0.7938(60)
4.000	0.8117(85)	0.835(25)	0.7907(16)	0.7909(28)
4.100	0.7906(63)	0.730(16)	0.8030(14)	0.8129(28)

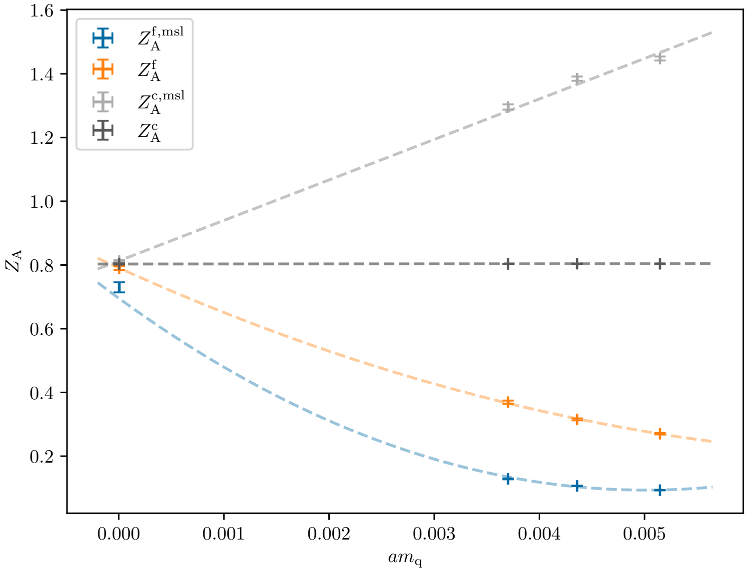

Figure 6.25: Example of the interpolation in the bare quark mass am_q at $\beta = 4.100$ (the values shown can be seen in table 6.5). Note that in comparable determinations [136,146], this is often plotted again the current quark mass. As these fits (in particular the quadratic ones) need more investigation, they are given without margins of error. The extrapolated values at the chiral limit, which are not shown here, are listed in table 6.6.

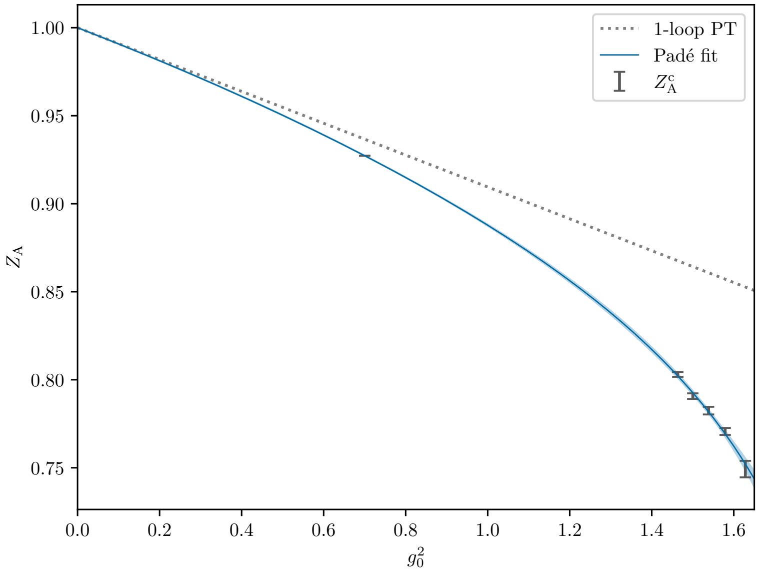

Figure 6.26: Constrained Padé fit to the values of Z_A^c interpolated to the chiral point. Note that the point at $g_0^2 = 0.7$ is not on the line of constant physics imposed on the other points, as it has a different lattice extent.

yet to be done. This is especially true for the cases in which the quadratic interpolations only have three points to fit and are therefore unreliable (see, in particular $\beta = 3.800$ in table 6.6). We also find that the full definition with the mass term, Z_A^f, included is compatible with the other definitions if the points are interpolated with a second order polynomial. This is not the case for the full definition neglecting these terms, $Z_A^{f,msl}$. The values found are also not well represented by a polynomial fit of second degree.

Going forward, we do not cite the extrapolated values of the full definition without the mass term $Z_A^{f,msl}$, as more insight into the mass dependence is needed. Potentially with a larger set of ensembles, such that also fits with polynomials of higher degree can be carried out reliably. The chirally interpolated points of the connected definitions listed in the table are however compatible apart from the full massless definition $Z_A^{f,msl}$. For the moment, the massive, connected definition of the renormalization is preferred. In figure 6.26 we show a fit of the form

$$Z_A = 1 - 0.090488 g_0^2 \frac{1 + a_1 g_0^2 + a_2 g_0^4}{1 + b_1 g_0^2} \tag{6.52}$$

to this definition of the renormalization constant. Note that the point at $g_0^2 = 0.7$ is not interpolated to the chiral point, however, as is evident from table 5.2, the ensemble `M32c1` that this data point is generated on is tuned well to the chiral limit, making the interpolation not strictly necessary. However, this point is also not on the line of constant physics imposed on the other points, especially in regard to the volume of the ensemble. The parameters

$$a_1 = -0.301(29)\,,\ a_2 = -0.052(18)\,,\ b_1 = -0.478(36) \tag{6.53}$$

describe the data well with $\chi^2/\mathrm{d.o.f.} = 0.954$ and the covariance matrix

$$\mathrm{cov}_{a_1,a_2,b_1} = \begin{pmatrix} 8.374254 \cdot 10^{-4} & 2.484293 \cdot 10^{-4} & 9.376311 \cdot 10^{-4} \\ 2.484293 \cdot 10^{-4} & 3.284594 \cdot 10^{-4} & 3.799650 \cdot 10^{-4} \\ 9.376311 \cdot 10^{-4} & 3.799650 \cdot 10^{-4} & 1.311376 \cdot 10^{-3} \end{pmatrix} . \tag{6.54}$$

Note that the 1-loop value in the equation above comes from the traditional Wilson clover action and is not derived in the exponential framework. We have therefore made a second attempt, without constraining the 1-loop value:

$$Z_{\mathrm{A}} = 1 - c_1 g_0^2 \frac{1 + a_1 g_0^2 + a_2 g_0^4}{1 + b_1 g_0^2} , \tag{6.55}$$

using this ansatz, the parameters

$$c_1 = -0.08475(3186) , \; a_1 = -0.2262(4507) , \; a_2 = -0.1466(5606) , \; b_1 = -0.5314(2909) \tag{6.56}$$

describe the values well. While the mean values of the fits are almost identical, the margins of error of the fit parameters of the unconstrained fit are large. This implies that evaluating the fit at in the regions where no data points are present, the margins of error of the fit are substantial as well. The covariance matrix

$$\mathrm{cov}_{c_1,a_1,a_2,b_1} = \tag{6.57}$$
$$\begin{pmatrix} 1.014958 \cdot 10^{-3} & 1.435858 \cdot 10^{-2} & -1.785905 \cdot 10^{-2} & -9.268970 \cdot 10^{-3} \\ 1.435858 \cdot 10^{-2} & 2.031304 \cdot 10^{-1} & -2.526514 \cdot 10^{-1} & -1.311279 \cdot 10^{-1} \\ -1.785905 \cdot 10^{-2} & -2.526514 \cdot 10^{-1} & 3.142451 \cdot 10^{-1} & 1.630954 \cdot 10^{-1} \\ -9.268970 \cdot 10^{-3} & -1.311279 \cdot 10^{-1} & 1.630954 \cdot 10^{-1} & 8.464765 \cdot 10^{-2} \end{pmatrix} .$$

shows that there are comparatively large covariances between the fit parameters. Thus – for the moment – we prefer the constrained fit.

Finally, we compare the renormalization of the axial-vector current we have determined with to the values at the same lattice spacing in the traditional case in figure 6.27. As was the case for c_{A}, we find the exponential Wilson clover action to be closer to the perturbative calculations than the traditional Wilson clover calculations for comparable lattice spacings.

6.2.3 Conclusion

We have seen that the mass effects of the renormalization constant we investigated are characteristically different from the mass effects seen in the literature [136, 146] that this investigation is based on. Better understanding of the mass effects in particular in the disconnected diagrams is needed. Dominant mass effects in $\mathrm{O}((am_{\mathrm{q}})^2)$ could however be characteristic of the exponential action. Hence, deeper investigation of the systematic effects could be fruitful. An example would be to test how the global fit that we implemented for c_{A} influences this behaviour, i.e. whether the behaviour changes when taking mass effects in the improvement into account. Also, in references [145, 146], the wavefunction method, that we used for c_{A} was also employed in the determination of the renormalization factor, to project onto pseudo-scalar states. This could be another avenue to pursue. Furthermore, we have seen that constraining the 1-loop value of the renormalization factor in the exponential Wilson clover framework would greatly benefit the interpolation in the coupling. This could either be carried out numerically or analytically. In case the numerical route is taken, one has to be careful in regard to the investigation of the role the volume plays in the determination.

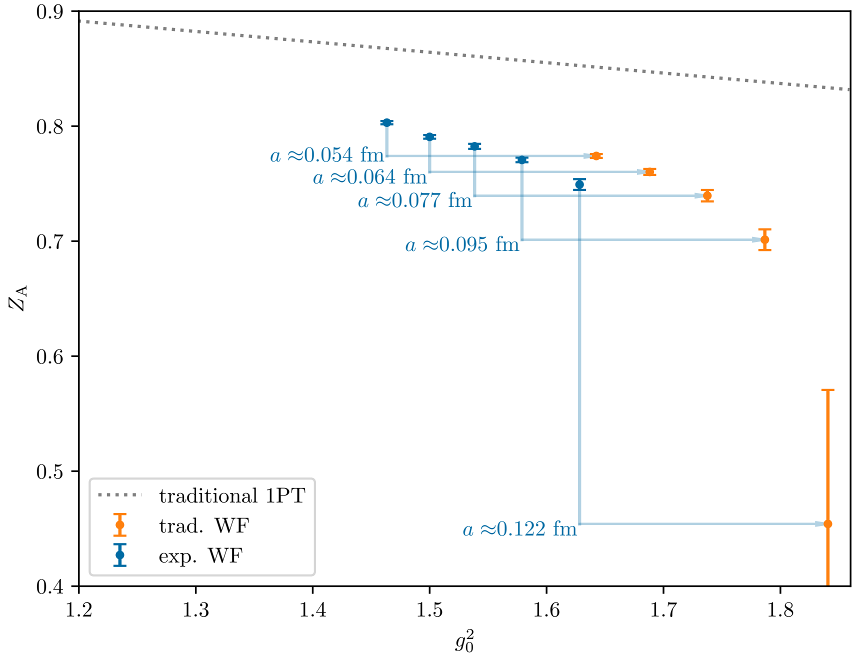

Figure 6.27: Comparison of the exponential Wilson clover case (Z_A^c) to the traditional Wilson clover case ([146, eq. 4.1]). The traditional case uses the full definition (Z_A^f). Note that the margins of error of the traditional points not taken from the paper, but instead come from a re-analysis of the data [147]. Furthermore, the point at $a \approx 0.122\,\mathrm{fm}$ is not part of the interpolation region of the traditional case and is only shown here for illustrative purposes.

Chapter 7

The vector current

Contrary to the axial-vector current, the improvement of the vector current relies on its renormalization. It is also dependent on the renormalization and improvement of the axial-vector channel, as we will see. We therefore first need to deal with the renormalization and only shortly explain the improvement, as it is out of the scope of this thesis. This chapter is structured accordingly, in reverse order compared to the previous one.

Another difference will become apparent quickly: We will be able to determine the overall renormalization, as was the case for the axial-vector current, but here we will also be able to discern the mass dependent (b_{V}, $\bar{b}_{\mathrm{V}}$) and mass independent parts (Z_{V}) of the renormalization. Knowledge of the renormalization and improvement of the vector current is of particular interest for semi-leptonic vector form factors, as we have seen in chapter 3.

In three-flavour theory, determinations of the factors discussed here have been carried out in the Schrödinger functional in [28, 148, 149] as well as on large volume ensembles and away from the chiral limit i.e. in [150].

7.1 Renormalization

The renormalization of the vector current is easily evaluated in the Schrödinger functional through the identity

$$\hat{Z}_{\mathrm{V}} = Z_{\mathrm{V}}(1 + b_{\mathrm{V}} a m_{\mathrm{q}} + \bar{b}_{\mathrm{V}} \mathrm{Tr}\,\{a M_{\mathrm{q}}\}) = \frac{F_1}{F_{\mathrm{V}}} + \mathrm{O}(a^2)\ , \tag{7.1}$$

in which we will call $\hat{Z}_{\mathrm{V}}$ the effective renormalization factor and F_1 and F_{V} are implicitly dependent on the valence- and sea-quark masses. In references [91, 149], the same technique has been employed in the quenched and three flavour setup. The fraction on the right-hand side of equation (7.1) can be evaluated to very high precision. Therefore, this equation may be used to estimate each factor on the left-hand side. This enables us to present determinations of all three factors, Z_{V}, b_{V} and $\bar{b}_{\mathrm{V}}$, in this context.

To estimate Z_{V}, as with the quantities examined in previous chapters, we first interpolate to the chiral limit $m_{\mathrm{q}} = \mathrm{Tr}\,\{M_{\mathrm{q}}\} = 0$. Variations in the sea-quark mass $m_{\mathrm{q}}^{\mathrm{sea}}$ and valence-quark mass $m_{\mathrm{q}}^{\mathrm{val}}$ are employed afterwards to estimate b_{V} and $\bar{b}_{\mathrm{V}}$. As in section 6.1.6, we make use of the bare quark masses listed in table 5.4 to define the chiral limit at the different lattice spacings for this study.

The rest of this section is organized as follows: We first derive equation (7.1), followed by the evaluation of the factors as seen in literature. For this, we will shortly describe the evaluation of single data points. Once these are evaluated, interpolations can be done in multiple ways. We will explore the literature procedures first, and will then follow it up with slightly different formulations to cross-check our results. We compare the strategies among each other and finally with the traditional clover case.

7.1.1 Setting up the renormalization condition

As was the case for the renormalization of the axial current we discussed, the renormalization of the vector current is gained from a Ward identity derived from equation (3.11c). In fact, it is derived straightforward from the vector transformation of the action shown in equation (3.12). Let us consider the vector-like variation of the operators appearing in F_1:

$$\delta^c_{\mathrm{V}}\langle O^e (O')^f\rangle \ . \tag{7.2}$$

The time interval of the support R of the variation is chosen as

$$[t_1, t_2] = [0, y_0] \ . \tag{7.3}$$

The lower time-boundary is affected by the transformation, but not the upper. The boundary fields in O^e transform like

$$\delta^c_{\mathrm{V}} O^e = -\alpha(x) f^{ce}_{g} O^g \ , \tag{7.4}$$

such that equation (3.12) becomes

$$-f^{ce}_{g}\langle O^g (O')^f\rangle = \mathrm{i}\int_{\partial R} d^3y \langle O^e (O')^f \mathrm{V}^c_0(y)\rangle \ , \tag{7.5}$$

where we have set $\mu = 0$. This relation is true for the renormalized currents. Reformulating it with correlation functions, we find that the left-hand side still has the form of F_1, while the right-hand side is written as

$$F_{\mathrm{V}}(x_0) = \mathrm{i}\frac{a^3}{6L^6}\sum_{x}\epsilon_{abc}\langle O'^a \mathrm{V}^b_0(x_0) O^c\rangle \ . \tag{7.6}$$

With these, we arrive at equation (7.1):

$$\hat{Z}_{\mathrm{V}} = Z_{\mathrm{V}}(1 + b_{\mathrm{V}} a m_{\mathrm{q}} + \bar{b}_{\mathrm{V}} a \mathrm{Tr}\{M_{\mathrm{q}}\}) F_{\mathrm{V}}(x_0) = F_1 + \mathrm{O}(a^2) \ . \tag{7.7}$$

The choice of pseudo-scalar external interpolators $\mathcal{O} = O$ is typical. Note, however, that this is not strictly necessary for them to be pseudo-scalar. In [28], the source operators were replaced by vector sources, which yielded better plateaus, but less statistical precision in the cases presented. For our analysis, we will therefore keep the standard choice of pseudo-scalar sources.

7.1.2 Calculating the effective renormalization

As the aim of this chapter calls for variation of the valence- and sea-quark masses independently of each other, a dataset with valence-quark scans on all ensembles available up to $\beta = 4.100$ was produced. The scanned points in mass parameter space are shown in figure 7.1. We evaluate $\hat{Z}_{\mathrm{V}}(m^{\mathrm{val}}_{\mathrm{q}}, m^{\mathrm{sea}}_{\mathrm{q}})$ at each point. The result of a single evaluation is shown in figure 7.2. In all cases, the plateau is exhibited well in the middle part of the lattice with a χ^2/d.o.f. of fits in the vicinity of 1. We opt for a plateau average over the middle half of the lattice ($x_0 = [0.25, 0.75]\ T$). This is a choice conservative enough on the ensembles investigated, without being influenced by the boundaries.

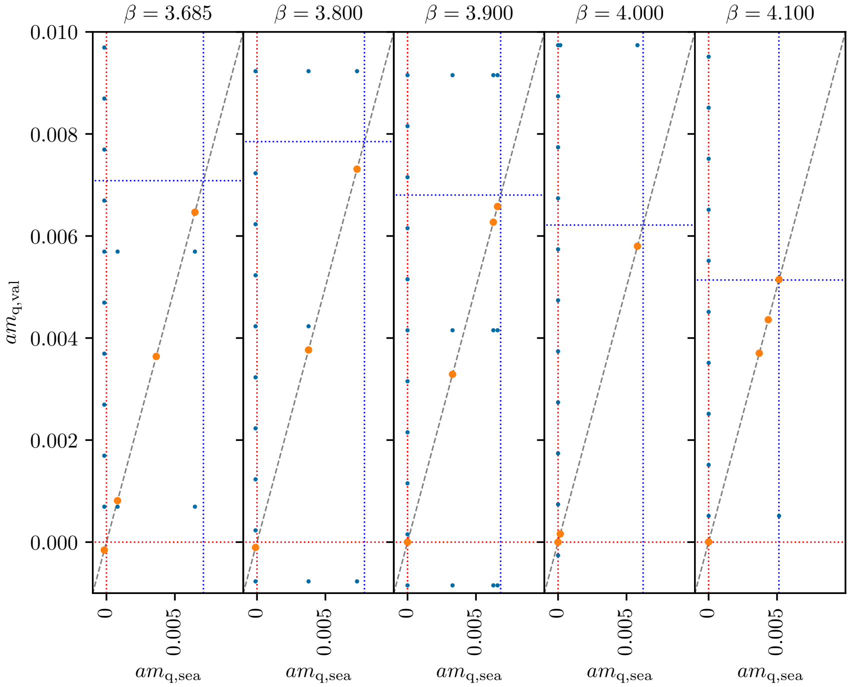

Figure 7.1: Overview over the scans of interest for this project. The dashed grey line shows the mass-degenerate quarks, with the orange points representing the measured points, where $m_{\mathrm{q}}^{\mathrm{val}} = m_{\mathrm{q}}^{\mathrm{sea}}$. The dotted red and blue lines show the place of the chiral and symmetric points, respectively. The blue dots show the measurements of non-degenerate quark masses, $m_{\mathrm{q}}^{\mathrm{val}} \neq m_{\mathrm{q}}^{\mathrm{sea}}$.

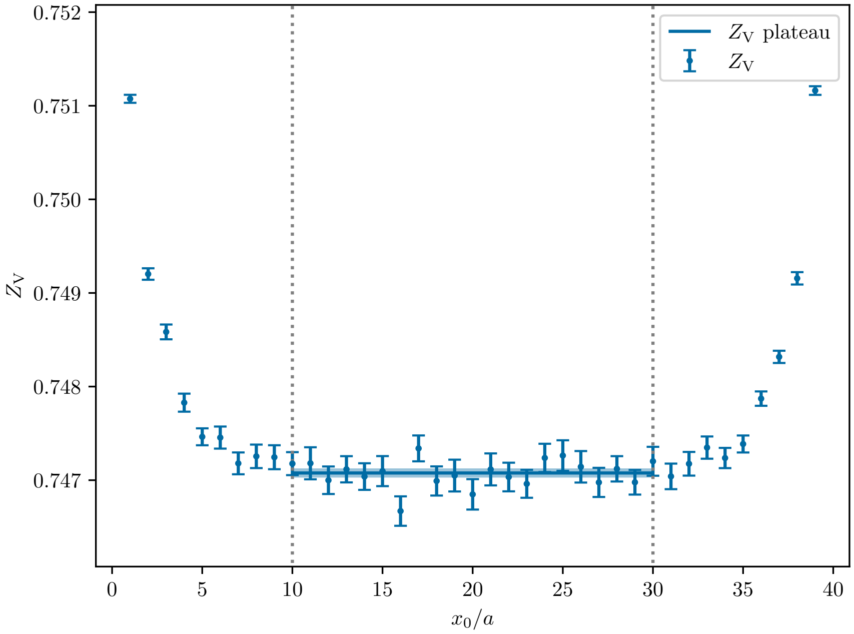

Figure 7.2: Example of the evaluated effective renormalization constant with the proposed plateau range on ensemble `C40c1`, with $m_\mathrm{q}^\mathrm{val} = m_\mathrm{q}^\mathrm{sea}$.

7.1.3 Interpolations from literature

To arrive at the mass independent renormalization, we extract $\hat{Z}_\mathrm{V}$ along the line of $m_\mathrm{q}^\mathrm{val} = m_\mathrm{q}^\mathrm{sea} = m_\mathrm{q}$ (grey, dotted line in figure 7.1) and interpolate the effective renormalization linearly as in figure 7.3, cancelling all mass effects for $m_\mathrm{q} \to 0$. The interpolations are carried out at each lattice spacing, such that an estimation of the mass-independent renormalization factor is extracted at each coupling similar to Z_A in the last chapter.

To estimate the mass improvement to the renormalization constant, we follow the lines of [149], in which two estimators are constructed: One estimates the factor attached to the valence-quark

$$R_\mathrm{V} = \partial_{am_\mathrm{q}^\mathrm{val}} \log\left(\hat{Z}_\mathrm{V}(am_\mathrm{q}^\mathrm{sea}; am_\mathrm{q}^\mathrm{val})\right) \xrightarrow[am_\mathrm{q}^\mathrm{val}\to 0]{} b_\mathrm{V}\ , \tag{7.8}$$

in which the sea-quark mass is fixed, while the other one estimates the combination of the valence- and sea-quark mass factors

$$\bar{R}_\mathrm{V} = \partial_{am_\mathrm{q}^\mathrm{sea}} \log\left(\hat{Z}_\mathrm{V}(am_\mathrm{q}^\mathrm{sea} = am_\mathrm{q}^\mathrm{val})\right) \xrightarrow[am_\mathrm{q}\to 0]{} (b_\mathrm{V} + 3\bar{b}_\mathrm{V})\ , \tag{7.9}$$

which can be combined with R_V to access $\bar{b}_\mathrm{V}$. The estimator R_V is evaluated along the vertical line $m_\mathrm{q}^\mathrm{sea} \approx 0$ (next to the dotted red line) in figure 7.1. For this purpose, the ensembles close to the chiral point are sampled at small valence-quark masses ($m_\mathrm{q}^\mathrm{val} = 0.001 \ldots 0.010$). The estimator $\bar{R}_\mathrm{V}$ is evaluated along the dashed grey line in the same figure which shows the line of degenerate quark masses. Note that the definitions given are only valid in the chiral limit, this being the reason for the small mass variations employed in the valence-quark mass. A great advantage of this method is the independence of the factor Z_V. We evaluate the estimators along the lines as needed by taking

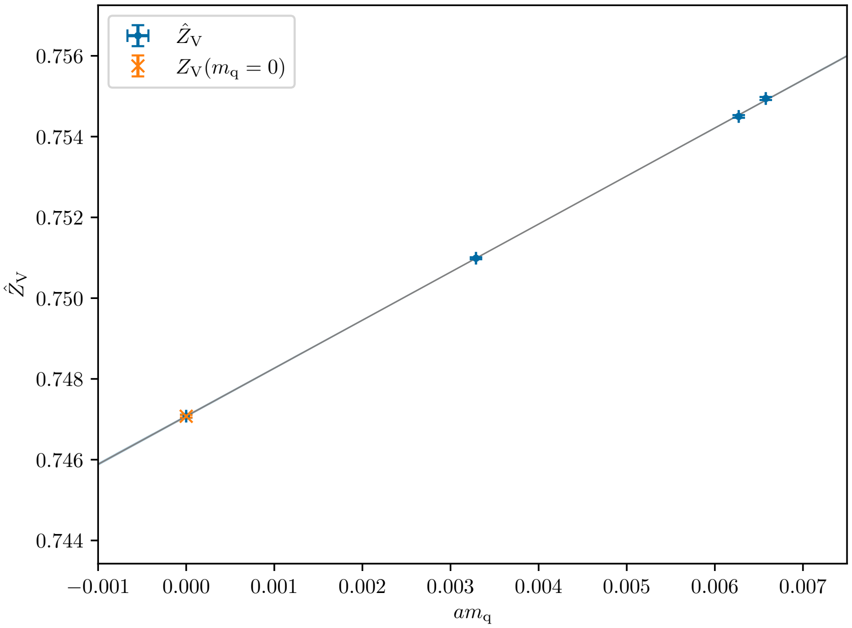

Figure 7.3: Linear extrapolation of the effective renormalization factors to the chiral point (orange ×) at inverse gauge coupling $\beta = 3.900$.

the logarithm of the data points calculated and interpolating linearly. The factor of the linear term is then evidently the estimator. Examples of the interpolations carried out are shown in figure 7.4. A first complete set of estimators for all coefficients is therefore already at hand, which we label *log* in the tables 7.1, 7.2 and 7.3.

7.1.4 Linear and two-dimensional fits

Inspecting equation (7.1), the derivative of the interpolation in figure 7.3 is evidently equivalent to the combined mass effect

$$\begin{aligned}\partial_{am_{\mathrm{q}}} Z_{\mathrm{V}} & \left(b_{\mathrm{V}} am_{\mathrm{q}}^{\mathrm{val}} + \bar{b}_{\mathrm{V}} a \mathrm{Tr}\left\{M_{\mathrm{q}}^{\mathrm{sea}}\right\}\right) \\ &= \partial_{am_{\mathrm{q}}} Z_{\mathrm{V}} \left(b_{\mathrm{V}} + 3\bar{b}_{\mathrm{V}}\right) am_{\mathrm{q}} \\ &= Z_{\mathrm{V}} \left(b_{\mathrm{V}} + 3\bar{b}_{\mathrm{V}}\right) \;,\end{aligned} \tag{7.10}$$

as $m_{\mathrm{q}}^{\mathrm{sea}} = m_{\mathrm{q}}^{\mathrm{val}} = m_{\mathrm{q}}$. Dividing by Z_{V}, we are able to compare this to the estimator $\bar{R}_{\mathrm{V}}$ in equation (7.9) from above. We will call this estimation $\bar{R}_{\mathrm{V}}^{\mathrm{lin}}$, and note that we already have this information from the linear extrapolation we did for Z_{V}. Similarly, we can fix $m_{\mathrm{q}}^{\mathrm{sea}}$ and interpolate linearly. Dividing by Z_{V}, we get the combined mass effect

$$\partial_{am_{\mathrm{q}}^{\mathrm{val}}} \left(b_{\mathrm{V}} am_{\mathrm{q}}^{\mathrm{val}} + \bar{b}_{\mathrm{V}} a \mathrm{Tr}\left\{M_{\mathrm{q}}^{\mathrm{sea}}\right\}\right) = b_{\mathrm{V}}^{\mathrm{lin}} \;, \tag{7.11}$$

such that a second pair of estimators is received. This method of estimation was already used in reference [91].

Lastly, we consider a fit in $(am_{\mathrm{q}}^{\mathrm{val}}, am_{\mathrm{q}}^{\mathrm{sea}})$ at the same time. As an ansatz we trivially

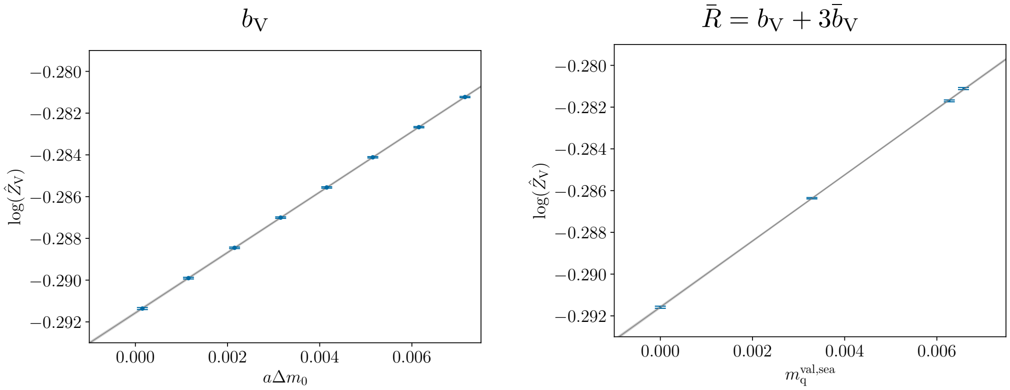

Figure 7.4: Interpolations for b_V and $\bar{R}_\mathrm{V}$ at $\beta = 3.900$ with the same scales on the x- and y-axes. Note the slight miss match equal to $3\bar{b}_\mathrm{V}$.

Table 7.1: Table of the interpolated values for Z_V at zero quark mass from form the interpolations along the line of $m_\mathrm{q}^\mathrm{val} = m_\mathrm{q}^\mathrm{sea}$ and from the global fit.

β	Z_V	$Z_\mathrm{V}^\mathrm{global}$
3.685	0.702042(66)	0.701962(65)
3.800	0.728707(43)	0.728662(39)
3.900	0.747075(32)	0.747065(27)
4.000	0.761628(18)	0.761630(19)
4.100	0.773787(17)	0.773778(17)
8.570	0.9187581(46)	—

employ

$$\begin{aligned} f(m_\mathrm{q}^\mathrm{val}, m_\mathrm{q}^\mathrm{sea}) &= b_0 \ \left(1 + b_1 \ \ am_\mathrm{q}^\mathrm{val} + b_2 \ \ a\mathrm{Tr}\left\{M_\mathrm{q}^\mathrm{sea}\right\}\right) \\ &= Z_\mathrm{V}\left(1 + b_\mathrm{V} \ am_\mathrm{q}^\mathrm{val} + \bar{b}_\mathrm{V} \ a\mathrm{Tr}\left\{M_\mathrm{q}^\mathrm{sea}\right\}\right) \ , \end{aligned} \tag{7.12}$$

and can simply read off the three parameters, which we will write from now on with the superscript *global*. Over all, we receive two estimations for Z_V, and three estimations for b_V and $\bar{b}_\mathrm{V}$ respectively, which are listed in the tables 7.1, 7.2 and 7.3.

The overall factor Z_V in particular is determined to very high degree with errors of O(0.01%). Note that the two determinations coincide, even at this accuracy. We will not fit them independently and only employ the determination from the linear (traditional) fit (as opposed to the global fit). Note also that the value at $\beta = 8.570$ is extracted on only one ensemble, `M32c1`, which is tuned to the chiral limit very well, as seen in table 5.2. Similarly, the values of b_V are mostly compatible with each other. Due to the slight changes observed, we will give interpolations for all three definitions in the next section. The values for $\bar{b}_\mathrm{V}^\mathrm{log}$ and $\bar{b}_\mathrm{V}^\mathrm{lin}$ are both defined by the respective differences $(\bar{R}_\mathrm{V} - R_\mathrm{V})/3$. They are fully compatible with each other and with the two-dimensional fit in most places.

For the time being, we employ the logarithmic method when needed as it is the closest to literature. We note however, that both other methods are equally valid and coincide with the results in most places.

Table 7.2: Table of the estimators for $b_{\rm V}$ from the three methods of determination discussed in the chapter: From the fit to the logarithm of the effective renormalization factors, from a fit directly to the effective renormalization factors both against the valence-quark mass, as well as a global fit in the sea- and valence-quark mass at the same time.

β	$b_{\rm V}^{\rm log}$	$b_{\rm V}^{\rm lin}$	$b_{\rm V}^{\rm global}$
3.685	1.534(17)	1.542(17)	1.531(15)
3.800	1.4750(61)	1.4821(67)	1.4982(33)
3.900	1.4463(48)	1.4546(57)	1.4598(30)
4.000	1.4112(24)	1.4198(26)	1.4212(18)
4.100	1.3807(24)	1.3872(28)	1.3907(20)

Table 7.3: Table of the estimators for $\bar{b}_{\rm V}$ from the three methods of determination discussed in the chapter: From the fit to the logarithm of the effective renormalization factors, both from a fit directly to the effective renormalization factors against the valence-quark mass and a global fit in the sea- and valence-quark mass at the same time.

β	$\bar{b}_{\rm V}^{\rm log}$	$\bar{b}_{\rm V}^{\rm lin}$	$\bar{b}_{\rm V}^{\rm global}$
3.685	0.2295(75)	0.2325(76)	0.2370(81)
3.800	0.0895(30)	0.0911(30)	0.0919(31)
3.900	0.0458(25)	0.0459(25)	0.0455(24)
4.000	0.0251(19)	0.0245(19)	0.0255(19)
4.100	0.0176(15)	0.0171(16)	0.0162(16)

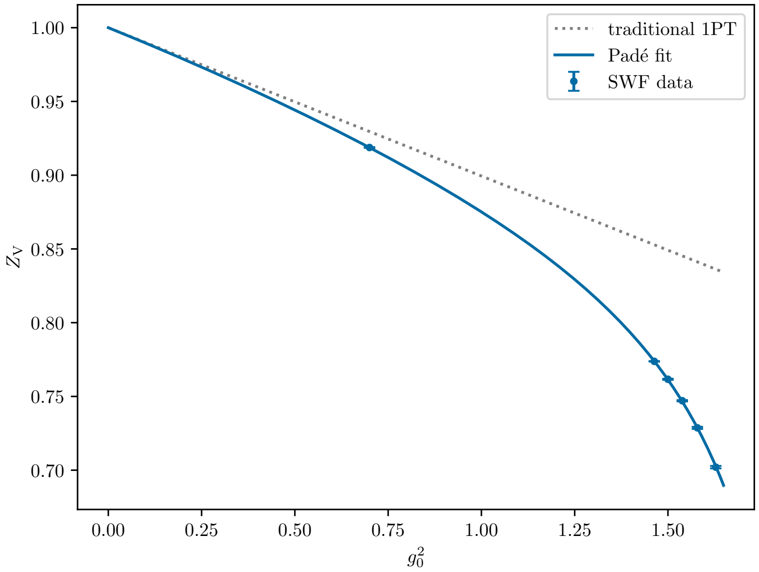

Figure 7.5: Interpolation of Z_V in the squared bare coupling g_0^2. Note that the values at $\beta = 4.370$ are not taken into consideration when interpolating, as the ensembles are far from the chiral limit.

7.1.5 Interpolation in the coupling

After evaluation of the mass-independent and mass-dependent renormalization parameters, we would like to interpolate them in g_0^2. We will start again with Z_V and inspect the interpolations of b_V and $\bar{b}_V$ later on.

Renormalization factor In figure 7.5, the renormalization factor Z_V is fitted against the squared bare coupling with a Padé ansatz of the form

$$Z_V(g_0^2) = 1 - 0.075427\ C_F\ g_0^2\ \frac{1 + a_1 g_0^2 + a_2 g_0^4}{1 + b_1 g_0^4} \tag{7.13}$$

with $C_F = 4/3$. The term in the front is the constraint from perturbation theory found in [140]. The parameters of the fit shown are

$$a_1 = -0.00170(71)\,,\ a_2 = -0.2738(16)\,,\ b_1 = -0.2554(21) \tag{7.14}$$

with which the fit reproduces the points with $\chi^2/\text{d.o.f.} = 1.0387$, when inflating the margins of error of the data points by a factor of 50. When not inflating the margins of error, the mean values of the fit parameters only change slightly and are statistically compatible with the ones cited. The reduced χ^2 is however ≈ 6000, because of which we discard the fit without inflating the errors.

Valence-quark mass factor As a second step, the valence-quark mass improvement factor is mapped out depending on the squared coupling. The values are well approximated by the polynomial

$$b_V(g_0^2) = 1 + 0.0886\ C_F\ g_0^2 + a_1 g_0^6 + a_2 g_0^8\ , \tag{7.15}$$

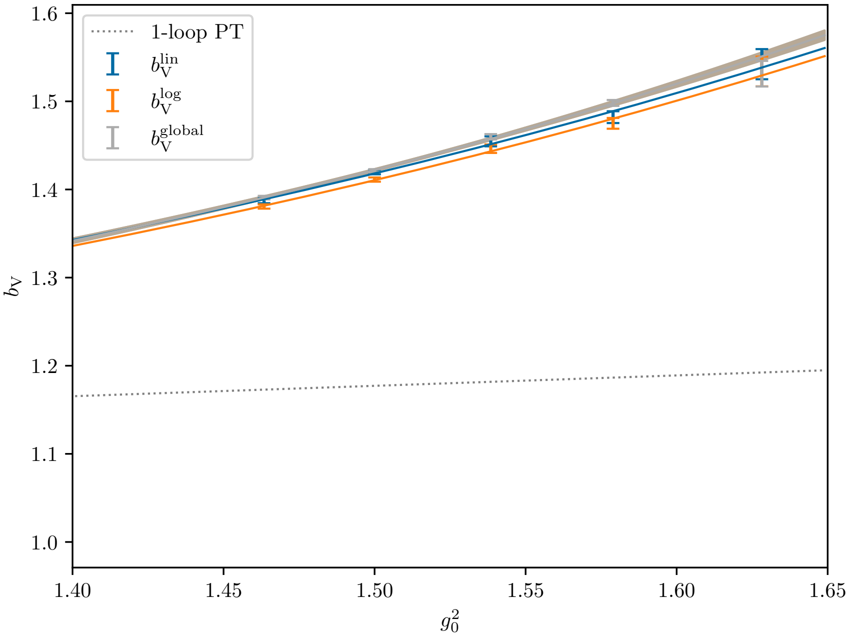

Figure 7.6: Plot of the three fits for the different determinations of b_V, with the 1-loop perturbative expectation as the dotted line.

in which the first term is again dictated by perturbation theory. The three lines of data produced here are described by the parameter sets

$$a_1 = -0.035(18)\,,\ a_2 = 0.070(12)\ , \tag{7.16}$$

$$a_1 = -0.031(20)\,,\ a_2 = 0.068(13)\ , \tag{7.17}$$

and

$$a_1 = -0.051(13)\,,\ a_2 = 0.0824(83) \tag{7.18}$$

for the logarithmic, the linear and the two-dimensional fits, respectively. Comparing these results to [149], we find that there the constraint to the 1-loop order was not necessary, as data much closer to the perturbative regime was known. Figure 7.6 shows the three fits with their respective data points.

Sea-quark mass factor At last, we also give two descriptions of $\bar{b}_\mathrm{V}(g_0^2)$. In the literature (cf. [149, fig. 4]), the estimation of this factor is done trough fitting $\bar{R}_\mathrm{V}(g_0^2)$ and $R_\mathrm{V}(g_0^2)$ separately, then employing their relation to $\bar{b}_\mathrm{V}(g_0^2)$ to estimate the factor. In that reference, $\bar{R}_\mathrm{V}(g_0^2)$ and $R_\mathrm{V}(g_0^2)$ were fitted with a Padé fit of the same kind, which is favourable when employing this subtraction. Remember also, as alluded to in section 2.6, this factor only plays a role at two-loop order in perturbation theory, making the factor generally small at small couplings. In our case, we found that the combined factor $\bar{R}_\mathrm{V}(g_0^2)$ is fitted best with the ansatz

$$\bar{R}_\mathrm{V}(g_0^2) = 1 + 0.0886\ C_\mathrm{F}\ g_0^2\ \frac{1 + a_1 g_0^2 + a_2 g_0^{10}}{1 + b_1 g_0^2}\ , \tag{7.19}$$

for which the parameters

$$a_1 = -0.5695(12)\ ,\ a_2 = -0.00050(67)\ ,\ b_1 = -0.5923(24) \tag{7.20}$$

yield an appropriate description of the logarithmic procedure. The results of the linear procedure are very similar. However, employing the polynomial given in equation (7.15) with the parameters (7.16) for b_{V}, we find a local maximum between $g_0^2 = 0$ and the first value investigated. As already discussed, at this time there are no ensembles at $g_0^2 = 0.7$ with mass greater zero that could be employed to strengthen the fit at these small couplings. It seems however unintuitive that the functions is non-monotonous.

Therefore, fits to the data directly at the points of the ensembles are explored. In this case, the evaluations listed in table 7.3 are fitted to, once with an exponential fit of the form

$$\bar{b}_{\mathrm{V}}(g_0^2) = a_1 g_0^4 e^{p_1 + (p_2/g_0^2)}\ , \tag{7.21}$$

with which we receive the parameters

$$a_1 = 6.88195392(67)\,,\ p_1 = 18.97(84)\,,\ p_2 = -38.1(1.3) \tag{7.22}$$

and once with a Padé fit of the form

$$\bar{b}_{\mathrm{V}}(g_0^2) = \frac{a_1 g_0^8 + a_2 g_0^{12}}{1 + b_1 g_0^2}\ , \tag{7.23}$$

for which the parameters

$$a_1 = -0.00198(50)\,,\ a_2 = 0.00114(23)\,,\ b_1 = -0.5948(22) \tag{7.24}$$

yield a good fit. The fits are shown in figure 7.7, however neither of the proposed functions is particularly desirable, but for different reasons. The exponential fit has a $\chi^2/\text{d.o.f.} \approx 11$, while the Padé fit is slightly negative at smaller values of the coupling. From the residues shown, we can see that the Padé fit carried out along the data that is shown in the plot describes the data best in the range of couplings investigated.

7.1.6 Comparison to traditional Wilson Clover fermions

As for c_{A} and Z_{A}, the values at the lattice spacings presented may be compared to literature for the three flavour case with traditional Wilson clover fermions carried out in [149] and [151]. This is shown in figure 7.8. As one can see, the factors Z_{V} and b_{V} in the exponential case are both closer to the 1-loop perturbation theory when compared to values at equal lattice spacing with the traditional action. For $\bar{b}_{\mathrm{V}}$, this is not always the case, and we can see that the difference changes sign when going to coarser lattices.

7.1.7 Conclusion

We have seen that, due to the simple expression given for Z_{V}, the renormalization factor was calculable up to a very high accuracy, with the two determinations presented matching.

As for the mass-improvements to the renormalization, b_{V} was also shown to be well determined through all three methods presented. The small deviations seen are mostly within margins of error of each other. For the moment, we prefer to stick with the (logarithmic) method employed in literature.

For $\bar{b}_{\mathrm{V}}$ in particular we have also seen that our determinations coincide. However, as for this quantity perturbative results would start at two loops, the interpolation over

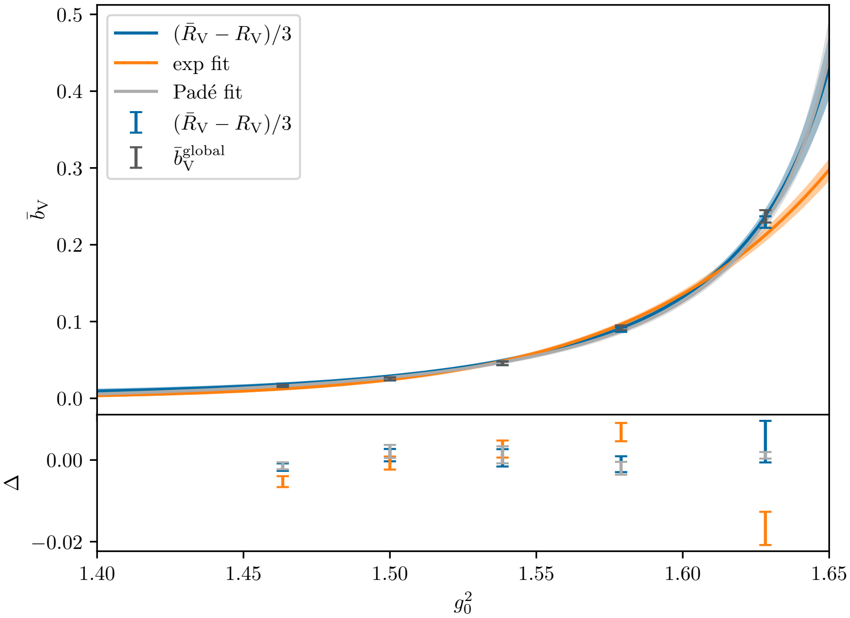

Figure 7.7: Three different fits for the sea-quark mass improvement to the renormalization. The discrete points are evaluations at the couplings investigated, once from the logarithmic method used in literature and once from the global method.

g_0^2 has clear disadvantages, which could only be lifted with the generation of more gauge field ensembles close to the perturbative limit.

Compared to results in the traditional case, we have seen that the exponential case has less cut-off effects overall. The only exception is the sea-quark mass improvement at large lattice spacings, which increases faster than in the traditional case. In conclusion, the renormalization and the mass improvements are well presented by our fits within the range of couplings considered here. However, the continuum approach needs to be investigated with care, when more gauge field ensembles are available at small couplings.

7.2 Improvement

The improvement of the vector current can also be determined through Ward identities. This method was first introduced in [152] and has already been applied to traditional Wilson clover fermions in [148] the respective 1-loop perturbative calculations have been carried out in [153].

The improvement of the vector current is not a direct aim of this thesis, however, in [87] this Ward identity method was implemented for the Schrödinger functional ensembles at hand. We want to shortly describe the method along the lines of [28] as it is an integral part of the improvement program we are working on in this part of the thesis.

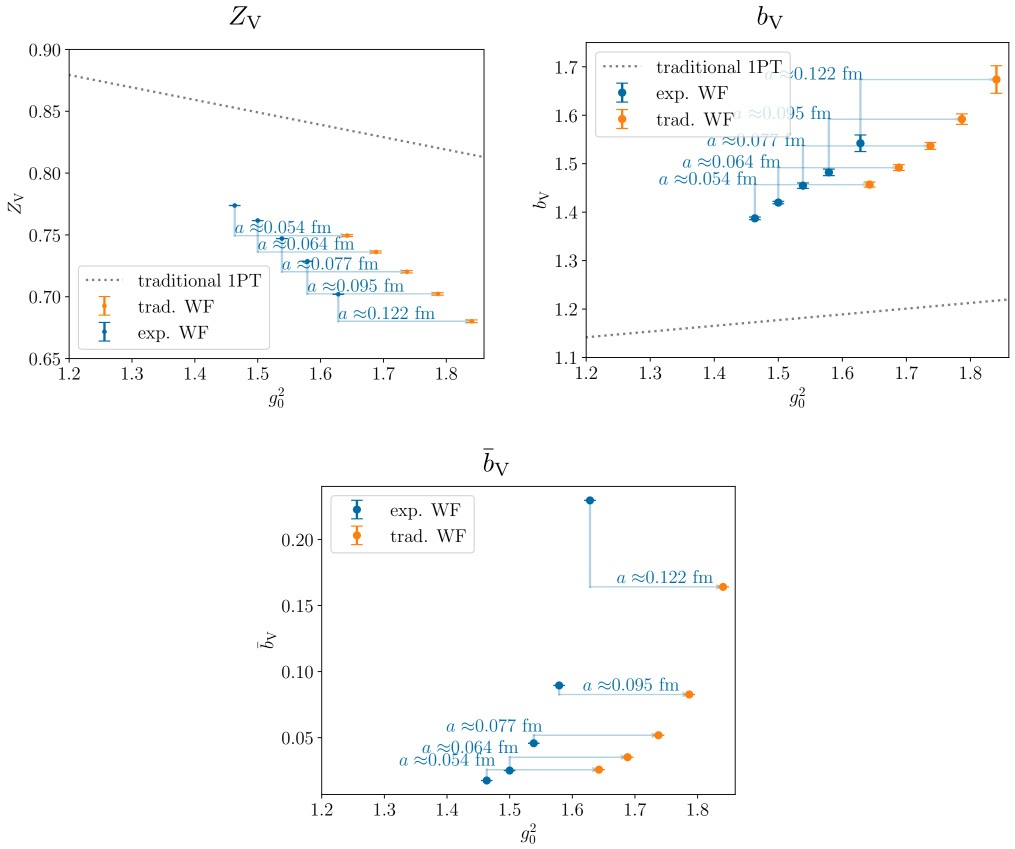

Figure 7.8: Comparisons of the renormalization factor $Z_{\rm V}$ and its mass improvements $b_{\rm V}$ and $\bar{b}_{\rm V}$ calculated here (blue) and on traditional Wilson clover fermions (orange). The orange points were created by evaluating [149, eq. (2.8) - (2.11)] at the points of equal lattice spacing.

7.2.1 Setup of the improvement condition

The setup is similar to the one for the axial-vector renormalization in the following way: Consider again the axial variation of the expectation value

$$\delta_{\mathrm{A}}^{a}\langle \mathrm{A}_{\nu}^{b}(y) O_{\mathrm{ext}}\rangle \ , \tag{7.25}$$

with an internal axial insertion ($y \in R$). This time, the external operator takes the form of $\mathcal{Q}$ from equation (2.47), such that there are only 3-point functions appearing in the expression received. This makes the appearing contractions easier, as we can choose the flavours such that only the connected diagrams appear, as discussed in section 2.9.2. The evaluation of the axial variation stays the same as in equation (6.42a) and the final discretized version is of a similar form:

$$\begin{aligned} a^3 \sum_{\vec{x}} \left[\langle (\mathrm{A}_0^a)^{\mathrm{RI}}(x) (\mathrm{A}_k^b)^{\mathrm{R}}(y) \mathcal{Q}_k^c\rangle\right]_{x_0=t_1}^{x_0=t_2} - 2am^{\mathrm{RI}} a^4 \sum_{\vec{x}} \sum_{x_0=t_1}^{t_2} \langle (\mathrm{P}^a)^{\mathrm{R}}(x) (\mathrm{A}_k^b)^{\mathrm{R}}(y) \mathcal{Q}_k^c\rangle \\ = \mathrm{i} f^{abd} \langle (\mathrm{V}_k^d)^{\mathrm{RI}} \mathcal{Q}_k^c\rangle + \mathrm{O}(a^2) \ , \end{aligned} \tag{7.26}$$

where the region R was again chosen as in equation (3.17) and the fact that the spatial components of the axial-vector current do not receive additional counter terms. Again, the relation is expressed in terms of correlation functions, with the renormalization factors and $\mathrm{O}(a)$ improvement terms written explicitly:

$$c_{\mathrm{V}} = \frac{Z_{\mathrm{A}}^2}{Z_{\mathrm{V}}} \frac{\left[k_{\mathrm{A}_0\mathrm{A}_k^{\mathrm{I}}(t_2,x_0)} - k_{\mathrm{A}_0\mathrm{A}_k^{\mathrm{I}}(t_1,x_0)} - 2m\tilde{k}_{\mathrm{PA}_k}(t_2,t_1)\right]}{a\partial_0 k_{\mathrm{T}}(x_0)} - \frac{k_{\mathrm{V}}(x_0)}{a\partial_0 k_{\mathrm{T}}(x_0)} + \mathrm{O}(a^2) \tag{7.27}$$

$$k_{\mathrm{AA}}^{\mathrm{I}}(y_0,x_0) = k_{\mathrm{AA}} + c_{\mathrm{A}} \partial_{y_0} k_{\mathrm{PA}}(y_0,x_0) \tag{7.27a}$$

$$k_{\mathrm{AA}}(y_0,x_0) = -\frac{1}{48}\frac{a^6}{L^3} f^{abc} \sum_{\vec{x}\vec{y}} \langle \mathrm{A}_0^a(y) \mathrm{A}_k^b(x) \mathcal{Q}_k^c\rangle \tag{7.27b}$$

$$k_{\mathrm{PA}}(y_0,x_0) = -\frac{1}{48}\frac{a^6}{L^3} f^{abc} \sum_{\vec{x}\vec{y}} \langle \mathrm{P}^a(y) \mathrm{A}_k^b(x) \mathcal{Q}_k^c\rangle \tag{7.27c}$$

$$\tilde{k}_{\mathrm{PA}}(t_1,t_2,x_0) = -\frac{1}{48}\frac{a^6}{L^3} f^{abc} \sum_{y_0=t_1}^{t_2} w(y_0) \sum_{\vec{x}\vec{y}} \langle \mathrm{P}^a(y) \mathrm{A}_k^b(x) \mathcal{Q}_k^c\rangle \ . \tag{7.27d}$$

As the analysis needed for the evaluation is outside the scope of this thesis, the only observation to be made is that this relation relies on Z_{V}, Z_{A} and c_{A} as prerequisites. As we have seen in section 6.2.2, the margins of error on Z_{A} are large compared to the other inputs needed. This fact is worsened, as Z_{A} enters quadratically. Especially with the preliminary values for Z_{A} given at the time, the margins of error reported in [87] are to be investigated again with final values of the improvement and renormalization.

Chapter 8

Renormalization of the quark mass

In the last chapters, we have seen how the axial-vector and vector currents are improved and renormalized. Before, in chapter 2.6, we had already seen that also parts of the action are renormalized multiplicatively. Now, we investigate the renormalization of the *subtracted bare quark mass* m_{q} as prescribed in equation (2.33). A second notion of the quark mass on the lattice was introduced through the PCAC relation in equation (3.15). As two quarks of different flavour i and j are potentially involved in the evaluation of the PCAC mass, we define the *current quark mass* as the average $m_{ij} = (m_i + m_j)/2$. In order to find suitable renormalization factors, these notions of the quark mass are combined in ratios that approximate the factors of interest in the chiral limit.

The higher level motivation behind renormalizing the quark mass is obvious: If we are able to relate the subtracted bare quark mass to the renormalized quark mass, a direct connection between some of the most fundamental parameters of QCD, the physical quark masses, and the simulation parameters of our lattice simulations can be established. For the research program this thesis is part of, this direct relation facilitates fixing the charm-quark mass via its physical value as an alternative to its determination through spectroscopic quantities.

We employ the renormalization scheme for the mass as introduced in section 2.6. The strategy to find the necessary renormalization factors was developed in the quenched theory in [154] with the two-flavour case following in [155]. Some improvements to the strategy were introduced in the three-flavour case [89], which we will follow for the most part. Let us start with a short introduction to the renormalization strategy itself, before we show the results received as part of the research carried out for this thesis.

8.1 The renormalized quark mass revisited

The subtracted bare quark mass $m_{\mathrm{q},i}$ of a quark of flavour i in presence of massive sea-quarks can be renormalized as

$$m_i^{\mathrm{R}} = Z_m \left\{ \left[m_{\mathrm{q},i} + (r_m - 1) \frac{\mathrm{Tr}\left\{M_{\mathrm{q}}\right\}}{N_{\mathrm{f}}} \right] + aB_i \right\} + \mathrm{O}(a^2) \tag{8.1}$$

$$B_i = b_m m_{\mathrm{q},i}^2 + \bar{b}_m m_{\mathrm{q},i} \mathrm{Tr}\left\{M_{\mathrm{q}}\right\} + (r_m d_m - b_m) \frac{\mathrm{Tr}\left\{M_{\mathrm{q}}^2\right\}}{N_{\mathrm{f}}} + (r_m \bar{d}_m - \bar{b}_m) \frac{\mathrm{Tr}\left\{M_{\mathrm{q}}\right\}^2}{N_{\mathrm{f}}} \,, \tag{8.1a}$$

which was originally introduced in [77] and extended to the non-degenerate quark case in [85]. The superscript „R“ is from now carried by renormalized quantities. The terms multiplying the trace of the sea-quark mass matrix $\mathrm{Tr}\left\{M_\mathrm{q}\right\}$ are out of scope for the presented work. The reader is referred to reference [89], where each term is briefly discussed. Neglecting the sea-quark mass terms, the renormalized quark mass can be expressed in terms of the subtracted bare quark mass as

$$m_i^\mathrm{R} = Z_\mathrm{m}(1 + ab_m m_{\mathrm{q},i}) m_{\mathrm{q},i} + \mathrm{O}(a\mathrm{Tr}\left\{M_\mathrm{q}\right\}) + \mathrm{O}(a^2) \; , \tag{8.2}$$

where evidently most terms in the additional term (8.1a) vanish and only Z_m and b_m are to be determined. Note, that the overall renormalization is a function of the scale parameter $Z_m(a\mu)$ and diverges logarithmically in the ultraviolet. The scale can be fixed, for example by a hadronic scheme. Working with Wilson quarks in the chiral limit is, as alluded to in section 2.8.2, only possible in the Schrödinger functional.

Let us now turn towards the current quark mass. Renormalizing each current, the fully renormalized PCAC relation is given by

$$\partial_\mu \left(\mathrm{A}_{ij}^\mathrm{RI}\right)_\mu \mathcal{O}^{ij} = 2am_{ij}^\mathrm{R}(\mathrm{P}_{ij}^\mathrm{R})\mathcal{O}^{ij} + \mathrm{O}(a^2) \; . \tag{8.3}$$

It is also an eligible definition of the quark mass. As constructed in equation (2.36), the renormalized and improved currents are:

$$\left(\mathrm{A}^\mathrm{RI}\right)_\mu = Z_\mathrm{A}\left(1 + b_\mathrm{A} am_\mathrm{q} + \bar{b}_\mathrm{A} a\mathrm{Tr}\left\{M_\mathrm{q}\right\}\right)\left(\mathrm{A}_\mu + ac_\mathrm{A}\partial_\mu \mathrm{P}\right) + \mathrm{O}(a^2) \; , \tag{8.4}$$

and

$$\mathrm{P}^\mathrm{R} = Z_\mathrm{P}\left(1 + b_\mathrm{P} am_\mathrm{q} + \bar{b}_\mathrm{P} a\mathrm{Tr}\left\{M_\mathrm{q}\right\}\right)\mathrm{P} + \mathrm{O}(a^2) \; , \tag{8.5}$$

in which the superscript „I“ denotes the improved currents. The renormalization factor $Z_\mathrm{P} = Z_\mathrm{P}(a\mu)$ is also a function of the scale that diverges logarithmically in the ultraviolet. Upon rewriting equation (8.3) with equations (8.4) and (8.5), the renormalized quark mass extracted from the PCAC relation is of the form

$$m_{ij}^\mathrm{R} = \frac{Z_\mathrm{A}}{Z_\mathrm{P}} m_{ij}\left[1 + (b_\mathrm{A} - b_\mathrm{P})am_{\mathrm{q},ij} + (\bar{b}_\mathrm{A} - \bar{b}_\mathrm{P})a\mathrm{Tr}\left\{M_\mathrm{q}\right\}\right] + \mathrm{O}(a^2) \; , \tag{8.6}$$

in which, by addition of a source term, we are able to identify each term with the appropriate correlation function, but the renormalization factors are yet to be determined.

Therefore, when we neglect the sea-quark mass terms, the renormalization of equations (8.2) and (8.6), amounts to the determination of Z_m, b_m, $Z_\mathrm{A}/Z_\mathrm{P}$, and $(b_\mathrm{A} - b_\mathrm{P})$.

8.2 Determination of the renormalization factors

The factors Z_m, b_m, $Z_\mathrm{A}/Z_\mathrm{P}$, and $(b_\mathrm{A} - b_\mathrm{P})$ – or combinations thereof – can be determined by a series of quark mass ratios [89, 154, 155]. We will only give a brief review of the strategy here and refer the reader to [89] for a discussion of each term appearing.

As a first step to determine the renormalization constants, the PCAC mass from equation (8.6) and renormalized subtracted quark mass from equation (8.1) are related. For this, we calculate the mean of two renormalized subtracted quark masses m_i^R and m_j^R

and equate it with the appropriate expression of the current quark mass, thus receiving

$$m_{ij} = \frac{Z_m Z_\mathrm{P}}{Z_\mathrm{A}} \left\{ \left[m_{\mathrm{q},ij} + (r_m - 1)\frac{\mathrm{Tr}\left\{M_\mathrm{q}\right\}}{N_\mathrm{f}} \right] + aB_{ij} \right\} + \mathrm{O}(a^2) \tag{8.7}$$

$$\begin{aligned} B_{ij} =& b_m \frac{m_{\mathrm{q},i}^2 + m_{\mathrm{q},j}^2}{2} - (b_\mathrm{A} - b_\mathrm{P}) m_{\mathrm{q},ij}^2 \\ &+ \left[\bar{b}_m - (b_\mathrm{A} - b_\mathrm{P})\frac{r_m - 1}{N_\mathrm{f}} - (\bar{b}_\mathrm{A} - \bar{b}_\mathrm{P}) \right] m_{\mathrm{q},ij} \mathrm{Tr}\left\{M_\mathrm{q}\right\} \\ &+ (r_m d_m - b_m) \frac{\mathrm{Tr}\left\{M_\mathrm{q}^2\right\}}{N_\mathrm{f}} \\ &+ \left[\left(r_m \bar{d}_m - \bar{b}_m\right) - (r_m - 1)\left(\bar{b}_\mathrm{A} - \bar{b}_\mathrm{P}\right) \right] \frac{\mathrm{Tr}\left\{M_\mathrm{q}\right\}^2}{N_\mathrm{f}} \ . \end{aligned} \tag{8.7a}$$

We note that in the combination

$$Z = \frac{Z_m Z_\mathrm{P}}{Z_\mathrm{A}} \tag{8.8}$$

the scale dependencies of $Z_m(g_0^2, a\mu)$ and $Z_\mathrm{P}(g_0^2, a\mu)$ exactly cancel, such that Z is scale independent [154]. Following [154, 155], we introduce three ratios for the evaluation of the renormalization factors:

$$R_m = \frac{2(am_{12} - am_{33})}{(am_{22} - am_{11})\ 2a\Delta} \xrightarrow{\Delta\ ,\ m_\mathrm{q} \to 0} b_m + \mathrm{O}(a; a\mathrm{Tr}\left\{M_\mathrm{q}\right\}) \ , \tag{8.9a}$$

$$R_\mathrm{AP} = \frac{2am_{12} - am_{11} - am_{22}}{(am_{22} - am_{11})\ 2a\Delta} \xrightarrow{\Delta\ ,\ m_\mathrm{q} \to 0} (b_\mathrm{A} - b_\mathrm{P}) + \mathrm{O}(a; a\mathrm{Tr}\left\{M_\mathrm{q}\right\}) \ , \tag{8.9b}$$

$$R_Z = \frac{am_{22} - am_{11}}{2a\Delta} + (R_\mathrm{AP} - R_m)(am_{11} + am_{22}) \xrightarrow{\Delta\ ,\ m_\mathrm{q} \to 0} Z + \mathrm{O}(a^2; a\mathrm{Tr}\left\{M_\mathrm{q}\right\}) \ , \tag{8.9c}$$

where, similar to the cases of b_V and c_A discussed earlier, the b-factors only need to be determined with ambiguities in $\mathrm{O}(a)$ for the theory to be correct to $\mathrm{O}(a^2)$. Note that the terms proportional to the sea-quark masses are neglected at this stage.

In equation 8.9, we have introduced the parametrization

$$a\Delta = \frac{am_{\mathrm{q},2} - am_{\mathrm{q},1}}{2} \ , \tag{8.10}$$

in which $m_{\mathrm{q},2} > m_{\mathrm{q},1}$. As the current quark mass m_{ij} depends on the mass parameters of the quarks participating in the current insertion, we can parametrize all masses appearing in equation (8.9) with $a\Delta$. For the ratios above, a third current quark mass is needed. This is „artificially“ constructed, following [89], as

$$m_{33}(a\Delta) = m_{22}(a\Delta/2) \ . \tag{8.11}$$

In principle, the limits in equation (8.9) can be taken in a point-by-point fashion. However, as $(am_{22} - am_{11}) \to 0$ and $a\Delta \to 0$, with fixed a, numerical instabilities are eminent, as discussed in [89, sec. 2.2]. An example of these numerical instabilities on the dataset at hand is shown in figure 8.1, where the estimator R_AP is evaluated on a point by point basis. In the same figure, we also show the solution to this problem. Instead of evaluating the estimators for each mass separately, it is customary (cf. reference [89]) to rewrite the estimators in equation (8.9) by approximating the current quark mass by a power series in the subtracted bare quark mass (or equivalently of Δ)

$$am_{ij}(am_{\mathrm{q},ij}, \Delta) = \sum_{n,k=0}^{\infty} C_{nk} (\Delta)^{2n} (am_{\mathrm{q},ij})^k \ . \tag{8.12}$$

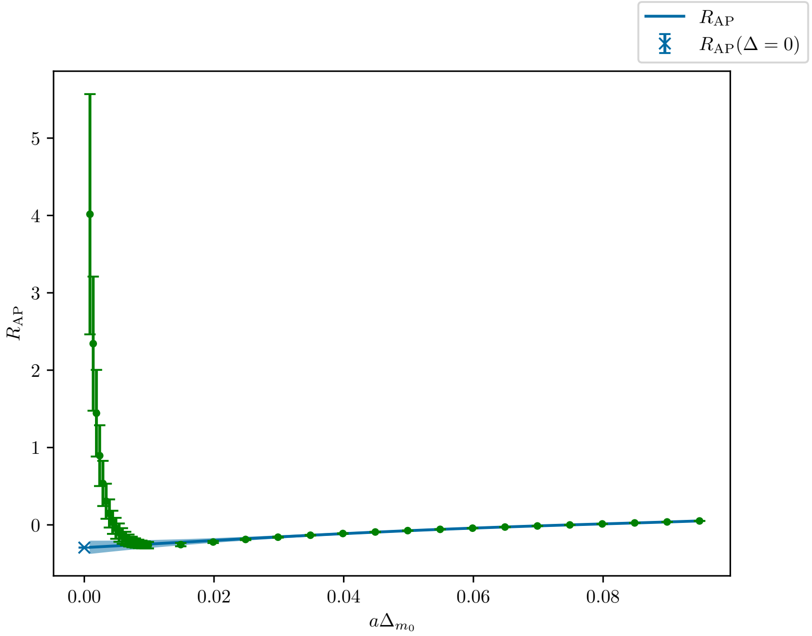

Figure 8.1: Evaluation of the ratio R_{AP} on a point-by-point basis (green points). The divergence when taking the limit $a\Delta \to 0$ on a point-by-point basis is clearly visible, contrary to the case of the evaluation via interpolation (with a polynomial of degree 6) discussed here (blue line).

By comparison of coefficients, one finds

$$\begin{aligned}
C_{00} &= Z\frac{a\mathrm{Tr}\left\{M_\mathrm{q}\right\}}{N_\mathrm{f}}\left\{(r_m-1)+(r_m d_m-b_m)\frac{a\mathrm{Tr}\left\{M_\mathrm{q}^2\right\}}{\mathrm{Tr}\left\{M_\mathrm{q}\right\}}\right. && \text{(8.13a)}\\
&\qquad\left.+\left[(r_m\bar{d}_m-\bar{b}_m)-(r_m-1)(\bar{b}_\mathrm{A}-\bar{b}_\mathrm{P})\right]a\mathrm{Tr}\left\{M_\mathrm{q}\right\}\right\}\ , && \text{(8.13b)}\\
C_{01} &= Z\left\{1+\left[\bar{b}_m-(\bar{b}_\mathrm{A}-\bar{b}_\mathrm{P})-(b_\mathrm{A}-b_\mathrm{P})\frac{r_m-1}{N_\mathrm{f}}\right]a\mathrm{Tr}\left\{M_\mathrm{q}\right\}\right\}\ , &&\\
C_{02} &= Z\left[b_m-(b_\mathrm{A}-b_\mathrm{P})\right]\ , && \text{(8.13c)}\\
C_{10} &= Zb_m\ . && \text{(8.13d)}
\end{aligned}$$

The particular masses employed in the ratios can be rewritten as the following power series

$$am_{11} = \sum_{k=0}^{\infty} C_{0k}(am_{\mathrm{q}1})^k\ , \tag{8.14a}$$

$$am_{22} = \sum_{k=0}^{\infty} C_{0k}(am_{\mathrm{q}1}+2a\Delta)^k\ , \tag{8.14b}$$

$$am_{12} = \sum_{n,k=0}^{\infty} C_{nk}(a\Delta)^{2n}(am_{\mathrm{q}1}+a\Delta)^k\ , \tag{8.14c}$$

whose derivatives are related through

$$\frac{1}{2}\frac{\partial m_{22}}{\partial\Delta}\Big|_{\Delta=0} = \frac{\partial m_{12}}{\partial\Delta}\Big|_{\Delta=0} = \frac{\partial m_{11}}{\partial m_{\mathrm{q},1}}\ . \tag{8.15}$$

When m_{22} and m_{12} are close to m_{11}, the series can be truncated after the second order, and m_{33} can be, by definition, constructed similarly:

$$am_{12}(\Delta) = am_{11}+N_1 a\Delta+N_2(a\Delta)^2+\mathrm{O}((a\Delta)^3) \tag{8.16a}$$

$$am_{22}(\Delta) = am_{11}+2N_1 a\Delta+4D_2(a\Delta)^2+\mathrm{O}((a\Delta)^3) \tag{8.16b}$$

$$am_{33}(\Delta) = am_{11}+N_1 a\Delta+D_2(a\Delta)^2+\mathrm{O}((a\Delta)^3)\ . \tag{8.16c}$$

We use these approximations to rewrite the ratios of quark masses in equation (8.9) as

$$R_m = \frac{N_2-D_2}{N_1} \xrightarrow{\Delta\,,\,m_\mathrm{q}\to 0} b_m+\mathrm{O}(a\Delta; a\mathrm{Tr}\left\{M_\mathrm{q}\right\})\ , \tag{8.17a}$$

$$R_\mathrm{AP} = \frac{N_2-2D_2}{N_1} \xrightarrow{\Delta\,,\,m_\mathrm{q}\to 0} (b_\mathrm{A}-b_\mathrm{P})+\mathrm{O}(a\Delta; a\mathrm{Tr}\left\{M_\mathrm{q}\right\})\ , \tag{8.17b}$$

$$R_Z = N_1-\frac{2D_2 am_{11}}{N_1} \xrightarrow{\Delta\,,\,m_\mathrm{q}\to 0} Z+\mathrm{O}\left((a\Delta)^2; a\mathrm{Tr}\left\{M_\mathrm{q}\right\}\right)\ . \tag{8.17c}$$

In conclusion, we can relate the three estimators of the renormalization factors with the help of a power series in the parameter Δ to the PCAC quark masses. At $\Delta = 0$, all three renormalization coefficients can furthermore be determined by the prefactors of the polynomials.

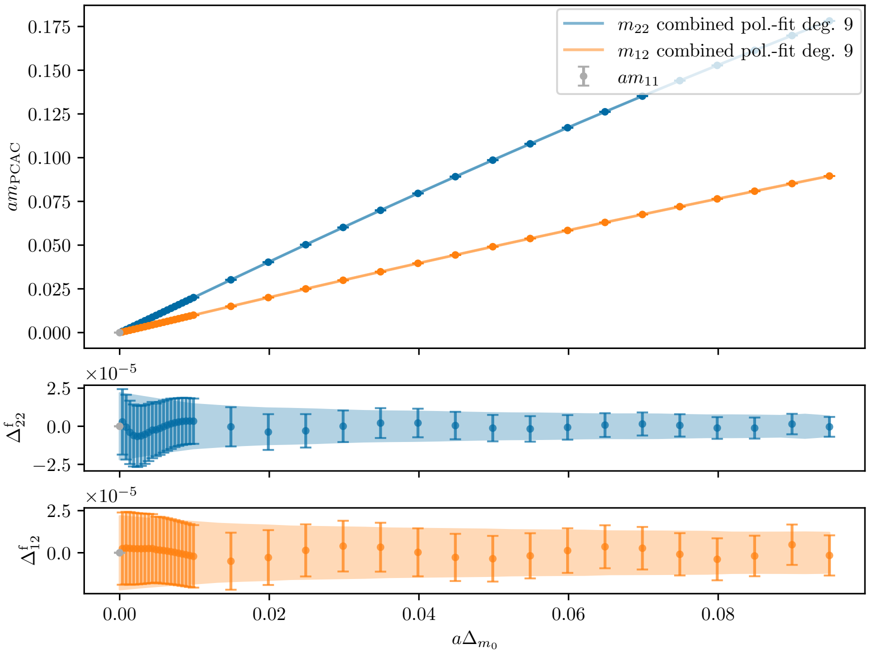

Figure 8.2: Example of an interpolation of degree 9 in the PCAC quark masses against the parameter $a\Delta$, taken from ensemble `D48c1`, close to the chiral limit. The upper plot shows the combined fits to the current quark masses. The lower plots the residues belonging to the two lines, showing how the margins of error of the data points and the interpolations overlap.

8.3 Analysis and encountered problems

We carry out valence-quark mass scans similar to the ones in section 7.1. However, in the presented case, the valence-quark mass was varied to larger bare quark mass parameters such that points $am_{\mathrm{q}}^{\mathrm{val}} = [am_{\mathrm{q},1},\ am_{\mathrm{q},1} + 0.2]$ were produced for the examined ensembles. We set the light quark mass equal to the sea-quark mass of the ensemble $am_{\mathrm{q},1} = am_{\mathrm{q}}^{\mathrm{sea}}$.

As an example, we look at ensemble `D48c1`, as it is the ensemble closest to the chiral limit (see table 5.1). This suppresses unwanted sea-quark mass terms as much as possible.

In figure 8.2 the interpolation of the data points that we extracted is shown with a combined fit of two polynomials of degree 9. As one can see from the residues, the polynomials describe the data well. In practice, the light-light current quark mass am_{11} is subtracted from both lines of data. Hence, the final fit is a combined fit in $a\Delta_{22}(a\Delta) = am_{22}(a\Delta) - am_{11}$ and $a\Delta_{12}(a\Delta) = am_{12}(a\Delta) - am_{11}$. As we truncate an infinite polynomial at small $a\Delta$, the particular degree of the polynomial is – in principle – not of concern. For example, the authors of reference [89] compared polynomial fits of degree 3 and 4 to show that the introduced ambiguities reduce in a controlled way.

In our determination, polynomials of this degree do not represent the data with high accuracy, as is exemplary shown in figure 8.3. In an attempt to improve this circumstance, we employed polynomials of higher degrees. On first sight, this eases the problem, but does not fully eliminate it. While in the literature, only very small patterns in the residues were observed (see e.g. [89, fig. 2] and [156]), in the case presented here, even relatively high degrees of polynomials still show patterns in the residues.

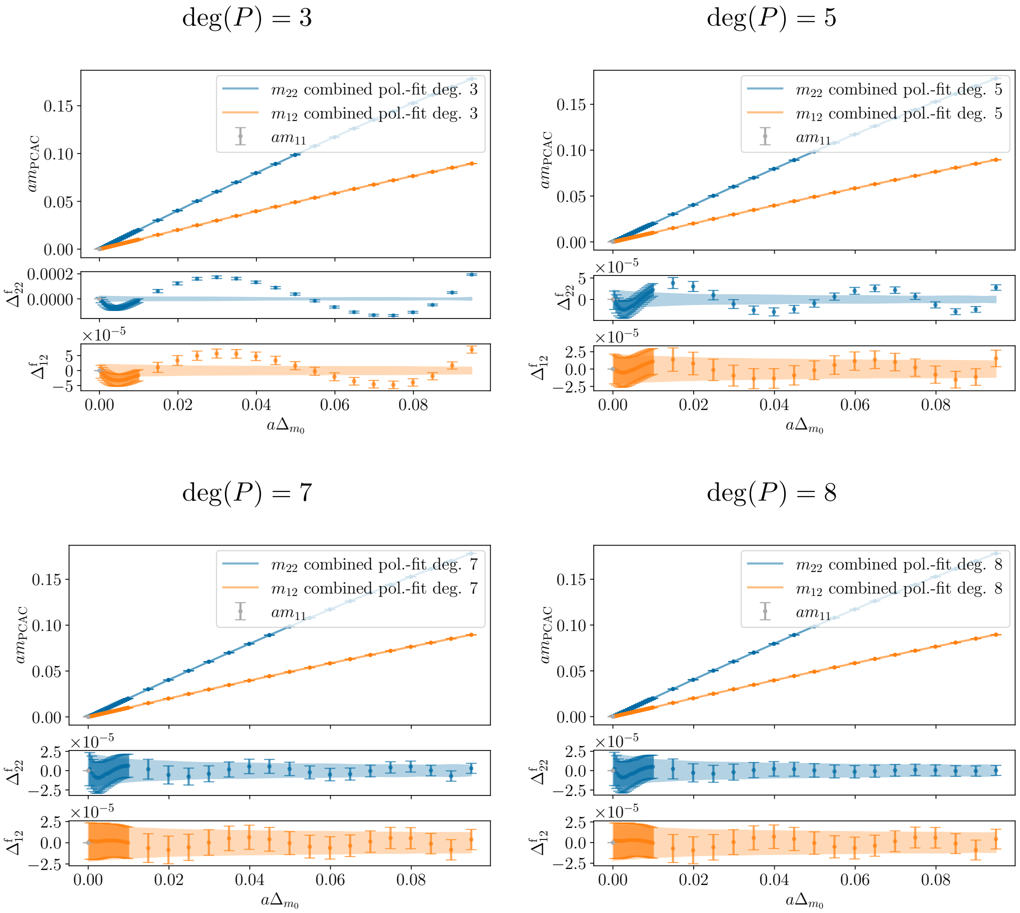

Figure 8.3: Fits to the data extracted from ensemble `D48c1` with different polynomials. The estimators for the three renormalization factors received from the interpolations shown here are listed in table 8.1. Compare also figure 8.2 for the interpolation with degree 9.

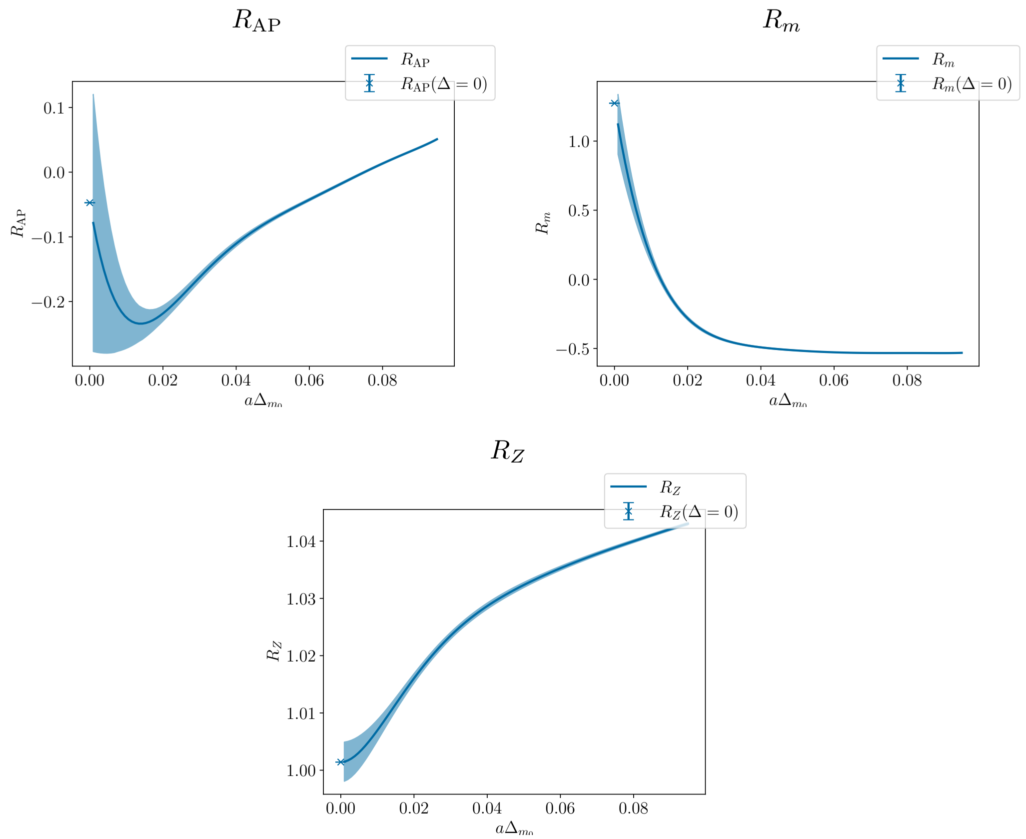

Figure 8.4: The interpolated estimators R_m, R_{AP}, and R_Z on the ensemble `D48c1`, belonging to the interpolation with a polynomial of degree 9 shown in figure 8.2. The apparent mismatches between the point in the chiral limit (blue x) and the come from the fact that the continued line diverges at $\Delta_{m_0} \to 0$ and can therefore not be plotted in the limit.

Furthermore, another problem emerges: Naively, one would expect that polynomials of higher degrees, which represent the data better, also yield better descriptions of the estimators R_m, R_Z, and R_{AP}. However, this is not the case in our determination. The three plots in figure 8.4 show the three estimators belonging to the fit shown in figure 8.2. They show undesirable features, as is evident in two ways: On the one hand, it seems the estimators follow the point-by-point estimation too closely, as is evident by the curvature of the estimators (see in particular R_{AP}) towards the chiral limit. Exclusion of this behaviour was the exact reason we started their description through polynomials to begin with. Comparing the determinations employing our 9$^{\mathrm{th}}$ degree polynomial to the determinations in the traditional clover case, we can see from the values we receive that further investigation is needed. On the other hand, apart from the comparison with earlier works, a reason to question the presented determination is the observation that the used strategy is highly sensitive towards the degree of the polynomial employed. This can be seen from the values listed in table 8.1, which shows how the estimators relying on the prefactors of the polynomials (cf. equation (8.17)), vary depending on the chosen degree of the polynomial. This is a major problem, as it illustrates the instability of the presented determination to the point that it cannot be trusted.

Table 8.1: Comparison table of estimators extracted from the prefactors of polynomials of various degrees at zero quark mass parameter difference.

deg(P)	$R_m(\Delta = 0)$	$R_Z(\Delta = 0)$	$R_{\mathrm{AP}}(\Delta = 0)$
3	-0.3892(84)	1.01980(94)	-0.2045(57)
4	-0.153(19)	1.0128(13)	-0.283(17)
5	0.139(33)	1.0084(16)	-0.330(40)
6	0.514(58)	1.0051(20)	-0.294(78)
7	0.92(11)	1.0028(25)	-0.19(12)
8	0.93(18)	1.0024(30)	-0.27(17)
9	1.27(25)	1.0014(35)	-0.05(23)

It would be interesting to see if this behaviour appears on other ensembles, however, only one other ensemble is approximately as well tuned as the one examined here (i.e. `C40c1`). We carried out the analysis on this second ensemble, which showed similar flaws. To further investigate the issue, a larger set of ensembles with similar properties are needed. With these at our disposal, we could carry out the analysis on them, and we would be able to better judge the reliability of the method at hand.

8.4 Possible solutions

While the tension in regard to the proper representation of the data on the one, and the expected behaviour of the estimators on the other hand is not yet fully solved, in the following we propose a few attempts as possible solutions to find a suitable polynomial:

Automating the polynomial choice An attempt to improve the situation could be to not lock the degree of the polynomial, but instead choose a polynomial P of degree $2 < \deg(P) < 9$ based on suitably defined criteria. The degree of the polynomial could for example be related to how well the data is described (e.g. by monitoring the reduced χ^2 of the fit) with a threshold where we expect it to over-fit the data. As the idea is to fit the data to a very high degree, the upper limit could be set very low (e.g. $\chi^2/\text{d.o.f.} = 0.25$).

This ansatz could protect from employing polynomials of too high degree, which could bypass the problems at hand. It does however also potentially lead to inconsistencies as the degree of the polynomial identified may change. This has to be monitored with care, especially in light of the results so far. We have already carried out tests of this procedure, however the parameters in regard to the maximal degree of the polynomial and how fit quality is monitored still need refinement.

Preliminary fitting Another idea to circumvent the posed problem is to determine the parameter N_1 (cf. equation 8.17) in a separate, preliminary fit. We choose a small region close to the origin, for example similar to the region taken for the determination of b_{V}. When $a\Delta$ is small, the fit is dominated by the linear term. Therefore, we first make a linear fit to the data in this region. As is the case for the larger fit, in the first linear fit, one may combine the two data lines $am_{22}(\Delta)$ and $am_{12}(\Delta)$ at hand. Once the parameter is determined, a fit with a higher degree polynomial is made including the fixed linear prefactor. The second fit then determines the parameters N_2 and D_2. In first tests, this ansatz did not describe the data to the same degree seen in the other fits. However, the estimators received were in the expected ballpark. A larger set of ensembles would be required to assess the stability of this ansatz.

Correcting the light quark mass In reference [89], the light quark mass am_{11} was not kept fixed in the fits. As described above, in the presented work, the light quark mass is fixed indirectly as a preparatory step for the fit, by subtracting it from the other current quark masses. In early tests of this project, this ansatz was investigated, however it was seen that, while it helps to reduce the absolute residues of the fits, it does not prevent the patterns appearing in the residues. It therefore only circumvents part of the problem. In particular, it does not subdue the instabilities seen in the estimators meaningfully.

Systematic errors Finally, an investigation of the margins of error of the data points may also alleviate parts of the problem. While the plateau fits to the PCAC masses are of high quality, one could find ways of adding systematic errors to the plateaus. A preliminary test in this regard was carried out by simply enlarging the margins of error by a factor of 3, such that the margins of error were about on par with those presented in reference [89]. This evidently improves the reduced χ^2 of the fit with lower polynomial degrees and suppresses the patterns seen in the residues.

Probably the solution to fitting the accumulated data lies somewhere in between the proposed ways. One could for example imagine fixing the linear factor, while opening the light quark mass for correction and follow up the preliminary fit with a second, higher polynomial fit.

8.5 Conclusion

We have seen that the determination of the estimators is hindered in two major ways:

We observe issues in regard to the choice of the degree of the polynomial employed. At this time, while the proposed solutions are promising in first tests, a proper investigation of each solution individually as well as of combinations of them is still missing.

In any case, the solutions need to be tested on a larger range of ensembles, as to judge their stability on multiple sets of data. This relates to a larger problem this investigation faces: The lack of ensembles tuned very accurately to the chiral limit and a lack of understanding of the inherent sea-quark mass terms in the formulated estimators.

The solution to this is evidently two-fold: On the numerical side, production of further extremely well-tuned chiral ensembles would suffice to make progress in this direction. On a larger scale, theoretical work in regard to the form of the $\mathrm{Tr}\left\{M_{\mathrm{q}}\right\}$ terms that spoil the exact estimation of the renormalization factors would be valuable. This would not only shed a light on the problems encountered in this analysis, but could also help to possibly formulate an estimation of the prefactors of said terms based on similar ideas as presented here. These prospects are, however, beyond the scope of this thesis.

As discussed in the preface of this chapter, once these problems are overcome, the findings could be employed in the context of the general research program aimed for with stabilized Wilson fermions as an alternative way of fixing the charm-quark mass. In that scenario, the mass parameter would not rely on spectroscopic quantities. However, lacking this, we opt for a determination of the charm-quark mass parameter relying on spectroscopy for the moment. The determination through spectroscopy is presented in chapter 10.

Part III

Meson decays and charmed physics

Chapter 9

OpenLat ensembles

In chapter 5, we have introduced a set of ensembles with Schrödinger functional boundary conditions. In the last part, we have seen that we can make great progress on renormalization and improvement by using these ensembles. However, for calculating physically significant observables, the reduced volume of Schrödinger functional ensembles may not be advantageous. As we have shortly alluded to in section 2.8, periodic boundary conditions are better suited for these calculations.

In the following, we want to make first steps towards calculations of physical observables that are connected to the charm-quark in the framework of stabilized Wilson clover fermions. As a prerequisite, we determine the charm-quark mass on the lattice in this framework and carry out preliminary scaling tests to estimate cut-off effects of physical observables that are easy to determine.

For this purpose, we introduce a new set of ensembles to this thesis, which are listed in table 9.1. These ensembles are part of the OpenLat ensembles. They were produced by the OpenLat initiative with the standard set for stabilized Wilson clover fermions. We therefore only introduce them briefly here and refer the reader to [157, 158] for a full introduction of the ensembles. Similar to the Schrödinger functional ensembles we have already introduced, these ensembles are also created with `openQCD` [126] version 2 and higher and the measurement of the reweighting factors and the flowed energy density E has already been carried out.

Table 9.1 gives an overview over the ensembles employed here. The Schrödinger functional ensembles we have used in part II were designed to fit the coupling range and spatial volume of these ensembles. As in chapter 5, we evaluate the parameter ϕ_4 similarly to the procedure described there. The main difference is the calculation of the effective mass in the axial-vector channel, which was carried out employing a slightly different definition of the mass that relies on the symmetry properties of the lattice. In particular, when periodic boundary conditions are present, we can exploit the forward and backward propagating modes of the mesons directly. Neglecting higher energy states, we can approximate the behaviour of the correlator as

$$C(x_0) = A\cosh\left(E\left(\frac{T}{2} - x_0\right)\right) \tag{9.1}$$

and

$$C(x_0) = A\sinh\left(E\left(\frac{T}{2} - x_0\right)\right) \tag{9.2}$$

for correlators with time-symmetry $\mathcal{T} = +1$ and $\mathcal{T} = -1$, respectively. The reader is referred to [30, ch. 2] for a derivation of the symmetries. For the moment, we will only

Table 9.1: List of large volume ensembles employed, subset of the ensembles by the OpenLat initiative. The ensembles have 6 different values of the inverse coupling β that can be related to the lattice spacing a. The hopping parameter κ (compare equation (2.21)) is the measure by which the mass of the quarks are given in the simulations. The lattice geometry is fully determined by the boundary conditions and the number of lattice sites T in time and L in space direction. ϕ_4, as introduced in this chapter is a dimensionless measure for the mass, that does not depend on the lattice spacing. The column #MDU shows the number of molecular dynamic units covered by all replica of the ensemble combined and is a measure of how „long“ the Monte-Carlo chain is in Monte Carlo time. Additionally, the column #M/C shows the fraction of configurations we did measurements on, (1/4) $\hat{=}$ one out of four configurations.

Ensemble	β	T	L	κ	a [fm]	ϕ_4	# MDU	#M/C
`a120m400`	3.685	96	24	0.1394305	0.1204(15)	1.1255(68)	11760	1/4
`a094m400`	3.800	96	32	0.1389630	0.0939(11)	1.1062(53)	27528	1/4
`a080m400`	3.900	96	48	0.1386030	0.07712(93)	1.1128(32)	5952	1/4
`a065m400`	4.000	96	48	0.1382720	0.06410(77)	1.1080(64)	2748	1/2

state that solving

$$\frac{C(x_0)}{C(x_0+a)} = \frac{\cosh\left(m\left(x_0 - \frac{T}{2}\right)\right)}{\cosh\left(m\left(x_0 + a - \frac{T}{2}\right)\right)} \tag{9.3}$$

or

$$\frac{C(x_0)}{C(x_0+a)} = \frac{\sinh\left(m\left(x_0 - \frac{T}{2}\right)\right)}{\sinh\left(m\left(x_0 + a - \frac{T}{2}\right)\right)} \tag{9.4}$$

for m (again depending on the time-symmetry), yields the effective mass of the correlator while exploiting the time-symmetry directly. The plateau of the mass is then taken only on the first half of the lattice, to avoid double-counting of the statistics. These are the equations by which we will calculate the effective masses in the rest of part III. For the calculation of ϕ_4 in table 9.1, the effective mass is extracted analogously to the strategy in section 5.1. We set up a two-state fit for to the effective mass in the first half of the lattice starting at $x_0 = 3$, as higher lying states are non-negligible on the first few time slices of the lattice. The start of the plateau range is set to be the x_0 for which equation (5.6),

$$\frac{c_1 \Delta_1}{c_0} e^{-\Delta_1 x_0} < \sigma_{\text{stat}}(x_0)/4 \ , \tag{9.5}$$

holds, where Δ_1 is again the energy difference between the ground and first excited state. The end is set to the point at which

$$\sigma_{\text{stat}}(x_0^{\text{end}} + a) > 0.03 \ m_{\text{eff}}(x_0^{\text{end}} + a) \ , \tag{9.6}$$

holds or at most at $x_0 = T/2-2$ to suppress numerical instabilities present in the middle of the lattice. An equivalent procedure will again be used in section 10.1 to extract effective masses in a similar scenario. The correlation functions in this part are calculated with the C++ program `Hadrons` [159], which is built on top of `GRID` [160].

Chapter 10

The charm-quark mass parameter

The physics program we aim for contains the decays of charmed mesons. However, so far, we have only looked at QCD with three degenerate flavours. To observe charm decays, we reintroduce charm-quarks as a quenched (non-dynamical) flavour, meaning the charm is only present in the valence-sector of the theory. As mentioned in section 2.3, effects from quenching the charm only add small systematic errors and are therefore ignored in our computations.

Since we are also ignoring the electromagnetic properties of quarks, the introduction of a charm-quark in the valence-sector only entails the introduction of an additional quark flavour with the correct mass. For this purpose, a physical observable X that is sensitive to the mass of the charm-quark m_c is calculated at different bare quark masses. Here, we will focus on the mass of charmed mesons (i.e. $X \in \{m_{\eta_\mathrm{c}}, m_D, m_{D_\mathrm{s}}, m_{D^*}, ...\}$). To compare it to physical masses, we need to introduce a scale parameter r, such that

$$r\ X(m_\mathrm{q}^\mathrm{val}) = r^\mathrm{phys} X^\mathrm{phys}(m_\mathrm{c}) \tag{10.1}$$

holds for the observable of our choice. The parameter r is chosen as $\sqrt{8t_0}$, similar to the scale introduced in section 5.1.1. For the lattices at hand we have calculated this parameter as part of the quantity ϕ_4.

Generally, the chosen quantity X should be known from experiment with small uncertainty, and we should also be able to determine the lattice equivalent of the quantity with small uncertainty as well. Apart from meson masses, popular candidates are decay rates or direct comparison of the renormalized current quark mass (see e.g. [161]). Also, as proposed in [124], ratios of renormalized charm and light quark masses can be employed, if the renormalization factors we have calculated in chapter 8 are known for the light and expected charm-quark mass. Determination of the charm-quark mass parameter via the renormalized charm-quark mass directly is not carried out here, as further inspection towards the sea-quark mass dependence of the factors calculated is needed.

In our determination, we are focusing on the masses of the η_c-meson, i.e., the lowest $c\bar{c}$ energy eigenstate in the pseudo-scalar channel, and its heavy-light pendant, the D-meson ($c\bar{l}$). Varying the valence-quark mass, similar to the scans carried out in chapters 7.1 and 8, we find the charm-quark masses. The scans in those chapters were modelled after the ones employed here to determine the current quark renormalization factors at the light- and charm-quark masses.

After the determination, we will show a small scaling test as to see whether the two masses indeed scale towards the same in the continuum. To avoid circular reasoning, the quantity employed for the determination of the charm-quark mass can of course not be regarded as a valid test or result of the tuned parameters. Instead, two mesons, the J/Ψ and the D^* are employed as a test subject.

First results of this project were communicated in our proceedings to the LATTICE conference 2023 [124].

10.1 Determination through spectroscopy

The determination of the charm-quark mass through spectroscopic quantities is a standard technique (see e.g. [161]). Its advantage is the straightforward evaluation of the quantities. We take strong inspiration from [162] for the analysis at hand.

In detail, the strategy is as follows: The charm-quark mass is fixed in our case through the mesons in the pseudo-scalar channel, η_c and D, whose masses we cite as

$$m_{\eta_\mathrm{c}} = 2978 \pm 6\,\mathrm{MeV} \quad [163] \tag{10.2a}$$

$$m_{\bar{D}} = (2m_D + m_{D_s})/3 = 1899.40 \pm 0.37\,\mathrm{MeV} \quad [162] \tag{10.2b}$$

These come about as follows: The $\bar{D}$-meson mass is the flavour averaged mass of D and D_s, as we are working at the $N_\mathrm{f} = 3$ flavour symmetric point. Effects from QED corrections have to be ignored in both masses, as isospin symmetry holds. In case of the η_c-mass, the mean value from [163] is employed as to account for missing disconnected $c\bar{c}$-diagrams. The margins of error are increased as in reference [162] to be compatible with the PDG value of $m_{\eta_\mathrm{c}} = 2984.10 \pm 0.40\,\mathrm{MeV}$ [64].

Spin-averaged combinations with the vector channel, i.e.

$$m_{\hat{D}} = (m_{\bar{D}} + 3m_{\bar{D}^*})/4 \, , \tag{10.3}$$

(where the $\bar{D}^*$ is constructed analogously to the $\bar{D}$) as in [164] were also explored in this project, however, we have seen that the averaging procedure is not of much value, due to larger margins of error in the vector channel (as was the case with traditional Wilson fermions, see reference [162]).

Remembering equation (2.45), we construct the lattice counterpart as follows: At large source-sink separations, we receive the effective mass of the meson ground-state on the lattice. We only have to define a start and an end of the plateau properly. Our strategy in this regard is the same as in section 5.1.1 and chapter 9, when evaluating ϕ_4. As in those evaluations, we assume that a fit ansatz of the form of equation (2.45) can approximate the calculated mass. We demand the statistical errors to be four times larger than the deviations due to the first excited state. Such that the inequality

$$\frac{c_1 \Delta_1}{c_0} e^{-\Delta_1 x_0} < \sigma_\mathrm{stat}(x_0)/4 \, , \tag{10.4}$$

holds for the plateau region. As described in chapter 9, we average the forward and backward propagating modes and only use the first half of the lattice for the subsequent fits. For the two masses calculated, two separate definitions of the end of the plateau are chosen:

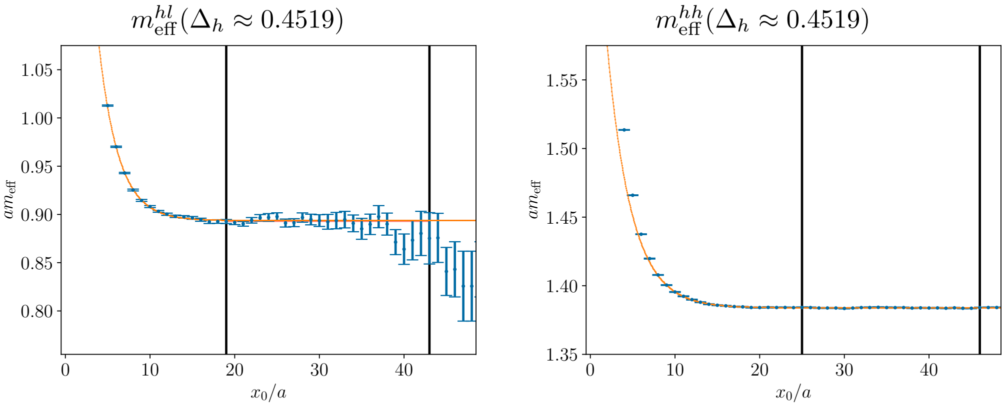

Figure 10.1: Example of a fit to the heavy-light- (left) and the heavy-heavy-meson mass (right), both taken on ensemble `a094m400`, in the vicinity of the found charm-quark mass.

heavy-light: In the case of the *heavy-light* mesons, that approximate the $\bar{D}$-meson mass, the end of the plateau is chosen such that

$$\sigma_{\text{stat}}(x_0^{\text{end}} + a) > 0.03 \; m_{\text{eff}}(x_0^{\text{end}} + a) \; . \tag{10.5}$$

The next time slice is the first time slice whose margins of error are larger than 3% of the mean value of the effective mass (see the example in figure 10.1 on the left).

heavy-heavy: In the case of the *heavy-heavy* mesons which approximate the η_{c}-meson mass, the condition employed above is not reached as the data does not admit margins of errors of this order. Instead, we define

$$x_0^{\text{end}} = (T/2) - 2 \; , \tag{10.6}$$

meaning the full potential of the correlator employed is used for the measurement. The -2 is only a protection from numerical inaccuracies at $T/2$ of the lattice that might appear due to the definition of the effective mass (see the example in figure 10.1 on the right).

Note that, after the plateau range is set, we take the plateau by means of a constant fit within the calculated range. This does not necessarily yield the (exact) same value of the ground state mass as the two-state fit. Employing these definitions, we scan the parameter range from the light to the charm-quark mass and compare the effective masses of the scanned mesons with their physical counterparts. Instead of searching for the parameter $m_{\text{q}}^{\text{val}}$ directly as demanded by equation (10.1), it is customary to re-parametrize the problem in terms of

$$\Delta_h = \frac{1}{2}\left(m_0^h - m_0^{\text{sym}}\right) = \frac{1}{4}\left(\frac{1}{\kappa^h} - \frac{1}{\kappa^{\text{sym}}}\right) \; . \tag{10.7}$$

Thus, the determination of the mass parameter is disconnected from the critical mass point. This helps with uncertainties (as m_0^{crit} has margins of error attached to it), and also eliminates the need to know said point in the first place. We follow the Gell-Mann–Oakes–Renner relation [134] as with ϕ_4, and linearize the squared effective mass $(am_{\text{eff}})^2$ around the charm-quark mass. For the final value of the hopping parameter, as is shown in figure 10.2, we only fit the effective masses locally: two points above and below the

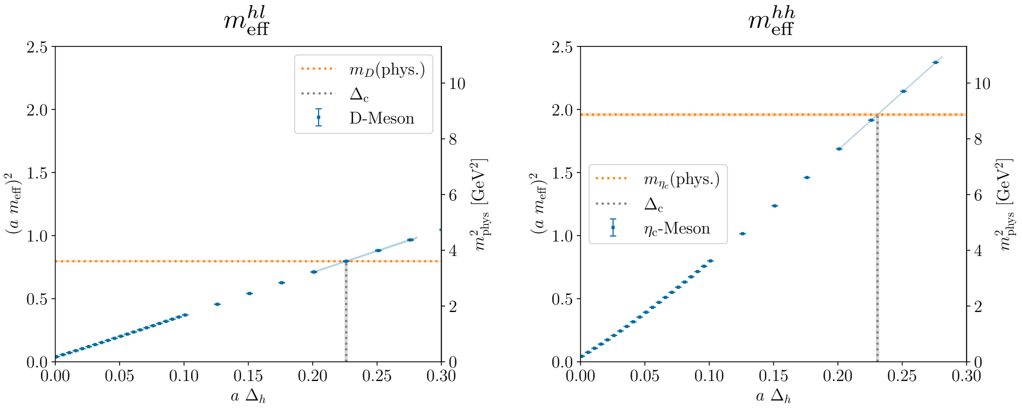

Figure 10.2: Linear interpolation of heavy-light (left) and heavy-heavy (right) squared meson masses on the ensemble `a094m400`. The orange line shows the reference masses of the $\bar{D}$- and η_c-mass from equations (10.2a) and (10.2b), respectively. Note that, while not visually discernible, the cross-point on the left-hand plot is in fact *above* the second point numerically.

Table 10.1: Table of the hopping parameters extracted at each inverse coupling with the η_c-meson and $\bar{D}$-meson as reference values.

β	$m_0^c\ (\eta_c)$	$m_0^c\ (\bar{D})$	$\kappa^c\ (\eta_c)$	$\kappa^c\ (\bar{D})$
3.685	0.2821(43)	0.2587(33)	0.11676(12)	0.117407(92)
3.800	0.0596(18)	0.0502(18)	0.123165(54)	0.123452(54)
3.900	-0.0501(13)	-0.05702(34)	0.126586(41)	0.126808(11)
4.000	-0.12085(98)	-0.1215(11)	0.128894(33)	0.128916(36)

final value of the hopping parameter. Following this procedure, we extract the mass parameters listed in table 10.1 as our result for the masses of the charm-quark on the lattices at hand.

10.2 Scaling tests

Once we found the mass parameters by means of the η_c- and $\bar{D}$-meson masses, we set out to estimate their scaling behaviour towards the continuum. Obviously, a different quantity is needed for this endeavour. As a very first step, we may look at the ambiguity of the charm-quark mass parameter itself, which is shown in figure 10.3, where we see that the differences vanish with $\mathrm{O}(a)$ towards the continuum.

However, as a proper scaling test, we calculate a different physical quantity than we used to determine the mass parameter. In the case presented, we have determined the charm-quark mass with the masses of the mesons in the pseudo-scalar channel. A valid test for the scaling of the mass parameter is therefore, for example, given by the masses of the respective vector channel mesons, the J/Ψ- and the $\bar{D}^*$-meson, which need to be calculated on each lattice. The continuum extrapolation should then land on the physical counterpart of the meson mass. The calculation follows a similar strategy as finding the charm-quark mass before, but backwards: From the scans employed for the

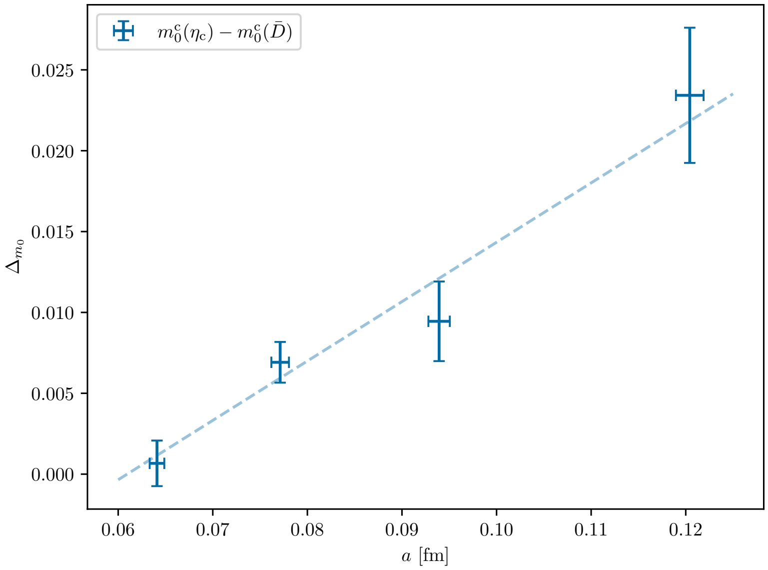

Figure 10.3: Ambiguity in the mass parameter introduced through the meson by which it is determined. In the range shown, the dependence on the lattice spacing is well approximated by a linear fit. Note that this is only used here to guide the eye, as a more complicated dependence is expected, when including more points towards the continuum limit.

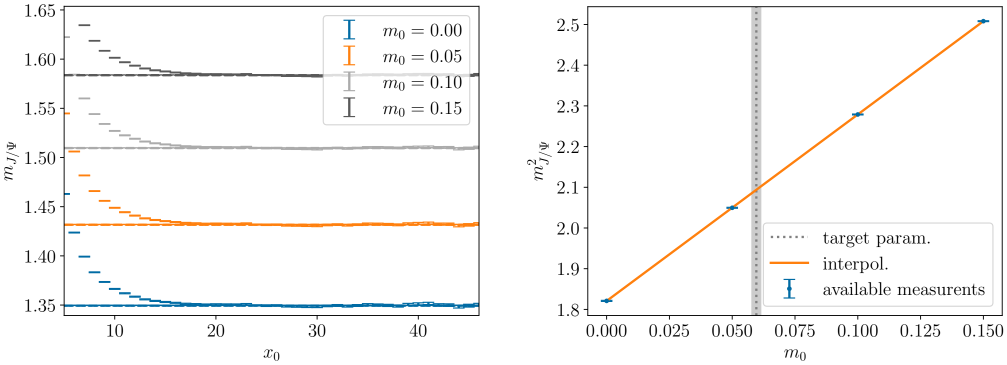

Figure 10.4: Fits of the effective masses of the J/Ψ-meson at different charm-quark masses (left) and interpolation to the desired mass parameter (right) in ensemble `a094m400`. The target parameter is determined via the η_c-meson.

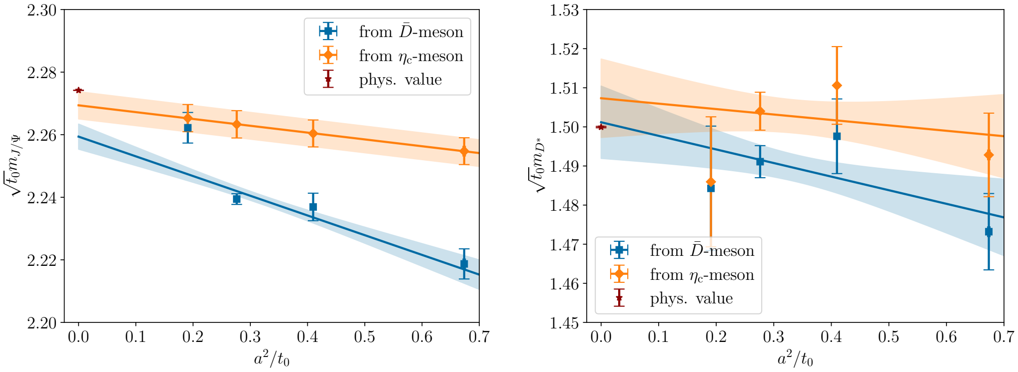

Figure 10.5: Scaling tests of the determined charm-quark hopping parameter in the vector channel. The right side showing the vector channel charmonium state J/Ψ, the left showing the flavour averaged $\bar{D}^*$-meson.

determination of the hopping parameter that we carried out, we select the same four masses in the valence-quarks. The effective masses of the vector mesons are calculated at these points, and we interpolate linearly in the squared effective mass to the desired hopping parameter, as shown in figure 10.4. The plateau conditions for the effective masses are the same as before. Carrying out these interpolations on all lattices available, we receive the effective masses of the J/Ψ- and $\bar{D}^*$-mesons.

These are interpolated towards the continuum, as shown in figure 10.5. The proposed fits are linear in a^2/t_0. For the limited statistics available at the moment, the scaling behaviour is fine for a first test. This is particularly true for the mass parameters determined from the η_c-meson evaluated for the mass of the J/Ψ-meson. Further investigation with higher statistics is clearly needed. Additional tests could then also be carried out in other channels.

10.3 Conclusion

We have determined the hopping parameters for the charm-quark on four lattices. Furthermore, we have seen that the continuum extrapolations of the mass channels are well controlled for the limited statistics, especially when looking at the meson masses determined for the J/Ψ-meson. As the effective mass plateaus of the η_{c}- and the J/Ψ-meson are both well-defined and show small cut-off effects, they yield a continuum limit close to the expected physical value. Nevertheless, it is desirable to increase statistics and add a smaller lattice spacing to improve the continuum limit especially for the heavy-light quarks. With these extensions, the continuum limit can be probed once more, including further quantities known from experiment. These tests could potentially also shed light on higher-order cut-off effects and a more robust estimation of the mass parameters is facilitated. As alluded to in the introduction to these determinations, the alternative determination through the current quark mass could be promising, when the renormalization factors for the quark mass we discussed in chapter 8 are understood better. For the time being, due to the lower cut-off effects visible, we tend towards the determination by the pseudo-scalar charmonium state η_{c}.

Chapter 11

Outlook

The various calculations carried out are part of a larger plan to prepare the framework of stabilized Wilson fermions for physics applications, with focus on charm-physics. Therefore, we want to focus here on concrete steps that are proposed to be carried out next in regard to exponential Wilson clover fermions and the stabilized ansatz.

Direct further investigations We have seen in some project parts that further investigation needs to follow up on some details. We refer the reader back to the chapters in question for detailed lists of proposals. In broad strokes, the next steps are the following:

- **Addition of further ensembles** While a large range of Schrödinger functional ensembles was already investigated, there are still cases in which further ensembles would be beneficial. In particular, an extension of the ensembles close to the perturbative regime is needed. On the one hand this would improve the estimation of the volume dependence of c_{A}, and by this further substantiate the computations that showed the perturbative prediction and the prediction in the traditional case to coincide. On the other hand this would also help to investigate the renormalization of the vector current at small couplings, for which the introduction of massive ensembles at these small couplings would be of interest. Another avenue in this regard is better tuning of the ensembles towards the chiral point. This would facilitate two projects: Determining the renormalization constants of the quark masses would greatly benefit from not needing to worry about sea-quark mass contamination. Also, the renormalization constant Z_{A} could benefit from a separate determination in the chirally rotated Schrödinger functional, for which these ensembles are a prerequisite. The determinations in reference [125] hinted at the possibility that better tuned ensembles are needed. However, the proposed extension alone would still lead to a mixed (rotated valence- and not-rotated sea-) setup.

- **New investigations with updated data** The improvement coefficients for the vector and tensor channels relies on the quantities determined here. A setup for these with exponential Wilson fermions has already been presented in [87]. The determinations of c_{A}, Z_{A} and Z_{V} is need to be completed before carrying out the calculations of these improvement coefficients again. While the determinations of c_{A}, Z_{A} and Z_{V} have progressed furthest of the presented, some work still remains to be done before returning to these issues.

- **Theoretical exploration** In light of the investigation of quark mass renormalization, further theoretical exploration is also needed. While in the case presented here, sea-quark mass effects are the most interesting, other investigations could help the projects presented here as well. In particular, perturbative calculations of the overall renormalization factors $Z_{\mathcal{O}}$ would benefit the presented investigations to a large degree, as was briefly discussed in chapter 7.1.

- **Renormalization of the pseudo-scalar density** Another investigation that needs to be carried out is the renormalization of the pseudo-scalar density (see e.g. [165] for a determination in $N_{\rm f} = 3$ Wilson clover quarks). While the strategy employed follows similar lines as the determination of $Z_{\rm V}$, the scale dependence was the reason this quantity was out of scope for this thesis.

Apart from these relatively immediate follow-up investigations, further physics oriented projects may be pursued with the projects carried out here as a ground layer.

Leptonic decay constants A physically interesting test for some quantities examined here are the leptonic decays of the D-meson. See [52, ch. 7] and references therein (for results relying on Wilson fermions see [162, 166]). As was the case when determining the charm-quark mass, this test would only be valid for the $N_{\rm f} = 3$-symmetric point with the ensembles at hand. However, as a proof of concept for the larger physics program based on OpenLat lattices, this could serve as an entry point for physically relevant quantities. The simulations are close to the ones already carried out for the determination of the charm-quark mass. While a first analysis can already be set up with the data at hand, the provided data would need to be interpolated to the correct charm-quark mass parameter (as was the case in our scaling tests). This is – at the current stage of the determination – an advantage, as the mass parameter has not yet been finalized. However, from an error-budget perspective, further calculations with a finalized charm-quark mass parameter could be valuable. The physics of the leptonic D-meson decay is similar to the pion-decay described in section 3.3, as this decay is mediated by the axial-vector current.

Semi-leptonic decays of the D-meson As already alluded to in section 3.3, the semi-leptonic form factors are of interest for the determination of the factors $V_{\rm cd}$ and $V_{\rm cs}$. A first percent-level determination of $V_{\rm cd}$ on the lattice has been reported by the Fermilab and MILC collaborations in [167] from $N_{\rm f} = 2+1+1$-flavour lattice QCD. Commonly, the semi-leptonic D-meson decay is parametrized by the form factors f_0 and f_+ (cf. equation (3.28b)) which can be determined from the lattice. This involves the evaluation of three-point correlation functions with the appropriate momenta as the lattice pendant to the physical decay. The setup of the decay is as depicted in figure 11.1 We have made first steps towards extracting the form factors along the lines of [106, 168], as the software setup in those references is similar to ours. An approximation of the renormalized matrix element is given in [168, eq. 4] by the ratio

$$R_1^{\mu} = 2\sqrt{\frac{E_i E_f}{D_1}}\sqrt{C_{if}^{\mu}(p_i, p_f)C_{fi}^{\mu}(p_f, p_i)} \approx Z_{\rm V}\langle P_f(p_f)|{\rm V}^{\mu}(q^2)|P_i(p_i)\rangle \tag{11.1}$$

$$D_1 = \frac{C_{ii}^{(2)}(p_i)C_{ff}^{(2)}(p_f)}{\hat{Z}_{\rm V}^{l}\hat{Z}_{\rm V}^{h}}\ , \tag{11.1a}$$

in which P_i and P_f are the pseudo-scalar initial and final state respectively (i.e., the D-meson and the pion), C^{μ} is the three-point function consisting of the initial pseudo-scalar state at t_i, a vector insertion at time t and the final pseudo-scalar state at t_f. $C^{(2)}$ are the two-point functions of the D-meson and the pion. It is non-trivial to see why, for large times, this ratio properly approximates the matrix element on the right-hand side,

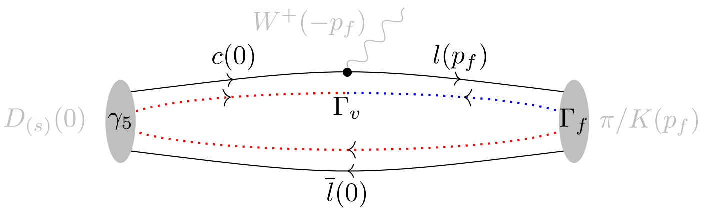

Figure 11.1: Sketch of the semi-leptonic $D_{(\mathrm{s})}$-meson decay (see also figure 3.1). In the present setup, the D-meson is at rest, such that the final state meson π/K and the W^+-boson have opposite momenta. The spectator quark does not carry momentum, while the light quark from the interaction is projected to the full momentum of the final state. The dotted red and blue lines show the „path" the calculations take, i.e., the final state is the source, from which the spectator quark is projected onto the initial state. The charm-quark is then produced at this sequential source and the vector boson is the sink.

as all exponentials in the correlators have to cancel. In the concrete setup pursued in our research program, the calculations are carried out as follows (cf. figure 11.1):

- For our convenience, the D-meson is left at rest ($p_i = 0$). As the charm-quark is heavier than the light quarks involved, this does not dramatically change the dynamics of the system, as the energy threshold of the decay is fulfilled nevertheless.
- As discussed in section 3, the W-boson vertex of the decay is equivalent to a vector current insertion V_μ^a at some time t with momentum q.
- As momentum conservation needs to be fulfilled and $p_i = 0$, $p_i = q + p_f$ is equivalent to $q = -p_f$.
- The spectator quark does not carry any momentum, the light quark coming from the interaction is the sole momentum carrier $l(p_f)$ in the resulting pion.

This project will also be carried out on the large volume ensembles that we introduced in chapter 9, still at the $N_\mathrm{f} = 3$-symmetric point. In general, various methods can be used to calculate the 3-point functions, which are discussed in [169] in terms of computational cost and accuracy. Of the methods described in the reference, we employ the sequential source strategy. This setup was extensively examined in [106] with domain wall fermions. The idea of the sequential solver method is illustrated in figure 3.1 with the dotted lines. In the case pursued, the spectator quark $\bar{l}(0)$ is produced from a source with Dirac-structure Γ_f at the final state. Its propagator is constructed and projected on the initial state. This is then employed as a source for the charm-quark c(0). From the source at the final state, another light-propagator $l(p_f)$ is produced with an attached momentum p_f. Finally, a vector insertion is placed at time t which carries momentum $-p_f$, as to adhere to momentum conservation. The great advantage of this setup is that, thanks to the software, multiple Dirac structures can be embedded at the source (final state) and sink (interaction point) without recalculating the propagators. Furthermore, as the light-quark is the one projected from the final to the initial state, the most cost intensive part of the calculation does not need to be carried out multiple times in one setting. This is particularly practical in the case that multiple charm-quark masses and pion momenta are to be covered. As a first step, we have implemented an appropriate workflow for the calculation on top of `Hadrons` [159] and successfully tested the energy-momentum relation for the pion correlation functions (C_{ff}) with various momenta p_f.

Chapter 12

Conclusion

In this thesis, we have worked on implementing improvement and renormalization for stabilized Wilson clover fermions, with the goal of investigating charm-physics in this framework. The basis for our investigations were two sets of ensembles, one with Schrödinger functional and one with periodic boundary conditions.

We have seen that the Schrödinger functional allowed us to determine a variety of quantities in regard to the improvement and renormalization of the axial-vector current, the vector current and the quark mass. While many challenges in regard to proper definitions of the investigated quantities were overcome, some adjustments are yet to be carried out.

A main concern was the determination of the improvement of the axial-vector current c_{A}. We were able to not only determine this at the chiral limit, but also to define it on a second line of constant physics, at the $N_{\mathrm{f}} = 3$-symmetric point, for which we investigated the quark mass dependency of the improvement constant. This investigation was carried out on a large set of ensembles, including six lattice spacings with masses at and between the two lines of constant physics.

Apart from the improvement, we have investigated various renormalization factors. In particular, we have seen that renormalization of the axial-vector current shows strong sea-quark mass effects, especially when considering disconnected contributions to the correlation functions involved. These effects need further investigation, as they are not present in similar studies carried out in the traditional Wilson clover framework. However, considering only connected contributions, a definition of this factor similar to the ones in the literature was found.

The renormalization of the vector channel, relying on simpler Ward identities, was determined reliably. We were also able to map out the valence- and sea-quark mass dependence of the renormalization. Considerations, for example in regard to the systematic error, are however yet to be inspected.

The renormalization of the quark mass on the other hand showed that, also methodically, there is still work to do for further renormalization of the stabilized Wilson framework. While a few solutions to the problems we faced in this regard were proposed, their thorough investigation will be time-consuming. From an analytical perspective, a project in this direction may have potential, especially in regard to the better understanding of sea-quark mass terms affecting the estimators that were used in the presented project. Investigation of these would not only benefit the project at hand, but may also push the boundaries on determinations of quantities involved in the renormalization of the quark mass by similar means.

By comparison to the traditional Wilson clover case, we can furthermore report that the quantities investigated indeed show lesser cut-off effects than the traditional case at the same lattice spacing. While this was suspected early on in the investigation of stabilized Wilson fermions, it is nevertheless reassuring that we can indeed confirm this suspicion for these technical quantities. Whether this suspicion also holds for physical observables is yet to be seen.

Apart from improvement and renormalization, we have also facilitated the investigation of charm-physics in the framework of stabilized Wilson clover fermions by providing a first determination of the charm-quark mass. Clearly, the determination itself would benefit from higher statistics. As we have seen, first scaling tests need further investigation, however for the limited statistics available they turned out well.

Overall, with this work we have opened the door for various projects in the framework of stabilized Wilson fermions. These include the investigation of quantities linked to charmed mesons, such their decay constants, but also other quantities relying on decays mediated by the axial-vector and vector current benefit from the presented work. We have seen within the investigated quantities, that we can confirm this approach to have smaller cut-off effects compared to the traditional approach. Quantities directly related to flavour physics should be investigated as soon as possible as to see if this statement holds for these as well.

Appendix A

The continuum approach of c_{A}

The improvement of the axial-vector current we have discussed in section 6.1 ended with the discussion of the interpolation of $c_{\mathrm{A}}(g_0^2)$. The final interpolation cited relies on the 1-loop perturbation-theory result

$$c_{\mathrm{A}} = -0.00603(3)g_0^2 + \mathrm{O}(g_0^4) \tag{A.1}$$

as found in [93, app. C].

Employing the ensembles `M` introduced in table 5.2, the value at infinite volume of $c_{\mathrm{A}}(g_0^2 = 0.7)$ was roughly estimated, by extrapolating the values from table A.1 in $(a/L)^2$ with fixed gauge coupling, which is shown in figure A.1. The plateau ranges employed are farther in the lattice than usual, at $x_0 = [0.25, 0.50]T$. We find $c_{\mathrm{A}}/g_0^2 = -0.00955(30)$ in the infinite volume limit. However, as the volume dependence is unclear and a fit linear in a/L, a value greater zero is reached, we conclude that this value, while not being the 1-loop value expected is close enough to further rely on the 1-loop value from [93].

Table A.1: Table of the results for c_A on the three ensembles in the perturbative regime with $\beta = 8.57$.

L	16	24	32
c_A	-0.02430(30)	-0.014768(58)	-0.01081(17)

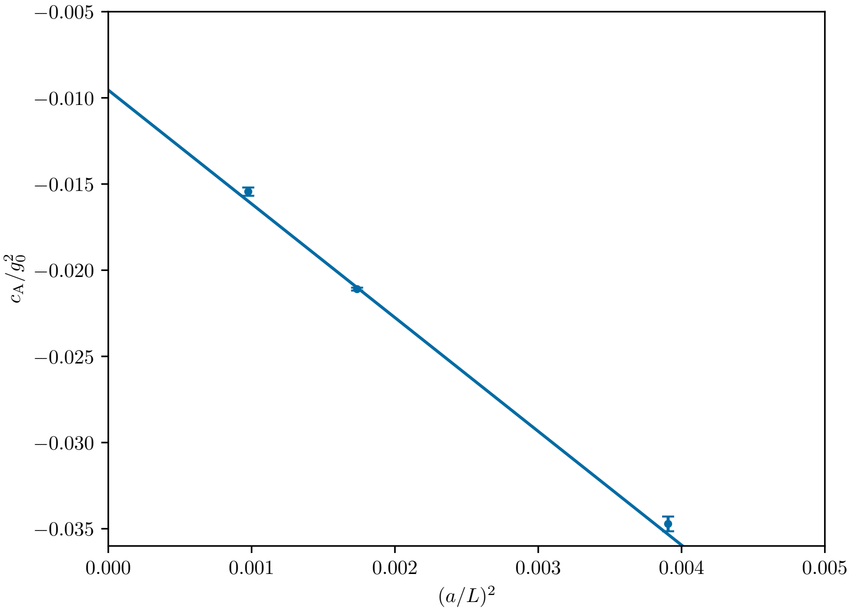

Figure A.1: Extrapolation of c_A on $(a/L)^2$, approaching infinite volume.

Appendix B

Discretization

B.1 Derivatives

While the discretization of derivatives is well known, the following equations have been gathered here for reference. The naming scheme is the same as the one in `pyerrors` [170]. In the package, definitions of the derivatives are as follows: The forward derivative is defined as

$$\partial f(x) \to \partial_f f(x) = \frac{f(x+a) - f(x)}{a} + \mathrm{O}(a)\ , \tag{B.1}$$

the backward derivative as

$$\partial f(x) \to \partial_b f(x) = \frac{f(x) - f(x-a)}{a} + \mathrm{O}(a)\ , \tag{B.2}$$

we call

$$\partial f(x) \to \partial_s f(x) = \frac{1}{2}(\partial_f + \partial_b) f(x) = \frac{f(x+a) - f(x-a)}{2a} + \mathrm{O}(a^2) \tag{B.3}$$

the symmetric derivative. The (Richardson-extrapolated), improved derivative is defined as

$$\partial f(x) \to \partial_i f(x) = \frac{f(x-2a) - 8f(x-a) + 8f(x+a) - f(x+2a)}{12a} + \mathrm{O}(a^4)\ . \tag{B.4}$$

The logarithmic derivative is defined as

$$\partial f(x) \to \partial_{\log} f(x) = \frac{f(x)\ln(f(x))}{h} \tag{B.5}$$

Similarly, the second derivative may be discretized in one the of following ways: The combination of the forward and backward derivative

$$\partial^2 f(x) \to \partial_s^2 f(x) = (\partial_f \partial_b) f(x) = \frac{f(x+a) - 2f(x) + f(x-a)}{a^2} \tag{B.6}$$

the combination of two symmetric derivatives

$$\partial^2 f(x) \to \partial_{ls}^2 f(x) = (\partial_s \partial_s) f(x) = \frac{f(x+2a) - 2f(x) + f(x-2a)}{4a^2} \tag{B.7}$$

which we call the large stencil second derivative. The improved second derivative is defined as

$$\partial^2 f(x) \to \partial_i^2 f(x) = \frac{-f(x+2a) + 16f(x+a) - 30f(x) + 16f(x-a) - f(x-2a)}{12a^2}\ . \tag{B.8}$$

B.2 Integration

Numerical integration is also well known. However, also for this we note the following definitions for quick reference: In these definitions, we suppose we want to integrate over a range $[p, q]$ with n points $x_n \in [p, q]$ at which we know the function $f(x)$. We identify $p = x_0$ and $q = x_n$. While a simple sum

$$\int_p^q f(x) \to \frac{1}{a} \sum_{i=0}^{n} f(x_i) \tag{B.9}$$

is the easiest way to integrate over some range, this approximation overestimates the influence of the outermost points. The trapezoidal rule weighs them accordingly:

$$\int_p^q f(x) \to \frac{1}{2a} \left(f(x_0) + f(x_n) \right) + \frac{1}{a} \sum_{i=1}^{n-1} f(x_i) \tag{B.10}$$

Appendix C

Correlation functions in the Schrödinger functional

For quick reference, the correlation functions that are of use for this thesis, that we use in the Schrödinger functional are listed here, according to the SFCF documentation [127, 171]. We begin with the two-point functions,

$$f_P = -\frac{1}{2}\frac{a^9}{V_3}\sum_{\vec{x}\vec{y}\vec{z}} \left\langle \bar{\psi}_2(x)\gamma_5\psi_1(x)\cdot\bar{\zeta}_1(\vec{y})\gamma_5\zeta_2(\vec{z})\right\rangle_{\mathrm{F}} \ , \tag{C.1}$$

$$g_P = -\frac{1}{2}\frac{a^9}{V_3}\sum_{\vec{x}\vec{y}\vec{z}} \left\langle \bar{\psi}_2(x)\gamma_5\psi_1(x)\cdot\bar{\zeta}'_1(\vec{y})\gamma_5\zeta'_2(\vec{z})\right\rangle_{\mathrm{F}} \ , \tag{C.2}$$

$$f_{A_0} = -\frac{1}{2}\frac{a^9}{V_3}\sum_{\vec{x}\vec{y}\vec{z}} \left\langle \bar{\psi}_2(x)\gamma_0\gamma_5\psi_1(x)\cdot\bar{\zeta}_1(\vec{y})\gamma_5\zeta_2(\vec{z})\right\rangle_{\mathrm{F}} \ , \tag{C.3}$$

$$g_{A_0} = +\frac{1}{2}\frac{a^9}{V_3}\sum_{\vec{x}\vec{y}\vec{z}} \left\langle \bar{\psi}_2(x)\gamma_0\gamma_5\psi_1(x)\cdot\bar{\zeta}'_1(\vec{y})\gamma_5\zeta'_2(\vec{z})\right\rangle_{\mathrm{F}} \ , \tag{C.4}$$

which are – each – the contraction of a pseudo-scalar source and the pseudo-scalar or axial current in the bulk. f and g are related through time inversion. The boundary-to-boundary correlators in the pseudo-scalar and vector channel are defined as

$$F_1 = -\frac{1}{2}\frac{a^{12}}{V_3^2}\sum_{\vec{u}\vec{v}\vec{y}\vec{z}} \left\langle \bar{\zeta}'_2(\vec{u})\gamma_5\zeta'_1(\vec{v})\cdot\bar{\zeta}_1(\vec{y})\gamma_5\zeta_2(\vec{z})\right\rangle_{\mathrm{F}} \ , \tag{C.5}$$

$$K_1 = -\frac{1}{6}\frac{a^{12}}{V_3^2}\sum_{\vec{u}\vec{v}\vec{y}\vec{z}k} \left\langle \bar{\zeta}'_2(\vec{u})\gamma_k\zeta'_1(\vec{v})\cdot\bar{\zeta}_1(\vec{y})\gamma_k\zeta_2(\vec{z})\right\rangle_{\mathrm{F}} \ , \tag{C.6}$$

For the determination of Z_{V} in chapter 7.1, we also need the three-point function

$$F_{\mathrm{V}_0} = -\frac{1}{2}\frac{a^{15}}{V_3^2}\sum_{\vec{u}\vec{v}\vec{x}\vec{y}\vec{z}} \left\langle \bar{\zeta}'_{1'}(\vec{u})\gamma_5\zeta'_1(\vec{v})\cdot\bar{\psi}_1(x)\gamma_0\psi_2(x)\cdot\bar{\zeta}_2(\vec{y})\gamma_5\zeta_{1'}(\vec{z})\right\rangle_{\mathrm{F}} \ . \tag{C.7}$$

Furthermore, we have introduced 4-point functions for the determination of Z_{A}, which have to following connected contributions:

$$F^{a}_{\mathrm{A_0A_0}} = -\frac{a^{18}}{4\cdot 2V_3^2}\sum_{\vec{x}\vec{y}\vec{v}\vec{u}\vec{w}\vec{z}} \left\langle \zeta_2'(\vec{u})\gamma_5\zeta_1'(\vec{v})\cdot\bar{\psi}_2(y)\gamma_0\gamma_5\psi_{2'}(y)\cdot\bar{\psi}_{2'}(x)\gamma_0\gamma_5\psi_2(x)\cdot\zeta_2(\vec{w})\gamma_5\zeta_1(\vec{z})\right\rangle_{\mathrm{F}} \ , \tag{C.8}$$

$$F^{d}_{\mathrm{A_0A_0}} = -\frac{a^{18}}{4\cdot 2V_3^2}\sum_{\vec{x}\vec{y}\vec{v}\vec{u}\vec{w}\vec{z}} \left\langle \zeta_2'(\vec{u})\gamma_5\zeta_1'(\vec{v})\cdot\bar{\psi}_2(x)\gamma_0\gamma_5\psi_{2'}(x)\cdot\bar{\psi}_{2'}(y)\gamma_0\gamma_5\psi_2(y)\cdot\zeta_2(\vec{w})\gamma_5\zeta_1(\vec{z})\right\rangle_{\mathrm{F}} \ , \tag{C.9}$$

$$F^{a}_{\mathrm{A_0\partial P}} = -\frac{a^{18}}{4\cdot 2V_3^2}\sum_{\vec{x}\vec{y}\vec{v}\vec{u}\vec{w}\vec{z}} \tilde{\partial}_{y_0}\left\langle \zeta_2'(\vec{u})\gamma_5\zeta_1'(\vec{v})\cdot\bar{\psi}_2(y)\gamma_5\psi_{2'}(y)\cdot\bar{\psi}_{2'}(x)\gamma_0\gamma_5\psi_2(x)\cdot\zeta_2(\vec{w})\gamma_5\zeta_1(\vec{z})\right\rangle_{\mathrm{F}} \ , \tag{C.10}$$

$$F^{d}_{\mathrm{A_0\partial P}} = -\frac{a^{18}}{4\cdot 2V_3^2}\sum_{\vec{x}\vec{y}\vec{v}\vec{u}\vec{w}\vec{z}} \tilde{\partial}_{y_0}\left\langle \zeta_2'(\vec{u})\gamma_5\zeta_1'(\vec{v})\cdot\bar{\psi}_2(x)\gamma_0\gamma_5\psi_{2'}(x)\cdot\bar{\psi}_{2'}(y)\gamma_5\psi_2(y)\cdot\zeta_2(\vec{w})\gamma_5\zeta_1(\vec{z})\right\rangle_{\mathrm{F}} \ , \tag{C.11}$$

$$F^{a}_{\mathrm{\partial PA_0}} = -\frac{a^{18}}{4\cdot 2V_3^2}\sum_{\vec{x}\vec{y}\vec{v}\vec{u}\vec{w}\vec{z}} \tilde{\partial}_{x_0}\left\langle \zeta_2'(\vec{u})\gamma_5\zeta_1'(\vec{v})\cdot\bar{\psi}_2(y)\gamma_0\gamma_5\psi_{2'}(y)\cdot\bar{\psi}_{2'}(x)\gamma_5\psi_2(x)\cdot\zeta_1(\vec{w})\gamma_5\zeta_2(\vec{z})\right\rangle_{\mathrm{F}} \ , \tag{C.12}$$

$$F^{d}_{\mathrm{\partial PA_0}} = -\frac{a^{18}}{4\cdot 2V_3^2}\sum_{\vec{x}\vec{y}\vec{v}\vec{u}\vec{w}\vec{z}} \tilde{\partial}_{x_0}\left\langle \zeta_2'(\vec{u})\gamma_5\zeta_1'(\vec{v})\cdot\bar{\psi}_2(x)\gamma_5\psi_{2'}(x)\cdot\bar{\psi}_{2'}(y)\gamma_0\gamma_5\psi_2(y)\cdot\zeta_1(\vec{w})\gamma_5\zeta_2(\vec{z})\right\rangle_{\mathrm{F}} \ , \tag{C.13}$$

$$F^{a}_{\mathrm{\partial P\partial P}} = -\frac{a^{18}}{4\cdot 2V_3^2}\sum_{\vec{x}\vec{y}\vec{v}\vec{u}\vec{w}\vec{z}} \tilde{\partial}_{x_0}\tilde{\partial}y_0\left\langle \zeta_2'(\vec{u})\gamma_5\zeta_1'(\vec{v})\cdot\bar{\psi}_2(y)\gamma_5\psi_{2'}(y)\cdot\bar{\psi}_{2'}(x)\gamma_5\psi_2(x)\cdot\zeta_1(\vec{w})\gamma_5\zeta_2(\vec{z})\right\rangle_{\mathrm{F}} \ , \tag{C.14}$$

$$F^{d}_{\mathrm{\partial P\partial P}} = -\frac{a^{18}}{4\cdot 2V_3^2}\sum_{\vec{x}\vec{y}\vec{v}\vec{u}\vec{w}\vec{z}} \tilde{\partial}_{x_0}\tilde{\partial}_{y_0}\left\langle \zeta_2'(\vec{u})\gamma_5\zeta_1'(\vec{v})\cdot\bar{\psi}_2(x)\gamma_5\psi_{2'}(x)\cdot\bar{\psi}_{2'}(y)\gamma_5\psi_2(y)\cdot\zeta_1(\vec{w})\gamma_5\zeta_2(\vec{z})\right\rangle_{\mathrm{F}} \ , \tag{C.15}$$

$$\tilde{F}^{a}_{\mathrm{PA_0}} = -\frac{a^{18}}{4\cdot 2V_3^2}\sum_{q_0=x_0}^{y_0}\sum_{\vec{q}\vec{y}\vec{v}\vec{u}\vec{w}\vec{z}} \left\langle \zeta_2'(\vec{u})\gamma_5\zeta_1'(\vec{v})\cdot\bar{\psi}_2(y)\gamma_0\gamma_5\psi_{2'}(y)\cdot\bar{\psi}_{2'}(q)\gamma_5\psi_2(q)\cdot\zeta_1(\vec{w})\gamma_5\zeta_2(\vec{z})\right\rangle_{\mathrm{F}} \ , \tag{C.16}$$

$$\tilde{F}^{d}_{\mathrm{PA_0}} = -\frac{a^{18}}{4\cdot 2V_3^2}\sum_{q_0=x_0}^{y_0}\sum_{\vec{q}\vec{y}\vec{v}\vec{u}\vec{w}\vec{z}} \left\langle \zeta_2'(\vec{u})\gamma_5\zeta_1'(\vec{v})\cdot\bar{\psi}_2(q)\gamma_5\psi_{2'}(q)\cdot\bar{\psi}_{2'}(y)\gamma_0\gamma_5\psi_2(y)\cdot\zeta_1(\vec{w})\gamma_5\zeta_2(\vec{z})\right\rangle_{\mathrm{F}} \ , \tag{C.17}$$

$$\tilde{F}^{a}_{\mathrm{P\partial P}} = -\frac{a^{18}}{4\cdot 2V_3^2}\sum_{q_0=x_0}^{y_0}\sum_{\vec{q}\vec{y}\vec{v}\vec{u}\vec{w}\vec{z}} \tilde{\partial}_{y_0}\left\langle \zeta_2'(\vec{u})\gamma_5\zeta_1'(\vec{v})\cdot\bar{\psi}_2(y)\gamma_5\psi_{2'}(y)\cdot\bar{\psi}_{2'}(q)\gamma_5\psi_2(q)\cdot\zeta_1(\vec{w})\gamma_5\zeta_2(\vec{z})\right\rangle_{\mathrm{F}} \ , \tag{C.18}$$

$$\tilde{F}^{d}_{\mathrm{P\partial P}} = -\frac{a^{18}}{4\cdot 2V_3^2}\sum_{q_0=x_0}^{y_0}\sum_{\vec{q}\vec{y}\vec{v}\vec{u}\vec{w}\vec{z}} \tilde{\partial}_{y_0}\left\langle \zeta_2'(\vec{u})\gamma_5\zeta_1'(\vec{v})\cdot\bar{\psi}_2(q)\gamma_5\psi_{2'}(q)\cdot\bar{\psi}_{2'}(y)\gamma_5\psi_2(y)\cdot\zeta_1(\vec{w})\gamma_5\zeta_2(\vec{z})\right\rangle_{\mathrm{F}} \ . \tag{C.19}$$

Acknowledgements

I would like to thank a few people, without whom this thesis would not have been possible.

First and foremost, I would like to thank Jochen Heitger and Patrick Fritzsch for the excellent supervision of my path in lattice QCD, the endless hours of helpful discussions on Fridays at noon that contributed to my understanding of lattice QCD and for their help in various organizational issues.

Furthermore, I would like to thank my colleagues, especially Jan-Philip Neuendorf, Pia Leonie Jones Petrak, Fabian Joswig and Simon Kuberski for their open ears and helpful input in all detail questions.

For proofreading, I would like to thank Jan-Philip Neuendorf, Katrin Greve, Richard von Eckardstein, Tobias Schröder, my sister, Maria Kuhlmann and Johannes Pirsch. They have read various pieces of the text each gave valuable and extensive feedback that this thesis needed.

I would like to thank my colleagues from the PALMA-team for the opportunity to work alongside them and them having my back in the last months of my PhD, when writing took most of my time. Also, I would like to thank them for the excellent management of the cluster that most of my calculations ran on.

I am also indebted to three people, Jonathan Spelsberg, Johannes Pirsch and Philipp Schulte, who accompanied me through my entire studies in Münster and who made especially my first semesters much more bearable.

Also, I would like to thank my parents for all their support and guidance during my studies and my PhD.

Finally, I would like to thank my girlfriend, Camille Delanes, for her love, her understanding when I „just had to look up one thing“ in the evening and for looking out for me, especially in the last months before the submission of this work.

Bibliography

[1] D. J. Griffiths, *Introduction to Elementary Particles.* Physics Textbook. Wiley-VCH, Weinheim, 2., rev. ed., 5. reprint ed., 2011.

[2] T. Aoyama et al., *The anomalous magnetic moment of the muon in the Standard Model*, *Physics Reports* **887** (Dec., 2020) 1–166, [`2006.04822`].

[3] R. Aliberti et al., *The anomalous magnetic moment of the muon in the Standard Model: An update*, June, 2025.

[4] **Muon** $g-2$ Collaboration, G. W. Bennett et al., *Final Report of the Muon E821 Anomalous Magnetic Moment Measurement at BNL*, *Physical Review D* **73** (Apr., 2006) 072003, [`hep-ex/0602035`].

[5] B. Abi et al., *Measurement of the Positive Muon Anomalous Magnetic Moment to 0.46 ppm*, *Physical Review Letters* **126** (Apr., 2021) 141801, [`2104.03281`].

[6] **The Muon** $g-2$ Collaboration, D. P. Aguillard et al., *Measurement of the Positive Muon Anomalous Magnetic Moment to 0.20 ppm*, *Physical Review Letters* **131** (Oct., 2023) 161802, [`2308.06230`].

[7] **The Muon** $g-2$ Collaboration, D. P. Aguillard et al, *Measurement of the Positive Muon Anomalous Magnetic Moment to 127 ppb*, June, 2025.

[8] **The Muon** $g-2$ Collaboration, D. P. Aguillard et al., *Detailed Report on the Measurement of the Positive Muon Anomalous Magnetic Moment to 0.20 ppm*, May, 2024.

[9] T. Albahri et al., *Measurement of the anomalous precession frequency of the muon in the Fermilab Muon g-2 experiment*, *Physical Review D* **103** (Apr., 2021) 072002, [`2104.03247`].

[10] T. Albahri et al., *Magnetic Field Measurement and Analysis for the Muon g-2 Experiment at Fermilab*, *Physical Review A* **103** (Apr., 2021) 042208, [`2104.03201`].

[11] T. Albahri et al., *Beam dynamics corrections to the Run-1 measurement of the muon anomalous magnetic moment at Fermilab*, *Physical Review Accelerators and Beams* **24** (Apr., 2021) 044002, [`2104.03240`].

[12] **KATRIN** Collaboration, M. Aker et al., *Direct neutrino-mass measurement based on 259 days of KATRIN data*, *Science* **388** (Apr., 2025) 180–185.

[13] **Belle, Belle II** Collaboration, I. Adachi et al., *Measurement of the $D^0 \to K^- \pi^+ e^+ e^-$ branching fraction and search for $D^0 \to \pi^+\pi^- e^+ e^-$ and $D^0 \to K^+ K^- e^+ e^-$ decays at Belle*, July, 2025.

[14] **Belle II** Collaboration, M. Abumusabh et al., *Search for* $e^+e^- \to \gamma\chi_{bJ}$ *(*$J = 0, 1, 2$*) near* $\sqrt{s} = 10.746$ *GeV at Belle II*, Aug., 2025.

[15] **BESIII** Collaboration, M. Ablikim et al., *First Measurement of the Decay Dynamics in the Semileptonic Transition of* $D^+(0)$ *into the axial-vector meson* $K^1(1270)$, *Physical Review Letters* **135** (Aug., 2025) 091801.

[16] **BESIII** Collaboration, M. Ablikim et al., *Search for* $\chi_{c1} \to \pi^+\pi^-\eta_c$ *via* $\psi(3686) \to \gamma\chi_{c1}$, Aug., 2025.

[17] **BESIII** Collaboration, M. Ablikim et al., *Precise Measurement of Chromo-Electric Dipole Moment of the Charm Quark*, July, 2025.

[18] J. K. Ahn et al., *Proposal of the KOTO II experiment*, Jan., 2025.

[19] **ATLAS, Belle II, C.M.S., LHCb** Collaboration, *Projections for Key Measurements in Heavy Flavour Physics*, Apr., 2025.

[20] **XENON** Collaboration, E. Aprile et al., *The XENONnT dark matter experiment*, *The European Physical Journal C* **84** (Aug., 2024) 784.

[21] CERN Yellow Reports: Monographs, *CERN Yellow Reports: Monographs, Vol. 10 (2020): High-Luminosity Large Hadron Collider (HL-LHC): Technical design report*, Dec., 2020.

[22] W. Bartmann, J.-P. Burnet, C. Carli, A. Chance, P. Craievich, M. Giovannozzi, C. Grojean, J. Gutleber, K. Hanke, A. Henriques, P. Janot, C. Lourenco, M. Mangano, T. Otto, J. H. Poole, S. Rajagopalan, T. Raubenheimer, E. Todesco, T. P. Watson, and G. Wilkinson, *Future Circular Collider Feasibility Study Report Volume 1: Physics and Experiments*, tech. rep., CERN Document Server, 2025.

[23] M. Benedikt, W. Bartmann, J.-P. Burnet, C. Carli, A. Chance, P. Craievich, M. Giovannozzi, C. Grojean, J. Gutleber, K. Hanke, A. Henriques, P. Janot, C. Lourenco, M. Mangano, T. Otto, J. H. Poole, S. Rajagopalan, T. Raubenheimer, E. Todesco, L. Ulrici, T. P. Watson, G. Wilkinson, and F. Zimmermann, *Future Circular Collider Feasibility Study Report Volume 2: Accelerators, technical infrastructure and safety*, tech. rep., CERN Document Server, 2025.

[24] J. Gutleber, L. Ulrici, and T. P. Watson, *Future Circular Collider Feasibility Study Report Volume 3: Civil Engineering, Implementation and Sustainability*, tech. rep., CERN Document Server, 2025.

[25] C. Gattringer and C. B. Lang, *Quantum Chromodynamics on the Lattice*, vol. 788 of *Lect. Notes Phys.* Springer, Berlin, 2010.

[26] I. Montvay and G. Münster, *Quantum Fields on a Lattice.* Cambridge Monographs on Mathematical Physics. Cambridge University Press, Mar., 1997.

[27] F. Knechtli, M. Günther, and M. Peardon, *Lattice Quantum Chromodynamics: Practical Essentials.* SpringerBriefs in Physics. Springer, 2017.

[28] F. Joswig, *Renormalisation and Improvement of Quark Bilinears with Applications to Charm Physics in Lattice QCD.* PhD thesis, Westfälische Wilhelms Universität Münster, 2021.

[29] S. Kuberski, *Standard Model Parameters in the Heavy Quark Sector from Three-Flavor Lattice QCD*. PhD thesis, Westfälische Wilhelms Universität Münster, 2020.

[30] J. Neuendorf, *Optimized Interpolators and Partially Twisted Boundary Conditions for Charm-Physics on the Lattice*. PhD thesis, Universität Münster.

[31] C. Wittemeier, *Non-Perturbative Renormalisation and Improvement of the Isovector Axial Current In three-Flavor Lattice QCD with Wilson Fermions*. PhD thesis, Westfälische Wilhelms Universität Münster, 2018.

[32] G. Münster and M. Walzl, *Lattice gauge theory: A short primer*, in *Zuoz Summer School on Phenomenology of Gauge Interactions*, no. MS-TPI-00-11, 2000. `hep-lat/0012005`.

[33] V. E. Barnes, P. L. Connolly, D. J. Crennell, B. B. Culwick, W. C. Delaney, W. B. Fowler, P. E. Hagerty, E. L. Hart, N. Horwitz, P. V. C. Hough, J. E. Jensen, J. K. Kopp, K. W. Lai, J. Leitner, J. L. Lloyd, G. W. London, T. W. Morris, Y. Oren, R. B. Palmer, A. G. Prodell, D. Radojičić, D. C. Rahm, C. R. Richardson, N. P. Samios, J. R. Sanford, R. P. Shutt, J. R. Smith, D. L. Stonehill, R. C. Strand, A. M. Thorndike, M. S. Webster, W. J. Willis, and S. S. Yamamoto, *Observation of a Hyperon with Strangeness Minus Three*, *Physical Review Letters* **12** (Feb., 1964) 204–206.

[34] O. W. Greenberg, *Spin and Unitary-Spin Independence in a Paraquark Model of Baryons and Mesons*, *Physical Review Letters* **13** (Nov., 1964) 598–602.

[35] **Hadron Spectrum** Collaboration, M. Peardon, J. Bulava, J. Foley, C. Morningstar, J. Dudek, R. G. Edwards, B. Joo, H.-W. Lin, D. G. Richards, and K. J. Juge, *A Novel quark-field creation operator construction for hadronic physics in lattice QCD*, *Phys. Rev. D* **80** (2009) 054506, [`0905.2160`].

[36] F. Joswig, F. Erben, M. T. Hansen, N. P. Lachini, and A. Portelli, *Exploring distillation at the SU(3) flavour symmetric point*, *PoS* **LATTICE2022** (Jan., 2023) 063, [`2211.15627`].

[37] F. Knechtli, T. Korzec, M. Peardon, and J. A. Urrea-Niño, *Optimizing creation operators for charmonium spectroscopy on the lattice*, *Physical Review D: Particles and Fields* **106** (Aug., 2022) 034501, [`2205.11564`].

[38] J. A. Urrea-Niño, J. Finkenrath, R. Höllwieser, F. Knechtli, T. Korzec, and M. Peardon, *Charmonium spectroscopy with optimal distillation profiles*, Jan., 2024.

[39] J. Neuendorf, G. Egbring, J. Heitger, R. Höllwieser, F. Knechtli, T. Korzec, and J. A. Urrea-Niño, *Optimized Distillation Profiles for Heavy-Light Spectroscopy*, `2401.05828`.

[40] P. Lacock, C. Michael, P. Boyle, and P. Rowland, *Orbitally excited and hybrid mesons from the lattice*, *Physical Review D* **54** (Dec., 1996) 6997–7009, [`hep-lat/9605025`].

[41] R. G. Edwards, B. Joó, and H.-W. Lin, *Tuning for Three-flavors of Anisotropic Clover Fermions with Stout-link Smearing*, *Physical Review D* **78** (Sept., 2008) 054501, [`0803.3960`].

[42] G. Aarts, C. Allton, A. Amato, P. Giudice, S. Hands, and J.-I. Skullerud, *Electrical conductivity and charge diffusion in thermal QCD from the lattice*, *Journal of High Energy Physics* **2015** (Feb., 2015) 186, [`1412.6411`].

[43] G. Aarts, C. Allton, J. Glesaaen, S. Hands, B. Jäger, S. Kim, M. P. Lombardo, A. A. Nikolaev, S. M. Ryan, J.-I. Skullerud, and L.-K. Wu, *Properties of the QCD thermal transition with $N_f = 2 + 1$ flavours of Wilson quark*, July, 2020.

[44] G. Aarts, C. Allton, R. Bignell, T. J. Burns, S. C. García-Mascaraque, S. Hands, B. Jäger, S. Kim, S. M. Ryan, and J.-I. Skullerud, *Open charm mesons at nonzero temperature: Results in the hadronic phase from lattice QCD*, Sept., 2022.

[45] R. Bignell, G. Aarts, C. Allton, M. N. Anwar, T. J. Burns, R. H. D'arcy, B. Jäger, S. Kim, M. P. Lombardo, S. Ryan, J.-I. Skullerud, and A. Smecca, *Finite temperature hadronic spectral properties*, May, 2025.

[46] P. Chen, *Heavy Quarks on Anisotropic Lattices: The Charmonium Spectrum*, *Physical Review D* **64** (July, 2001) 034509, [`hep-lat/0006019`].

[47] **CP-PACS** Collaboration, M. Okamoto et al., *Charmonium Spectrum from Quenched Anisotropic Lattice QCD*, *Physical Review D* **65** (Apr., 2002) 094508, [`hep-lat/0112020`].

[48] A. C. Lichtl, *Quantum Operator Design for Lattice Baryon Spectroscopy*, Jan., 2007.

[49] S. Basak, R. G. Edwards, G. T. Fleming, K. J. Juge, A. Lichtl, C. Morningstar, D. G. Richards, I. Sato, and S. J. Wallace, *Lattice QCD determination of patterns of excited baryon states*, *Physical Review D* **76** (Oct., 2007) 074504, [`0709.0008`].

[50] J. J. Dudek, R. G. Edwards, N. Mathur, and D. G. Richards, *Charmonium excited state spectrum in lattice QCD*, *Physical Review D* **77** (Feb., 2008) 034501, [`0707.4162`].

[51] C. J. Morningstar and M. Peardon, *The glueball spectrum from an anisotropic lattice study*, *Physical Review D* **60** (July, 1999) 034509, [`hep-lat/9901004`].

[52] Aoki, Y. et al., *FLAG Review 2024*, `2411.04268`.

[53] I. Campos, P. Fritzsch, M. Hansen, M. K. Marinkovic, A. Patella, A. Ramos, and N. Tantalo, *openQ*D code: A versatile tool for QCD+QED simulations: Collaboration*, *The European Physical Journal C* **80** (Mar., 2020) 195.

[54] P. Boyle, M. D. Carlo, F. Erben, V. Gülpers, M. T. Hansen, T. Harris, N. Hermansson-Truedsson, R. Hodgson, A. Jüttner, F. Ó. hÓgáin, A. Portelli, J. Richings, and A. Z. N. Yong, *Isospin-breaking corrections to light-meson leptonic decays from lattice simulations at physical quark masses*, `2211.12865`.

[55] L. Bushnaq, I. Campos, M. Catillo, A. Cotellucci, M. Dale, P. Fritzsch, J. Lücke, M. K. Marinković, A. Patella, and N. Tantalo, *First results on QCD+QED with C* boundary conditions*, *Journal of High Energy Physics* **2023** (Mar., 2023) 12.

[56] A. Altherr, I. Campos, J. Coles, A. Cotellucci, J. A. Fernández De La Garza, R. Gruber, T. Harris, J. Komijani, J. Lücke, S. Maier, M. Marinkovic, L. Parato, A. Patella, S. Rosso, P. Tavella, and H. Vogt, *O(a)-improved QCD+QED Wilson Dirac operator on GPUs*, in *Proceedings of The 41st International Symposium on*

Lattice Field Theory — PoS(LATTICE2024), (Liverpool, UK), p. 280, Sissa Medialab, Feb., 2025.

[57] M. D. Carlo, M. T. Hansen, N. Hermansson-Truedsson, and A. Portelli, *QED_r: A finite-volume qed action with redistributed spatial zero-momentum modes*, Jan., 2025.

[58] A. Altherr, I. Campos, A. Cotellucci, R. Gruber, T. Harris, J. Komijani, F. Margari, M. K. Marinkovic, L. Parato, A. Patella, S. Rosso, N. Tantalo, and P. Tavella, *Comparing QCD+QED via full simulation versus the RM123 method: U-spin window contribution to a_μ^{HVP}*, June, 2025.

[59] U. Husemann, *Top-Quark Physics: Status and Prospects*, *Progress in Particle and Nuclear Physics* **95** (July, 2017) 48–97, [`1704.01356`].

[60] J. Heitger and R. Sommer, *A strategy to compute the b-quark mass with non-perturbative accuracy*, *Nuclear Physics B - Proceedings Supplements* **106–107** (Mar., 2002) 358–360, [`hep-lat/0110016`].

[61] D. Guazzini, R. Sommer, and N. Tantalo, *Precision for B-meson matrix elements*, *Journal of High Energy Physics* **2008** (Jan., 2008) 076–076, [`0710.2229`].

[62] A. Conigli, J. Frison, P. Fritzsch, A. Gérardin, J. Heitger, G. Herdoiza, S. Kuberski, C. Pena, and H. Simma, *B-physics observables in the continuum from a combination of static and relativistic results*, in *Proceedings of European Network for Particle Physics, Lattice Field Theory and Extreme Computing — PoS(EuroPLEx2023)*, (Berlin, Germany), p. 005, Sissa Medialab, June, 2024.

[63] S. Cali, K. Eckert, J. Heitger, F. Knechtli, and T. Korzec, *Charm sea effects on charmonium decay constants and heavy meson masses*, *The European Physical Journal C: Particles and Fields* **81** (Aug., 2021) 733, [`2105.12278`].

[64] **Particle Data Group** Collaboration, Navas, S. et al., *Review of Particle Physics*, *Physical Review D* **110** (Aug., 2024) 030001.

[65] K. G. Wilson, *Confinement of quarks*, *Physical Review D: Particles and Fields* **10** (1974), no. 8 2445–2459.

[66] K. Symanzik, *Some topics in quantum field theory*, in *6th International Conference on Mathematical Physics - Congress of Association for Mathematical Physics*, no. DESY-81-068, C81-08-11-4, p. 47, 1981.

[67] P. Weisz, *Continuum limit improved lattice action for pure Yang-Mills theory (I)*, *Nuclear Physics B* **212** (Feb., 1983) 1–17.

[68] G. Curci, P. Menotti, and G. Paffuti, *Symanzik's improved lagrangian for lattice gauge theory*, *Physics Letters B* **130** (Oct., 1983) 205–208.

[69] M. Lüscher and P. Weisz, *On-shell improved lattice gauge theories*, *Communications in Mathematical Physics* **97** (Mar., 1985) 59–77.

[70] Y. Iwasaki, *Renormalization Group Analysis of Lattice Theories and Improved Lattice Action. II – four-dimensional non-abelian SU(N) gauge model*, Nov., 2011.

[71] T. DeGrand, A. Hasenfratz, P. Hasenfratz, and F. Niedermayer, *Fixed point actions for SU(3) gauge theory*, *Physics Letters B* **365** (Jan., 1996) 233–238.

[72] P. Hasenfratz and F. Niedermayer, *Fixed-point actions in 1-loop perturbation theory*, *Nuclear Physics B* **507** (Dec., 1997) 399–415.

[73] P. Hasenfratz, *Prospects for perfect actions*, *Nuclear Physics B - Proceedings Supplements* **63** (Apr., 1998) 53–58.

[74] U. Wenger, K. Holland, A. Ipp, and D. I. Müller, *HMC and gradient flow with machine-learned classically perfect fixed point actions*, in *Proceedings of The 41st International Symposium on Lattice Field Theory — PoS(LATTICE2024)*, (Liverpool, UK), p. 466, Sissa Medialab, Feb., 2025.

[75] K. Holland, A. Ipp, D. I. Müller, and U. Wenger, *Machine-learned RG-improved gauge actions and classically perfect gradient flows*, Apr., 2025.

[76] B. Sheikholeslami and R. Wohlert, *Improved continuum limit lattice action for QCD with Wilson fermions*, *Nuclear Physics B* **259** (1985), no. 4 572.

[77] M. Lüscher, S. Sint, R. Sommer, and P. Weisz, *Chiral symmetry and O(a) improvement in lattice QCD*, *Nuclear Physics B* **478** (1996) 365–400, [`hep-lat/9605038`].

[78] M. Lüscher, S. Sint, R. Sommer, P. Weisz, and U. Wolff, *Non-perturbative O(a) improvement of lattice QCD*, *Nuclear Physics B* **491** (1997) 323–343, [`hep-lat/9609035`].

[79] K. Jansen and R. Sommer, *O(a) improvement of lattice QCD with two flavors of Wilson quarks*, *Nuclear Physics B* **530** (Oct., 1998) 185–203, [`hep-lat/9803017`].

[80] **CP-PACS, JLQCD** Collaboration, N. Yamada et al., *Non-perturbative O(a)-improvement of Wilson quark action in three-flavor QCD with plaquette gauge action*, *Physical Review D* **71** (Mar., 2005) 054505, [`hep-lat/0406028`].

[81] **CP-PACS, JLQCD** Collaboration, S. Aoki et al., *Nonperturbative $O(a)$ improvement of the Wilson quark action with the RG-improved gauge action using the Schrödinger functional method*, *Physical Review D* **73** (Feb., 2006) 034501, [`hep-lat/0508031`].

[82] N. Cundy, M. Göckeler, R. Horsley, T. Kaltenbrunner, A. D. Kennedy, Y. Nakamura, H. Perlt, D. Pleiter, P. E. L. Rakow, A. Schäfer, G. Schierholz, A. Schiller, H. Stüben, and J. M. Zanotti, *Non-perturbative improvement of stout-smeared three flavour clover fermions*, *Physical Review D* **79** (May, 2009) 094507, [`0901.3302`].

[83] F. Tekin, R. Sommer, and U. Wolff, *Symanzik improvement of lattice QCD with four flavors of Wilson quarks*, *Physics Letters B* **683** (Jan., 2010) 75–79, [`0911.4043`].

[84] J. Bulava and S. Schaefer, *Improvement of $N_f = 3$ lattice QCD with Wilson fermions and tree-level improved gauge action*, *Nuclear Physics B* **874** (Sept., 2013) 188–197, [`1304.7093`].

[85] T. Bhattacharya, R. Gupta, W. Lee, S. R. Sharpe, and J. M. S. Wu, *Improved bilinears in lattice QCD with non-degenerate quarks*, *Physical Review D: Particles and Fields* **73** (2006), no. LA-UR-05-8131 034504, [`hep-lat/0511014`].

[86] M. Lüscher, *Advanced lattice QCD*, in *Les Houches Summer School in Theoretical Physics, Session 68: Probing the Standard Model of Particle Interactions*, no. DESY-98-017, p. 229, 1998. `hep-lat/9802029`.

[87] S. Khajenooriranjbar, *The Improved Vector and Tensor Current with Traditional and Stabilised Wilson Fermions*, Master's thesis, Universität Münster, Münster, Jan., 2025.

[88] M. D. Schwartz, *Quantum Field Theory and the Standard Model.* Cambridge University Press, New York, 2014.

[89] G. M. de Divitiis, P. Fritzsch, J. Heitger, C. C. Köster, S. Kuberski, and A. Vladikas, *Non-perturbative determination of improvement coefficients* b_m *and* b_A*-*b_P *and normalisation factor* $Z_m Z_P/Z_A$ *with* N_f*= 3 wilson fermions*, *The European Physical Journal C: Particles and Fields* **79** (Sept., 2019) 797, [`1906.03445`].

[90] J. Heitger, F. Joswig, P. L. J. Petrak, and A. Vladikas, *Ratio of flavour non-singlet and singlet scalar density renormalisation parameters in* N_f*=3 QCD with Wilson quarks*, `2101.10969`.

[91] M. Lüscher, S. Sint, R. Sommer, and H. Wittig, *Non-perturbative determination of the axial current normalization constant in O(a) improved lattice QCD*, *Nucl.Phys. B* **491** (1997) 344–364, [`hep-lat/9611015`].

[92] M. Lüscher, *Stochastic locality and master-field simulations of very large lattices*, *Epj Web of Conferences* **175** (2018) 01002, [`1707.09758`].

[93] A. Francis, P. Fritzsch, M. Lüscher, and A. Rago, *Master-field simulations of O(a)-improved lattice QCD: Algorithms, stability and exactness*, *Computer Physics Communications* **255** (Oct., 2020) 107355, [`1911.04533`].

[94] K. Symanzik, *Schrödinger representation and Casimir effect in renormalizable quantum field theory*, *Nuclear Physics B* **190** (July, 1981) 1–44.

[95] M. Lüscher, R. Narayanan, P. Weisz, and U. Wolff, *The Schrödinger functional — a renormalizable probe for non-abelian gauge theories*, *Nuclear Physics B* **384** (Oct., 1992) 168–228.

[96] S. Sint, *On the Schroedinger functional in QCD*, *Nuclear Physics B* **421** (June, 1994) 135–156, [`hep-lat/9312079`].

[97] M. Lüscher, *The Schrödinger functional in lattice QCD with exact chiral symmetry*, *Journal of High Energy Physics* **2006** (May, 2006) 042–042, [`hep-lat/0603029`].

[98] S. Cali, F. Knechtli, and T. Korzec, *How much do charm sea quarks affect the charmonium spectrum?*, *The European Physical Journal C* **79** (July, 2019) 607, [`1905.12971`].

[99] M. Maggiore, *A Modern Introduction to Quantum Field Theory.* Oxford University Press, 2005.

[100] E. Noether, *Invariante Variationsprobleme*, *Nachrichten von der Gesellschaft der Wissenschaften zu Göttingen, Mathematisch-Physikalische Klasse* **1918** (1918) 235–257.

[101] B. Pontecorvo, *Inverse Beta Processes and Nonconservation of Lepton Charge*, *Sov. Phys. JETP* **7** (1958) 172–173.

[102] Z. Maki, M. Nakagawa, and S. Sakata, *Remarks on the Unified Model of Elementary Particles*, *Progress of Theoretical Physics* **28** (Nov., 1962) 870–880.

[103] M. Kobayashi and T. Maskawa, CP-*Violation in the Renormalizable Theory of Weak Interaction*, *Progress of Theoretical Physics* **49** (Feb., 1973) 652–657.

[104] M. E. Peskin and D. V. Schroeder, *An Introduction to Quantum Field Theory.* Addison-Wesley, Reading, USA, 1995.

[105] N. Cabibbo, *Unitary Symmetry and Leptonic Decays*, *Physical Review Letters* **10** (June, 1963) 531–533.

[106] M. Marshall, *Lattice Determination of Semi-Leptonic, Heavy-Light Meson Decay Form Factors.* PhD thesis, The University of Edinburgh, Mar., 2024.

[107] M. Crisafulli, G. Martinelli, V. Hill, and C. Sachrajda, *A lattice study of semileptonic decays of d-mesons*, *Physics Letters B* **223** (June, 1989) 90–96.

[108] U. Wolff, *Monte Carlo errors with less errors*, *Computer Physics Communications* **156** (2003) 143, [`hep-lat/0306017`].

[109] W. K. Hastings, *Monte Carlo Sampling Methods Using Markov Chains and Their Applications*, *Biometrika* **57** (1970) 97–109.

[110] M. Luescher, *A Portable High-Quality Random Number Generator for Lattice Field Theory Simulations*, *Computer Physics Communications* **79** (Feb., 1994) 100–110, [`hep-lat/9309020`].

[111] S. Duane, A. Kennedy, B. J. Pendleton, and D. Roweth, *Hybrid Monte Carlo*, *Physics Letters B* **195** (Sept., 1987) 216–222.

[112] M. Lüscher, *Computational Strategies in Lattice QCD*, May, 2010.

[113] U. Wolff, *Critical slowing down*, *Nuclear Physics B - Proceedings Supplements* **17** (1990), no. BI-TP-89-35 93–102.

[114] N. Madras and A. D. Sokal, *The Pivot algorithm: A highly efficient Monte Carlo method for selfavoiding walk*, *Journal of Statistical Physics* **50** (1988) 109–186.

[115] M. D. Wilkinson, M. Dumontier, I. J. Aalbersberg, G. Appleton, M. Axton, A. Baak, N. Blomberg, J.-W. Boiten, L. B. da Silva Santos, P. E. Bourne, J. Bouwman, A. J. Brookes, T. Clark, M. Crosas, I. Dillo, O. Dumon, S. Edmunds, C. T. Evelo, R. Finkers, A. Gonzalez-Beltran, A. J. Gray, P. Groth, C. Goble, J. S. Grethe, J. Heringa, P. A. 't Hoen, R. Hooft, T. Kuhn, R. Kok, J. Kok, S. J. Lusher, M. E. Martone, A. Mons, A. L. Packer, B. Persson, P. Rocca-Serra, M. Roos, R. van Schaik, S.-A. Sansone, E. Schultes, T. Sengstag, T. Slater, G. Strawn, M. A. Swertz, M. Thompson, J. van der Lei, E. van Mulligen, J. Velterop, A. Waagmeester, P. Wittenburg, K. Wolstencroft, J. Zhao, and B. Mons, *The FAIR Guiding Principles for scientific data management and stewardship*, *Scientific Data* **3** (Mar., 2016) 160018.

[116] F. Joswig, S. Kuberski, J. T. Kuhlmann, and J. Neuendorf, *Pyerrors: A python framework for error analysis of Monte Carlo data*, `2209.14371`.

[117] C. R. Harris, K. J. Millman, S. J. van der Walt, R. Gommers, P. Virtanen, D. Cournapeau, E. Wieser, J. Taylor, S. Berg, N. J. Smith, R. Kern, M. Picus, S. Hoyer, M. H. van Kerkwijk, M. Brett, A. Haldane, J. F. del Río, M. Wiebe, P. Peterson, P. Gérard-Marchant, K. Sheppard, T. Reddy, W. Weckesser, H. Abbasi, C. Gohlke, and T. E. Oliphant, *Array programming with NumPy*, *Nature* **585** (Sept., 2020) 357–362, [`2006.10256`].

[118] D. Maclaurin, D. Duvenaud, and R. P. Adams, *Autograd: Effortless Gradients in Numpy*, in *ICML 2015 AutoML Workshop*, vol. 238, (IJCLab), p. 5, 2015.

[119] J. D. Hunter, *Matplotlib: A 2d graphics environment*, *Computing in Science & Engineering* **9** (2007), no. 3 90–95.

[120] Halchenko, Y. et al., "DataLad: Distributed system for joint management of code, data, and their relationship."

[121] F. Mölder, K. P. Jablonski, B. Letcher, M. B. Hall, C. H. Tomkins-Tinch, V. Sochat, J. Forster, S. Lee, S. O. Twardziok, A. Kanitz, A. Wilm, M. Holtgrewe, S. Rahmann, S. Nahnsen, and J. Köster, *Sustainable data analysis with Snakemake*, *F1000Research* **10** (Jan., 2021) 33.

[122] J. T. Kuhlmann, *On improvement and renormalisation of the axial current in three flavour lattice QCD with stabilised Wilson Fermions*, Master's thesis, Unisersität Münster, Apr., 2022.

[123] P. Fritzsch, J. Heitger, and J. T. Kuhlmann, *On improvement of the axial-vector current with stabilised Wilson fermions*, in *PoS*, vol. LATTICE2022, p. 287, Jan., 2023. `2212.11063`.

[124] P. Fritzsch, J. Heitger, F. Joswig, and J. T. Kuhlmann, *Towards charm physics with stabilised Wilson fermions*, in *40th International Symposium on Lattice Field Theory*, Jan., 2024. `2401.05885`.

[125] J. Bode, *Non-perturbative renormalisation of quark currents in QCD with three flavours of Wilson fermions using the chirally rotated Schrödinger functional*, Master's thesis, Universität Münster, Münster, July, 2024.

[126] M. Lüscher, S. Schäfer, J. Bulava, I. Campos, and A. Rago, "openQCD, simulation programs for lattice QCD."

[127] C. Wittemeier, *Implementation of a program for QCD and HQET correlation functions in the Schrodinger functional*, Master's thesis, Westfälische Willhelms Universität Münster,, 2012.

[128] R. Sommer, *Scale setting in lattice QCD*, Jan., 2014.

[129] M. Lüscher, *Properties and uses of the Wilson flow in lattice QCD*, *JHEP* **08** (2010) 071, [`1006.4518`].

[130] M. Lüscher and P. Weisz, *Perturbative analysis of the gradient flow in non-abelian gauge theories*, *Journal of High Energy Physics* **2011** (Feb., 2011) 51, [`1101.0963`].

[131] M. Lüscher, *Chiral symmetry and the Yang–Mills gradient flow*, *JHEP* **04** (2013), no. 123 123, [`1302.5246`].

[132] M. Bruno, T. Korzec, and S. Schaefer, *Setting the scale for the CLS* $2+1$ *flavor ensembles*, *Physical Review D* **95** (Apr., 2017) 074504, [`1608.08900`].

[133] **RQCD** Collaboration, G. S. Bali, S. Collins, P. Georg, D. Jenkins, P. Korcyl, A. Schäfer, E. E. Scholz, J. Simeth, W. Söldner, and S. Weishäupl, *Scale setting and the light baryon spectrum in N_f=2+1 QCD with Wilson fermions*, `2211.03744`.

[134] M. Gell-Mann, R. J. Oakes, and B. Renner, *Behavior of Current Divergences under SU 3 × SU 3*, *Physical Review* **175** (Nov., 1968) 2195–2199.

[135] M. Guagnelli, J. Heitger, R. Sommer, and H. Wittig, *Hadron Masses and Matrix Elements from the QCD Schrödinger Functional*, *Nuclear Physics B* **560** (Nov., 1999) 465–481, [`hep-lat/9903040`].

[136] M. Della Morte, R. Hoffmann, and R. Sommer, *Non-perturbative improvement of the axial current for dynamical Wilson fermions*, *JHEP* **03** (2005), no. DESY-05-026, HU-EP-05-08, SFB-CPP-05-07 029, [`hep-lat/0503003`].

[137] T. Kaneko, S. Aoki, M. D. Morte, S. Hashimoto, R. Hoffmann, and R. Sommer, *Non-perturbative improvement of the axial current with three dynamical flavors and the Iwasaki gauge action*, *Journal of High Energy Physics* **2007** (Apr., 2007) 092–092, [`hep-lat/0703006`].

[138] J. Bulava, M. D. Morte, J. Heitger, and C. Wittemeier, *Non-perturbative improvement of the axial current in N_f=3 lattice QCD with Wilson fermions and tree-level improved gauge action*, *Nuclear Physics B* **896** (May, 2015) 555–568, [`1502.04999`].

[139] M. Della Morte, R. Hoffmann, F. Knechtli, R. Sommer, and U. Wolff, *Non-perturbative renormalization of the axial current with dynamical Wilson fermions*, *JHEP* **07** (2005), no. HU-EP-05-23, SFB-CPP-05-18, DESY-05-064 007, [`hep-lat/0505026`].

[140] S. Aoki, K.-i. Nagai, Y. Taniguchi, and A. Ukawa, *Perturbative renormalization factors of bilinear quark operators for improved gluon and quark actions in lattice QCD*, *Phys. Rev. D* **58** (1998) 074505, [`hep-lat/9802034`].

[141] P. Korcyl and G. S. Bali, *Non-perturbative determination of improvement coefficients using coordinate space correlators in $N_f = 2+1$ lattice QCD*, *Physical Review D* **95** (Jan., 2017) 014505, [`1607.07090`].

[142] S. Sint, *The chirally rotated Schrödinger functional with Wilson fermions and automatic O(a) improvement*, *Nuclear Physics B* **847** (2011) 491–531, [`1008.4857`].

[143] M. Dalla Brida, S. Sint, and P. Vilaseca, *The chirally rotated Schrödinger functional: Theoretical expectations and perturbative tests*, `1603.00046`.

[144] M. Dalla Brida, T. Korzec, S. Sint, and P. Vilaseca, *High precision renormalization of the flavour non-singlet Noether currents in lattice QCD with Wilson quarks*, *The European Physical Journal C: Particles and Fields* **79** (Jan., 2019) 23, [`1808.09236`].

[145] M. Della Morte, R. Sommer, and S. Takeda, *On cutoff effects in lattice QCD from short to long distances*, *Physics Letters B* **672** (Mar., 2009) 407–412.

[146] J. Bulava, M. D. Morte, J. Heitger, and C. Wittemeier, *Non-perturbative renormalization of the axial current in $N_\mathrm{f} = 3$ lattice QCD with Wilson fermions and tree-level improved gauge action*, *Physical Review D: Particles and Fields* **93** (June, 2016) 114513, [`1604.05827`].

[147] P. Fritzsch, "private communications." 2025.

[148] J. Heitger and F. Joswig, *The renormalised O(a) improved vector current in three-flavour lattice QCD with Wilson quarks*, *The European Physical Journal C: Particles and Fields* **81** (Mar., 2021) 254, [`2010.09539`].

[149] P. Fritzsch, *Mass-improvement of the vector current in three-flavor QCD*, *JHEP* **06** (June, 2018) 015, [`1805.07401`].

[150] A. Gerardin, T. Harris, and H. B. Meyer, *Non-perturbative renormalization and $O(a)$-improvement of the non-singlet vector current with $N_\mathrm{f} = 2 + 1$ Wilson fermions and tree-level Symanzik improved gauge action*, *Physical Review D* **99** (Jan., 2019) 014519, [`1811.08209`].

[151] J. Heitger, F. Joswig, A. Vladikas, and C. Wittemeier, *Non-perturbative determination of c_V, Z_V and Z_S/Z_P in N_f=3 lattice QCD*, *Epj Web of Conferences* **175** (2018), no. MS-TP-17-17 10004, [`1711.03924`].

[152] M. Guagnelli and R. Sommer, *Nonperturbative O(a) improvement of the vector current*, *Nuclear Physics B - Proceedings Supplements* **63** (1998), no. DESY-97-173, CERN-TH-97-256 886–888, [`hep-lat/9709088`].

[153] S. Sint and P. Weisz, *Further results on O(a) improved lattice QCD to one-loop order of perturbation theory*, *Nuclear Physics B* **502** (Sept., 1997) 251–268, [`hep-lat/9704001`].

[154] M. Guagnelli, R. Petronzio, J. Rolf, S. Sint, R. Sommer, and U. Wolff, *Nonperturbative results for the coefficients b_m and $(b_A - b_P)$ in $O(a)$ improved lattice QCD*, *Nuclear Physics B* **595** (2001), no. DESY-00-131, HUB-EP-00-32, ROM2F-2000-28 44–62, [`hep-lat/0009021`].

[155] P. Fritzsch, J. Heitger, and N. Tantalo, *Non-perturbative improvement of quark mass renormalization in two-flavour lattice QCD*, *JHEP* **08** (2010), no. MS-TP-10-06, SHEP-1010 074, [`1004.3978`].

[156] C. C. Köster, *Non-peturbative Determination of Improvement Coefficients and Renormalization Factors in Three-Flavor lattice Quantum Chromodynamics with Wilson Quarks*, Master's thesis, Unisersität Münster, Münster, June, 2020.

[157] F. Cuteri, A. Francis, P. Fritzsch, G. Pederiva, A. Rago, A. Shindler, A. Walker-Loud, and S. Zafeiropoulos, *Gauge generation and dissemination in OpenLat*, Feb., 2023.

[158] F. Cuteri, A. Francis, P. Fritzsch, G. Pederiva, A. Rago, A. Shindler, A. Walker-Loud, and S. Zafeiropoulos, *Progress in generating gauge ensembles with Stabilized Wilson Fermions*, in *PoS*, vol. LATTICE2023, p. 048, Dec., 2023. `2312.11298`.

[159] Antonin Portelli, N. Lachini, F. Erben, F. Joswig, mmphys, rrhodgson, Fionn Ó hÓgáin, guelpers, P. A. Boyle, N. Asmussen, A. Barone, RChrHill, JPRichings, rabbott99, S. Bürger, J. Lee, and rabbott999, "Aportelli/Hadrons: Hadrons v1.4." Zenodo, June, 2023.

[160] P. A. Boyle, A. Yamaguchi, G. Cossu, and A. Portelli, *Grid: A next generation data parallel C++ QCD library*, `1512.03487`.

[161] J. Heitger, F. Joswig, and S. Kuberski, *Determination of the charm quark mass in lattice QCD with 2+1 flavours on fine lattices*, *JHEP* **05** (May, 2021) 288, [`2101.02694`].

[162] S. Kuberski, F. Joswig, S. Collins, J. Heitger, and W. Söldner, *D and D_s decay constants in $N_\mathrm{f} = 2 + 1$ QCD with Wilson fermions*, `2405.04506`.

[163] B. Colquhoun, L. J. Cooper, C. T. H. Davies, and G. P. Lepage, *Precise determination of decay rates for $\eta_c \to \gamma\gamma$, $J/\psi \to \gamma\eta_c$ and $J/\psi \to \eta_c e^+ e^-$ from lattice QCD*, *Physical Review D* **108** (July, 2023) 014513, [`2305.06231`].

[164] J. Heitger, F. Joswig, and S. Kuberski, *Towards the determination of the charm quark mass on N_f=2+1 CLS ensembles*, in *PoS*, vol. LATTICE2019 of *PoS*, p. 092, Oct., 2019. `1909.05328`.

[165] I. Campos, P. Fritzsch, C. Pena, D. Preti, A. Ramos, and A. Vladikas, *Non-perturbative quark mass renormalisation and running in N_f=3 QCD*, *Eur. Phys. J. C78 (2018) no.5, 387* **78** (May, 2018) 387, [`1802.05243`].

[166] A. Bussone, A. Conigli, J. Frison, G. Herdoíza, C. Pena, D. Preti, A. Sáez, and J. Ugarrio, *Hadronic physics from a Wilson fermion mixed-action approach: Charm quark mass and $D_{(s)}$ meson decay constants*, Sept., 2023.

[167] A. Bazavov, C. DeTar, A. X. El-Khadra, E. Gámiz, Z. Gelzer, S. Gottlieb, W. I. Jay, H. Jeong, A. S. Kronfeld, R. Li, A. T. Lytle, P. B. Mackenzie, E. T. Neil, T. Primer, J. N. Simone, R. L. Sugar, D. Toussaint, R. S. V. de Water, and A. Vaquero, *D-meson semileptonic decays to pseudoscalars from four-flavor lattice QCD*, *Physical Review D* **107** (May, 2023) 094516, [`2212.12648`].

[168] P. Boyle, L. D. Debbio, F. Erben, J. Flynn, A. Jüttner, M. Marshall, A. Portelli, J. T. Tsang, and O. Witzel, *Semileptonic $D \to \Pi\ell N$, $D \to K\ell\nu$ and $D_s \to K\ell\nu$ decays with 2+1f domain wall fermions*, Jan., 2022.

[169] R. Evans, G. Bali, and S. Collins, *Improved Semileptonic Form Factor Calculations in Lattice QCD*, *Physical Review D* **82** (Nov., 2010) 094501, [`1008.3293`].

[170] F. Joswig, J. T. Kuhlmann, S. Kuberski, and J. Neuendorf, "Pyerrors."

[171] C. Wittemeier and F. Joswig, *Correlation Functions in SFCF, documentation to SFCF.* ALPHA collaboration, 2019.

Lebenslauf